OPTICAL AND MAGNETIC MANIPULATION OF HYBRID MICRO AND NANOPARTICLE SENSORS

by

Rodney Ray Agayan

A dissertation submitted in partial fulfillment
of the requirements for the degree of
Doctor of Philosophy
(Applied Physics)
in The University of Michigan
2008

Doctoral Committee:

Professor Raoul Kopelman, Chair
Professor Charles R. Doering
Professor Theodore B. Norris
Associate Professor Alan J. Hunt
Associate Professor Jens-Christian D. Meiners

“I learned this, at least, by my experiment: that if one advances confidently in the direction of his dreams, and endeavors to live the live which he has imagined, he will meet with a success unexpected in common hours. He will put some things behind, will pass an invisible boundary; new, universal, and more liberal laws will begin to establish themselves around and within him, or the old laws be expanded, and interpreted in his favor in more liberal sense, and he will live with the license of a higher order of beings. In proportion as he simplifies his life, the laws of the universe will appear less complex, and solitude will be not be solitude, nor poverty poverty, nor weakness weakness. If you have built castles in the air, your work need not be lost; that is where they should be. Now put the foundations under them.”

–Henry David Thoreau, *Walden*

DEDICATION

For Jenny

ACKNOWLEDGMENTS

First and foremost, I would like to thank my research advisor Professor Raoul Kopelman. His creativity, never-ending enthusiasm, and absolute love of science have been infectious from the start. Even to this day, I am continually amazed by his insight and breadth of knowledge, both intellectually and personally. Despite the almost insurmountable challenges that ensued, I will always appreciate the sense of freedom he's given me to pursue whatever direction I wanted, and, ultimately, to become an independent researcher.

I would also like to thank my committee members for their support, even after all these years. To Professor Ted Norris, whose series of optics classes were some of the most memorable examples of high quality teaching as well as high volume note-taking. I thank Professor Charlie Doering for agreeing to serve on my committee, having conversed with me via email only a few semesters before my defense. Even as an acquaintance, he revealed to me the value of knowing a theoretical mathematician who can eloquently explain my abstract notions and turn them into meaningfully tangible equations.

Also deserving acknowledgment are a number of collaborators, without whom none of this work would have been possible. Thanks to Professor Christoph Schmidt who collaborated with Professor Kopelman and essentially got me started with optical tweezers. We needed a microscope and some expertise, he needed a new applied physics student to absorb as much information as possible – it was the perfect collaboration. I also thank Professor Fred Gittes and Erwin Peterman who helped out with much of the original resonance trapping theory and experiment. The International Institute also aided in funding further collaboration at the Vrije Universiteit in the Netherlands. Thanks to Professor Roy Clarke and Vladimir Stoica, who provided helpful discussions on magnetism and let me borrow their Gauss probe on many occasions.

I thank Nancy Kerner for supporting me so many semesters and giving me an opportunity to see how creative teaching can truly be.

In my 'ten-ure' in the Kopelman Lab, the number of group members deserving my gratitude is truly too high to list. I am especially grateful to Eric Monson, whose sense of design and penchant for visualization inspired my own interests in the same fields. To Susan Barker, who provided me with a place to stay during a few weeks of my first summer in Ann Arbor. To Steve Parus, for fixing the argon laser AND the Tsunami AND the spectrometers AND… Special thanks to Brandon McNaughton, for getting me into nonlinear dynamics, for being an applied physicist in this sea of chemists, as well as for just being a good friend. Thanks to Ron Smith for these last minute excursions and for eating out three to four times a week.

I would also like to thank Manix Narayanan and Aarthi Rao for housing me this last semester, your kindness sees no end. Thanks to Ravin, it's comforting to have someone fighting the same battles at the same time.

Some other influences I would like to thank: Bill Banyai, a true inter-disciplinarian who helped me get into graduate school and Thomas J. Walsh, my high school physics teacher who introduced me to my first laser.

Last but not least, I thank my family and friends. Thanks to my parents and my sister for their long distance support. My deepest gratitude goes to my fiancée, Jenny – Thank You for putting up with me and the life of a scientist during this entire process.

This work was supported by NSF grant DMR 0455330, NCI contract NO1-CO-37123 and NIH grant R21CA125297-01A1.

TABLE OF CONTENTS

CHAPTER

LIST OF FIGURES

LIST OF TABLES

ABSTRACT

OPTICAL AND MAGNETIC MANIPULATION OF HYBRID MICRO AND NANOPARTICLE SENSORS

by

Rodney Ray Agayan

Chair: Raoul Kopelman

Microparticles and nanoparticles have been used in a wide variety of applications ranging from biomedical to optical and electronic technologies. The microscopic and mesoscopic size scale of single particles makes them ideal tools for probing the local environments of biological cells, sensing the viscous properties of fluids and surfaces on the microscale, and interacting with photonic and magnetic fields. But the effectiveness of these particle systems is limited by the ability to manipulate and control them in predictable ways.

In this work, two methods of microparticle and nanoparticle manipulation are investigated, namely optical tweezers (OT) and magnetic rotation. OT provide a mechanically non-invasive means of grasping microparticles and nanoparticles, utilizing focused laser light. Moreover, particles driven by magnetic rotation in viscous media exhibit nonlinear dynamical motion and are a subclass of systems known as nonuniform oscillators. Both the individual and combined synergistic use of these control schemes is

studied, in particular, on hybrid particles systems comprised of several materials, including both dielectric microspheres and metallic or magnetic colloids.

Classical electromagnetic theory was developed to describe the wavelength dependence of OT forces acting on a trapped, resonantly absorptive particle. Enhancements in the trapping strength could be obtained via near-resonance tuning of the laser wavelength. Experimental observation of this phenomenon on our hybrid particles was inhibited by increased destabilizing forces at the micron scale and the emergence of heating effects at high laser intensities often used in OT.

Using reduced laser intensities in conjunction with magnetic rotation, hybrid particles could be two-dimensionally trapped and rolled at a substrate surface. Changes in the nonlinear dynamical motion of the particles were measured to distinguish particle roughness and surface friction.

The response of rigid dimers of hybrid particles to optical and magnetic manipulation was studied. Observed changes in the dynamical motion with increased optical perturbation strength, using both numerical modeling and experiment, were investigated in terms of scattering forces, magnetization and heat generation from absorptive interactions.

Finally, the escape into the third-dimension of a magnetic dimer of hybrid particles undergoing nonuniform rotation was studied experimentally and compared to both theory and numerical simulation.

CHAPTER 1

INTRODUCTION

At its inception, the work described in this thesis was originally motivated by the desire to optically manipulate nanosensors for cellular measurements. The difficulties of stably trapping and controlling nanoscale, dielectric sensors and the reality of heat generation with metallic nanosensors complicated our use of optical tweezers for intra-cellular sensing. Combined optical and magnetic manipulation schemes, however, offered extra-cellular control for both micro- and nanoscale probes. For completeness, the original motivations are described as well as the rationale that encouraged the evolution of later experiments.

The direction of research in the Kopelman Group, as well as in many general fields of biotechnology, has been towards the creation of micro- and nanoscale probes for a variety of intra- and extra-cellular applications. The development of PEBBLE (Photonic Explorers By Biologically Localized Embedding) technology [1, 2] has provided a platform for sub-cellular, biochemical analyte imaging inside living cells as well as photodynamic therapy of brain cancers. But with the development of nanoscale sensors comes the natural desire to control and manipulate them non-invasively on an individual basis. Optical and magnetic manipulation schemes have been proposed as possible means of providing this single-particle control. Hybrid particle systems comprised of different materials of both micron and nanometer size can afford further utility as long as the salient features of the system as a whole supersede the potential incompatibility of the distinct materials themselves. This thesis serves to describe many features of such optical and magnetic manipulation of hybrid particle sensors.

1.1 PEBBLE Sensors

In the last several decades, biosensing technology in the Kopelman Group has experienced a gradual trend towards smaller and smaller probe sizes (see Figure 1.1). The miniaturization of microelectrodes and fiber optic sensors has improved detection limits and response times [3-5]; however, simultaneous insertion of multiple sensors of these kinds can cause considerable physical perturbation to the cell. Fluorescent indicator dyes have been developed which are capable of sensing numerous biologically significant analytes (i.e., sodium, potassium, calcium, chloride, H+), as well as gases (i.e., oxygen, carbon dioxide, and nitric oxide). Although their small size makes them physically non-invasive, these dye molecules may affect a cell chemically, or even poison it. In addition, components in the cell such as proteins may interfere, affecting the dye's response, or the dye molecules may be sequestered into cell organelles or membranes.

In order to combine the physical non-invasiveness, speed, and reduced detection limit of dye molecules with the chemical non-invasiveness, sensitivity and selectivity of fiber probes, our group has developed fluorescent nanosphere sensors known as PEBBLEs. These PEBBLEs are porous polymer or glass spheres containing, among other components, fluorescent indicator dyes. Their small size, roughly 20-200 nm in diameter, reduces the physical perturbation to the cell. The pores in the biocompatible matrix are large enough to allow the appropriate analytes to diffuse in, but small enough to prevent proteins from entering the PEBBLE, as well as preventing dye molecules from escaping and being sequestered in the cell.

Our group has utilized several delivery schemes to place PEBBLEs inside cells, nevertheless each method has it drawbacks. Administering probes via pico-injection is physically invasive, and specifying location within the cell is mechanically difficult. Delivery of PEBBLEs using the gene gun method is less invasive, but controlled positioning of probes is practically unfeasible. Non-invasive liposomal delivery is also non-specific, dispensing most probes to the cytoplasm, and its efficacy can depend on cell type. All three methods suffer from the inability to controllably position the probes to specific regions of interest in the cell, for example near organelles, next to ion channels, or within the nucleus.

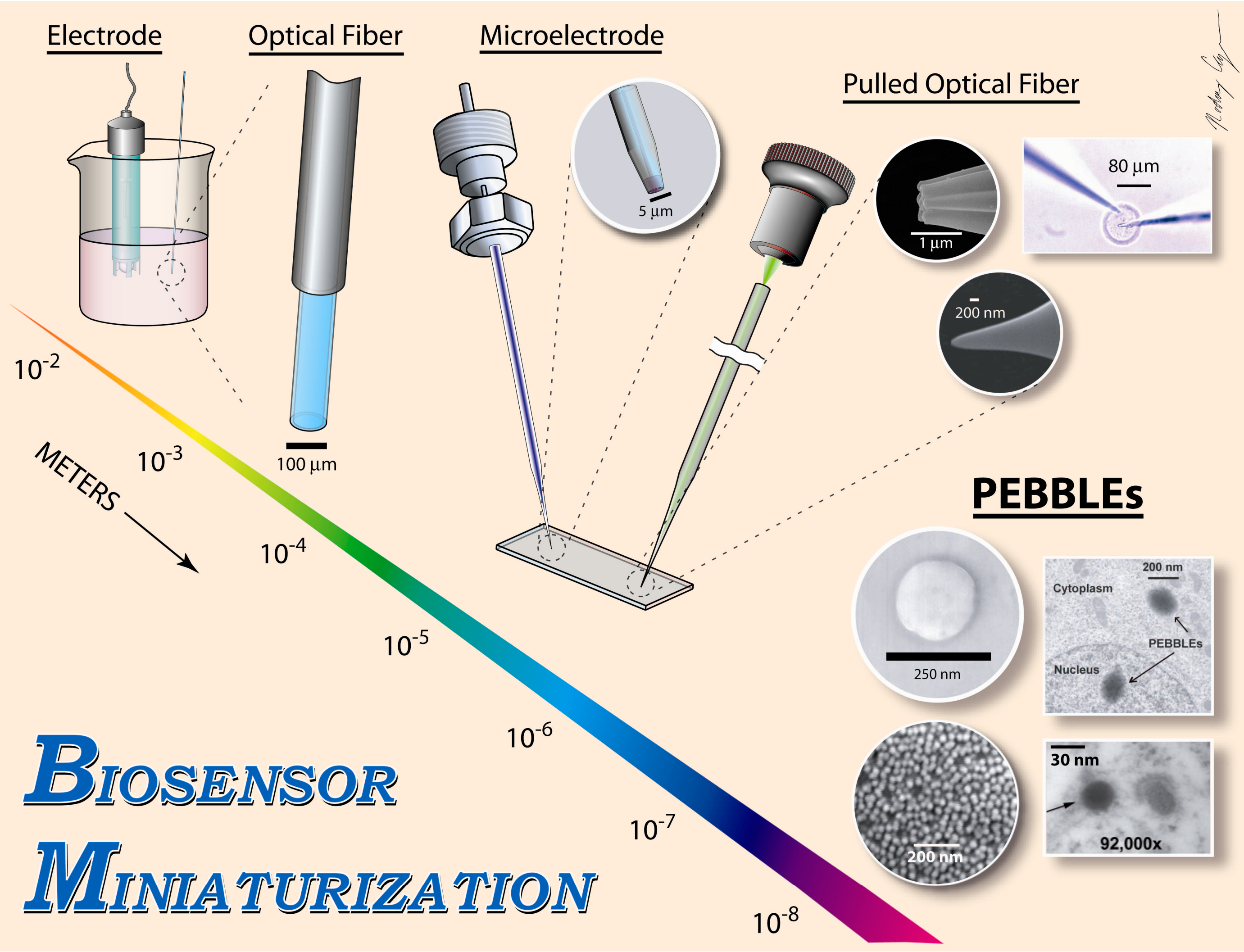

Figure 1.1 Research directions of the Kopelman Group: biosensor miniaturization in the last several decades.

To measure the underlying mechanism of ion concentrations in cellular functions or monitor analyte transport properties across cell membranes using PEBBLEs, ideally, one would like the capability of maneuvering a single nanoscale probe to precise locations within and around the cell. One must be able to manipulate the probe firmly enough without disturbing either the cell's activity or the probe's functionality. Manipulation methods using optical radiation or magnetic fields offer potential solutions.

1.2 Optical and Magnetic Manipulation

1.2.1 Optical Tweezers

Optical tweezers are a mechanically non-invasive means of grasping microparticles and nanoparticles using focused laser light [6-9]. They have been used to manipulate organelles and sub-cellular structures within the cytosol of plant cells [10-12], amoeba [13], and mitotic cells [14]. PEBBLEs have also been trapped with optical tweezers to measure the local pH in water and near a glass interface [15]. Because watery, biological samples tend to be optically similar to PEBBLE matrices (index of refraction $n \sim 1.33\text{-}1.5$), intra-cellular optical tweezing of the probes sometimes results in the movement of cellular components as well. To control a PEBBLE, one must develop a means of specifically manipulating only the probe while maintaining the cell environment as relatively optically transparent to the trapping light.

Gold colloids of 40 nm diameter are known to undergo increased trapping strengths compared to polystyrene spheres of similar size due to the increased optical volume, or polarizability [16]. It has also been suggested in the literature [8] that absorptive particles with resonantly large polarizabilities should experience enhanced optical tweezing forces. In Chapter 2, we develop theory that predicts the occurrence of these enhancements with proper tuning of the laser wavelength near resonance [17, 18]. Such a property is especially attractive for trapping metallic colloids in which plasmon resonances can be excited to generate enhanced radiation forces [19]. Furthermore, particles that exhibit strong surface-enhanced Raman scattering (SERS) signals can experience optically induced aggregation, or "optical binding," using optical tweezers [20].

1.2.2 Magnetic Rotation

Magnetic manipulation has also been used to control magnetic particles of micron or nanometer size for a variety of biological applications [21-24]. Magnetic tweezers, analogous to optical tweezers, require high magnetic field gradients to apply translational forces on magnetic particles for intra-cellular studies [25-27]. Such gradients can be generated within the vicinity (~microns) of arrangements of magnetic pole structures using permanent magnets or electromagnets with iron cores. Stably trapping ferromagnetic particles in three-dimensions is difficult due to the magnetic analog of the Optical Earnshaw theorem [9]. Alternatively, using uniform magnetic fields or at distances far from magnetic pole structures, magnetic particles no longer experience strong translational forces, but they can still be oriented rotationally to align with the external field. The latter magnetic rotation schemes have been employed extensively in the Kopelman Group for a variety of applications [28-33] including improvement of signal-to-background measurements in microscopy imaging [34] and bacteria detection [35]. In this thesis, only orientational magnetic tweezing of this type was considered.

1.2.3 Dynamical Motion

Particles that are either optically trapped or magnetically rotated in viscous media can undergo measurable changes in their dynamical motion which enable their use as sensors of the local environment. For example, the low frequency components of the translational Brownian fluctuations of a particle in an optical trap are damped in comparison to those for free-diffusion [36]. This effect can be quantified by observing microscopic position fluctuations of the particle in the frequency domain. The characteristic frequency which signals the transition from damped low-frequency components to unaffected high-frequency components depends on both the trap stiffness and the viscosity of the surrounding fluid. By measuring this characteristic frequency as a function of laser intensity, we observed a decrease in the fluid viscosity due to increased temperatures resulting from light absorption of our hybrid particles (Chapter 3).

Magnetic particles driven by magnetic rotation in viscous media exhibit nonlinear dynamical motion and are a subclass of systems known as nonuniform oscillators [37].

At low frequencies, the particles orient to align with the rotating magnetic field resulting in synchronous rotation. At frequencies higher than can be supported by viscous drag, the particles can exhibit asynchronous, nonlinear, oscillatory motion. The equations that govern such motion can also describe a driven, overdamped pendulum in viscous media, the synchronization of flashing fireflies, as well as the dynamics of Josephson junctions [37].

Changes in the nonlinear dynamical motion of the particles near a surface were measured to distinguish particle roughness and surface friction (Chapter 4). With combined optical illumination and magnetic rotation, further modification of the nonlinear dynamics was observed using both numerical modeling and experiment. The results were investigated in terms of trapping forces, magnetization and heat generation from absorptive interactions (Chapter 4-6). At high frequencies, magnetic particles can also escape the expected plane of rotation. Observations of this three-dimensional oscillatory motion of extended magnetic particles was compared to theory previously developed by Caroli and Pincus [38].

1.3 Hybrid Particle Systems

The entities that are manipulated and described here have been termed “hybrid particles.” The definition of a hybrid particle assumed throughout this thesis is any heterogeneous particle system that can be tailored to the demands of the experiment. Numerous core-shell architectures have been developed which utilize the optical properties of a metallic or semiconductor core combined with a specified shell to modify functionalization and dispersion properties for such applications as drug delivery, catalysis, and colloidal assembly, to name just a few [39-41]. The individual materials often serve different functions while the combination can provide multiplexing capabilities or enhanced performance. For example, efficient energy flow devices have been developed using composites formed by blending inorganic quantum dots and organic conjugated polymers [42]. The photophysical properties of the semiconductors combined with the processing capabilities of the polymer leads to improved fabrication materials. The probe constituents considered here tend to include polymeric or glass matrices, fluorophores, and magnetic or metal colloids, either micro- or nanoscale.

PEBBLEs themselves can be considered hybrid moieties which may contain other components in addition to fluorescent dyes. Ionophores and enzymes can be added to change the selectivity for certain analytes using tandem-sensing schemes. Multiple dyes can be placed in a single PEBBLE to enable simultaneous sensing of different chemical species, or provide a means of ratiometric self-calibration. Also, antibodies may be attached to the outside of the PEBBLE to allow targeted positioning.

Another specific type of hybrid particle involves nanoparticles consisting of dielectric cores coated by metallic shells (core-shells) that exhibit strong surface plasmon resonances [43-45]. Plasmon resonances are collective oscillations of the conduction electrons of noble metals such as gold, silver, and platinum. The shells may be complete coatings or comprised of many individual nanoparticles. A prominent feature of these hybrid plasmonic core-shell systems is that the wavelength of the resonance can be tuned by the shape and size of the nanoparticles as well as the relative thickness of the outer shell compared to the core [46-50]. Such a property complements the enhanced optical tweezing effects previously mentioned.

A third class of hybrid particles considered in this thesis is characterized as dielectric cores half-coated with metallic shells. The anisotropy of these particles, either optical [28-33, 46, 51-54], magnetic [28-33, 46, 54], or electric [51] depending on the shell material, makes them exemplary devices for signaling rotational fluctuations, inducing preferential orientation in external fields, or enabling directed self-assembly in collections of particles. Rigid dimers or doublets of individual hybrid particles, either core-shell or half-coated, can also provide this anisotropy.

1.4 Challenges

The manipulation of hybrid particles with potentially conflicting material properties poses serious challenges. For example, the move towards smaller PEBBLEs has been prompted by their distinct advantages: minimal physical invasiveness, higher spatial resolution, faster response speed, and lower absolute detection limit. One disadvantage for smaller PEBBLEs, however, is the increased difficulty of controlling them with optical tweezers. Maximal trapping force scales with particle volume for particles small compared with the laser wavelength. Thus, a method for maximizing the trapping force at small probe sizes is desirable. A selective enhancement of trapping strength would also provide a degree of specificity in optical tweezing, i.e., enable one to trap only probe particles in a crowded environment, such as the inside of a cell.

By incorporating metallic colloids or other particles that experience enhanced trapping forces into our PEBBLEs, only the probe becomes preferentially trappable compared to cellular constituents, and optical tweezing specificity can be obtained. A potential drawback to this solution, however, is the notion that these metallic colloids can generate significant heat due to absorption at the high laser intensities typically required for single-beam gradient optical tweezing. This property has even been considered as a means for photo-thermal therapeutic medicine [55]. The temperature increase at the focus of a trapping beam in water ranges from 10-30° K/W depending on the laser wavelength and trapped object (cells, liposomes, polystyrene or silica microspheres) [56-60] and up to 44° K/W in glycerol [61]. In the presence of highly absorbing metallic structures, heating is significantly increased by a factor of 5-20 [62-64], again depending on the wavelength, solution, metal material, and number of colloids in the focus. Seol et al. calculated the rise in the surface temperature of a 50 nm gold colloid to be 266° K/W [64].

In an effort to reduce complications due to heat generation of metallic colloids, we sought to trap micron sized silica cores with colloidal gold shells with low particle loading and minimized colloid aggregation (Chapter 3). The larger transparent silica cores were easily trappable, while the absorptive metallic colloids in their reduced number might still provide an enhancement. Although heating was still apparent, these hybrid particle systems proved useful for later experiments, especially when magnetic material was incorporated into the surrounding shell.

Dielectric-metal core-shell magnetic hybrid particles pose their own challenges. Translational radiation forces due to optical tweezers at typical laser intensities (10^6 – 10^7 W/cm^2) are much larger than translational magnetic forces when the magnetic pole structure is far from the sample or the magnetic field gradient is weak. In contrast, magnetic rotational torques tend to be much larger than analogous optical torques, although at these laser intensities, orientational alignment of absorptive particles may not be negligible and magnetic colloid loading may need to be adjusted. Magnetic colloid loading also influences the stability of the optical trap. Incorporation of metallic or magnetic colloids also increases hybrid particle density, thus encouraging sedimentation in fluidic samples. Glycerol-water mixtures or other solutions may be needed to perform experiments away from surfaces. Furthermore, strong optical tweezing forces are confined to particles that lie within the optical trap. Uniform magnetic fields affect all ferromagnetic particles within the field region while the particles themselves can affect the dynamics of other particles in close proximity. Although this problem is easily circumvented by use of low particle concentrations, it does restrict the minimum allowable spatial distance between magnetic probe measurements. Tailoring both the components of the particle system and the applied manipulation schemes is possible and likely necessary to facilitate the use of hybrid particle systems as valuable sensing tools.

This thesis is ordered almost chronologically, in part because ideas and concepts that were developed and learned in the early projects provided knowledge to help us devise and accomplish new experiments. More specific details of the chapters are as follows:

Chapter 2 is the publication found in Ref. [18], parts of which were also published in an SPIE paper found in Ref. [17]. This chapter introduces much of the literary background for optical tweezers and provides a classical electromagnetic theoretical treatment for describing the gradient and scattering forces on Rayleigh particles in a paraxially focused laser beam as a function of the laser wavelength. The original publication included enhancements of up to 50 times; however, minor portions of the numerical analysis were in error. The corrected sections are provided in this thesis. The corrected enhancements of trapping stiffness are smaller, but an additional section was added showing that larger enhancements could be achieved with materials having narrower absorption linewidths.

Chapter 3 was published as an SPIE paper found in Ref. [65]. This chapter introduces the experimental realization of optical tweezing and explores the attempt at observing enhanced optical tweezing stiffness for a variety of hybrid particles, each comprised of several materials. One class of particles was made of dielectric microspheres embedded with fluorescent dye. Another consists of dielectric-metal, core-shell microparticles. The fluorescent dye-loaded samples did not exhibit the hoped for strong resonance enhancement, a result assumed to be due to the low dye-loading efficiency. The core-shell microspheres did show increased trap stiffness, but it was determined that this observation was due to increased heat absorption caused by the metallic colloidal shell covering these microspheres. Dielectric cores half-coated with metal could not be measured as they could not be stably trapped with single-beam gradient optical tweezers.

Chapter 4 looks at the experimental manipulation of hybrid microspheres comprised of polystyrene cores with shells of magnetic colloids. These particles could not be trapped three dimensionally with single beam gradient optical tweezers, but they could be confined radially on top of a glass surface. The addition of a rotating magnetic field enabled these microspheres to roll while slipping along the surface. Two magnetic microsphere types with different roughness, as well as two different glass surfaces, one untreated and one PEGylated, were tested. Indications of nonlinear rolling motion that resembled the motion of nonuniform oscillators appeared. This chapter will be submitted for publication in the Journal of Applied Physics.

Chapter 5 is an in-depth numerical study of the combined optical and magnetic rotational manipulation of an absorptive/scattering particle. The equations that govern the motion of a standard nonuniform oscillator are derived and the effect of the strength of the added optical perturbation is studied. The interplay between optical and magnetic torques is investigated using numerical analysis techniques to reveal the nonlinear motional dynamics that result. The relevance of these results to experimental considerations is also addressed. This chapter will be submitted for publication in Physical Review E.

Chapter 6 is an account of the experimental methods used to observe nonuniformly rotating particles and to consistently analyze the data recorded, i.e. without human bias. These techniques were used in two publications, Refs. [54, 66]. The addition of an optical perturbation is also looked at. Results revealed that the observed increase in rotation rate was most likely due to heat absorption caused by the magnetic colloids of the microsphere systems. This chapter will be submitted for publication in the Journal of Magnetism and Magnetic Materials.

Chapter 7 is an experimental and numerical corroboration of the Caroli and Pincus theory on the three-dimensional response of a magnetic grain in a rotating magnetic field [38]. The qualitative features of the dynamic motion are found to be consistent in all methods of analysis. Two regimes of motion were observed: one was rotation restricted to a plane; the other was rotation such that the particle's easy axis traced out the surface of a cone in 3-dimensional space. This chapter will be submitted for publication in Physical Review E.

CHAPTER 2

OPTICAL TRAPPING NEAR RESONANCE ABSORPTION

Since Ashkin and colleagues' original work on optical trapping [67], the effect of radiation forces on atoms and dielectric particles has been exploited greatly. Although different theoretical models can be used to calculate optical forces for different configurations and particle-size regimes, the forces acting on matter, from angstrom-size atoms to micron-sized plastic or silica beads, originate from the same physical phenomenon, namely momentum exchange between radiation and matter.

The simplest optical trap is the single-beam gradient trap, or "optical tweezers." Originally proposed as an atom trap [68], optical tweezers have been used extensively in biology, chemistry and colloid physics [7, 69, 70]. Experiments have also revealed limitations of optical tweezers. The absorption of watery biological samples in the ultraviolet, visible and far-infrared range requires that optical tweezers operate at near-infrared wavelengths to minimize damage. A disadvantage of optical tweezers in comparison, for example, to magnetic manipulation is that in a crowded environment, such as inside a cell, force is exerted indiscriminately. Another limitation is the maximum force available with optical tweezers while avoiding damage to the specimen and to conventional optics. Optical tweezers operating under 1 W of average laser power can exert forces of up to about 100 pN – enough to stall mechano-enzymes and stretch DNA [7]. Stronger forces typically are needed to move irreversibly organelles such as chloroplasts or nuclei within cells. Somewhat larger forces can be reached with alternative trap geometries [6] or high-index particles. Maximal force scales with particle volume ($\sim d^3$, d = particle diameter) for particles small compared with the laser wavelength and becomes independent of particle radius in the ray-optics regime. Smaller particles have a faster dynamic response and are therefore often advantageous for use as dynamic probes [15, 36]. Thus a method for maximizing trapping force at a given particle size is desirable. A selective enhancement of trapping strength would also provide a degree of specificity in optical tweezing, i.e. enable one to trap probe particles preferentially in a crowded environment. In this paper, we consider optical trapping of an absorptive particle near its resonant absorption frequency, but not directly on-resonance. The particle's complex refractive index is increasing strongly, and trapping forces as well as absorption are expected to be enhanced.

To calculate rigorously the force acting on a neutral particle, one needs to solve the Maxwell equations for the electromagnetic fields with boundary conditions appropriate for the given system. If the particle diameter d is much larger than the radiation wavelength ($d >> \lambda$), one can operate in the limit of geometrical optics in which the electromagnetic fields behave locally as plane waves. In this limit, diffraction can be neglected and momentum exchange is calculated from refraction and reflection of plane waves. For very small particle sizes ($d << \lambda$), in the Rayleigh regime, the instantaneous electric field extending across the particle diameter can be approximated as uniform. The particle is then treated as a simple, induced dipole oscillating in a harmonic electric field. Momentum exchanges that yield forces on the particle are calculated as interactions between the field and the dipole.

Radiation forces can be described similarly in both the geometrical optics and Rayleigh regimes. In both limits, the total force on the particle can be resolved into two components: the dissipative scattering force pointing in the direction of the incident light [67, 71, 72] and the conservative gradient force, along the intensity gradient [6, 68, 72, 73]. To obtain a stable trap with a single focused laser beam, the gradient force must exceed the scattering force to generate a potential well that is at least as deep as the particle's thermal energy due to Brownian motion.

Trap stability depends on the geometry of the applied field and on properties of the trapped particle and the surrounding medium. The forces generally depend on particle size and the relative index of refraction $n = n_p/n_m$ where n_p and n_m are the indices of the particle and medium, respectively [6]. In the geometrical optics regime, maximal trap strength is particle size-independent, but increases with n over some intermediate range until, at larger values of *n*, the scattering force exceeds the gradient force. The scattering force on a non-absorbing Rayleigh particle of diameter *d* is proportional to its scattering cross section, thus the scattering force scales with the square of the polarizability (volume) [74, 75], or as d^6. The gradient force scales linearly with polarizability (volume), i.e. it has a d^3-dependence [8, 75, 76]. Svoboda and Block [16] demonstrated the refractive index dependence by showing that the trapping force for gold Rayleigh particles is ~7 times that of latex particles - a ratio equal to the ratio of their respective polarizabilities. Since the dependences on polarizability for the scattering and gradient forces are quadratic and linear, respectively, stable single-beam trapping only occurs for particles smaller than some maximum threshold size. Thus in the Rayleigh regime, trap strength will also be maximal for particular values of *n* and *d*.

It has been suggested in the literature [8] that absorptive particles with resonantly large polarizabilities should experience enhanced laser tweezing forces. To date, optical tweezers commonly have been used at frequencies far from any resonances in the trapped particles, whereas the excitation frequency dependence of optical forces on atoms has been studied in great depth. The dispersive nature of the gradient force of a single focused laser beam on sodium atoms was demonstrated experimentally through measurement of the on-axis atomic-beam intensity as a function of laser frequency [77]. Near resonance, the scattering force is dominant thus increasing the on-axis atomic intensity. More than 15 GHz away from resonance, only the gradient force is significant. A quantum mechanical derivation of the radiation pressure on a stationary, two-level atom also reveals this frequency dependence of the trapping forces [74, 78]. The gradient force can be associated with the potential created by the 'light shift' (Stark shift) [79] of the atomic levels when the laser frequency is detuned away from resonance. For detuning below resonance, the light shift is negative and an optical potential well is formed at the focus. Ideally, for positions very close to the focus (<< Rayleigh range) the scattering force is minimized and the gradient force provides a conservative restoring force proportional to the atom's distance from the focus. Detuning above resonance creates a positive light shift, forcing atoms to be ejected from the beam focus. Tuning exactly on resonance maximizes absorption thus maximizing the scattering force while minimizing the gradient force.

In a dielectric particle or macromolecule, numerous transitions can contribute to the absorption profile and resonant transitions are usually broadened. Nevertheless, we expect a small particle, i.e. a collection of interacting dipoles, to behave qualitatively similarly when the excitation frequency is varied. At present, however, there is no rigorous theory that specifies the frequency dependence of radiation-induced forces in the Rayleigh regime in terms of macroscopic parameters such as the refractive index or dielectric susceptibility of the particle and its environment.

We proposed [17, 18] an approximate classical method for estimating the scattering and gradient forces on a neutral particle in terms of macroscopic parameters. We considered a Rayleigh particle in an electromagnetic field and modeled the induced dipole as a classical oscillator. We then obtained the frequency dependences of the scattering force, gradient force and trap strength. Note: MKS units are used throughout.

2.1 Radiation Forces in a Focused Paraxial Gaussian Beam

To obtain expressions for the trapping forces on a particle, we first determine the appropriate equations for a single atomic dipole and then use the Clausius-Mosotti Equation [74] in the limit of a dilute gas to connect to macroscopic quantities. Consider a linear dipole $\boldsymbol{p} = \varepsilon_0 \alpha \boldsymbol{E}$ where $\boldsymbol{E}$ is the applied field, $\alpha = \alpha' + i\alpha''$ is the complex, first order, frequency-dependent polarizability (a scalar for an isotropic material), and ε_0 is the vacuum electric permittivity. The radiation-induced forces acting on this dipole have been derived from the non-relativistic Lorentz force. With index notation, the time averaged forces are [9, 80]:

$$\langle \boldsymbol{F}_g \rangle = \frac{\varepsilon_0}{2} \mathrm{Re}\left[\hat{\boldsymbol{x}}_j \alpha' E_{\boldsymbol{k}}^* \frac{\partial E_{\boldsymbol{k}}}{\partial x_j} \right] = \frac{\varepsilon_0}{4} \left[\hat{\boldsymbol{x}}_j \frac{\partial}{\partial x_j} (E_{\boldsymbol{k}}^* \alpha' E_{\boldsymbol{k}}) \right], \tag{2.1}$$

$$\langle \boldsymbol{F}_s \rangle = \frac{\varepsilon_0}{2} \mathrm{Re}\left[-i\hat{\boldsymbol{x}}_j \alpha'' E_{\boldsymbol{k}}^* \frac{\partial E_{\boldsymbol{k}}}{\partial x_j} \right] = \frac{\varepsilon_0}{2} \mathrm{Im}\left[\hat{\boldsymbol{x}}_j E_{\boldsymbol{k}}^* \alpha'' (\frac{\partial E_{\boldsymbol{k}}}{\partial x_j}) \right] \tag{2.2}$$

where $\hat{\boldsymbol{x}}_j$ are the Cartesian-coordinate unit vectors and $\boldsymbol{F}_{\mathrm{g}}$ and $\boldsymbol{F}_{\mathrm{s}}$ are the gradient force and scattering force, respectively. The E_{k} variables are the components of the electric field amplitude.

For Rayleigh scattering, one naively might take α to be a simple real polarizability (proportional to the volume of the particle) so that $\alpha'' = 0$ which would make the scattering force zero. However closer inspection of scattering by a non-absorbing sphere [80-82] shows that even in this case α effectively contains an imaginary part $\alpha'' \neq 0$ which is proportional to the volume squared. This is due to the radiation reaction on the oscillating dipole, causing a phase shift between the dipole $\boldsymbol{p}$ and the applied field $\boldsymbol{E}$. This energy loss makes the scattering force $\langle \boldsymbol{F}_s \rangle$ nonzero even in the absence of absorption. In the series expansion of α for particles that are small with the wavelength, this volume-squared term is the lowest-order imaginary term. When a resonance is approached there will be a lower-order imaginary term that is proportional to volume.

To model the spatial distribution of the electric field in an optical trap, we assume a paraxial Gaussian beam focused by a lens [83]. This approximation breaks down for focusing with large numerical aperture (NA), which is often required for optical tweezers. The parameter $s = \lambda_m/2\pi w_0$ can provide a measure of the accuracy of the approximation. Here λ_m is the wavelength of the light in a surrounding medium of index n_m and w_0 is the beam radius in the focus (the $1/e^2$ radius of the intensity). Barton and Alexander [84] state that the paraxial approximation, a description to zeroth-order in s, will contain average errors in the electric field of ~9.47% for $s = 0.20$ and ~15.3% for $s = 0.30$. For a medium with index $n_m = 1.52$, these values of s correspond to NA's of 0.56 (convergence half angle $\theta = 22°$) and 0.78 ($\theta = 31°$), respectively. Thus future calculations for the radiation forces will have corresponding uncertainties depending on the NA chosen.

The field at a distance z from the beam focus and a radial position r from the beam axis (in cylindrical coordinates) is in the Gaussian approximation (see Figure 2.1):

$$\boldsymbol{E}(r) = \boldsymbol{E}_0 \sqrt{\frac{2}{\pi}} \frac{w_0}{w(z)} \exp\left(-\frac{r^2}{w^2(z)}\right) \exp\left(i \frac{k_m r^2}{2R(z)}\right) \exp\left(ik_m z + i\eta(z)\right); \tag{2.3}$$

where

$$w^2(z) = w_0^2 \left[1 + \left(\frac{z}{z_0}\right)^2\right], \tag{2.4}$$

$$R(z) = z\left[1 + \left(\frac{z_0}{z}\right)^2\right], \text{ and} \tag{2.5}$$

$$\eta(z) = \tan^{-1}\left(\frac{z}{z_0}\right). \tag{2.6}$$

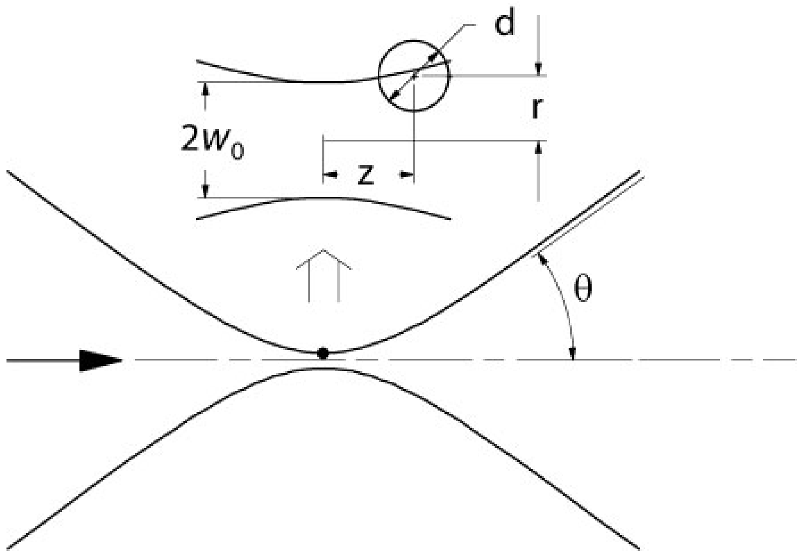

Figure 2.1 Focus geometry as discussed in text.

Here $z_0 = \pi w_0^2/\lambda_m$ and $k_m = 2\pi/\lambda_m$, where w_0 is again the beam radius in the focus and λ_m is the wavelength of the light propagating in a surrounding medium of index n_m. The convergence half angle is given by $\theta = \tan^{-1}(\lambda_m/\pi w_0)$. The value of w_0 will depend on the wavelength of the incident light, the beam radius w_i entering the lens, the lens focal length f, and the refractive index of the surrounding material in which the focus is located ($w_0 = f\lambda_m/\pi w_i$). Performing the appropriate coordinate conversions to Eq. (2.3) and inserting the result into Eqs. (2.1) and (2.2), we obtain the following components for the gradient force:

$$\hat{\boldsymbol{z}} \cdot \langle \boldsymbol{F}_g \rangle = -\frac{\varepsilon_0}{\pi} \alpha' |\boldsymbol{E}_0|^2 z \frac{w_0^4}{z_0^2} \left[\frac{1}{w^4(z)} - \frac{2r^2}{w^6(z)} \right] \exp\left(-\frac{2r^2}{w^2(z)} \right), \tag{2.7}$$

$$\hat{\boldsymbol{r}} \cdot \langle \boldsymbol{F}_g \rangle = -\frac{2\varepsilon_0}{\pi} \alpha' |\boldsymbol{E}_0|^2 r \frac{w_0^2}{w^4(z)} \exp\left(-\frac{2r^2}{w^2(z)} \right), \tag{2.8}$$

and for the scattering force:

$$\hat{\boldsymbol{z}} \cdot \langle \boldsymbol{F}_s \rangle = \frac{\varepsilon_0}{\pi} \alpha'' |\boldsymbol{E}_0|^2 \frac{w_0^2}{w^2(z)} \left[k_m \left(1 - \frac{r^2}{2} \frac{(z^2 - z_0^2)}{(z^2 + z_0^2)^2} \right) + \frac{w_0^2}{z_0 w^2(z)} \right] \exp\left(-\frac{2r^2}{w^2(z)} \right), \tag{2.9}$$

$$\hat{\boldsymbol{r}} \cdot \langle \boldsymbol{F}_s \rangle = \frac{\varepsilon_0}{\pi} \alpha'' |\boldsymbol{E}_0|^2 \frac{w_0^2}{w^2(z)} \frac{k_m r}{R(z)} \exp\left(-\frac{2r^2}{w^2(z)} \right). \tag{2.10}$$

Equivalent expressions have been previously derived [75]. For a position sufficiently close to the beam axis ($r < w/\sqrt{2}$), the gradient force is directed toward the trap focus provided that α' is positive. The strengths of the gradient and scattering forces are proportional to the real and imaginary components of the polarizability, respectively. For a stable trap, the gradient force must exceed the scattering force over a large enough region of space such that a potential well is formed deep enough to trap the particle. Thus the ratio between the real and imaginary parts of the polarizability can provide a measure of the trap depth.

2.2 Models of Response

For a dipole with a single resonant absorption frequency, the classical electron oscillator (CEO) model [74] provides a simple analytical solution for the complex polarizability. In the CEO model of absorption, an induced dipole with natural oscillation frequency ω_0 is driven by an ac electric field. Derived from the Lorentz force equation, assuming the dipole approximation [85], the equation of motion for the dipole with mass m and moment $\boldsymbol{p} = q\boldsymbol{x}$ is

$$\frac{d^2\boldsymbol{x}}{dt^2} + 2\gamma\frac{d\boldsymbol{x}}{dt} + \omega_0^2\boldsymbol{x} = \frac{q\boldsymbol{E}}{m}. \tag{2.11}$$

We have assumed a harmonic restoring force, and a damping force has been included to account for the radiation of power. The rate constant γ includes both radiative and non-radiative decay, as well as decay due to dephasing collisions [86]. Remembering that $\boldsymbol{p} = \varepsilon_0\alpha\boldsymbol{E}$, the frequency domain solution of the polarizability is then

$$\alpha(\omega) = \alpha' + i\alpha'' = \frac{q^2}{m\varepsilon_0}\frac{\omega_0^2 - \omega^2 + 2i\gamma\omega}{\left(\omega_0^2 - \omega^2\right)^2 + 4\gamma^2\omega^2}. \tag{2.12}$$

Using this result in Eqs. (2.7)-(2.10), one obtains the gradient and scattering forces on a single dipole as functions of position in space and laser frequency.

If the resonance frequency ω_0 is much larger than the damping parameter γ (weak damping), then α'' will be significant only for $\omega \approx \omega_0$. The polarizability can then be written as

$$\alpha' + i\alpha'' = \frac{q^2}{2m\varepsilon_0\omega_0\gamma}\left[\frac{(\omega_0 - \omega)\gamma}{(\omega_0 - \omega)^2 + \gamma^2} + i\frac{\gamma^2}{(\omega_0 - \omega)^2 + \gamma^2}\right]. \tag{2.13}$$

The imaginary part α'' has a Lorentzian lineshape, while the real part α' is positive for $\omega < \omega_0$, thus red-detuned frequencies are required for attractive gradient forces near the trap focus. A collection of oscillators with a homogeneously broadened transition will also have an imaginary response with a Lorentzian lineshape. If the oscillators in a collection have slightly different resonant frequencies randomly distributed about some central value, the overall imaginary response is broadened inhomogeneously and can have a Gaussian lineshape. In either case, if the system's response obeys causality and is linear in the electric field, the real and imaginary components of the polarizability are connected through the Kramers-Kronig (KK) relations [87, 88].

The dispersive behavior of the radiation-induced forces can be extended to macroscopic media. The simplest case of a macroscopic system is a dilute gas of non-interacting, neutral atoms. The total trapping force for such a sample is acquired by multiplying Eq. (2.13) by the factor NV where N is the number density of dipoles and V is the total trapped volume of the sample, and inserting the appropriate component into Eqs. (2.7)-(2.10). In such a system, the electric field $\boldsymbol{E}$ induces a polarization density defined by $\boldsymbol{P} = N\boldsymbol{p} = \varepsilon_0\chi\boldsymbol{E}$, where $\chi = (\chi_p - \chi_m)/(1 + \chi_m)$ is the relative susceptibility of the sample with respect to the surrounding medium. The polarizability (a microscopic parameter) and susceptibility (a macroscopic parameter) are thus related by the simple relation $\chi = N\alpha$.

In many cases, the trapped particle is a more complex system such as a crystalline or amorphous solid with multiple resonant frequencies and interacting dipoles affected by local fields. In this situation, the relation between polarizability and susceptibility is more complicated than a proportionality constant. The Clausius-Mossotti equation can be employed [74], which for a dielectric particle in some medium takes the form:

$$\alpha = \frac{3}{N}\left(\frac{\varepsilon_p/\varepsilon_m - 1}{\varepsilon_p/\varepsilon_m + 2}\right), \tag{2.14}$$

where $\varepsilon_{p,m} = 1 + \chi_{p,m}$ are the complex dielectric constants of the particle and medium, respectively. Using Eq. (2.14) in Eqs. (2.7)-(2.10), the scattering and gradient forces on a particle are attained in terms of the macroscopic properties of the particle and its surrounding medium. The real and imaginary parts of the refractive index $n_{p,m} = \varepsilon_{p,m}^{1/2}$ of the particle (medium) can be linked using suitable KK relations [89]. If we assume a

Beer's Law dependence for the on-axis intensity, $I(r=0,z)=I_0\exp(-2k''z)=I_0\exp(-az)$ and $k=k'+ik''=n\omega/c$ is the complex wave vector, the imaginary part of the index $n=n'+in''$ is related to the absorption coefficient a by $a=2n''\omega/c$. If the absorption spectrum of a Rayleigh particle can be acquired experimentally over a large enough frequency range, the associated scattering and gradient forces on the particle can be determined.

If the dielectric constant of the particle is close to that of the medium ($\varepsilon_p/\varepsilon_m \sim 1$), we obtain from Eq. (2.14) the relation for a dilute gas in air or vacuum, $\chi = N\alpha$. The imaginary component of the relative susceptibility χ'' is much less than unity, thus we obtain a simple connection between the macroscopic absorption and microscopic polarizability:

$$a = N\alpha''\omega/c\,. \tag{2.15}$$

We expect the radiation forces to have the same qualitative behavior in this case as for a denser dielectric. Thus, we consider the spectrum of a single absorption peak of a dielectric crystal and model its associated polarizability using the CEO, Lorentzian and Gaussian descriptions along with the KK relations. We then calculate scattering and gradient forces on the dielectric particle and compare trapping strengths. An experimental realization of a relatively dilute system might be a dielectric particle densely loaded with fluorescent dye [dye density = 0.7×10^{25} m^{-3} for 2.0 μm diameter FluoSphere beads (Molecular Probes, 4849 Pitchford Avenue, Eugene, OR)].

2.3 Numerical Analysis

We consider the scattering and gradient forces on a dielectric particle with a single resonant frequency in the visible region of the spectrum immersed in a medium with a purely real refractive index $n_\mathrm{m} = 1.52$ (typical value for oil immersion lenses). Numerical apertures corresponding to certain convergence angles are calculated assuming this refractive index. As an example for a material we consider pink ruby. The trapped particle is assumed spherical with a radius of 10 nm and dipole density of 2.7×10^{25} m^{-3} (density of Cr^{3+} in ruby). The simplest case of a dilute gas sample is calculated by determining the forces on a single dipole and multiplying by NV. Using the CEO picture for polarizability [Eq. (2.13)], the absorption as given by Eq. (2.15) is fit to one of the peaks of ruby [90]. This curve is labeled the "CEO fit" in Figure 2.2. By using the results from this fit, we determine parameters for comparable Lorentzian and Gaussian α'', assuming the same peak amplitude, central frequency and half-width-half-maximum as the CEO α'': $\alpha''_{\max} = 1.77 \times 10^{15}$ m^3, $\omega_0 = 4.67 \times 10^{15}$ rad/s, HWHM = 0.274×10^{15} rad/s. Although these values correspond to an absorption peak of pink ruby (Cr_2O_3:Al_2O_3), the quantities are arbitrary and are included simply to illustrate the concept of resonant trapping. The functional forms of the $\alpha''(\omega)$ fits and appropriate parameters are summarized in Table 2.1. Resulting absorption curves corresponding to the Lorentzian and Gaussian models are also shown in Figure 2.2.

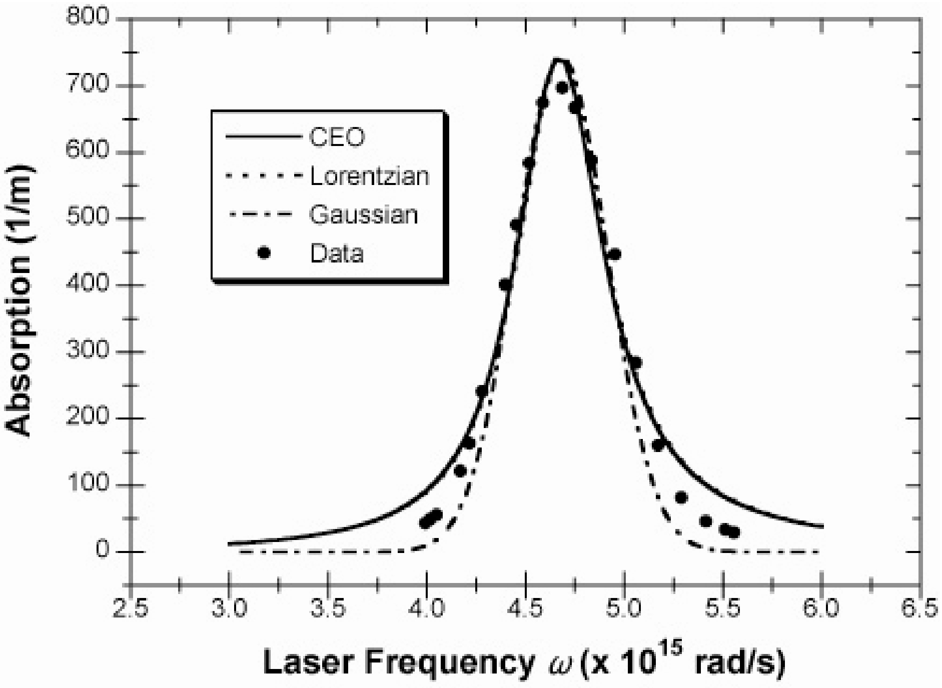

Figure 2.2 Absorption spectrum of dilute sample with particle number density = 2.7×10^{25} m^{-3} and sample radius = 10 nm; $a_{\max} = 745$ m^{-1} at $\omega_0 = 4.67 \times 10^{15}$ rad/s; HWHM = 0.274×10^{15} rad/s. Datapoints from a single-absorption peak of ruby[31] are fit with the CEO model of α''. Lorentzian and Gaussian forms of α'' with the same amplitude and width are determined, and their corresponding absorption spectra are plotted.

Fit Parameter	Fit Type CEO	 Lorentzian	 Gaussian
$\alpha''(\omega)$	$\dfrac{A_E\omega}{(\omega_0^2-\omega^2)^2+4\omega^2\gamma_E^2}$	$\dfrac{A_L}{(\omega_0-\omega)^2+\gamma_L^2}$	$A_G\exp\left(-\dfrac{(\omega_0-\omega)^2}{\gamma_G^2}\right)$
α''_{max}	$A_E/4\omega_0\gamma_E^2$	A_L/γ_L^2	A_G
HWHM	γ_E	γ_L	$\gamma_G\sqrt{\ln 2}$

Table 2.1 Functional form of fitting curves and fit parameters for imaginary polarizability.

2.3.1 Kramers-Kronig Consistent Response

To obtain the real components of the polarizability, we use the KK relations. Keefe [91] shows that the CEO line shape is consistent with formal restrictions owing to causality and with requirements for the KK transform to hold between the real and imaginary parts of the polarizability. The Lorentzian and Gaussian forms are not consistent. These forms, however, can be modified in more than one way to meet the necessary requirements. For the Lorentzian case, we derived the KK consistent form to be

$$\alpha''(\omega)=A_L\frac{\omega}{\omega_0}\left[\frac{1}{(\omega_0+\omega)^2+\gamma^2}+\frac{1}{(\omega_0-\omega)^2+\gamma^2}\right], \tag{2.16}$$

where A_L is a constant. For a narrow peak ($\gamma << \omega_0$) and at positive frequencies, this approximates the usual Lorentzian

$$\alpha''(\omega)\approx\frac{A_L}{(\omega_0-\omega)^2+\gamma^2}. \tag{2.17}$$

The exact KK transform for α'' in Eq. (2.16) is

$$\alpha'(\omega)=\frac{A_L}{\gamma\omega_0}\left[\frac{\gamma^2+\omega_0(\omega_0+\omega)}{(\omega_0+\omega)^2+\gamma^2}+\frac{\gamma^2+\omega_0(\omega_0-\omega)}{(\omega_0-\omega)^2+\gamma^2}\right]. \tag{2.18}$$

A similar procedure can be followed in the Gaussian case. We derived the KK consistent form

$$\alpha''(\omega)=A_G\frac{\omega}{\omega_0}\left[\exp\left(-\frac{(\omega-\omega_0)^2}{\gamma^2}\right)+\exp\left(-\frac{(\omega+\omega_0)^2}{\gamma^2}\right)\right] \tag{2.19}$$

where A_G is a constant. This is approximately

$$\alpha''(\omega) \approx A_G \exp\left(-\frac{(\omega-\omega_0)^2}{\gamma^2}\right) \tag{2.20}$$

for a narrow peak at positive frequencies. The KK transform for Eq. (2.19) is

$$\alpha'(\omega) = \frac{2}{\sqrt{\pi}} \frac{A_G \gamma}{\omega_0}\left[1 - \frac{\omega}{\gamma} D\left(\frac{\omega-\omega_0}{\gamma}\right) - \frac{\omega}{\gamma} D\left(\frac{\omega+\omega_0}{\gamma}\right)\right], \tag{2.21}$$

where Dawson's integral [92] is given by

$$D(x) = \exp\left(-x^2\right)\int_0^x \exp(t^2)dt \cdot \tag{2.22}$$

Keefe [91] gives different but likewise consistent forms. Using Eqs. (2.7)-(2.10), (2.17), (2.18), (2.20) and (2.21), the radiation forces were evaluated for each model. The range of convergence angles θ over which a trap exists depends on the relative strengths of the scattering and gradient forces. At smaller θ, the scattering force may exceed the gradient force everywhere, and the effective potential may have no points of stable equilibrium. If θ is large, a trap usually exists, at least far enough away from resonance; however, the Gaussian beam approximation breaks down.

2.3.2 Enhancements in Trap Stiffness

The trap stiffness κ can be defined as the effective spring constant of the expression for the total force acting on the particle at the minimum of the optical potential well. We calculate this stiffness by specifying θ, taking the derivative of the total force,

$$\kappa_j = -\left[\frac{\partial}{\partial x_j}\left(\hat{\boldsymbol{x}}_j \cdot \left\langle \boldsymbol{F}_g + \boldsymbol{F}_s \right\rangle\right)\right]\Bigg|_{\text{minimum}} \tag{2.23}$$

and evaluating at the coordinates of the effective potential minimum. There is no summation over repeated indices in Eq. (2.23). Owing to cylindrical symmetry, the trap always occurs at $r = 0$. We determine the z-location of the trap by finding the roots of the total force. Roots corresponding to potential extrema with negative trap stiffness and z-locations upstream of the focus are discarded.

Even without a frequency-dependent polarizability, we expect the trap strength to increase with increasing laser frequency because the potential width scales with wavelength. The harmonic approximation to the Gaussian intensity profile at the focus is

$E^2 \propto \exp(-2r^2/w_0^2) \approx 1\text{-}2r^2/w_0^2$ from which the radial trap stiffness is calculated as $\kappa \propto 1/w_0^2 \propto 1/\lambda^2$. Thus, trivially we expect the trap stiffness to scale as an inverse square power of wavelength, if we keep the field strength E_0 constant for different wavelengths. Thus, to see only the effect of the frequency-dependent polarizability on trapping force enhancement we have plotted the scaled stiffness $\lambda^2\kappa$ for the CEO, Lorentzian, and Gaussian models, each as a function of λ in Figure 2.3, Figure 2.4, and Figure 2.5, respectively.

Figure 2.3 shows the scaled stiffness calculated with the CEO curve fit for the absorption for different convergence angles. At smaller θ, trapping can only occur for wavelengths far from resonance (λ_0 = 0.403 μm) since the scattering force tends to dominate the gradient force. At these angles, even if the absolute trap stiffness were higher near resonance than far-off resonance, the enhancement would be primarily due to the decrease in wavelength. As θ is increased, the gradient of the beam focus increases and trapping can occur closer to resonance. Comparison of the two graphs in Figure 2.3 indicate that for a given $\theta \leq 45°$ and λ, the radial trap strength κ_r is up to 1 order of magnitude larger than the axial trap strength κ_z. Also, for a given θ, the wavelengths corresponding to the maximum radial and axial trap stiffness have similar values, always remaining above resonance as indicated in Figure 2.6. The wavelength for maximum radial stiffness is shifted towards slightly lower wavelengths, compared with that for the axial stiffness. For all three cases, trapping in the radial direction is slightly easier than in the axial direction for a given wavelength, since a slightly smaller θ is required for maximum stiffness. On resonance, absorption is greatest, and the scattering force is at its maximum, therefore there is no trapping. The overall result is that trapping is only enhanced for wavelengths red-detuned from resonance.

Figure 2.4 and Figure 2.6(b) describe trap characteristics assuming the Lorentzian form of α'' and Figure 2.5 and Figure 2.6(c) describe the same for the Gaussian form of α''. The results for the Lorentzian system are similar to those for the CEO model, since the resonant frequency is much larger than the resonance width (ω_0/γ = 17). For a convergence angle of θ = 50°, calculations reveal that the scaled axial trap stiffness increases by a factor of 1.1 while the radial stiffness increases by a factor of 1.2

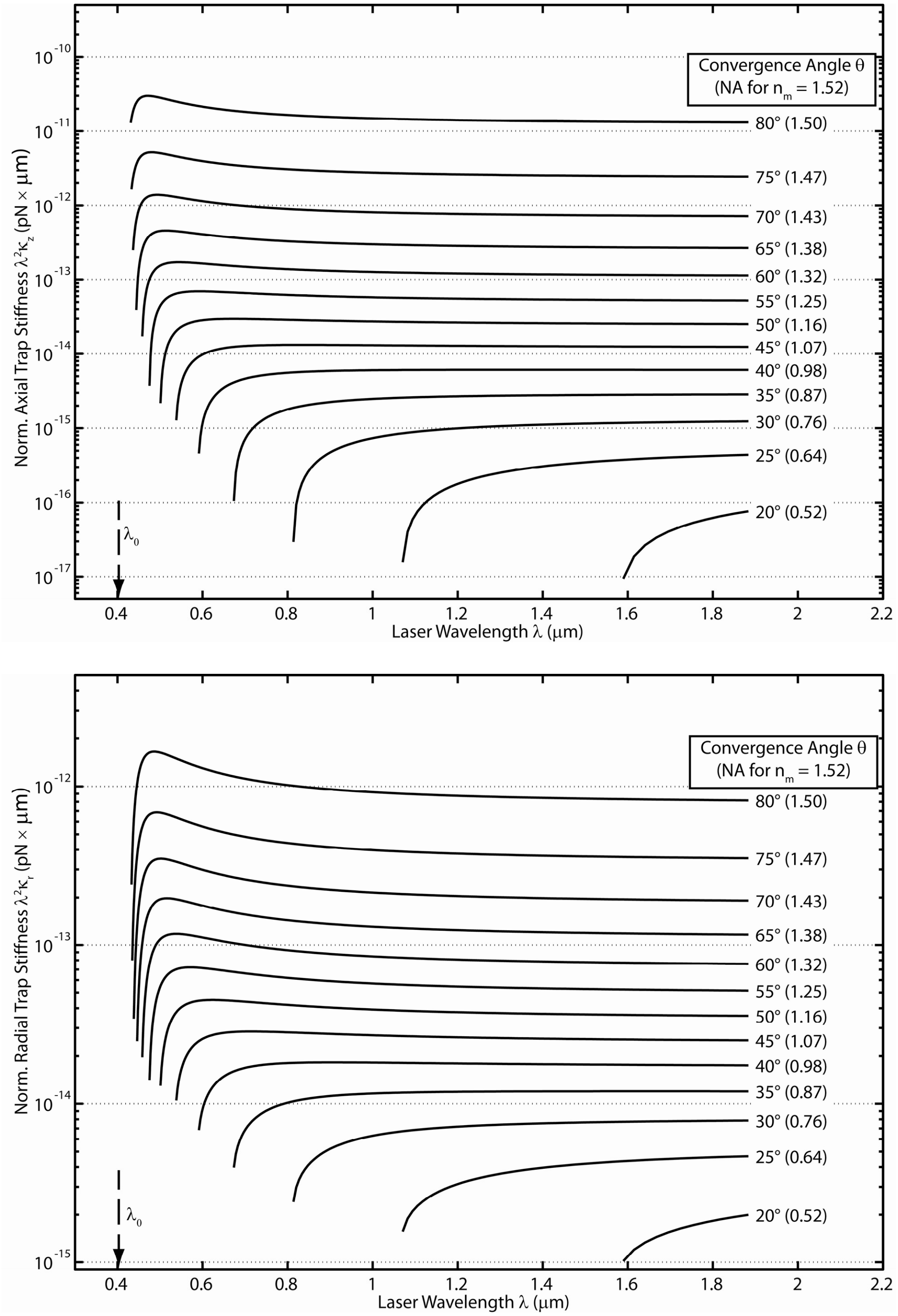

Figure 2.3 Plots of scaled trap stiffness for CEO absorption fit. The stiffness κ is multiplied by λ^2 to correct for the trivial (non-resonant) wavelength dependence. Radial (bottom) trap stiffness κ_r is generally larger than the axial (top) stiffness κ_z for a given convergence angle. At $\theta = 50°$ (NA = 1.16), the axial and radial stiffnesses increase by a factor of 1.1 and 1.2, respectively, compared to far off-resonant frequencies. For angles < 20° (NA < 0.52) no trapping occurs within the wavelength range shown.

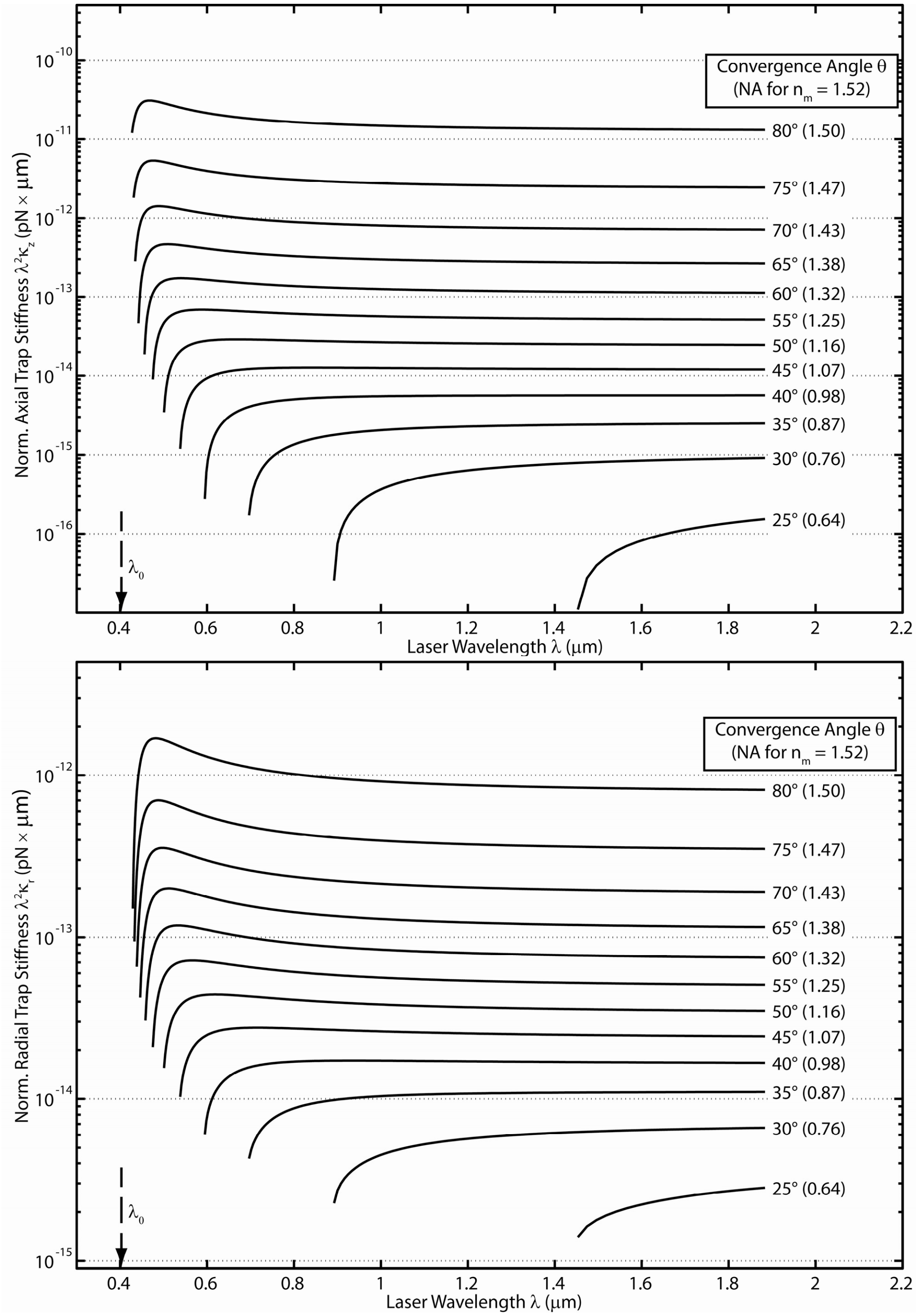

Figure 2.4 Plots of scaled trap stiffness for Lorentzian absorption fit. The stiffness κ is multiplied by λ^2 to correct for the trivial (non-resonant) wavelength dependence. These results are similar to those for the CEO fit since the resonant frequency is much larger than the resonance width ($\omega_0/\gamma = 17$). At $\theta = 50°$ (NA = 1.16) the axial stiffness increases by a factor of 1.1 compared to far off-resonant frequencies whereas the radial stiffness increases by a factor of 1.2.

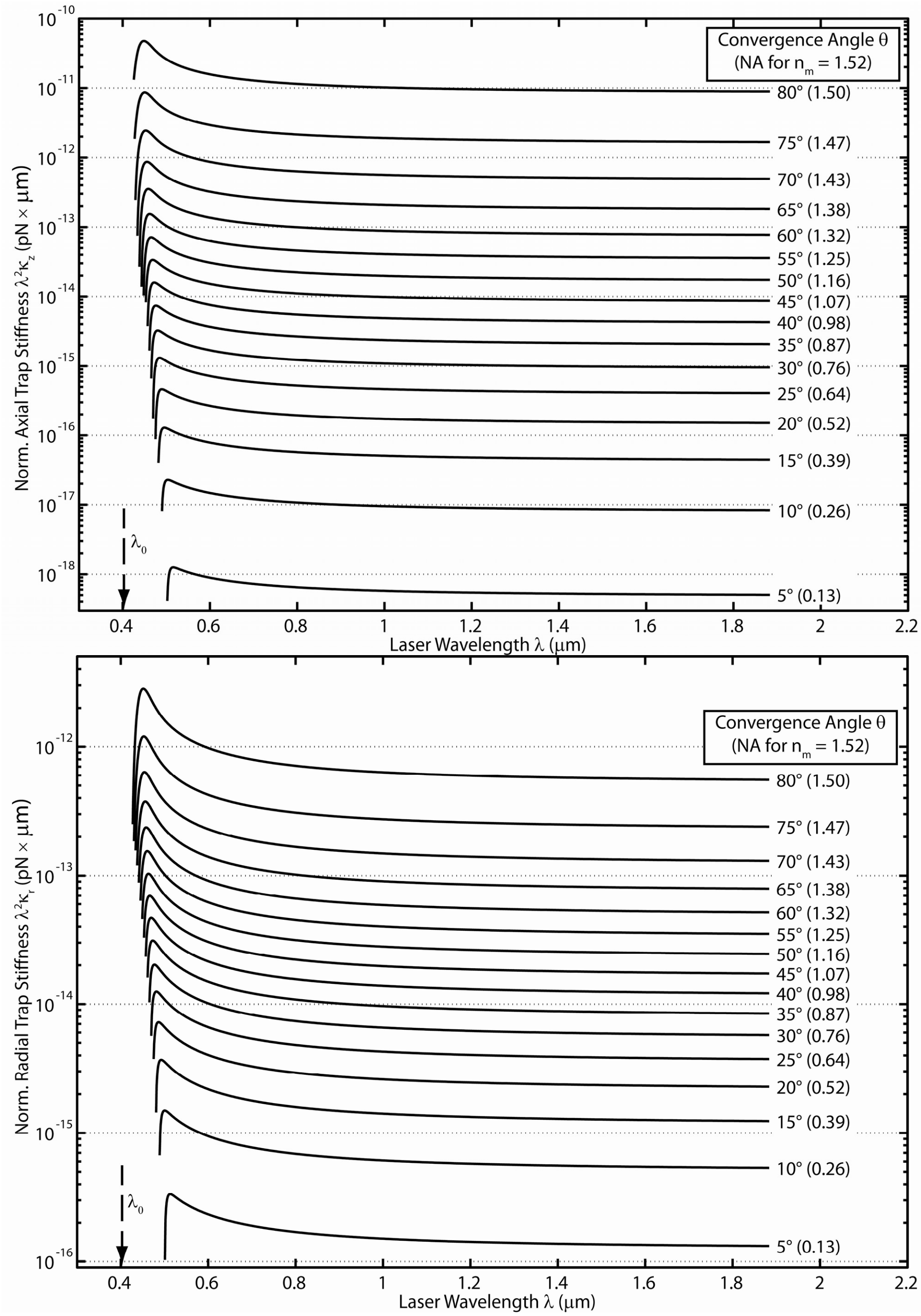

Figure 2.5 Plots of scaled trap stiffness for Gaussian absorption fit. The stiffness κ is multiplied by λ^2 to correct for the trivial (non-resonant) wavelength dependence. The overall stiffness values are similar to those for previous fits at far off-resonant frequencies. The total wavelength range over which a trap exists, however, is larger. Trapping enhancement is also possible for smaller θ. This results from the lack of long tails in the absorption spectrum that are present in the CEO and Lorentzian fits. At $\theta = 50°$ (NA = 1.16) the stiffness increases as one approaches resonance by a factor of 4.1 in the axial direction and 4.2 in the radial direction compared to far off-resonant frequencies. Convergence angle does not appear to strongly affect the rate of increase in trap stiffness; it only determines how close to resonance a trap can exist and the absolute value of the stiffness.

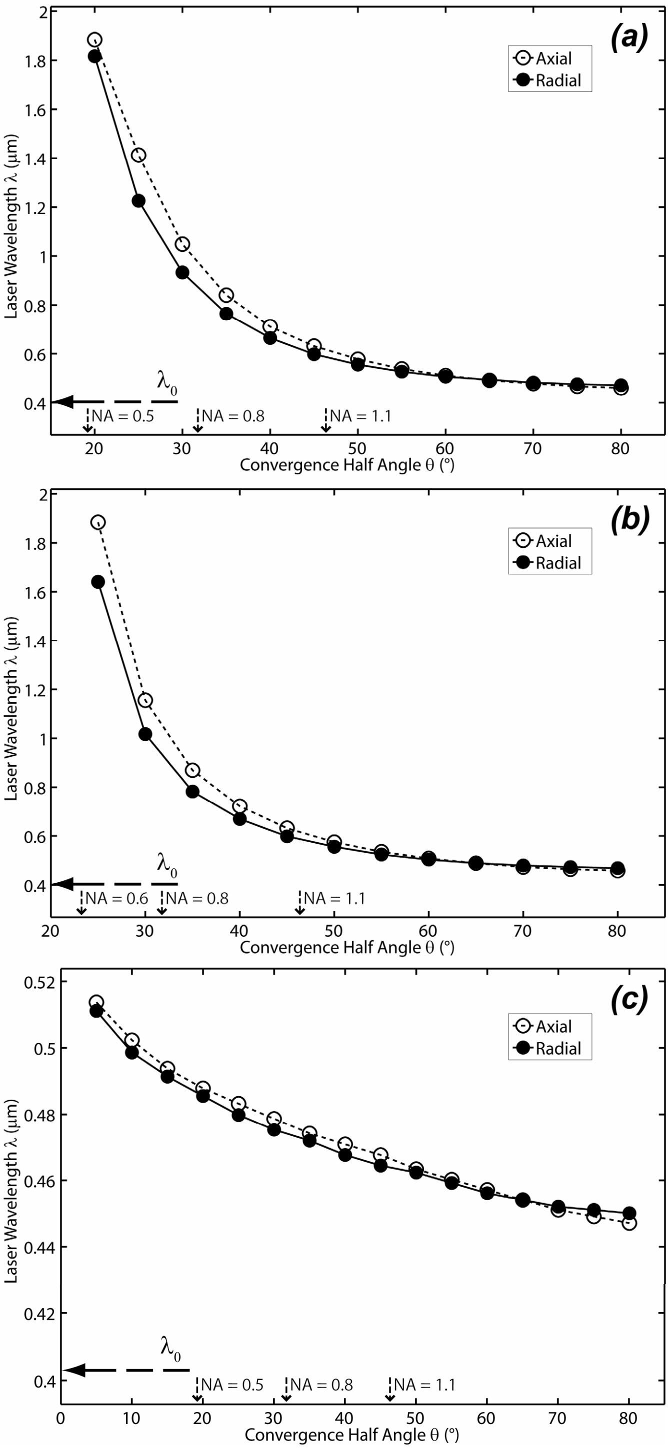

Figure 2.6 Plots of wavelengths corresponding to maximum trap stiffness for varying θ. For the (a) CEO, (b) Lorentzian, and (c) Gaussian models of absorption. Vertical arrows along the *x*-axis indicate where typical NA's (i.e. 0.5, 0.8, 1.1) occur. Generally, radial trap stiffness is larger than axial, requiring a slightly smaller convergence angle for maximum stiffness at a given wavelength. For θ much smaller than 20° (NA = 0.52) no trap exists for the CEO and Lorentzian models.

compared to off-resonant values. For the Gaussian system, the stiffness curves have similar off-resonant values but have a larger wavelength range over which a trap exists. This arises from the lack of long tails in the absorption spectrum, which are present in the Lorentzian and CEO functional forms (See Figure 2.2). Calculations for the Gaussian case show that for $\theta = 50°$, the axial and radial trap stiffnesses increase from far off-resonant frequencies by a factor of 4.1 and 4.2, respectively. It is physically reasonable that trapping strength depends greatly on the nature of the sample, in particular, on the absorption profile at slightly off-resonant wavelengths. Inhomogeneously broadened materials that have sharp absorption peaks may have off-resonant trapping strengths that are larger than homogeneously broadened materials with similar absorption peak widths. Materials in which spectral lines are broadened by a mixture of these two mechanisms, i.e. those with Voigt profiles, will have intermediary off-resonant trapping strengths. In any case, approaching a resonance from the red-detuned side can enhance trap stiffness. The more pronounced enhancement effect due to the lack of long tails in the Gaussian profile vs. the Lorentzian and CEO profiles suggests there are increased enhancements for narrower spectral linewidths. To investigate this dependence on linewidth, we repeated our analysis of trap stiffness vs. frequency for absorption profiles with 1/4 and 1/10 the width, respectively, of our original ruby absorption spectrum. These narrower profiles correspond to a HWHM of 6.85×10^{13} rad/s and 2.74×10^{13} rad/s, respectively. A summary of the results is shown in Table 2.2 for a convergence angle of $\theta = 50°$. As the linewidth narrows, the CEO profile approaches the Lorentzian shape; consequently, the trapping stiffness ratios for these two models agree. The enhancements increase by a factor approximately 3/4 the ratio of the original linewidth to the narrowed linewidth. For the Gaussian case, the enhancement grows in comparison to that for the CEO and Lorentzian cases. In particular, the enhancements increase by a factor approximately equal to the ratio of the original linewidth to the narrowed linewidth. In all cases, the increase in trapping stiffness is slightly larger in the radial direction than in the axial direction.

The increased absorption near resonance can cause increased heating at the focus of the trapping beam. It can be shown that for non-resonant trapping the temperature rise is due mostly to the solvent, and not the trapped particle [61]. The calculation in reference

Fit Type		**Linewidth** Normal width	¼ width	1/10 width
CEO	Axial	1.1	3.3	7.8
	Radial	1.2	3.7	8.8
Lorentzian	Axial	1.1	3.3	7.8
	Radial	1.2	3.7	8.8
Gaussian	Axial	4.1	16	39
	Radial	4.2	16	41

Table 2.2 Ratios of maximum trap stiffness near resonance to stiffness off-resonance for a convergence angle of $\theta = 50°$.

[61] assumes among other approximations a weakly absorbing particle. This assumption will break down when the frequency is tuned exactly on resonance. In the cases studied here, the detuning from resonance is sufficient enough, and the density of dye is approximated as low, so that the heating effects can be estimated with the formalisms of reference [61]. A volume of water (thermal conductivity: 0.60 W/(m K)) with closest boundary 10 μm away illuminated by a 1064 nm, 100 mW focused beam will experience an equilibrium temperature rise of roughly 0.98° K. A 500 nm diameter ruby particle (thermal conductivity: 40 W/(m K) [93], absorption as in CEO model of Figure 2.2) trapped in the same volume of water by the same beam will experience a temperature-rise correction of -0.18° K. Looking at Figure 2.6(a) at 600 nm, a wavelength close to that for maximum trap strength, and accounting for the dispersion of water [94], the temperature increase is estimated as 0.022° K for the water alone. The presence of a ruby particle at this wavelength introduces a correction of -1.1×10^{-4} °K. Thus, heating at an excitation wavelength corresponding to maximum trap strength can be lower than far-off resonance depending on the characteristics of the surrounding medium.

2.4 Conclusions

We have used classical electromagnetic theory to derive the spatial and frequency dependences of the scattering and gradient forces on a single dipole present in a focused paraxial Gaussian light beam. The distribution of these radiation forces depends on both the intensity profile of the incident beam and the microscopic properties of the induced dipole as manifested by its polarizability. We have shown that for this classical dipole, the dispersive nature of the real part of the polarizability and the resonant profile of the imaginary part with respect to laser frequency produces an optical potential well whose trapping stiffness can be tuned. Directly on resonance, the gradient force becomes negligible compared to the scattering force and a state of stable equilibrium does not exist for the dipole. Approaching resonance from the red-detuned side, the gradient force can peak while the scattering force still has a small fraction of its value at resonance. This provides an enhanced trap with stiffness about 1-4 times (depending on the functional form of the absorption spectrum) larger than the stiffness at far-off resonance frequencies in the cases we looked at. In general, the effect is stronger when the dipole's imaginary polarizability component is sharp, i.e. Gaussian rather than Lorentzian. In such cases, the scattering force rapidly drops off within a width $\sim 3\gamma$ (frequency) of the resonance whereas the gradient force reaches its maximum value at an off-resonant frequency. The enhancement in trapping stiffness also grows with decreasing linewidths for all profile types.

In a system of interacting dipoles, for which we have not performed a detailed analysis, the radiation forces on the sample can be related to macroscopic properties such as the index of refraction or electric susceptibility. Several models and their validity as a function of particle size have been discussed in the literature [80]. In any case, as in the case of a single dipole, linear response theory imposes a relation between the gradient and scattering forces if the incident field is not so strong as to induce nonlinear interactions. At frequencies about γ below a sharp resonance, the absorption should also be small enough such that the gradient force exceeds the scattering force, leading to resonant enhancement of the effective trap stiffness. It is expected that red-detuned optical tweezing near sharp resonance lines in absorptive solids or liquids will then also afford enhanced trapping opportunities [19, 95, 96].

CHAPTER 3

OPTICAL MANIPULATION OF MICRO AND NANOPARTICLE SYSTEMS

In this work, optical tweezers are used to manipulate metal-silica hybrid particles with prospects of measuring light-matter interactions. A surge of advances in recent years [97-100] has made optical tweezers a promising technique for motion control of mesoscopic systems in physics, chemistry, and biology. Much of the progress has focused on modification of the laser beam configuration to enable multiple trap positions via time-sharing [101], beamsplitting [102], using diffractive optical elements [103], or using spatial light modulators [104]. Other schemes utilize beams with spin or angular momentum, such as circularly polarized light and Laguerre-Gaussian beams, or rotated asymmetric beam patterns to generate torque on the trapped particle [98-100]. Much less work has been done concerning modification of the trapped particle itself, nonetheless some developments worth mentioning include schemes for trapping metals [100], the optical tweezing of non-spherical particles [105], the optical fabrication and tweezing of a light-driven turbine [106], optical tweezing of particles with resonance absorption peaks [18], and the optical tweezing of core-shell colloidal systems [107].

There is growing interest in the use of hybrid nanosystems such as core-shell colloidal systems outside the field of optical tweezing. Single-nanoparticle surface-enhanced Raman scattering (SERS) has been observed using heterogeneous systems comprised of compound dielectric-metal [108] and dielectric-semiconductor materials [109]. The effects of localized surface plasmon resonances which enable such enhanced optical properties have been studied for optically trapped metal nanoparticles [19, 110, 111], however little has been done on optically trapped hybrid systems. Another application of hybrid nanoparticles is in sub-cellular magnetic resonance imaging [112] and chemical imaging with biosensing probes [1]. In particular, fiber-based silica-gold-fluorophore systems have been used as selective nitric-oxide sensors [1, 3-5]. Also, nanosystems consisting of dielectric particles half-coated with metal have been fabricated to allow sensing with increased signal-to-background ratios and for microrheological studies [28, 31]. Nanoparticle versions of these biosensors combined with optical tweezing can provide a non-invasive means of intracellular investigation.

In this chapter, the optical tweezing of several types of hybrid particles are investigated. Dielectric microspheres containing fluorophores are examined in an attempt to experimentally observe near-resonance optical tweezing effects. The behavior of dielectric-metal core-shell and core-half-shell nanoparticles in optical traps are also studied. Although the resonance theory developed in the previous chapter applies to particles in the Rayleigh regime, extension of the notion of enhanced resonance trapping to particles with diameters on the order of or much larger than the trapping wavelength is intuitively satisfying. Macroscopic properties like the electric susceptibility are analogous to the microscopic polarizability, and can be related through the Clausius-Mossotti equation [74]. In addition, the real and imaginary parts of the refractive index of a dielectric particle can be linked with suitable KK relations [87, 88, 91]:

$$n(\omega) = 1 + P\int_{-\infty}^{\infty} \frac{d\omega'}{\pi} \frac{k(\omega')}{\omega' - \omega}, \tag{3.1}$$

$$k(\omega) = 1 + P\int_{-\infty}^{\infty} \frac{d\omega'}{\pi} \frac{n(\omega') - 1}{\omega' - \omega}, \tag{3.2}$$

where $n + ik$ is the complex, frequency dependent index of refraction. Furthermore, microsphere coatings comprised of colloidal particles can exhibit plasmon resonances that can provide enhanced trapping. At frequencies slightly red-detuned from resonance, the real refractive index peaks while the imaginary refractive index (absorption) is reduced compared to on-resonance. We expect for a macroscopic particle that the incident laser light is refracted more strongly, thus the particle feels a stronger gradient force towards the focus. Since the absorption is reduced, the particle also feels less of a scattering force than at resonance. Both of these factors suggest that the trapping will be enhanced at near-resonant frequencies even for macroscopic particles.

To investigate the trapping of our hybrid particles, we observed their position fluctuation dynamics while held in our optical tweezers. By comparing trap stiffness among a variety of particle types, we gained information on the light-particle interaction strengths. In particular, we found that many of our core-shell particles were ejected from the trap. The few particles that could be three-dimensionally confined did not experience significant differences in trapping dynamics compared to blank particles. In addition, these particles showed an apparent increased trap stiffness resulting from reduced viscosity of the surrounding medium. It was speculated that this reduction was due to heat generation by the absorptive metallic colloids of the hybrid particles. Further image analysis provided qualitative effects of asphericity and optical anisotropy due to half-shells on laser trapping stability.

3.1 Theory

The most appropriate theoretical description of neutral particle trapping using single-beam gradient optical tweezers depends on the particle size relative to the wavelength of the trapping beam. For particle diameters much smaller than the wavelength ($d << \lambda$), the particle, described in the Rayleigh regime, is treated as a simple, induced dipole oscillating in a harmonic electric field [9, 18]. In this regime, trapping forces can be resolved into two components [74]: a scattering component, in the direction of the incident light, and a gradient component, along the intensity gradient. Stable trapping for a single-beam gradient trap occurs when the gradient force exceeds the scattering force to generate a potential well deeper than the particle's thermal energy due to Brownian motion. It is believed that the scattering force on a non-absorbing Rayleigh particle is proportional to its scattering cross section, so the scattering force scales with the square of the polarizability (volume) [72, 75], or as d^6. The gradient force scales linearly with polarizability (volume) [8, 75], thus having a d^3 dependence. These quadratic and linear dependences on polarizability for the scattering and gradient forces, respectively, suggest that stable three-dimensional single-beam trapping occurs only for particles smaller than some maximum threshold size. Svoboda and Block [16] use this polarizability dependence to explain increased trapping forces for gold Rayleigh particles over latex particles of similar size surrounded by water.

For particles with diameters much larger than the trapping wavelength ($d >> \lambda$), conventional theory assumes the geometrical optics regime in which trapping forces can be attributed to momentum exchange due to the refraction and reflection of plane waves [6, 100]. In this size regime, dielectric particles are readily trapped in three dimensions whereas metallic particles are difficult to trap three-dimensionally because scattering, reflection, and absorption are increased.

To quantify trap strength, one can analyze the particle's position behavior as the particle falls in the trap [113, 114], while the trap is moved relative to the surrounding medium [56, 113, 115, 116], or as the particle experiences dynamic position fluctuations due to Brownian motion in a stationary trap [16, 36, 56, 117, 118]. The last method, which we utilize in the current work, assumes a particle surrounded by a medium of dynamic viscosity η trapped in a harmonic potential well subject to a microscopic random thermal force. The small Reynolds numbers of practical systems indicate that viscous forces dominate over inertial forces [36], thus the particle's motion can be described by the reduced Langevin equation:

$$\gamma_{trans}\dot{x} + \kappa x = F(t), \tag{3.3}$$

where x and $\dot{x}$ are the particle position and velocity, respectively, γ_{trans} is the hydrodynamic drag coefficient equal to $3\pi\eta d$ for a sphere, and κ is the trap stiffness or harmonic force spring constant. Fourier domain solutions of this system are well known and deviations often present in experiment have been studied in great detail [36, 117, 119, 120]. One finds that, in the frequency domain, the power spectral density (PSD) of the position fluctuations follows a Lorentzian profile:

$$S(f) = S_0 \frac{f_c^2}{f_c^2 + f^2} \tag{3.4}$$

with low-frequency PSD amplitude $S_0 = 4\gamma_{trans} k_B T / \kappa^2$ and corner frequency $f_c = \kappa / 2\pi\gamma_{trans}$, where k_B is Boltzmann's constant and T is absolute temperature. Note, for a given solvent, the corner frequency is proportional to the trap stiffness. If the particle is isotropic and trapped stably in three dimensions, the gradient force dominates the scattering force and is given by [9]:

$$\langle F_g \rangle = \frac{\varepsilon_0}{4}\mathrm{Re}[\chi]\nabla(|E|^2), \qquad (3.5)$$

where ε_0 is the vacuum electric permittivity, χ is the particle susceptibility (or polarizability for Rayleigh particles) and E^2 is proportional to the laser beam power. Equating this to a harmonic restoring force $-\kappa x$, we see that if the gradient force dependence on laser power is linear, the corner frequency will also be proportional to laser power.

If a trapped particle remains close to the minimum of the potential well created by the laser beam, a harmonic potential is expected. The positions visited by the particle will then be Boltzmann-distributed as given below:

$$N(x) = N_0 \exp\left(-\frac{\kappa x^2}{2k_B T}\right). \qquad (3.6)$$

Our core-shell hybrid nanosystems consisted of both nanoscale Rayleigh particles and larger microscale particles. Rigorous electromagnetic theory has not been found in the literature to describe such systems; however, some effects are expected. For a 1 μm silica particle with a shell layer containing 40 *nm* metallic colloids, the total polarizability of the system is increased compared to pure silica. In addition, a shell of metallic colloids reflects less than a pure metallic coating or film, which could also increase trapping strength. The addition of metallic nanoparticles to a macroscopic 1 μm silica particle can be treated as a small perturbation in the scattering and absorption cross section of a pure silica particle; thus, position fluctuations for the hybrid particle system should be qualitatively similar to those for a pure dielectric particle. For our half-shell hybrid nanoparticles, the shell thickness was maintained below the skin depth; therefore, reflection was minimized. The optical anisotropy of a half-shell particle caused more drastic changes in trapping behavior.

3.2 Hybrid Particle Preparation and Characterization

To investigate the effects of metal composition on hybrid-particle optical trapping, various particle configurations were fabricated and characterized. Single particles from each sample were then optically trapped, and their motion dynamics recorded. The data was then analyzed to gain qualitative and quantitative information about the trap's properties. The near-infrared microspheres were also compared to microspheres with an absorption peak in the yellow region of the spectrum.

Dye-loaded dielectric microspheres were first studied in an effort to observe a near-resonant enhancement due to the embedded fluorophores. The remainders of our sample particle-systems were comprised of a spherical dielectric core surrounded by an outer layer or shell of metal. The core consisted of commercially available silica microspheres while the outer shell is incorporated either by attaching gold or silver colloids, or via vapor deposition.

3.2.1 Fluorescent Probes

Both dye-loaded polystyrene beads and blank commercial polystyrene microspheres (Molecular Probes, FluoSpheres® carboxylate-modified microspheres) were optically trapped for comparison. The dye-loaded microspheres were 1.0 *μm* diameter and contained either near-infrared fluorophores designed to be excited at 715 *nm* and emit at 755 *nm* or yellow microspheres excited at 505 *nm* that emitted at 515 *nm* (see Figure 3.1).

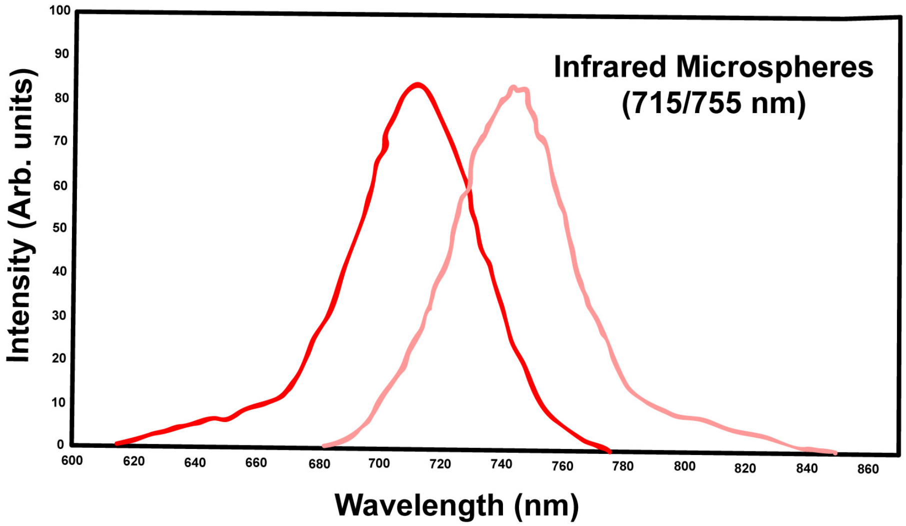

Figure 3.1 Excitation and emission spectra of NIR Fluospheres (Molecular Probes).

3.2.2 Aminated Silica Cores

A total of 212 mg of 0.97 *μ*m diameter dry silica microspheres (Bangs Labs, Fishers, Indiana) were suspended in 40 mL of ethanol (99.5%, A.C.S. reagent grade, absolute, 200 proof) in a 100 mL round bottom flask. In order to provide amine groups to the surface of the silica, 1 mL of 3-aminopropyltriethoxysilane (99%, Aldrich, St. Louis, Montana) was added to the suspension. Amine functionalization of the silica particles is known to facilitate synthesis of silica-noble metal core-shell microspheres [121]. The reaction was allowed to run for 2 hours and 15 minutes in the sealed 100 mL round bottom flask with constant magnetic stirring to provide even distribution of the amine functionalization to the silica particles. The particles were filtered using a 0.8 μm ATTP Isopore™ Membrane filter (Millipore, Billerica, Massachusetts). They were re-suspended in ethanol to wash off any unreacted material and then filtered again. The particles were suspended in 10 mL of MilliQ de-ionized water for use.

3.2.3 Silica-Gold Core-Shell Microspheres

1 mL of a 5 nm diameter gold colloid (Ted Pella, Inc., Redding, California) suspension was added to a 20 mL scintillation vial. Because the colloid is certified to have been washed of all reactants during synthesis, citrate must be added to enable attachment of the colloids to the amine groups on the silica microspheres [121]. A 1 mL aliquot of 34 mM sodium citrate solution (99%, A.C.S. reagent grade, Alfa Aesar, Ward Hill, Massachusetts) was added in order that the citrate ion would ligate the 5 nm gold colloid. After mixing, 1 mL of the amine functionalized silica microspheres was added to the scintillation vial. The mixture color changed from light red to deep red. The suspension was sonicated to re-suspend dark red particles that may have settled out of solution. After sonication, the suspension was centrifuged at 5000 rpm for 10 minutes. All of the particles at the bottom of the centrifuge tube, post-sonication, were deep-red in color while the solution was clear suggesting little unattached gold colloid had suspended. The clear solution was removed using a Pasteur pipette, and the particles were re-suspended in 10 mL of ethanol. Centrifugation and re-suspension in ethanol was repeated once more. The particles were filtered with the 0.8 μm ATTP Isopore™ filter until dry and re-suspended in 10 mL of de-ionized water for use.

For silica-gold core-shell particles containing larger gold colloids, a similar fabrication procedure was performed with the initial volumes being 0.100 mL of the amine functionalized silica combined with 1.00 mL of the 34 mM sodium citrate solution. A 10 mL aliquot of 40.3 nm diameter gold colloids (Ted Pella) was added, and the suspension was placed in an ultrasonic bath for 90 minutes. Upon removal from the bath, dark red particles quickly began to settle.

3.2.4 Silica-Silver Core-Shell Microspheres

Silver colloids of <5 nm diameter were synthesized according to the method described in the literature [122]. A 100 mL round bottom flask was cleaned with Alconox (White Plains, New York), rinsed, and dried thoroughly. After drying, 47.5 mL of MilliQ de-ionized water was added. The de-ionized water was de-oxygenated by bubbling with nitrogen gas for 30 minutes. Subsequent reactions all took place under vigorous stirring (1200 rpm).

After de-oxygenation, a 0.500 mL aliquot of 30 mM sodium citrate was added to the water and allowed to mix for several seconds. Next, 1.00 mL of 5 mM silver nitrate solution (EM Science, Gibbstown, New Jersey) was added to the mixture and allowed to mix for several seconds. After 0.500 mL of 50 mM sodium borohydride solution (99%, Aldrich) was added, the solution immediately turned a pale yellow color. The solution was then stirred for 30 seconds more before adding 0.500 mg/mL of poly(vinyl)pyrrolidone (M_w = 55,000 g/mol, Aldrich). The suspension turned dark yellow in color and was stirred an additional 30 minutes.

A 1 mL aliquot of the <5 nm silver colloid suspension was added to a scintillation vial, along with 1 mL of de-ionized water. The 34 mM sodium citrate was not needed (as in the preparation of silica-gold samples) because the citrate ion was still present from the colloid synthesis. 1 mL of the amine functionalized silica microspheres was added to the colloid suspension, immediately making the solution cloudy. Over time, all of the silica-silver core-shell particles came out of suspension and collected on the bottom of the scintillation vial. This mixture was filtered using the 0.8 μm ATTP Isopore™ filter. The particles were washed with several ethanol rinses, and dry particles were re-suspended in 10 mL of de-ionized water for experiments.

Again, silica-silver core-shell particles containing larger silver colloids were also fabricated with a similar procedure. Starting volumes were 0.100 mL of the amine functionalized silica and 1.00 mL of the 34 mM sodium citrate solution. 10 mL of

40 ± 5 nm silver colloids (Ted Pella) were added, and the suspension was sonicated. After sonication, yellow particles started to settle.

3.2.5 Silica-Metal Core-Half-Shell Microspheres

MOONs (MOdulated Optical Nanoprobes) can be fabricated by coating one hemisphere of nanoparticles with an opaque metal as illustrated in Figure 3.2. Our procedure utilizes commercially available silica nano- and microspheres (Bang's Labs) in combination with a gold sputter chamber.

Silica particles with a diameter of 1.0 μm and 2.0 μm were separately suspended in water and deposited onto a glass microscope slide with a micropipette. The solutions dried on the microscope slide leaving near single layers of microspheres. The slide was then inserted into a Vacuum Desk-II Cold Sputter-Etch Unit (Denton Vacuum, Inc., Cherry Hill, NJ) and gold was sputtered onto the slide for 40 and 80 seconds, respectively. Sputtering was performed under vacuum, which allowed the gold to travel in a linear fashion, coating only the top hemisphere of the particles. This creates a material anisotropy, the top hemisphere of the spheres being metallic and the bottom

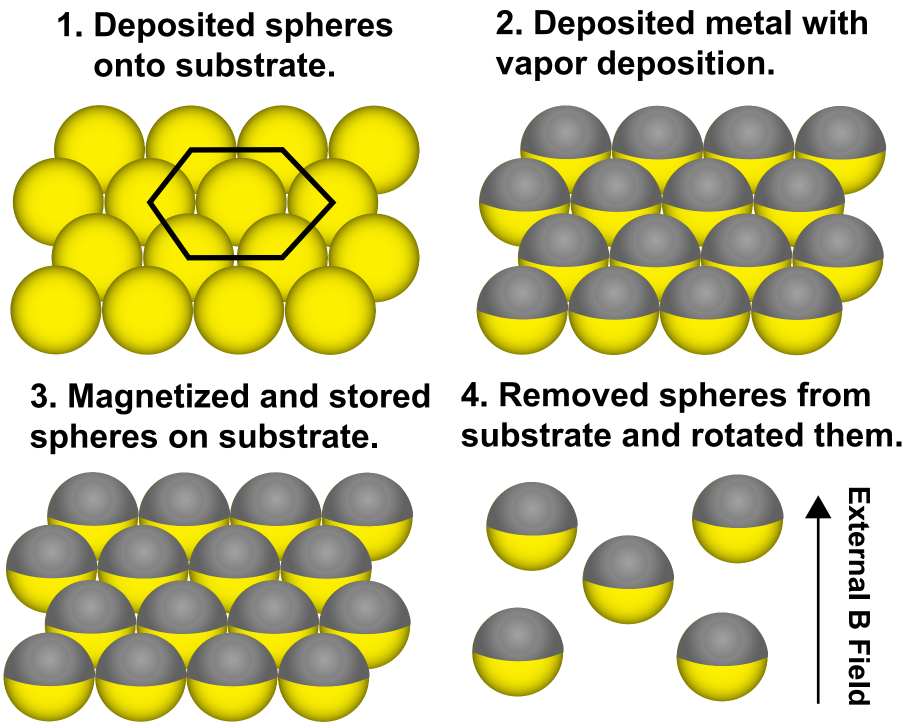

Figure 3.2 Fabrication process of gold coated polystyrene spheres.

hemispheres being silica. The coated particles on the microscope slide have a long shelf life and can be removed from the microscope slide long after they have been coated. We removed the gold coated particles by using an artist's paintbrush. To suspend the coated particles, we sonicated the brush in water for a short amount of time.

3.2.6 Characterization Methods

For our MOONs, in order to find the thickness of gold that corresponds to a specific duration of sputter coating, we used an optical microscope (Olympus IMT-II) interfaced via LabVIEW with a spectrometer (Acton Research Corp., Acton, MA) to measure transmission of bright field light through the gold coated slide. Attenuation caused by the presence of the gold was then determined by dividing the intensity of light transmitted through the coated slide by the intensity of light transmitted through an uncoated region of the same slide. From this attenuation and given that the skin depth of gold is 17 nm at a wavelength of 589 nm [123], we calculated that the gold layer was approximately 6.7 ± 0.5 nm for a 40 s coating (dashed line) and 12 ± 1 nm for 80 s (solid line). The error corresponds to the standard deviation estimated by measuring at different points on the gold coated slide. It is worthwhile to note that rough surfaces are not coated as easily as smooth surfaces. So, the actual gold layer thickness on the silica microspheres was most likely smaller than our calculated value.

Hybrid nanoparticles in solution were dried and characterized using scanning and transmission electron microscopy (SEM, TEM). Examples of silica-silver core-shell particles are shown in Figure 3.3. So as to not obscure the presence of the gold half-shell,

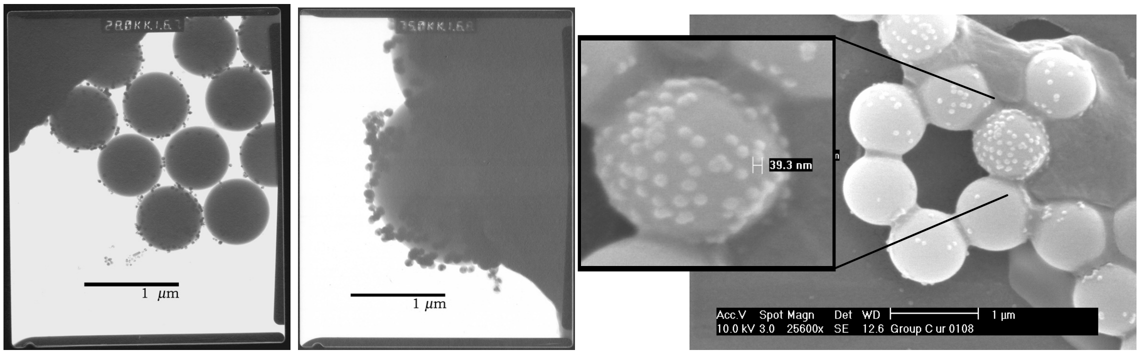

Figure 3.3 TEM (a, b) and SEM (c, inset) images of 1 micron silica-40 nm silver core-shell particles.

MOONs were not coated with an additional metal, as is typical prior to SEM imaging. Enough contrast remained to distinguish the boundary of the gold coating against the silica matrix.

3.3 Experimental Procedure

To investigate the resonance-enhanced trapping effect on dye-loaded microspheres, experiments were conducted in collaboration with Christoph F. Schmidt and Erwin Peterman, both currently at the Vrije Universiteit in the Netherlands. A schematic of the instrumental setup is shown in Figure 3.4. This system is similar to the setup used to investigate metal-coated hybrid particles. A Ti:sapphire (Coherent, Mira 900 diode pumped or Spectra Physics, Tsunami, pumped by a Millenia XsJs) laser system was used to trap our samples. The trapping beam, tunable from 730-900 *nm*, was focused by a 100X (NA = 1.3) oil immersion objective and recollected with a condenser. The back focal plane of the condenser was imaged onto a quadrant photodiode for position detection measurements [124]. To measure the trap stiffness, the power spectral density of these position fluctuations was acquired and fit to a Lorentzian profile. The corner frequency of this curve can be related to the trap stiffness through a proportionality constant [125]. At each trapping wavelength, it was ensured that the corner frequency dependence on power was linear. This provided a means of calibration for differences in beam power at different trapping wavelengths. The laser was set to emit continuous-wave near infrared (NIR) radiation. Fluorescent microspheres were trapped at various wavelengths while our core-shell samples were trapped at 760 nm, accomplished by reducing the bandwidth of the laser enough to inhibit pulsed radiation. The trapping beam then passed through an adjustable neutral density filter wheel to control power. The beam diameter was expanded to just overfill the back aperture of the trapping optics. Beam steering mirrors directed the laser light through a dichroic mirror into either a home-built train of optics or a commercial inverted optical microscope (IX71, Olympus). The home-built system was qualitatively similar to our partially commercialized one, thus we describe only the specifics of our partially commercial system. Custom-assembled detection and illumination optics were attached to the microscope above the stage using mechanical rails. Upon entering the microscope, the beam was deflected by a hot mirror.

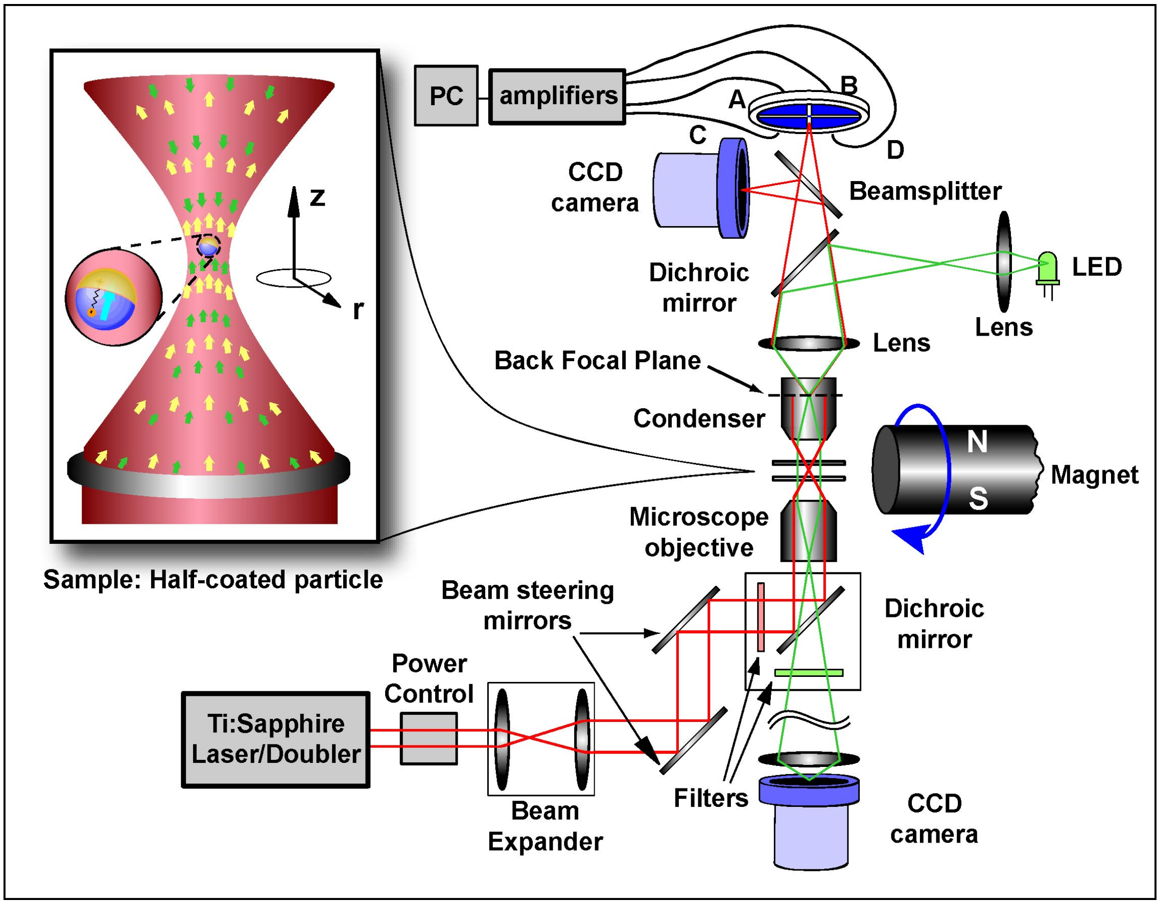

Figure 3.4 Experimental schematic of optical tweezers setup. The apparatus is a conventional system with both reflection and transmission illumination capabilities.

The hot mirror reflected NIR, was partially reflective for ultraviolet light, but transmitted visible. The NIR beam was then focused by a 100X (NA = 1.3) oil immersion objective (UPlanFl, Olympus), thus forming the optical trap near the sample plane. Light forward-scattered by the trapped object interfered with the incident laser light and was then recollected by a condenser comprised of another oil immersion objective (PlanApo 60X, NA = 1.4, Olympus). The back focal plane of the condenser was imaged onto a quadrant photodiode (Pacific Silicon Sensor, Inc., Westlake Village, CA) for position detection measurements [92]. Difference voltage signals for the x- and y-axes and sum voltages from the quadrant diode were amplified and fed into a digitizing oscilloscope (TDS 420, Tektronix) which was interfaced to a computer via LabVIEW. To aid in alignment, light impinging upon the quadrant diode was also split using a non-polarizing beamsplitter and viewed using a ccd camera (Watec). Samples were placed on the translation stage in a chamber consisting of two #0 cover slips separated by double stick tape (~100 μm thick) and sealed with grease to reduce evaporation and convection currents. When measuring fluorescent probes, our sample chambers contained only either dye-loaded microspheres or blank ones. For our core-shell experiments, two separate regions were formed for a given pair of cover slips, one containing blank silica particles, the other containing hybridized forms of the silica particles (either core-shell or half-shell). Two methods of illumination were possible: (1)for fluorescent probes, transmission from above using an LED of visible wavelength (usually green, max. intensity = 525 nm) and (2) fore dielectric-metal core-shell samples, reflection from below using a mercury arc lamp. The sample plane could be imaged in either mode using another ccd camera (Photometrics, CoolSNAP ES) placed on the trinocular tube above the eyepiece of the microscope. Reflection mode was especially helpful by providing more contrast compared to regular bright-field transmission to distinguish metallic coated particles from blank particles near the sample plane.

Samples were trapped in water approximately 10 μm above the bottom cover slip and their position fluctuations in time were recorded. Each particle was held for several seconds to ensure stable laser tweezing before the time trace was started. To make certain we were operating in the linear regime, 5-10 particles were trapped at approximately 8-10 different laser beam powers. Half-shell particles could not be stably trapped using our single-beam gradient optical tweezers; nevertheless, position trajectories were imaged and recorded.

3.4 Data Analysis

The following data analysis procedure was performed at a series of laser powers for each particle type. Quadrant diode voltage fluctuation time traces were acquired in three channels: two difference voltage traces for the radial dimensions (x and y), and one sum voltage trace for all diodes. For each radial dimension, a histogram of the voltages was recorded to ensure a Boltzmann distribution. Note, a Boltzmann distribution is expected for position; however, if the particle is close to the trap center, the relationship between position and voltage can be assumed linear [97]. Curves that exhibited behavior that deviated from a Boltzmann distribution were discarded.

The x- and y-dimension curves were both normalized by dividing by the sum voltage trace. For each radial dimension, the power spectral density (PSD) estimate was calculated using the “periodogram [92]” function of MATLAB. The periodogram calculates the modulus-squared of a fast Fourier transform of the finite, digital voltage time series. The resulting PSDs were averaged, and the final mean PSD was binned logarithmically in frequency, a noise reduction technique otherwise known as “blocking” [119, 120]. Using least squares curve-fitting, a Lorentzian profile was fit to each PSD curve according to Eq. (3.4). To avoid effects due to low frequency errors from beam pointing fluctuations and high frequency errors from detector response [119, 120] or aliasing [126], only points with abscissa between 10^1 Hz and about half the Nyquist frequency [92] (one fourth the sampling frequency of our detection) were used in the fit. Fit parameters were the corner frequency, in Hz, and the PSD amplitude S_0, in units V^2/Hz. S_0 can be converted to nm^2/Hz after calibrating volts to nanometers, either by inducing a known spatial displacement of the particle and measuring the voltage, by estimating the rms displacement from the voltage histograms, or by assuming the Stokes’ force is in equilibrium with the optical restoring force [118]. The corner frequency is related to trap stiffness by proportionality constant assuming the solvent viscosity is constant.

Because half-coated particles could not be stably trapped, only image video recordings were acquired, analyzed qualitatively and compared to phenomena in previous literature.

3.5 Results

Figure 3.5 shows typical voltage fluctuation time trace curves. The particular data shown represents an optically trapped 1 μm silica-5 nm gold core-shell particle, although the position fluctuation time traces for fluorescent particles are qualitatively similar. Figure 3.6 indicates a histogram of the voltage time traces from Figure 3.5. Since the positions visited by the particle are Gaussian distributed in accordance with Eq. (3.6), the assumption that the voltage-position relationship is linear for trapped particles is justified. There appears to be a slight shift of the trap center as well as a small amount of asymmetry. This is probably caused by minor misalignment and detector crosstalk

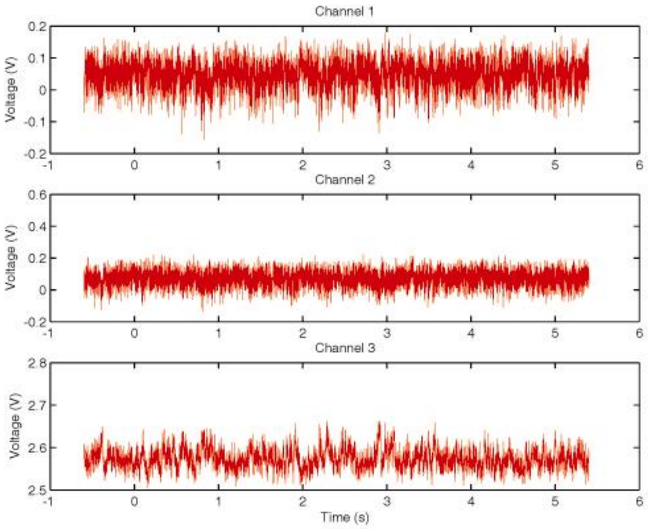

Figure 3.5 Typical voltage fluctuation time traces. Channels 1, 2 and 3 are the x-difference, y-difference and sum voltages, respectively.

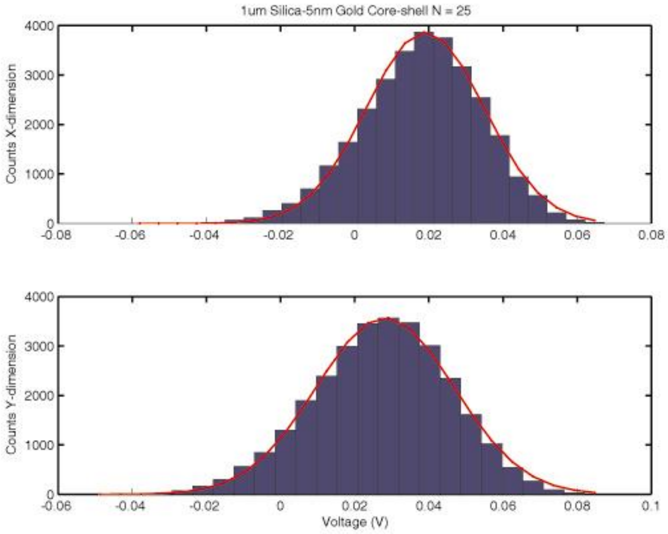

Figure 3.6 Histograms of visited voltages. For particles close to the trap focus, the voltage, which is proportional to position, is Boltzmann distributed.

between radial directions. After normalization, the PSDs are calculated for each dimension. The original PSD, the blocked PSD, and the Lorentzian fit are plotted on the same graph in Figure 3.7. All PSDs and fits for this particle type are plotted in Figure 3.8. This procedure was done for each particle, both fluorescent and core-shell ones, at a series of laser powers ranging from 1-150 mW entering the trapping objective.

3.5.1 Fluorescent Probes

The trap stiffnesses in the *x*- and *y*-directions for both the fluorescent and blank polystyrene microspheres are summarized in Figure 3.9 and Figure 3.10. The data is not conclusive in that it is not clear if a trapping enhancement has occurred. This has been attributed to several factors. First, the width of the absorption peak of the fluorescent microspheres is too broad to see an enhancement at a well-defined wavelength (see Figure 3.1). Second, the dye concentration itself may be too low in the microspheres, thus providing less actual effective material to trap. A better sample for trapping may be a particle with a narrower absorption peak width and higher concentration of excitable molecules. Potentially appealing samples also include gold or silver colloids and polyphenyl crystals. Although highly reflective, gold and silver have relatively large polarizabilities [16] compared to polystyrene, even in the NIR, and they exhibit sharp plasmon resonances that may contribute to increased tweezing strengths [19, 95, 96, 127]. The resonances typically occur in the blue-green region of the spectrum, thus trapping at these wavelengths is feasible for a "proof-of-principle" experiment rather than an actual biochemical experiment. Polyphenyl crystals may also have comparatively sharp spectral features with center wavelengths more compatible with our available laser sources.

3.5.2 Silica-Metal Core-Shell Hybrid Particles

Our silica-metal core-shell hybrid particles were optically manipulated with the same procedure. The presence of metallic colloids introduces the possibility for nonlinear effects at high powers. To better determine if the laser powers used in our experiments were low enough to remain in the linear regime, we looked at the dependence of corner frequency on power for each particle type. Results are shown in Figure 3.11. For each

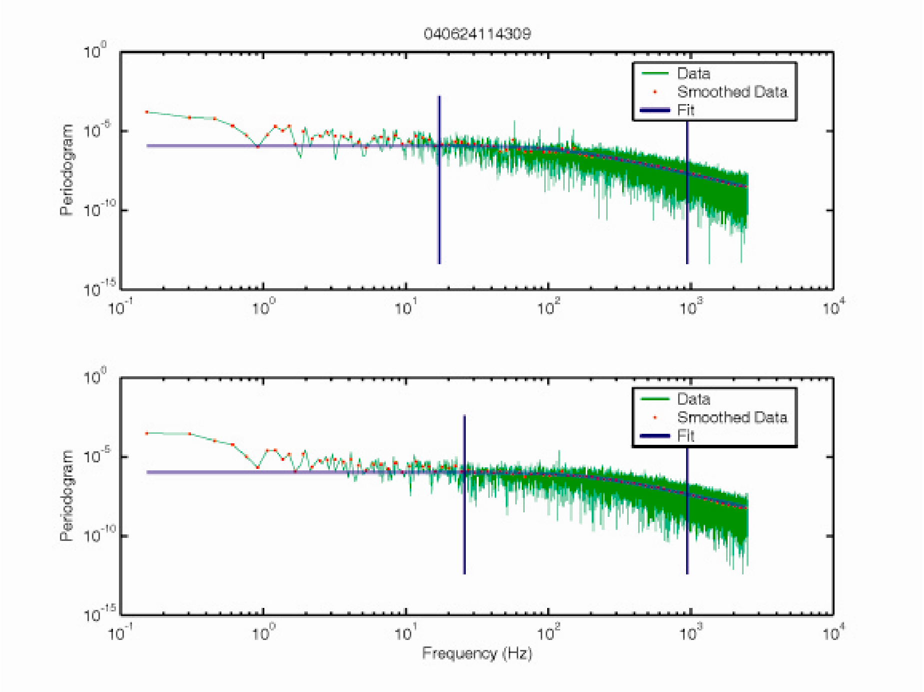

Figure 3.7 Individual x- and y- dimension PSDs for a 1 μm silica-5 *nm* gold core-shell particle (thin line). A Lorentzian profile (thick line) is fit to the logarithmically binned data (red dots).

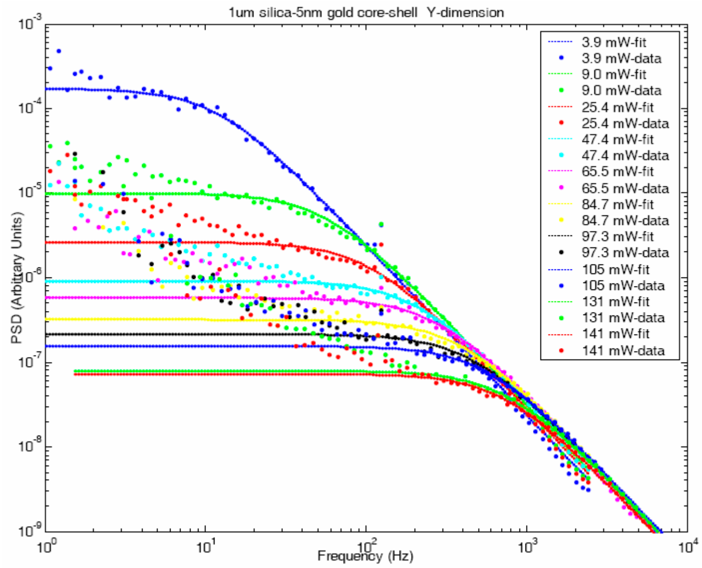

Figure 3.8 PSD as a function of laser beam power. Low frequency noise from beam point fluctuations is evident.

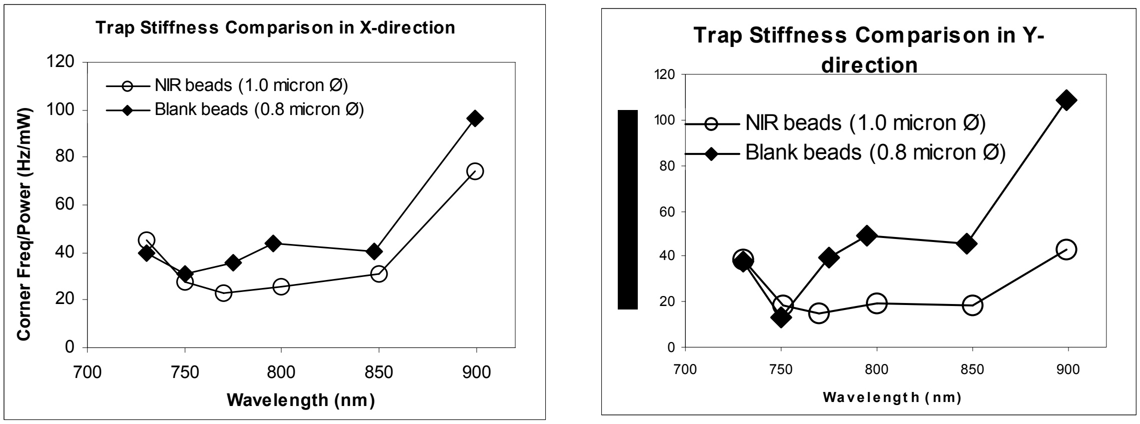

Figure 3.9 Trap stiffness calculations comparing near-infrared microspheres (715/755 nm ex/em) with blank microspheres.

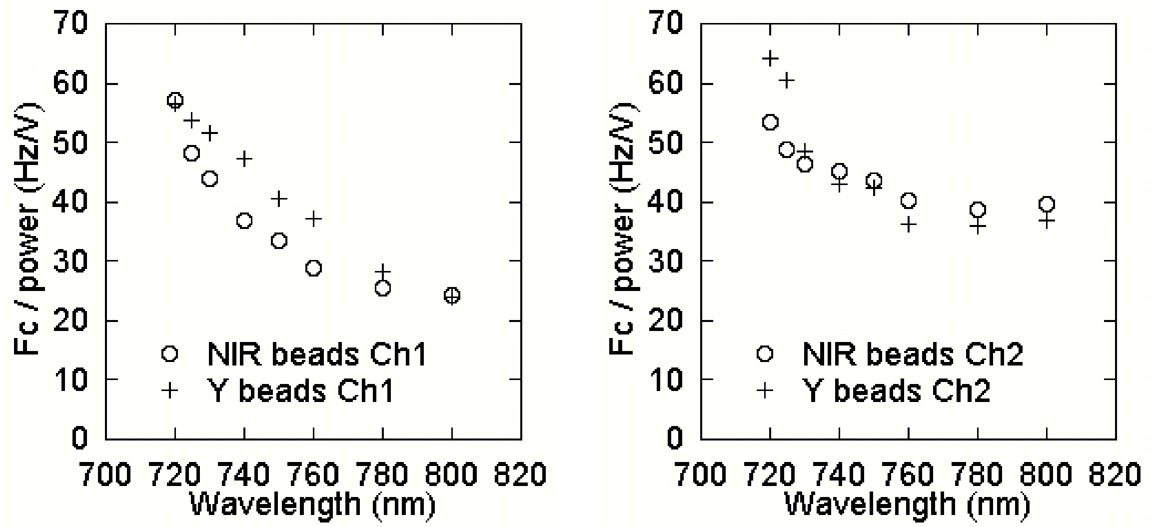

Figure 3.10 Trap stiffness calculations comparing near infrared microspheres (715/755 nm ex/em) with yellow microspheres (505/515 nm ex/em).

individual plot of Figure 3.11, we see two regions: a low power regime with a lower f_c/power (slope) and a high power regime with higher f_c/power (steeper slope). This can be explained by considering decreased solvent viscosity due to increased heat absorption at high laser powers. Since, however, this effect is not markedly increased when comparing blank particles to metal-containing particles, several conclusions can be made. One possibility is that the metal colloids are too small to provide much more than a small perturbation. In this case, heat absorption is mostly due to the solvent and the silica. In

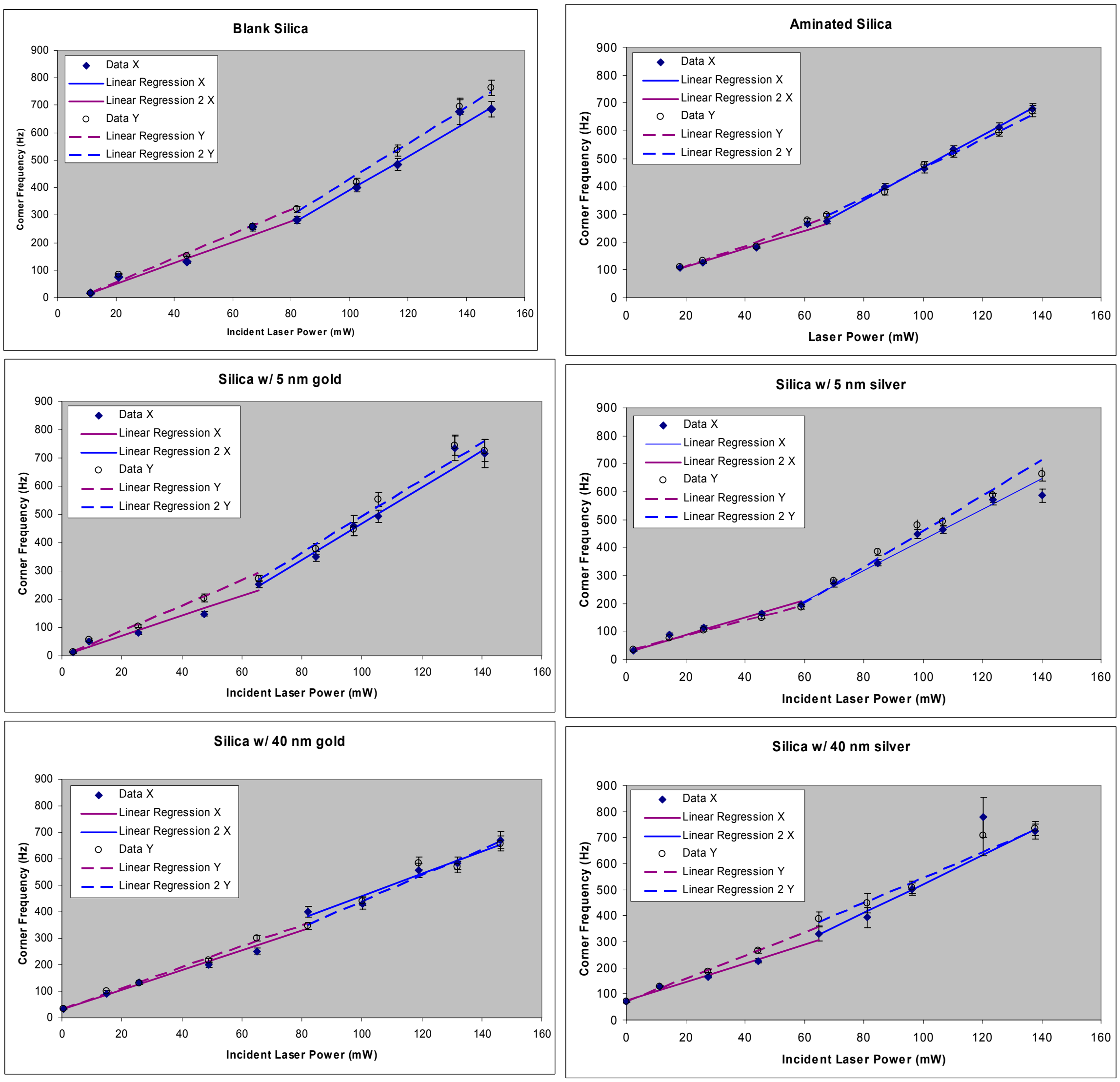

Figure 3.11 (a-f) Corner frequency dependence on laser beam power. In all plots two regimes are evident: a low power region with lower f_c/power and a high power region with higher f_c/power. The larger slope is attributed to increased solvent viscosity with increased heat absorption. No significant difference is apparent between blank particles and coated particles, nor between particles with 5 nm shells and particles with 40 nm shells.

addition, the metal shell does not hinder the optical trap to any measurable degree. This is clear from Table 3.1 in which the corner frequency per power is tabulated at high and low power for each particle type. There is no appreciable difference in trap stiffness between blank silica, aminated silica, and silica with 5 nm colloid shells. A slight drop in trap stiffness occurs for 40 nm colloid shells – this may be signaling the onset of limited trapping stability due to the increased scattering and reflection from the metal colloids

	f_c/Power			
	X-dimension		**Y-dimension**	
Particle	***Low Power***	***High Power***	***Low Power***	***High Power***
Silica	3.83±0.09	6.17±0.39	4.44±0.08	6.54±0.35
Silica-amine	3.25±0.15	5.83±0.27	3.66±0.12	5.26±0.20
Silica-am-5nm gold	3.54±0.12	6.41±0.42	4.52±0.14	6.52±0.37
Silica-am-5nm silver	3.08±0.09	5.48±0.19	2.71±.08	6.39±0.20
Silica-am-40nm gold	3.74±0.11	4.18±0.47	3.95±0.09	4.90±0.37
Silica-am-40nm silver	3.60±0.16	5.54±0.59	4.39±0.14	4.87±0.51

Table 3.1 Summary of corner frequency per power measurements for silica-gold core-shell microspheres.

observed by others [128]. If the colloid presence has a small effect, trapping of hybrid particle probes will have the same behavior as simpler homogeneous particles - a desirable outcome when sensing is most significant. This suggests, however, that no enhancement has occurred due to increased polarizability. Another possibility is that few colloids actually remained on the silica cores. Particle uniformity is a nontrivial issue in the fabrication of nanoparticle systems. The distribution of colloid coverage on silica cores is likely to be large in our samples. Thus, trapping events between different particles may not be comparable. This is also true of our half-shell particles. Coating thickness can vary drastically from particle to particle within a single sample.

3.5.3 Silica-Gold Core-Half-Shells

For our silica-gold core-half-shell particles, or MOONs, no three-dimensionally stable trapping was observed. Most particles that diffused below the trap were quickly confined radially but were then forced upwards by the axial scattering force. In several extraordinary, yet repeatable cases a MOON would remain in the lower cone of the laser beam below the focus. The particle would undergo fast rotations about the optical axis while continuously being bumped by random fluctuations in all directions. If the trap location were slowly moved relative to the surrounding medium, the particle would continue its clockwise circular trajectory about the beam focus, verifying that it was truly loosely confined to the lower cone of the laser beam. Similar rotational behavior has been described using Laguerre-Gaussian beams [126].

3.6 Conclusions

We have optically manipulated several hybrid particle systems including fluorophore-embedded dielectric microspheres and microspheres comprised of silica-gold and silica-silver. Our analysis of trap stiffness measurements reveals several possibilities. The trapping of core-shell hybrid systems fabricated using spatially separated colloids for shells is possible. Redistribution of the colloids such that the shell covers approximately half of the core induces a strong asymmetry in the particle that strongly hinders conventional, stable, three-dimensional optical trapping, but it may offer schemes for yet unstudied rotational phenomena.

Several improvements must be made before conclusive data can be acquired. Trapping force-constant analysis techniques must take into account all sources of error present in practical measurements, including unintentional filtering due to detection equipment, aliasing (distortion that arises from sampling at to low a frequency) from digital recording equipment, and viscosity changes due to surface proximity and heat absorption. Another aspect of concern is the design of a fabrication method that can provide more uniform distributions of the same hybrid particle. Our MOON fabrication scheme requires the creation of a monolayer of core particles such that there are few defects. Defects in the monolayer result in a low throughput percentage of properly coated microspheres as well as increased debris comprised of the coating material alone without cores. Solutions to these problems include the development of a wide-area low-defect monolayer fabrication [129] and precise, repeatable, half-coat manufacture using molecular beam epitaxy [35].

CHAPTER 4

SLIPPING RESISTANCE OF A MAGNETIC MICROSPHERE ROLLING AT A GLASS-WATER INTERFACE

The study of micro- and nanotribology has been gaining great interest in modern technology. In particular, knowledge of such effects as friction, adhesion, and lubrication at submerged surfaces on the micro- and nanoscale is crucial in the development of many cell sorting and cell separation devices based on micro electro mechanical systems (MEMS) and microfluidic chips [130, 131]. In addition, such knowledge can help us better understand and potentially mimic the mechanisms of locomotion of some cellular biological systems [132].

Surfaces can greatly affect the hydrodynamic motion of nano- and microscale objects. Optically torqued nanorods have been shown to undergo transitions from motor to rocking behavior due to interactions with a nearby surface [133]. Wax microdisks optically trapped at an opposing wall can exhibit switchback oscillations representative of a Hopf bifurcation [134]. The physical properties of surfaces themselves can also be engineered to provide specific adhesive and frictional qualities through nano-patterning [135, 136]. In numerous biological systems of interest, the dynamics of locomotion depend on surface-cell interactions. For example, the rolling velocities of white blood cells are mediated by density and binding affinity, among numerous other properties of certain selectin-coated surfaces [137, 138]. The oscillatory angular motion of magnetotactic bacteria in rotating magnetic fields can also be affected by the rotational drag near a surface [139, 140].

In this study, we report on a simple method for comparing the frictional properties of submerged surfaces on the micron scale. By observing changes in the motion of a magnetic microsphere slipping while rotating on a planar surface, we have differentiated between untreated glass substrates and substrates with polymeric coatings. In addition, the effects of particle surface roughness were investigated.

The motion of magnetic microparticles rotationally slipping near a glass surface was studied both for particles freely rolling along the surface as well as particles spatially confined by optical tweezers. Without the optical trap, particles rolled while slipping along the surface at different velocities depending on the rotation frequency of an external magnetic field. For low frequencies, the velocity of locomotion while slipping increased with the rotation rate. Beyond a certain threshold, the rolling velocity of the microsphere would decrease. This sharp change in motional behavior was often accompanied by a slight change in the overall direction of rolling. With the laser on, the particles were trapped but, while slipping, they roll towards one side of the potential well created by the light intensity. Increasing the magnetic rotation rate further tended to shift the particle even farther from the trap center until a threshold was reached after which the particle did not usually escape, but rather, remained confined while continually slipping against the glass surface, but residing closer to the trap center. Similar changes in angular direction of motion were observed at high rotation rates. Similar motion was repeatable rotating in the opposite direction.

Drastic changes in the rotational motion of micro-objects are characteristic of the behavior of overdamped driven nonlinear oscillators [37, 54, 133, 141, 142]. Such systems exhibit two classes of motional behavior: (1) linear phase-locked rotation at low external driving frequencies and (2) nonlinear phase-slipping rotation at high external driving frequencies. In the rolling-while-slipping systems described here, such nonlinear behavior at least partially contributes to the motion we've observed. Additional effects due to surface-microsphere interactions are proposed and investigated.

4.1 Experimental Details

4.1.1 Sample Preparation

To explore the frequency dependence of the drag coefficient near a surface, single polystyrene microspheres coated with magnetic particles (Spherotech, Inc., Libertyville, IL) of nominally 9 ± 1 μm diameter were studied using bright field microscopy in reflection mode. Two types of microspheres were used: carboxylated and amine-functionalized. The difference in surface roughness can be seen in Figure 4.1. A 1:100 dilution of particle stock solution (1% w/v) in de-ionized water was prepared. To aid in preventing particles from sticking to the glass surface as well as to each other, this solution was further mixed with 10% aqueous sodium dodecyl sulfate (SDS) in a 1:10 10% SDS:particle ratio. The final particle mixture was then magnetized for several minutes by a 1400 Oe field to saturation. After vortexing the solution at 3000 rpm for 15 seconds to separate aggregates, about 40 μL of the solution was inserted between two glass cover slips separated approximately 100 μm with double-stick tape and sealed with vacuum grease to prevent convection. Because the ratio between the sample chamber thickness and the microsphere radius was sufficiently large [143], hydrodynamic effects due to the top glass surface were neglected.

Glass cover slips (Erie Scientific Co, Portsmouth, NH) of thickness #0 were used for the sample cell either directly from the package untreated or coated with polyethylene glycol (PEG) to inhibit sticking to the glass caused by non-specific binding of the

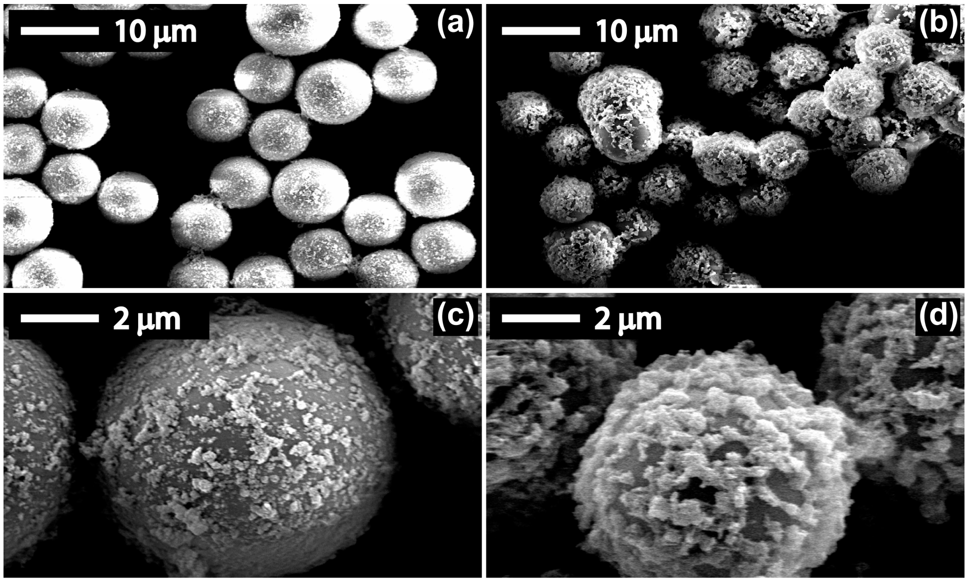

Figure 4.1 Scanning electron microscope images of (a), (c) amine-functionalized magnetic microspheres and (b), (d) carboxylated magnetic microspheres. Images (a) and (b) show the distribution of particle size was about 7-11 μm for both microsphere types. Amine-functionalized microspheres appeared to have less magnetic material and a decreased surface roughness compared to the carboxylated ones.

magnetic particles. The following pegylation procedure was adapted from the literature [144]. Cover slips were first cleaned with 10:90, 50:50, and then 90:10 mixtures of methanol and methylene chloride, consecutively, for 15 minutes each in an ultrasonic bath. The cover slips were then thoroughly rinsed with Nanopure water. After rinsing, the cover slips were immersed in a 30:70 mixture of 30% H_2O_2/H_2SO_4 for 30 min. This was followed by another rinsing and drying, after which the cover slips were then silanized by immersing in a solution of 1% 3-glycidoxypropyl trimethoxysilane in dried toluene for 24 hours. This was followed by an acetone wash. In order to hydrolyze the epoxide, the cover slips were placed in a 100 mM NaCl solution, at a pH ~4 for 3 hours, and then washed again with Nanopure water. Oxidative cleavage of the diols was accomplished by oxidizing them with a 5 mM $NaIO_4$ solution for 8 hours, followed by another Nanopure water rinse and drying. Pegylation was accomplished by placing the cover slips in 17 mM PEG-amine (2000 MW) in $CHCl_3$ for 15 min. The excess solution was removed and the cover slips were placed in an oven at 74^o C for 40 hours. The pegylated cover slips were then vigorously washed with Nanopure water and dried with nitrogen.

Verification of the presence of the PEG coating was accomplished by measuring the contact angle of a droplet of de-ionized water placed on a cover slip of each batch using the static sessile drop technique. Presence of the PEG layer reduced wetting of the glass surface, thus exhibiting a contact angle of 59 ± 3° compared to untreated cover slips which displayed a contact angle of 31 ± 4° (see Figure 4.2). This increase in contact angle for PEGylated glass agrees with measurements conducted by others in the literature [138].

4.1.2 Optical and Magnetic Manipulation

Particles were observed on an inverted microscope (Olympus IX-71) utilized for both bright field imaging and optical tweezing. To induce rolling, particles were simultaneously rotated about a single axis (x-axis) using an external rotating magnet located above the sample plane. Rotation rates ranged from 0-5.5 *Hz*. The amplitude of the magnetic field strength at the sample plane was 5-10 Oe. Light from a xenon arc

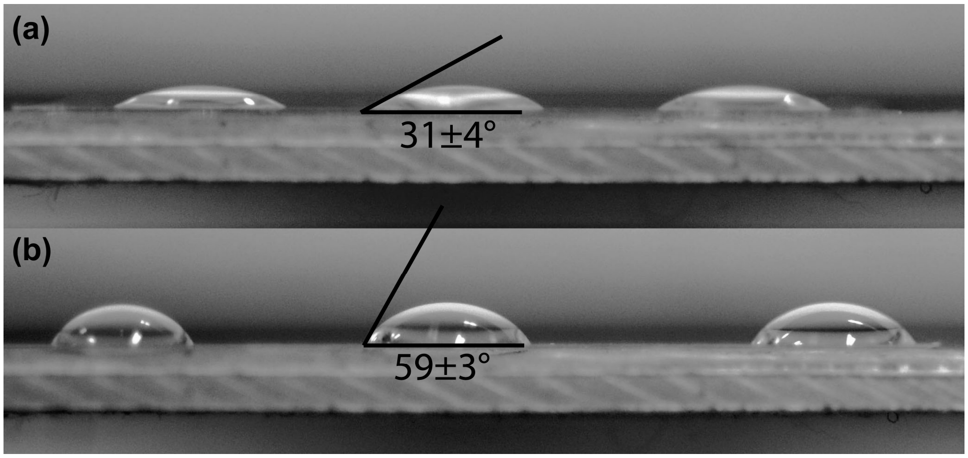

Figure 4.2 Static sessile drop technique for distinguishing (a) uncoated glass from (b) PEGylated glass cover slips. The increased contact angle on PEGylated slides (59 ± 3°) compared to untreated slides (31 ± 4°) was due to reduced wetting of the glass surface.

lamp in the visible range of the electromagnetic spectrum was coupled into a 100X (NA = 1.3) oil immersion (oil refractive index $n = 1.513$) objective and used to illuminate the sample. The visible light reflecting off particles in the field of view was recollected by the objective and delivered to a ccd camera (Roper Scientific, Photometrics CoolSNAP ES, 1392x1040, ~30 frames/s) for image analysis. Because the particle systems contained magnetic material which was much more reflective than the surrounding medium, signals were significantly brighter than background scattering from the aqueous solution itself. To observe particles rotationally slipping in place, 780 *nm* laser light from a Ti:sapphire laser in continuous wave mode was focused by the same objective using a dichroic beam splitter to create optical tweezers capable of trapping the particle near the bottom glass surface of the sample cell. Just before the ccd camera, the laser light was optically filtered to prevent saturation over bright field signals reflecting from the sample.

Laser illumination intensity entering the objective ranged from 1-5 mW/cm^2 by changing the laser power using a variable neutral density filter. Higher intensities induced stronger scattering forces that would lift particles upward off the glass surface in the z-direction. The optimum intensity was just below this threshold. At this level, the radial trapping forces were strong enough to keep the particle confined to a localized region of the xy-plane but the axial scattering force could not overcome the force due to gravitational sedimentation, thus maintaining the particle close to the glass surface. In addition, due to aberrations arising from oil-glass and glass-water index of refraction mismatches, optical tweezing gradient forces were typically most efficient only about 8-10 μm above the bottom glass cover slip (based on previous measurements with uncoated polystyrene microspheres).

The z-position of the glass surface was determined by locating the focus at which the smallest diameter reflected laser spot was observed with the ccd camera. The height of the center of each particle above the glass surface was then estimated using the focus knob of the microscope calibrated to be approximately 1 μm between markings. Particle centers were typically 5-10 μm above the glass, thus the particle surface was typically within a particle radius from the glass surface. With the laser trap off, systems in which the surfaces of the microsphere and glass were separated by a distance greater than 5 μm did not roll while being rotated and this data were thus discarded.

4.1.3 Image Analysis

Bright field images of particles collected with the ccd camera were analyzed using the Metamorph Imaging Analysis (Molecular Devices, Sunnyvale, CA) software package. From these images, the actual particle diameter was measured after the inter-pixel distance was calibrated using a USAF resolution target plate. In addition, particle location in the xy-plane was tracked as a function of time.

The image in Figure 4.3(a) is a snapshot of one measurement focused below the equator of the particle. Small magnetic colloids can be seen on a circular region of the particle surface. Colloids outside of this ring are out of focus and thus cannot be seen. In Figure 4.3(b), the microscope was set to focus on the equator of the particle, thus the microsphere edge can be seen reflecting and scattering the xenon lamp illumination forming a bright circular ring. Faint concentric rings of larger diameter indicate light interference near the particle edge. This focus was approximately 8 μm from the glass surface, thus the particle, measured to be 9.0 ± 0.2 μm in diameter, was within a radius from the glass surface, but not necessarily in direct contact. The location

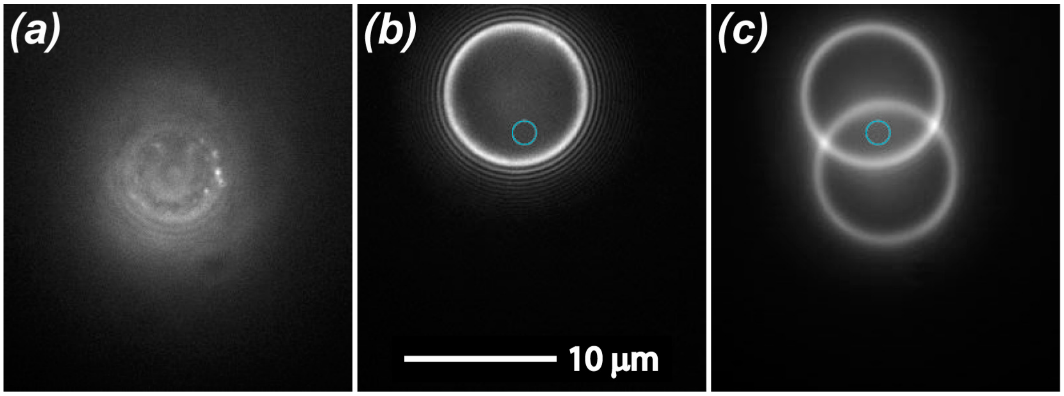

Figure 4.3 Aminated magnetic microspheres viewed under reflection mode microscopy. (a) Focused below the equator of the microsphere, magnetic colloids can be seen on the surface around a ring of focus. (b) Microsphere rotated by an external magnetic field rolling away from the center of an optical trap indicated by the blue circle. (c) Overlay of averaged images of the same optically trapped microsphere rolling due to either clockwise or counter-clockwise magnetic rotation.

of the laser trap is indicated by the blue circle with diameter corresponding to twice the size of the actual beamwaist at the focus. The magnetic field was rotated such that the particle rolled towards one end of the potential well created by the trap. The particle continued to rotationally slip but translationally fluctuated about a central position as determined by tracking the x- and y-coordinates of the center of the ring.

In order to observe if the motion is symmetric with respect to the rotation direction, the results of two measurements – one for each rotation – were overlaid onto one image. The image in Figure 4.3(c) depicts such an overlay. All snapshots were averaged for each rotation direction to obtain two blurred rings symmetrically displaced from the trap location. The axis joining the centers of the two rings is not perfectly aligned to the coordinate system of the ccd camera. This deviation shown in Figure 4.3(c) of about 10 degrees was due to a slight misalignment of the external magnet and was accounted for in our coordinate-tracking algorithm.

To quantify the rolling and slipping behavior of the microspheres, digital movies were recorded of the particle motion while magnetically rotated either with or without the optical trap present. Particle location in the xy-plane was measured using the "threshold image" centroid-tracking method in Metamorph. This tracking scheme isolates bright images by applying an intensity threshold to each frame before calculating the center of mass of the bright object. The threshold was manually set such that the recognized object region did not extend far beyond the bright ring, thus minimizing background, and the central region within each ring was partially recognized as part of the object. The search region was approximately 3-4 pixels larger than the object region in both height and width. The percentage match between frames was set to between 50-75%. This percentage match can fall below this threshold if the brightness of the object changes, such as when the particle rolls across an unevenly illuminated field of view. In such cases, the threshold was readjusted to match the prior criteria. This position tracking scheme is known to provide an accuracy of about 10 *nm*, depending on the noise level [145]. After tracking, coordinates were adjusted to account for the angular deviation previously discussed.

4.2 Theoretical Considerations

It is well known that in the low-Reynolds number regime the drag force $\boldsymbol{F}$ and torque $\boldsymbol{T}$ on a sphere of radius R infinitely far from a surface rotating with angular velocity $\dot{\boldsymbol{\theta}}$ and translating with velocity $\boldsymbol{v}$ in a fluid of dynamic viscosity η are given by

$$\boldsymbol{F}_{sphere} = -\gamma_{trans}\boldsymbol{v} \tag{4.1}$$

and

$$\boldsymbol{T}_{sphere} = -\gamma_{rot}\dot{\boldsymbol{\theta}}\,, \tag{4.2}$$

where $\gamma_{trans} = 6\pi\eta R$ and $\gamma_{rot} = 8\pi\eta R^3$ are the translational and rotational friction coefficients of a sphere, respectively. The dot-notation corresponds to differentiation with respect to t. As one approaches a surface, and assuming a no-slip boundary condition of the fluid at the surface, the friction coefficients increase. For small sphere-center-to-plane distances h, the friction coefficients should be multiplied by the corrections factors c_{trans} and c_{rot}, respectively [146]:

$$c_{trans} = \left[1 - \frac{9}{16}\left(\frac{R}{h}\right) + \frac{1}{8}\left(\frac{R}{h}\right)^3 - \frac{45}{256}\left(\frac{R}{h}\right)^4 - \frac{1}{16}\left(\frac{R}{h}\right)^5\right]^{-1} \tag{4.3}$$

and

$$c_{rot} = 1 + \frac{5}{16}\left(\frac{R}{h}\right)^3 . \tag{4.4}$$

Note, for Eq. (4.3), the translation direction is parallel to the plane. As the gap width $h - R$ approaches zero, lubrication theory [146] must be considered and the corrections are no longer valid. In such situations, the asperities on the sphere contact the wall and it becomes likely that the no-slip boundary condition of the fluid no longer holds [146, 147]. At these surface proximities and low Reynolds numbers, shear-induced lift forces are negligible [136]. Nevertheless, contact between the particle and the surface may consist of rolling-while-slipping, or "skipping," behavior mediated by the surface roughness of either side, further complicating the situation.

There have been several theoretical descriptions of the rolling and slipping motion of rough low-Reynolds number spheres in a viscous fluid down an inclined plane under the influence of gravity [148, 149]. These treatments, however, do not deal with the motion of rotationally driven spheres, such as magnetically rotated microspheres. For such systems, nonlinear behavior arises when the external driving fields rotate at frequencies faster than can be supported by the rotational drag. For a magnetic microsphere aligning with an external rotating magnetic field, this nonlinear behavior emerges from an equation of motion involving a balance of torques given as

$$I\ddot{\theta} + \gamma_{rot}\dot{\theta} = mB\sin(\Omega t - \theta) \tag{4.5}$$

where I is the moment of inertia of the particle, m is the magnetic moment of the microsphere, Ω is the rotation frequency of the external magnetic field of strength B and θ is again the phase angle of the microsphere with respect to the lab frame. Eq. (4.5) can be written in dimensionless form by substituting $\Omega_c = mB/\gamma_{rot}$, $\tau = \Omega_c t$, and $\phi = \Omega t - \theta$. Furthermore, operation in the low Reynolds number regime [150] allows the inertial term to be neglected to obtain

$$\frac{d\phi}{d\tau} = \frac{\Omega}{\Omega_C} - \sin(\phi), \tag{4.6}$$

which is known as the nonuniform oscillator equation [37, 54, 133, 141, 142]. Nonuniform oscillators described by Eq. (4.6) are characterized by the following solution for the average rotation rate:

$$\left\langle \dot{\theta} \right\rangle = \begin{cases} \Omega & \Omega \le \Omega_c \\ \Omega - \sqrt{\Omega^2 - \Omega_c^2} & \Omega \ge \Omega_c \end{cases}. \tag{4.7}$$

The critical external frequency Ω_C is the frequency at which the oscillator abruptly transitions from being in-phase with the rotations of the driving field to being in a state in which the phase angle continually slips with respect to that of the external field.

At frequencies well below Ω_C, an increase in the driving frequency would be accompanied by an increase in the microsphere rotation rate and thus a proportionate increase in the drag. At a surface, this effective drag torque is the rotational viscous drag given by Eq. (4.2) and Eq. (4.4) combined with frictional drag due to the surface. This additional friction may be caused by interactions between the particle and surface such as electrostatic and van der Waals forces, as well as roughness of both the microsphere and surface. If the microsphere is rolling or skipping, the increased rotation rate results in higher rolling velocity. At driving frequencies above Ω_C, the average rotation rate decreases because the microsphere cannot keep up. The microsphere continually slips with respect to the external field and, at a surface, even lower rolling velocities result. When a magnetic microsphere is optically trapped at a surface, similar behavior is expected. At low external rotation frequencies, the proportionately increasing drag torque from the surface displaces the microsphere further from the trap. At lower frequencies, the average rotation rate decreases along with the effective surface drag and the microsphere finds a balance closer to the trap center. For displacements less than the particle radius, we expect a Hookian (linear) dependence of the restoring force on the displacement. Thus, position profiles with frequency have the same qualitative form as the effective surface drag as a function of frequency.

4.3 Preliminary Results

To establish appropriate ranges for experimental parameters such as laser power and rotation rate, aminated microspheres on uncoated cover slips were first tested. Other parameters such as alignment angle of the rotation axis were also maintained throughout the remainder of the experiments. The preliminary results shown here illustrate the method of analysis, and procedures were representative of all experiments conducted.

4.3.1 Free-Rolling Microspheres

With the laser off, microspheres rolled along an almost-linear trajectory on an uncoated glass surface while rotated by an external magnetic field, either clockwise or counterclockwise. Figure 4.4(a) shows the linear displacement along the *y*-axis of a 9.0 ± 0.2 *μm* aminated magnetic microsphere from its original position as a function of time for several magnetic rotation frequencies. The displacement is measured along the *y*-axis, a direction approximately perpendicular to the axis of rotation determined as follows. Along the axis of rotation, the microsphere typically remained less than 0.5 *μm* from its original position at $t = 0$. Occasionally, at higher frequencies (~3 Hz), instead of rolling along the same direction as at lower frequencies, the trajectory would have a significant component along the rotation axis, sometimes deviating up to 15° deg from the low frequency trajectories in these preliminary results. The *y*-axis is thus determined as the direction that the microsphere rolled at the lowest measurable non-zero rotation rate. The rolling velocities, determined from the fitted slopes shown in Figure 4.4(a), increased with frequency until a threshold was reached. A summary of these slopes is provided in Figure 4.4(b). At higher rotational frequencies the rolling velocity decreased along the *y*-axis and was sometimes associated with slightly increased velocities along the *x*-axis.

For a 9 *μm* diameter particle at a rotation rate of 0.5 *Hz*, rolling without slipping requires a translational velocity of about 14 *μm/s*. Our particle rolled at 1 *μm/s*, thus even at rotation rates below the threshold for reduced rolling velocity, microsphere-slipping was occurring. At or near the surface, even in the presence of SDS, the particles experienced some drag component that was frequency-dependent. This does not necessarily imply that the viscosity was non-Newtonian, just that the rolling resistance consisted of the standard Stokes drag [Eqs. (4.1)-(4.4)] as well as a frequency-dependent friction induced by surface interactions.

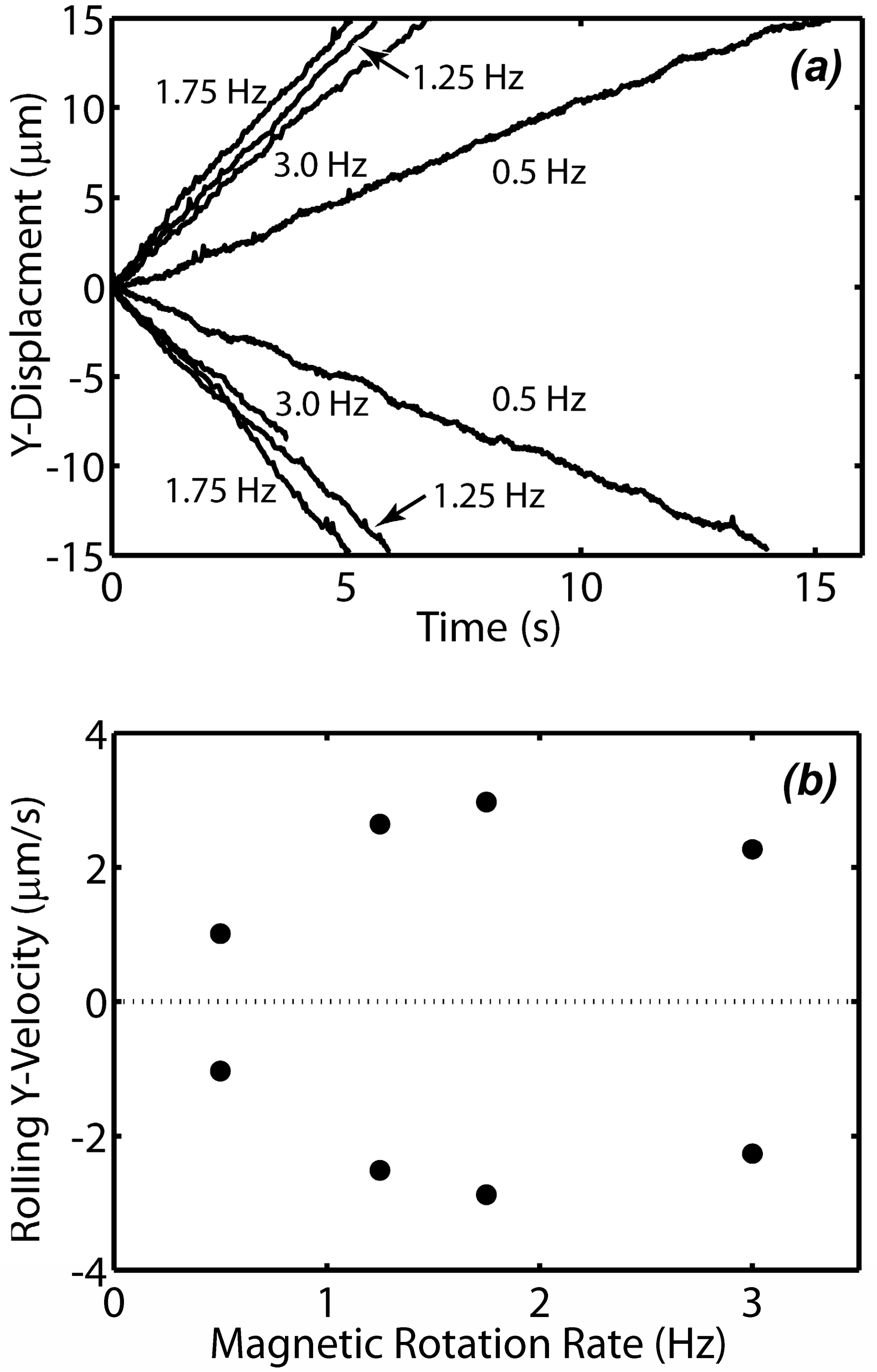

Figure 4.4 (a) Linear displacement perpendicular to the axis of rotation of a 9.0 ± 0.2 *μm* aminated magnetic microsphere from its original position as a function of time for several magnetic rotation frequencies, both clockwise (+) and counterclockwise (-). (b) Rolling velocity magnitude increases with rotation frequency until a threshold is reached near 2 *Hz*. Above this threshold, the rolling velocity magnitude decreases.

4.3.2 Optically Trapped Microspheres

Similar experiments were conducted for microspheres trapped by optical tweezers. Instead of rolling across the surface, the microspheres were spatially confined by the optical potential well. In such cases, the microsphere was displaced from the trap center to a position at which the trap restoring force counteracted the surface drag force that would have, otherwise, induced rolling.

Overlaid, averaged image stacks for the same 9.0 ± 0.2 *μm* magnetic microsphere manipulated at different rotational frequencies and laser powers are shown in Figure 4.5. For higher laser powers, the trap stiffness was larger causing the particle to be pulled closer to the center of the trap. This is visually indicated by the increased area of the region of overlap between rings. At a given laser power, as the rotation frequency was increased, the microsphere moved farther from the trap center. A threshold was reached, i.e. at 3.0 *Hz*, at which point, increased slipping (reduced rolling friction) at the glass surface caused the particle to reside closer to the trap center. This can be visualized by the decreasing area of overlap with increasing rotational frequency until the threshold at which point the area of overlap has slightly increased. This behavior was repeatable and reversible by adjusting the magnetic rotation frequency.

To quantify these results, the x- and y- coordinates of the microsphere image were tracked. As in the case of free-rolling, microspheres trapped and rotated at larger magnetic frequencies would experience forces along the rotation axis. Deviations from the axis perpendicular to the rotation axis were as high as 7° in preliminary results. The direction of the y-axis was again determined by the direction of displacement for the lowest measurable non-zero rotation rate. At zero-frequency, microspheres can settle into preferential orientations due to protrusions in the surface of the particle. Because of stiction, the particle position may not coincide with the center of the trap.

Histograms of the center coordinate of the trapped microsphere adjusted to the appropriate coordinate system were calculated using MATLAB (The Mathworks, Inc) analysis functions. These histograms are shown in Figure 4.6 for a laser power of 5 *mW*. The graphs in the top row are for one rotation direction, the bottom row for the opposite direction. The trap is located at the origin ($x = 0, y = 0$). The graphs in Figure 4.6 along with the images of Figure 4.5 verify that the rotational drag due to the microsphere

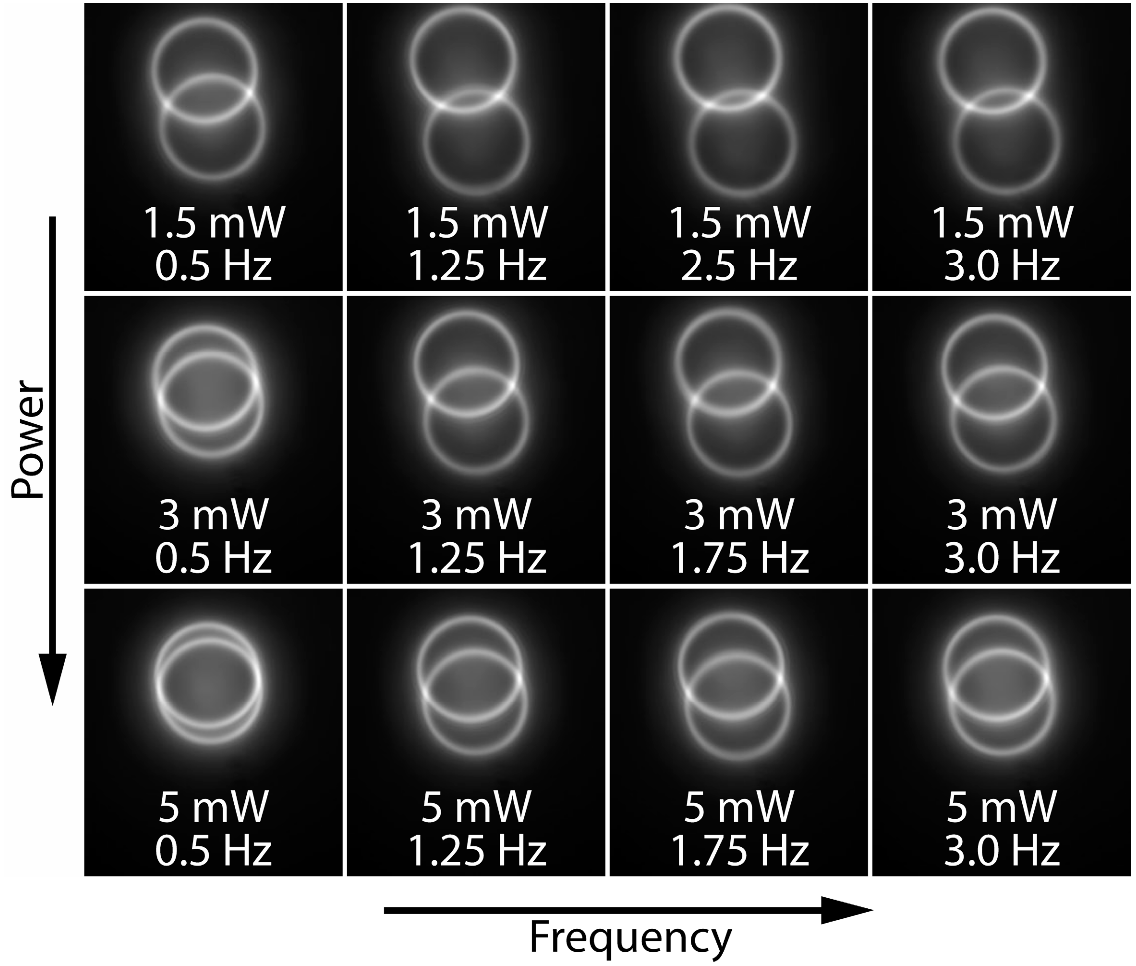

Figure 4.5 Overlaid, averaged image stacks for an optically trapped 9.0 ± 0.2 μm aminated magnetic microsphere manipulated at different rotational frequencies, both clockwise and counter-clockwise, and at varying laser powers. Displacement from the trap center was symmetric between both rotation directions. The amplitude of the displacement can be visualized by comparing the area of overlap between rings. An increase in laser power pulls the microsphere closer to the trap center. An increase in rotational frequency displaces the trap further until a threshold is reached.

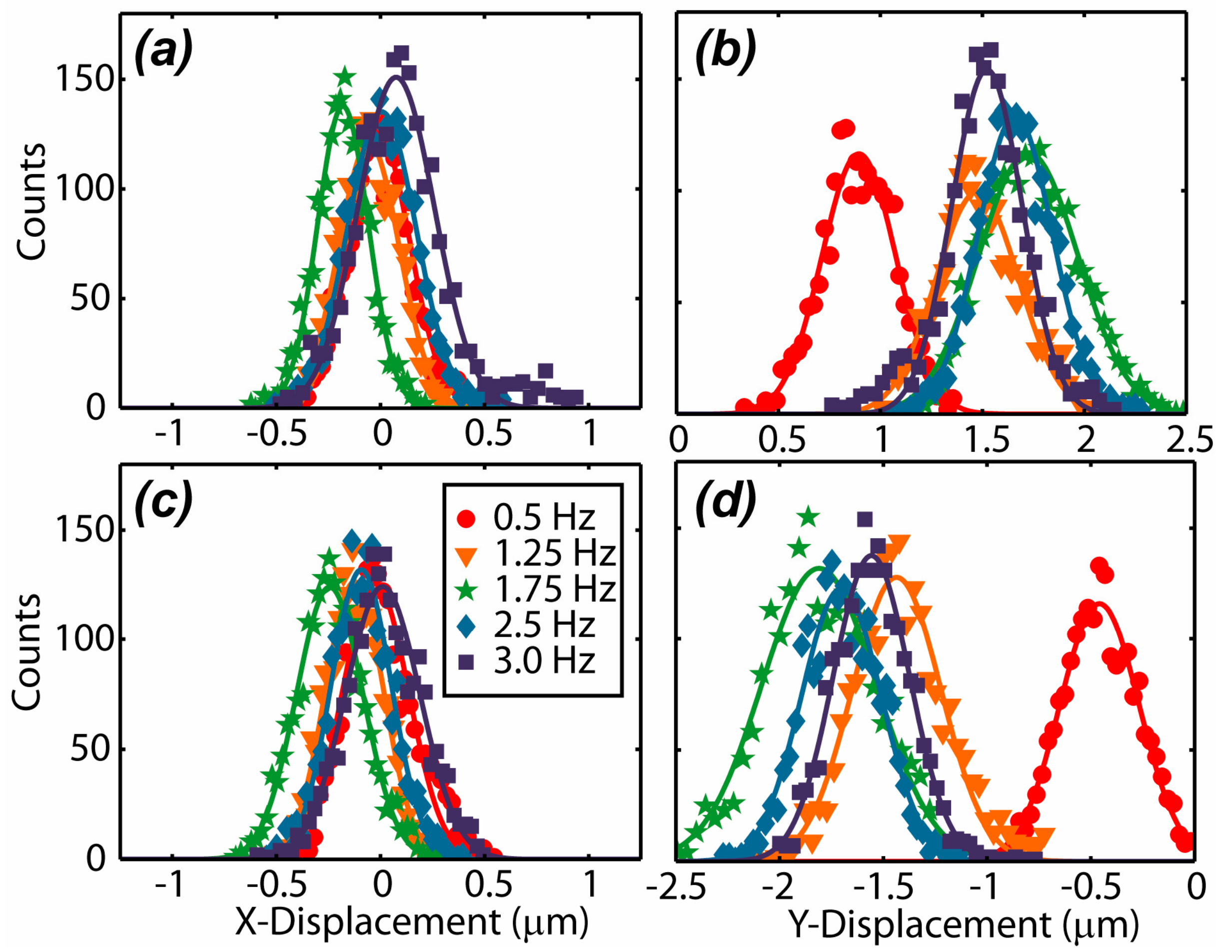

Figure 4.6 Histograms of the center coordinate of an aminated magnetic microsphere optically trapped at a surface by a 5 mW/cm^2 laser beam and rotated by an external magnet. Graphs (a) and (b) are for one rotation direction while (c) and (d) are for the opposite direction. Rotational drag due to the microsphere rolling while slipping at the surface induced an overall positional shift away from the trap center at (0,0). The displacement along the y-axis was significantly larger than along the x-axis.

slipping at the surface induced an overall positional shift in the y-direction while the average displacement in the x-direction remained closer to the trap center.

Using MATLAB's nonlinear least-squares fitting routine *nlinfit*, each histogram was well-fitted to a Gaussian profile of the form:

$$N(x_i) = a_1 \exp(-\frac{(x_i - a_2)^2}{{a_3}^2}) \tag{4.8}$$

where a_i are the fit parameters and x_i is either the x- or y-displacement. The Gaussian form indicates the microsphere experienced a normal (Boltzmann) distribution of positions even though the particle was displaced by the magnetically-induced rolling friction of the surface. The width of this distribution tended to be slightly larger than that resulting from damped Brownian motion of the particle trapped in the optical harmonic potential well at the surface without magnetic rotation. The maximum displacement in these preliminary results was less than 4 μm – a distance smaller than the particle radius. We expect the restoring force of the optical trap to obey Hookian dynamics, in other words, behave linearly with displacement. Furthermore, the dependence of the central position of the microsphere on rotational frequency proportionately reflects the dependence of the total effective drag torque on the microsphere due to the combined surface frictional torque and the torque of the surrounding fluid.

A plot of the center y-displacement from the trap for different magnetic rotational frequencies and laser powers is shown in Figure 4.7. The errorbar for each point, corresponding to the estimated standard deviation for the fitted position coefficient a_2 in Eq. (4.8), is smaller than the diameter of each marker with the maximum standard deviation over all measured displacements being 0.018 μm. For a given laser power, at low magnetic rotation frequencies, the microsphere resided close to the trap center. As the magnetic rotation rate was increased, the microsphere's average position shifted away from the trap center. At these farther distances, the increased rotational drag due to the presence of the surface balanced the increased restoring force of the optical trap. At frequencies near 2-2.5 *Hz* and above, the surface drag reached a threshold at which point the microsphere, while still slipping, was stably pulled closer to the trap. Video images revealed the microsphere remained in focus at its equator to within 0.5 μm (the minimum change in the z-focus that produced a noticeable change in observed focus). This

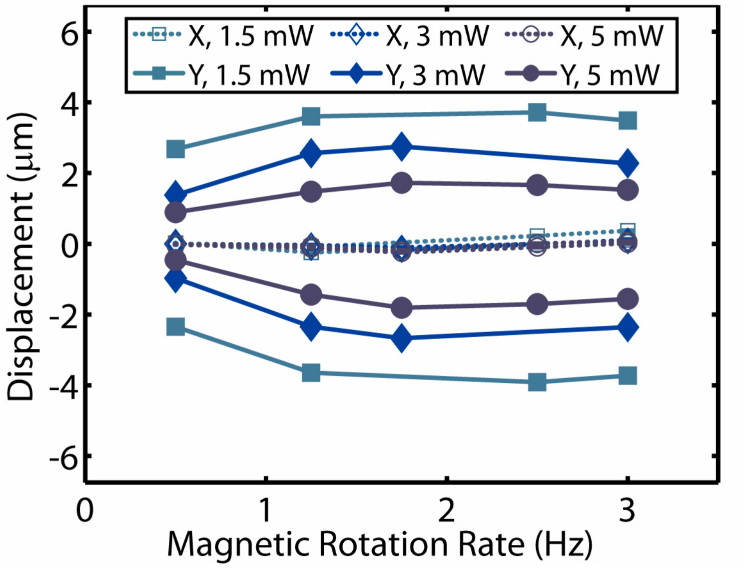

Figure 4.7 Displacement from trap center for a rolling-while-slipping aminated magnetic microsphere optically trapped at a surface by varying laser powers and magnetically rotated at varying frequencies. Dotted lines indicate *x*-displacement while solid lines indicate *y*-displacement. Positive *y*-displacements occurred for clockwise rotation of the external magnet while negative *y*-displacements occurred for counter-clockwise rotations. In all cases, the microsphere displacement magnitude increases with rotation frequency until a threshold is reached. Above the threshold, increased slipping causes the microsphere to be pulled closer to the trap center.

suggests contact with the surface continued, at least intermittently, but the effective rotational frictional drag coefficient at the surface was frequency dependent, being reduced at higher frequencies.

These preliminary results provided the appropriate range of laser powers and rotational rates needed to observe the effect of interactions between the glass surface and a rotating magnetic microsphere. Such interactions are determined by the physical properties of both the substrate and the particle. We investigated both of these aspects by comparing the motion dynamics for the following modifications: (1) blank glass cover slips vs. cover slips coated with PEG and (2) rough carboxylic magnetic microspheres vs. smoother amine-functionalized magnetic microspheres. In addition, we increased the resolution of rotation frequencies in an effort to more closely observe the dynamics near the threshold for reduced friction.

4.4 Results and Discussion

4.4.1 PEGylation vs. Non-PEGylation

Amine-functionalized magnetic microspheres were rolled along glass cover slips, both with and without a thin coating of PEG, at various rotation rates. Microspheres from the same batch were also rotated while held in an optical trap with an incident laser power of 3 mW/cm^2. The results of these two experiments are summarized in Figure 4.8(a) and (b), respectively, in which the measurements for clockwise and counter-clockwise rotation have been averaged. To account for microsphere size, velocities for free-rolling particles were normalized by the circumference at the equator and displacements for trapped particles were normalized by the radius of the particle.

Without the optical trap, rolling speed was larger along the y-axis for microspheres on blank cover slips than for those on PEG-coated ones for frequencies larger than 1 *Hz*. For blank slides, the dependence on frequency indicates a sharp discontinuity at 2.5 *Hz*. For frequencies below this, the rolling speed increases proportionately with magnetic rotation rate while for larger frequencies the rolling speed decreases with rotation rate. This behavior is similar to the dynamics described by Eq. (4.7) of nonlinear oscillators far from an interface. The critical frequency Ω_C of such an oscillator is equal to mB / γ_{rot} where m is the magnetic moment of the particle, B is the strength of the external magnetic field and γ_{rot} is the rotational drag of the surrounding medium. Below this critical frequency, the particle is phase-locked, rotating synchronously with the external rotating magnetic field. The dashed line in Figure 4.8(a) shows the similarity in rotational response of the amine-functionalized microsphere on an untreated glass cover slip to that of a nonlinear oscillator. A reduction factor was introduced on the right side of Eq. (4.7) to account for the presence of the surface. The equation was then linear least squares fit to the data to acquire a critical frequency $\Omega_C = 2.48$ *Hz* and a reduction factor of 0.060. This reduction factor quantifies the continual slipping of the microsphere even below the apparent critical frequency. The rolling speed was only a small fraction of the external rotation rate in the low-frequency regime. A linear fit of the first three points of the corresponding data gives a slope of normalized rolling speed/rotation rate = 0.058 ± 0.018 and a non-zero intercept at $\Omega = 0$. We expect both the non-zero

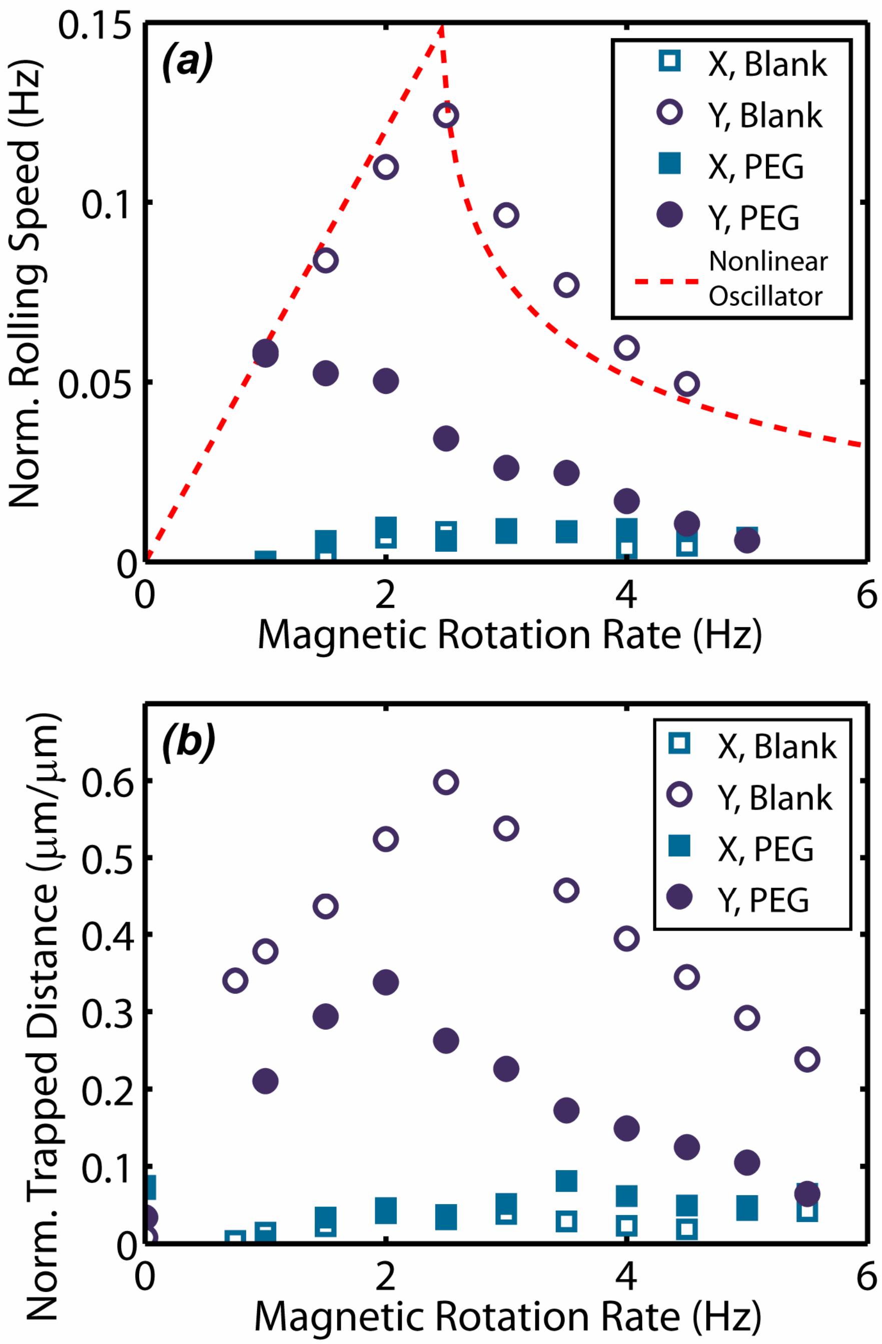

Figure 4.8 (a) Normalized speed of amine-functionalized magnetic microspheres rolled along glass cover slips, both with and without a thin coating of PEG, at various rotation rates. Data points show averages over both rotation directions. Normalization is performed by dividing the rolling velocity by the circumference of the microsphere; therefore, normalized speeds less than one indicate rolling with slipping (skipping). The dashed line indicates the average rotation rate in *Hz* of a standard nonlinear oscillator multiplied by a reduction factor to account for friction due to the surface. (b) Normalized distance of the same magnetic microspheres optically trapped by a laser beam with 3 mW/cm^2 of incident laser power on both uncoated and pegylated glass cover slips. Normalization is performed by dividing the trapped displacement by the particle radius. Data points show averages over each rotation direction.

intercept and a slope slightly less than our nonlinear oscillator reduction factor since the microsphere must transition from rolling without slipping to skipping. Our results indicate that this difference in slope is negligibly small in our system which suggests the transition from rolling without slip to skipping occurs at very low rotation frequencies.

The critical frequency of these amine-functionalized magnetic microspheres away from the surface could not be determined easily since the microspheres appeared to rotate phase-locked even at frequencies as high as ~10 *Hz* (the mechanical limit of our magnetic rotation system). For our microspheres at the surface, this critical rate drops to 2.48 *Hz*, indicating the additional drag due to the presence of the surface. In addition, for standard nonlinear oscillators, Eq. (4.7) predicts a much steeper decrease in rotation rate just above the critical frequency. The more shallow decrease of our data suggests the frequency-dependence of the interaction with the surface is more complicated than pure Stokes drag.

For PEG-coated slides, the rolling speed was always less than that for blank slides. This is expected since the interaction between the microspheres and blank cover slips was increased, as evidenced by general increased non-specific binding with the surface. The PEG coating inhibits this binding effect and, as a result, the microspheres cannot gain as much traction with the surface. Consider the following model of individual magnetic colloids interacting with the surface as the microsphere rotates. For low rotation frequencies, there is some likelihood of interaction – adhesion or binding – with the surface. During some of these colloid-surface interaction events, the microsphere rolls forward. An increase in rotation rate corresponds to an increased number of interactions resulting in a proportionately increased microsphere rolling speed. Beyond a certain frequency threshold, the duration of interaction between a colloid and the surface is decreased, reducing the likelihood that torque-generating events can occur. Asperities on the microsphere may experience more total contact with the surface, but less actual events that induce rolling. Thus the particle slips more often and experiences reduced rolling speeds.

The rolling speed decreased with increasing rotation rate on PEG-coated slides, although a slight discontinuity appears near 2 *Hz*. This discontinuity, as well as the frequency threshold for blank slides, is consistent in the results for the experiments conducted with microspheres trapped by optical tweezers, as shown in Figure 4.8(b).

With the optical trap present, the same two-regime behavior occurs. At low frequencies, the displacement from the trap center increased with rotation rate while at higher frequencies beyond a certain threshold, the microsphere was pulled closer to the trap center. In this case, the position information corresponds to actual frictional forces that acted on the microsphere in opposition to forces due to the optical trap. The evident disparity at low frequencies between optically trapped microspheres on PEG-coated slides (decreasing speed) and those on uncoated slides (increasing speed) can be explained as follows. When optical tweezers were applied to the microspheres, the laser power was set such that the axial scattering force on the particle was reduced to prevent lifting of the microsphere off the surface. Even at these reduced powers, the gradient force is strong enough to radially trap the particle. The axial gradient force can also pull the particle downwards applying a small load to maintain slipping-contact between the glass surface and colloids of the microsphere, thus inducing the microsphere to roll away from the trap. In the absence of the optical trap, no such load exists and the microsphere can shift upwards away from the surface enough to cause increased slipping, thus pulling the microsphere closer to the trap.

One should notice at low frequencies, the trend for optically trapped microspheres as well as microspheres free-rolling on blank glass indicates a linear increase. Extrapolation of this data to zero frequency yields a positive non-zero rolling speed or displacement. Such results indicate that the microsphere transitions from rolling without slipping, which would yield a linear trend of unity slope, to rolling with slipping.

Another noticeable feature of the data represented in Figure 4.8 is the non-zero rolling speeds and trapped positions along the x-axis. Although small in comparison to corresponding values along the y-axis, these measurements indicate that the trajectories were not purely perpendicular to the rotation axis, but also had components along the rotation axis. The angle of deviation of these trajectories from the y-axis averaged over both rotation directions is shown in Figure 4.9. It has been shown that differences in the angle of rolling trajectories can result from motion of nanoscale objects with geometrically distributed facets rolling on commensurate surfaces [151]. In our system, however, the microspheres had randomly distributed magnetic colloids and the glass surfaces were also expected to have a random distribution of potentially adhesive contact

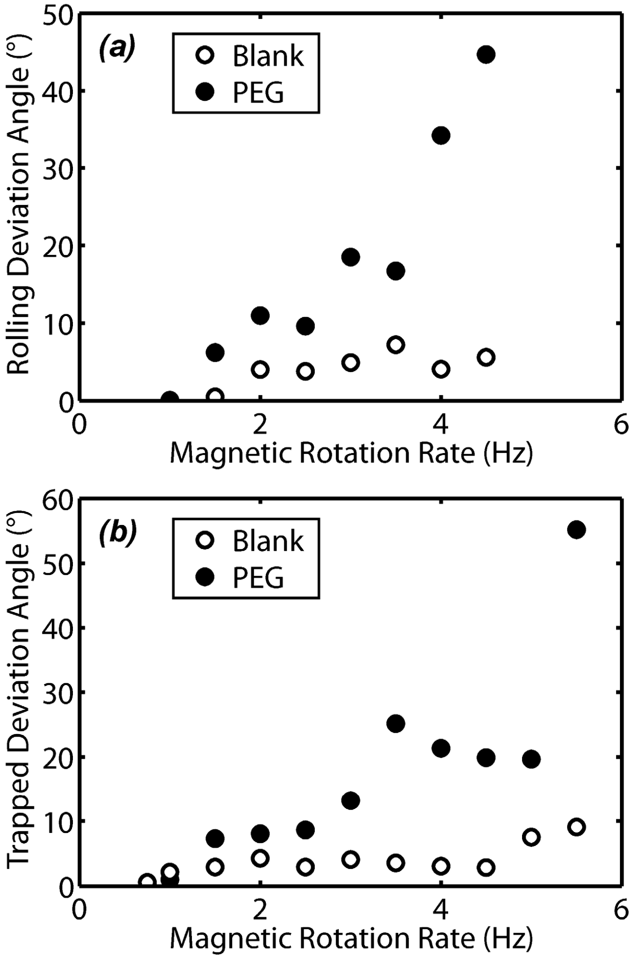

Figure 4.9 Deviation angle for amine-functionalized magnetic microspheres (a) free-rolling and (b) optically trapped on either PEG-coated or uncoated glass cover slips. Data points represent the average of the magnitudes over both rotation directions. The increase in angle with rotation frequency suggests the magnetic moment of the microsphere escapes into the third dimension along the rotation axis of the external magnetic field.

points. The observed increased deviation angle at higher rotation rates suggests the magnetic moment of the microsphere, instead of aligning with the magnetic field by rotating end over end, no longer remained in the plane perpendicular to the rotation axis. This escape into the third dimension has been described in other magnetically driven systems [38, 139] and is explored in more detail in Chapter 7.

4.4.2 Particle Roughness

Two distinct types of magnetic microspheres were rotated on glass cover slips, again with and without pegylation at varying external rotation rates. As shown in the scanning electron microscope (SEM) images in Figure 4.1, carboxylated microspheres appeared to have more magnetic material and an increased surface roughness in comparison to amine-functionalized ones. In addition, the carboxylated microspheres tended to irreversibly bind to the uncoated cover slips if the rotation rate was below 1.5 *Hz*. The effect of microsphere roughness on hydrodynamic motion perpendicular to a plane (sedimentation) has been studied in great detail [152, 153]. In these experiments, we sought to compare the effects of microsphere roughness for motion parallel to a surface. Results for the carboxylated microspheres free-rolling and confined by an optical trap are shown in Figure 4.10(a) and (b), respectively. These results will be compared to the measurements on amine-functionalized microspheres shown in Figure 4.8 where appropriate.

In all cases of free-rolling microspheres studied here, the rolling velocities on blank cover slips were generally faster than those of the same microsphere type on PEGylated cover slips at the same rotation rate. The increased traction on blank slides enabled the microspheres to experience increased torques and thus roll faster along the surface. For the rougher carboxylated microspheres, the ratio of normalized rolling speed to rotation rate given by the slope of the linear fit indicated in Figure 4.10(a) was 0.051 ± 0.006 for the blank cover slip. This value is similar to that calculated for the aminated microspheres on blank cover slips; thus, in the low frequency regime, the slipping friction is approximately the same as for untreated slides. For the PEG-coated cover slips, however, the rougher carboxylic particles introduced slightly more friction, giving a positive slope of 0.049 ± 0.008 as opposed to negative slope of the smoother amine-functionalized microspheres which rolled slower with increasing rotation rate.

This last difference mentioned suggests another behavioral distinction in the rolling motion of the rougher carboxylic microspheres vs. smoother amine-functionalized ones. The sharp threshold between increasing and decreasing rolling speed, typically signaling the transition from phase-locked rotation to phase-slipping, occurred at significantly higher rotation rates for rougher carboxylic microspheres than for the smoother amine-functionalized ones. With nonlinear oscillators in the bulk fluid, increased drag shifts the threshold frequency Ω_C to lower frequencies. Alternatively, at a surface, an increase in the surface drag shifts the threshold for rolling speed to higher frequencies since this drag

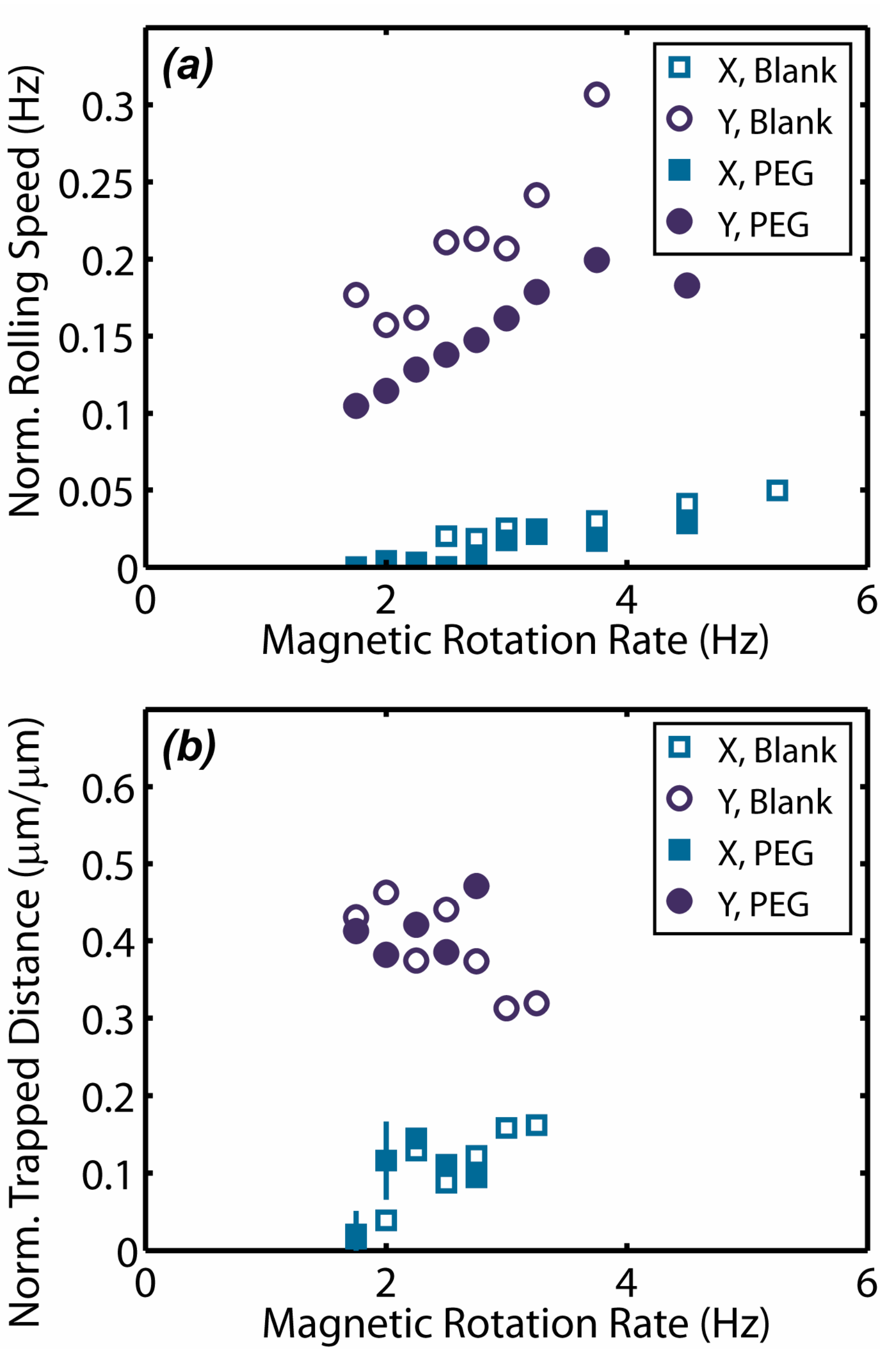

Figure 4.10 (a) Normalized speed of carboxylated magnetic microspheres rolled along glass cover slips, both with and without a thin coating of PEG, at various rotation rates. Data points are averages of each rotation direction. (b) Normalized distance from the trap center of the same magnetic microspheres optically trapped by a laser beam with 1 mW/cm^2 of incident laser power on both uncoated and PEGylated glass cover slips.

provides the traction necessary to induce rolling. We see for blank cover slips, the carboxylated microspheres reached the threshold near 4 *Hz* while on blank cover slips the rolling speed continued to increase over all frequencies measured despite the increase in angular deviation suggested by the increased speed along the *x*-direction.

For optically trapped, carboxyl magnetic microspheres, the results were not as conclusive. Figure 4.10(b) indicates the average distance from the trap center for varying rotation rates. The data appears to fluctuate significantly, revealing no clear sign of a threshold or suggestive trend. Several factors attributed to this contrast in results. First, since the carboxylated microspheres had characteristically more magnetic material than the aminated ones, scattering forces were increased. A lower laser intensity of 1 mW/cm^2 was necessary to prevent the scattering force from lifting the microspheres off the glass surface. This weaker laser power also reduced the gradient force that is necessary to trap the microspheres. It is possible the carboxylated microspheres experienced a reduced load and thus were more likely to fluctuate in the *z*-direction, causing less contact with the surface and overall less effective surface drag. Second, large asperities on the surface of the carboxylated microspheres caused the microsphere to shift position while rotating in the optical trap, thus causing the large in error in several measurement indicated in Figure 4.10(b). This may have been a combination of skewed orientation on the glass surface as well as optically induced rotation due to the magnetic colloids. It is conceivable that such fluctuations could cause errors in the normalized distance from the trap center up to 0.05. Last, the carboxylated microspheres had a tendency to bind to blank cover slips much more readily than the aminated ones, especially at very low frequencies. Consequently, measurements below 1.75 *Hz* could not be acquired before the microspheres irreversibly bound to the surface.

Angular deviations for both free-rolling and optically trapped carboxylic microspheres are shown in Figure 4.11. Results for each rotation direction were averaged. The deviation is not as strong as for the amine-functionalized magnetic microspheres. This suggests that the interactions between the surface and the rougher, more adhesive carboxylic microspheres were suppressing tendencies for the magnetic moment to rotate out of plane. In addition, the data appears noisier which we suspect is a consequence of the numerous asperities found on the microsphere surface.

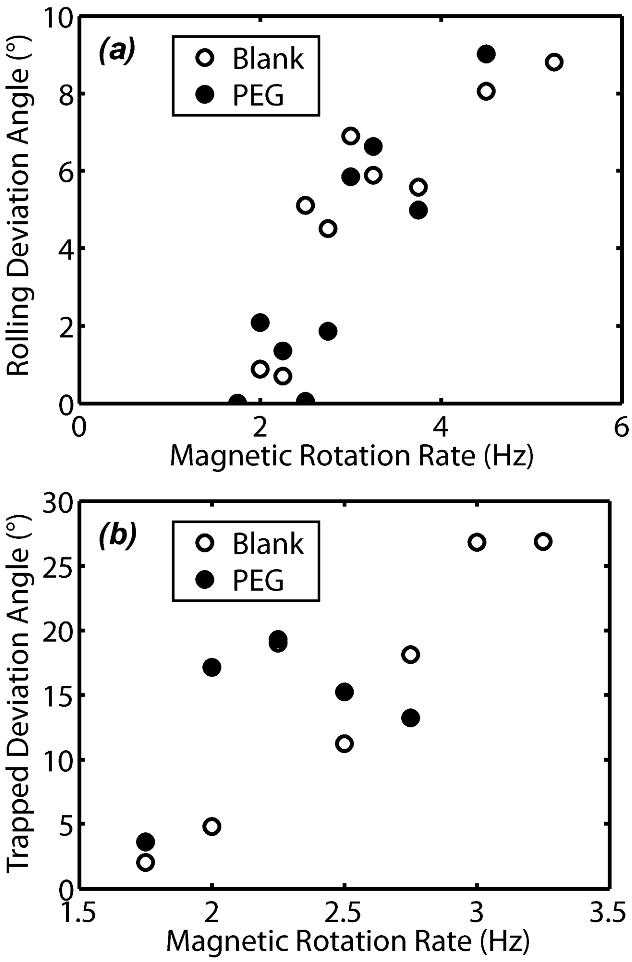

Figure 4.11 Angle deviation for carboxylated magnetic microspheres (a) free-rolling and (b) optically trapped on PEG-coated and uncoated glass cover slips. The increase in angle with rotation frequency is not as strong as for smoother amine-functionalized microspheres. This suggests escape of the magnetic moment into the third dimension is partially suppressed by surface-microsphere interactions.

For both amine-functionalized and carboxylated magnetic microspheres rotating while optically trapped, we've neglected effects due to changes in temperature resulting from the absorption of laser light. Absorption by the surrounding aqueous solution is negligible at such low laser intensities [61] as temperatures are expected to increase less than 0.05° *K* and the index of refraction of water is only weakly dependent on the temperature [154]. Absorption by the magnetic colloids followed by heat transfer to the surrounding fluid, however, can reduce the fluid viscosity. This effect may contribute to scattered data for optically trapped carboxylic magnetic microspheres. For the aminated microspheres, measurements in each rotation directions gave similar results, thus we neglected the possibility of heat accumulation during the experiment.

4.5 Conclusions and Future Work

We've developed an experimental technique for studying the motional behavior of rotationally driven magnetic microspheres rolling while slipping on a glass planar surface. Our results justify the notion that both the surface roughness and hydrodynamic interactions of different microspheres and planar surfaces can be distinguished. In particular, microspheres and surfaces with increased drag characteristics experience increased rolling speed and trapped displacement at low rotational frequencies. At higher frequencies, increased slipping can occur and behavior characteristic of nonlinearly oscillating, driven magnetic microspheres can be observed, including escape of the magnetic moment into the third dimension causing off-angle surface rolling.

A more detailed theoretical study is required to predict the hydrodynamic motion of rotationally driven microspheres on rough surfaces. Studies have previously been conducted on the rotational and translational behavior of rough non-colloidal spheres pulled by gravity down inclined planes [148, 149]. It is unclear, however, whether similar theoretical treatments involving the balance of drag forces and torques can be easily applied to these rotationally-driven rough microspheres rolling and slipping on flat planes.

If one could measure the magnetic moment of a single particle, this would help distinguish whether variations in magnetic content from microsphere to microsphere versus the effective drag are contributing more to shifts in the threshold frequency for different surfaces. Also, precise measurement of the height of the microsphere with respect to the glass surface in real time, for example by using total internal reflection microscopy techniques [152, 155], could elucidate the phenomenon of rolling while slipping by verifying when microsphere-surface contact is occurring.

CHAPTER 5

SIMULTANEOUS OPTICAL AND MAGNETIC TORQUE MANIPULATION OF NONUNIFORMLY ROTATING MAGNETIC PARTICLES

A wide range of varied and interesting phenomena can be described by a single class of nonlinear dynamics systems known as nonuniform oscillators [37]. Perhaps the most familiar of these applications to physicists is the problem of a rotating pendulum in a viscous fluid driven by a constant torque. The same equations that characterize this pendulum have also be used to describe the synchronization of oscillating neurons, the dynamics of superconducting Josephson junctions, and more recently, the behavior of submerged micro- and nanoscale particles driven by rotating fields [33, 54, 66, 133, 139-142], despite the vast difference in time scales for all of these systems.

The nonuniform nature of the motion of these overdamped microscale rotationally oscillating systems is typically manifested by the emergence of two distinct behavioral regimes: linear motion at low driving frequencies, and nonlinear motion at high driving frequencies. In particular, the nonlinear regime arises from applied frequencies that are faster than can be supported by the viscous drag in the system. In such cases, the micro-object exhibits slipping motion as it rotates. As a result, the average rotation rate in this nonlinear regime becomes slower than the rotation rate in the linear regime where the micro-object rotates synchronously with the applied field without slipping.

Numerous methods of manipulation of microscale objects have been developed. Most nonuniform oscillators have been systems actuated by rotating magnetic fields [33, 54, 66, 139-141] since the magnetic moment is expected to align with the external magnetic field. Nonuniformly oscillating systems that utilize an optical torque have also been realized through the use of such tools as optical tweezers [133, 142]. Optical torques can be generated in a variety of ways. The dipole moment of a microparticle will tend to align with the polarization of an incident laser beam. This results from the transfer of angular momentum between the particle and the spin angular momentum of the light beam. Thus mechanical rotation of the linear polarization direction or alignment with elliptically or circularly polarized light can induce rotation of anisotropic or birefringent micro-objects about the axis of the laser light [156, 157]. Shaped laser beams with specified orbital angular momentum have also been used to rotate absorptive microparticles [126, 158, 159] in the same plane. In addition, systems that use the scattering and absorptive properties of the microparticle can also induce rotation about the beam axis [53, 106, 160] or about an axis perpendicular to the beam axis [161]. Combinations of magnetic and optical manipulation schemes have also been explored in great detail [162-165].

In this work, we consider the combined manipulation of a micro-object using both magnetic and optical fields. The micro-object is modeled as an optically anisotropic microsphere or rigid dimer of such microspheres that exhibits strong scattering or absorption and is larger than the light beam focus. The light beam is assumed to be spatially fixed with no orbital angular momentum and with an arbitrary polarization while the magnetic field rotates at a fixed frequency about an axis perpendicular to the beam axis. The optically significant cross sectional area of the microsphere varies with rotation angle, thus the applied optical torque varies correspondingly. Similar applications of the projection of the cross sectional area has been used to rotate other microscale objects [53, 166]. Depending on the alignment between the beam and the microparticle, the applied optical torque can act cooperatively with or in opposition to the magnetic torque. We focus on the case of optical torque magnitudes that are much smaller than magnetic torque magnitudes, thus the optical contribution is modeled as a small perturbation. The generality of our analysis, however, makes the study applicable to systems that utilize alignment of the particle polarizability with the beam polarization to provide optical torque, especially with larger optical torque magnitudes. In addition, the forces do not have to be optical in nature, but can be any force whose dynamics obey the model equations.

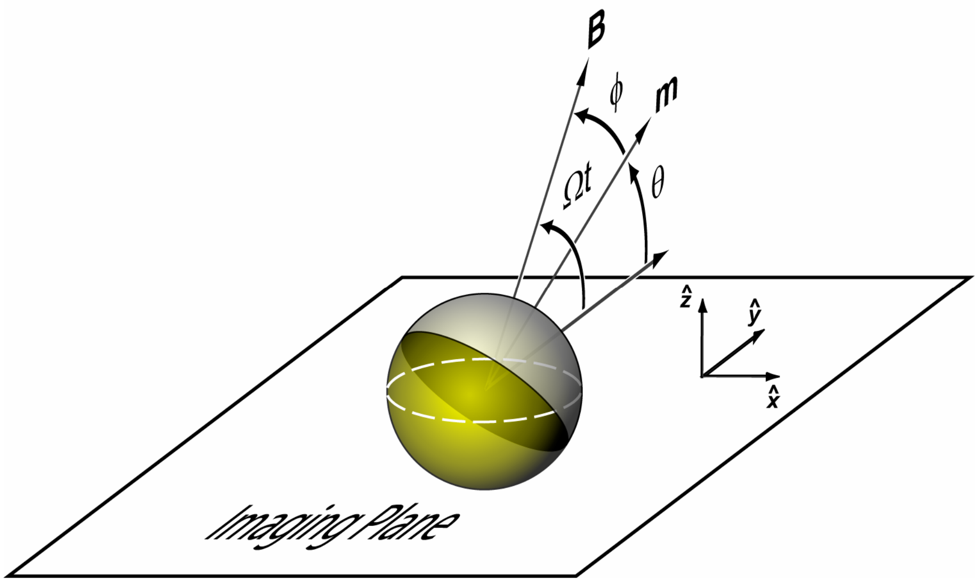

Figure 5.1 Schematic representation of a rotationally driven magnetic particle. The rotation axis is along the $\hat{\boldsymbol{x}}$ direction. ***B*** is the external magnetic field vector and ***m*** is the magnetic moment of the particle. The phase lag of the moment behind the field is given by $\Omega t - \theta$.

To investigate the effects of combined magnetic torque and optical torque as a perturbation, we first provide the salient features of the standard nonlinear oscillator. Techniques used to describe the system in the absence of optical torque are then applied to the combination of manipulation schemes. Several geometries are modeled and compared, and the results are investigated in terms of the prospect of experimental realization.

5.1 The Standard Nonuniform Oscillator

Let us assume for simplicity that rotation of our object only occurs in a 2-dimensional plane. A more general treatment of the system describing out-of-plane rotation is given in Chapter 7. For convenience with descriptions of our experimental setup, we choose the plane of rotation to be the $\hat{y} - \hat{z}$ plane of the fixed lab reference frame as shown in the diagram in Figure 5.1.

The parameters of relevance are the following:

$\boldsymbol{B}$ = Magnetic field vector
$\boldsymbol{m}$ = Magnetic moment of the particle; this coincides with the geometric orientation of the particle
Ωt = phase angle of $\boldsymbol{B}$ with respect to the lab frame
θ = phase angle of $\boldsymbol{m}$ with respect to the lab frame
ϕ = phase lag of $\boldsymbol{m}$ behind $\boldsymbol{B}$

The equation of motion describing this system in terms of the generalized coordinate θ indicates a sum of torques:

$$I\ddot{\theta} + \gamma_{rot}\dot{\theta} = mB\sin(\Omega t - \theta) . \tag{5.1}$$

where I is the moment of inertia of the particle, γ_{rot} is the rotational friction coefficient and dot notation refers to differentiation with respect to time t. The first term on the left is an inertial term, the second is torque due to drag from the surrounding viscous media, and the term on the right of the equality sign is the magnetic torque on the particle obtained from the cross product of the magnetic moment and magnetic field vectors: $\boldsymbol{N}_{mag} = \boldsymbol{m} \times \boldsymbol{B}$. A dimensionless form of this equation is obtained using the following substitutions:

$$\Omega_c = \frac{mB}{\gamma_{rot}} ,\ \tau = \Omega_c t ,\ \phi = \Omega t - \theta . \tag{5.2}$$

The dimensionless equation of motion is

$$-\frac{I\Omega_c}{\gamma_{rot}}\frac{d^2\phi}{d\tau^2} + \Omega_N - \frac{d\phi}{d\tau} = \sin(\phi) , \tag{5.3}$$

where $\Omega_N = \Omega / \Omega_C$ is the external rotation rate normalized by the critical frequency. The inertial term can be neglected in systems with low Reynolds number [150] (in our system $\mathrm{Re} \approx 10^{-7}$) to give what is known as the nonuniform oscillator equation [37]:

$$\frac{d\phi}{d\tau} = \Omega_N - \sin(\phi) . \tag{5.4}$$

The steady-state solution for Eq. (5.4) gives $\phi = \sin^{-1}(\Omega_N)$ and requires $\Omega_N \leq 1$. In this regime, after an initial transient, the phase between $\boldsymbol{B}$ and $\boldsymbol{m}$ remains locked, both vectors rotating synchronously with angular velocity Ω.

For $\Omega_N \geq 1$, Cēbers and Ozols [139, 140] provide the following solution for the phase:

$$\phi = 2\arctan\left[\frac{1}{\Omega_N} + \sqrt{1-\left(\frac{1}{\Omega_N}\right)^2}\tan\left(\sqrt{1-\left(\frac{1}{\Omega_N}\right)^2}\frac{\Omega_N(\tau-\tau_0)}{2}\right)\right] \tag{5.5}$$

where τ_0 is an arbitrary time instant. Note, Eq. (5.5) indicates that ϕ is a multi-valued function, the solutions of which are separated by 2π. If this phase is restricted to values between $-\pi$ and π, then ϕ represents the angular difference between the direction of the magnetic field $\boldsymbol{B}$ and that of the magnetic moment $\boldsymbol{m}$ at any dimensionless time τ. In our treatment here, ϕ represents the total accumulated phase lag between $\boldsymbol{m}$ and $\boldsymbol{B}$, the magnitude of which can exceed π if the magnetic field laps the magnetic moment while it rotates. In this case, the appropriate solution for ϕ at a time τ is determined by the number of laps that have occurred.

To gain a clearer picture of the dynamics of motion for $\Omega_N \geq 1$, one can integrate Eq. (5.4) to solve for the period *T*, defined here as the time for ϕ to complete a full revolution:

$$T = \int dt = \frac{1}{\Omega_C}\int_0^{2\pi}\frac{d\tau}{d\phi}d\phi = \int_0^{2\pi}\frac{d\phi}{\Omega - \Omega_C \sin\phi} = \frac{2\pi}{\sqrt{\Omega^2 - \Omega_C^2}} \tag{5.6}$$

This requires that the particle slips. If the particle were to rotate uniformly in phase with the magnetic field (at Ω), then *T* would be undefined since ϕ never reaches one full revolution (not even half a revolution, since beyond π the particle would slip). The angular velocity of the magnetic moment, averaged over long times, or equivalently over one period *T,* can then be expressed as:

$$\left\langle \dot{\theta} \right\rangle = \frac{\theta_f - \theta_i}{t_f - t_i} = \frac{\Omega T - 2\pi}{T} = \Omega - \sqrt{\Omega^2 - \Omega_c^2}\ . \tag{5.7}$$

Thus, for $\Omega_N \geq 1$, as the magnetic field rotates at angular velocity Ω, the particle cannot keep up and undergoes back and forth slipping rotation. The phase lag between the two accumulates and the magnetic moment takes longer to complete a full cycle. The solutions for the average rotation rate of the particle are summarized as follows:

$$\langle \dot{\theta} \rangle = \begin{cases} \Omega & \Omega \le \Omega_c \\ \Omega - \sqrt{\Omega^2 - \Omega_c^2} & \Omega \ge \Omega_c \end{cases}. \tag{5.8}$$

5.2 Models of Optical Torque

The addition of an external optical radiation force was modeled in several ways. In all cases, it is assumed that the particle containing magnetic material is too large and reflective/absorptive to be trapped via conventional single beam gradient forces from optical tweezers despite the high numerical aperture often used in experiment. As a result, the force on the particle is purely the scattering force applied, inducing rotation just as water provides torque for a water wheel.

In practice, the particle may undergo translation either due to the force of the laser beam and/or Brownian motion. One can follow the translational motion of the system using particle tracking methods. Nevertheless, in the models described here, the force can be assumed weak enough that translation of the particle is negligible. In addition, for simplicity, we assume the force profile is uniform in the *z*-direction and the force points only in the +*z*-direction. In experiment, the particle actually lies in the vicinity of the focus of a laser beam. If, however, the particle does not move too far out of the focal plane, the direction of the force will point predominantly in the +z-direction. A vector diagram for the additional force is indicated in Figure 5.2.

The following parameters have been introduced into the system:

$\boldsymbol{F}$ = total optical force applied to the rotating particle
$\boldsymbol{r}$ = optical moment; this is not necessarily the dipole moment of the system, but rather a vector associated with a physical geometrical orientation of the particle
β = phase angle of $\boldsymbol{F}$ with respect to the lab frame; this is always $\pi/2$ in this treatment
δ = phase angle between $\boldsymbol{r}$ and $\boldsymbol{m}$; since both $\boldsymbol{r}$ and $\boldsymbol{m}$ are fixed to a specific orientation of the particle, this angle must be constant; in this treatment it is assumed to be zero

Several geometries of the particle or rotating object were modeled. A description is provided for each. In all cases, the magnetic field is assumed to be rotating with angular velocity Ω.

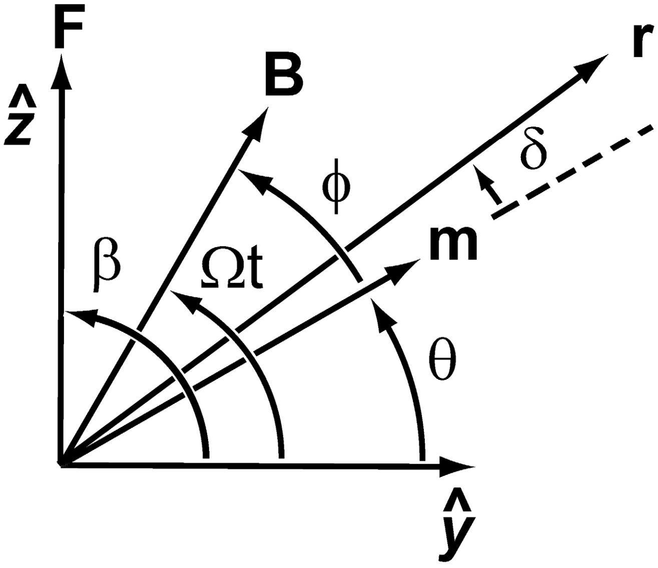

Figure 5.2 Coordinate system for a rotationally driven magnetic particle perturbed by an optical force per area $\boldsymbol{F}$ at a fixed angle β with respect to the lab frame. The optical moment of the particle $\boldsymbol{r}$ is a vector associated with a specific geometrical orientation of the particle. It deviates from the magnetic moment by an angle δ.

5.2.1 Optical Force Applied at Center of Anisotropic Particle

This model assumes the force profile $f(x,y)$ is constant in the x- and y-directions over a region centered on the particle. The optical anisotropy of the rotating object causes the optical force to induce rotation. In the case indicated on the left in Figure 5.3, the metal half-coating provides optical anisotropy. Once the particle rotates beyond $\pi/2$, the optical force, since it's centered, will then induce rotation in the opposite direction. If the torque amplitude generated by the optical force is much less than the induced magnetic torque, we still expect the particle to rotate full cycles, just not at a uniform angular velocity. If the optical torque exceeds that due to magnetic torque, we would expect the particle to be forced into an orientation with the metal coating downstream of the laser beam. In practice, forces this large will translate the particle out of the focus center. Such translation is not modeled here.

The particle is modeled as an anisotropic cross sectional area (see Figure 5.3, right) with optical moment $\boldsymbol{r}$ attached to the particle. One might recognize $\boldsymbol{r}$ as the moment arm for calculating the optical torque $\boldsymbol{N}_{opt} = \boldsymbol{r} \times \boldsymbol{F}$. In actuality, an integration of the force profile over the cross sectional area is necessary to calculate the total torque. For our

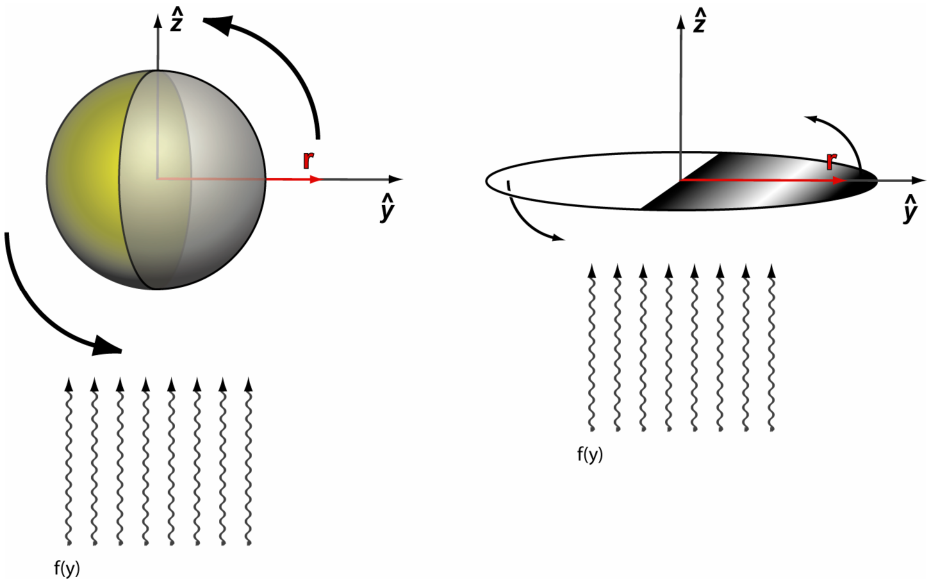

Figure 5.3 Schematic representation of an optically anisotropic magnetic particle acted upon by a rotating magnetic field and an optical force with constant profile *f*(x,y) centered on the particle. A half-coated magnetic microsphere (left) is modeled as an anisotropic cross sectional area (right) with optical moment ***r***.

purposes here, let $|\boldsymbol{r}| = r$ be proportional to the cross sectional area over which the optical force is applied and *rF* still has standard units of torque. Since our force is in the *z*-direction, and using the angles shown in Figure 5.2, we can calculate the torque as

$$N_{opt} = rF\sin(\beta - (\delta + \theta)). \tag{5.9}$$

If we assume the magnetization direction coincides with the easy axis of the particle – an axis often defined by the orientation of the particle, we can set $\delta = 0$. Since ***F*** points in the *z*-direction, $\beta = \pi/2$ and Eq. (5.9) reduces to

$$N_{opt} = rF\sin(\pi/2 - \theta). \tag{5.10}$$

Note, for $\pi/2 < \theta < 3\pi/2$, the metal coating is oriented on the –*x* side and the optical force torques the particle in the opposite direction, as we expect.

5.2.2 Optical Force Applied Off-Center of Anisotropic Particle

If we shift the force profile such that it is no longer directed at the center of the particle but rather slightly off the *z*-axis (see Figure 5.4), most of the optically generated force applies a torque to the particle all in the same direction. Using the cross sectional model, we see that for $\theta > \pi/2$ the torque on the metallic portion is minimized. The

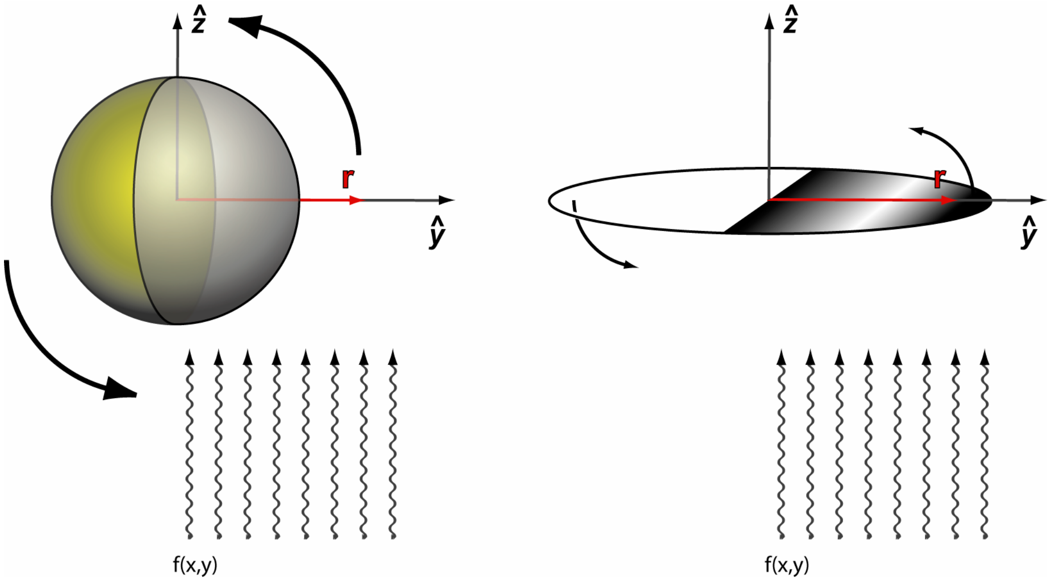

Figure 5.4 Schematic representation of an optically anisotropic magnetic particle acted upon by a rotating magnetic field and an optical force with constant profile *f*(x,y) off-center from the particle. A half-coated magnetic microsphere (left) is modeled as an anisotropic cross sectional area (right) with optical moment ***r***.

uncoated portion of the particle moves into the force profile region, but since this material is typically a dielectric with much lower absorption than the metal, the torque generated is neglected. Thus, only when $\theta > 3\pi/2$ or the metallic portion resides at +*x* quadrants is a torque generated. In other words, if $n\pi < \beta - (\delta + \theta) < (n+1)\pi$ where n is even, the torque is the familiar $rF\sin(\beta - (\delta + \theta))$. If, instead, we have $n\pi < \beta - (\delta + \theta) < (n+1)\pi$ where n is odd, the torque on the system is zero. Assuming again that $\beta = \pi/2$ and $\delta = 0$, this can be summarized by the following expression:

$$N_{opt} = rF\frac{\sin(\pi/2 - \theta) + \left|\sin(\pi/2 - \theta)\right|}{2} \tag{5.11}$$

For the actual case of a half-coated spherical particle of finite thickness, a torque could be generated even at $\theta > \pi/2$ since a portion of the coating exists in the +*x* region. In practice, this would be remedied by using relatively narrow force profile sufficiently off-center.

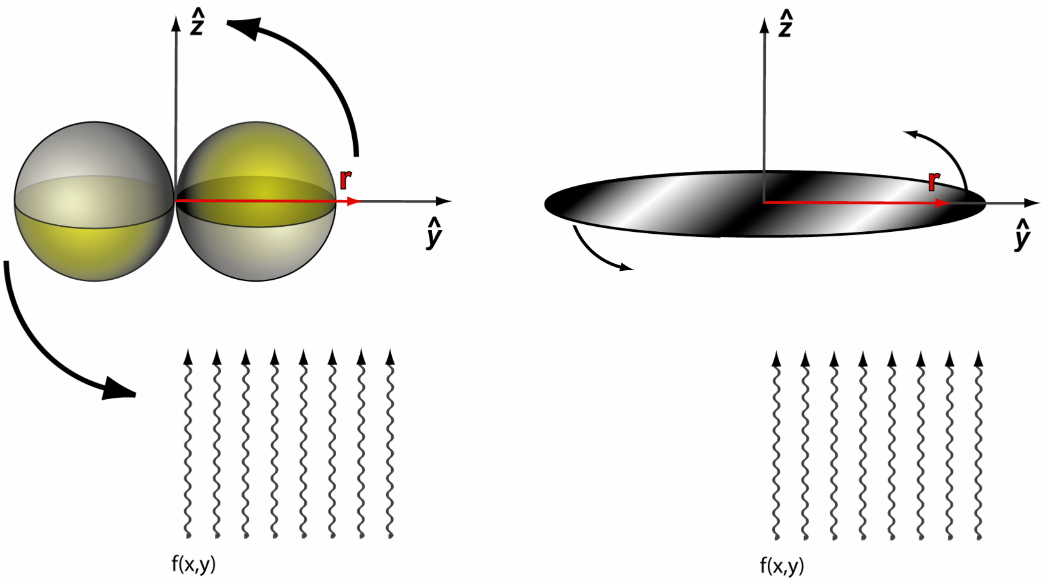

Figure 5.5 Schematic representation of a symmetric magnetic particle acted upon by a rotating magnetic field and an optical force with constant profile *f*(x,y) off-center from the particle. A rigid dimer of half-coated magnetic microspheres (left) is modeled as an anisotropic cross sectional area (right) with optical moment ***r*** along the axis joining the two spheres.

5.2.3 Optical Force Applied Off-Center of a Symmetric Particle

In this model, the rotating object is optically symmetric about the rotation axis, but the force profile, although still constant over its region of extent, is centered such that only a portion of the object experiences the optical force, thus inducing a torque about the axis of magnetic rotation. An example of such a symmetric particle, shown in the illustration in Figure 5.5, is a rigid dimer consisting of two half-coated magnetic spheres. Optical rotation symmetry is required, thus any symmetric dimer will suffice, including two uncoated, magnetic spheres. The same conditions on the amplitude of the force apply. When the particle rotates such that $\theta > \pi / 2$, one portion of the dimer exits the region of the force profile while the other enters the region. As a result, the torque applied to the dimer is always in the same direction. Using the cross sectional area model again, the torque in this case is

$$N_{opt} = \left| rF \sin(\pi / 2 - \theta) \right| . \tag{5.12}$$

Again, for the physical case of a dimer, when $\theta = \pi/2$, the force profile can still apply a torque. The zero approximation is valid if the edge of the force profile is at or beyond one particle radius from the magnetic rotation axis.

In all three models described, the torque, when present, has a sinusoidal form. We can add this term to the magnetic torque to give a new equation of motion:

$$I\ddot{\theta} + \gamma\dot{\theta} = mB\sin(\Omega t - \theta) + N_{opt}\,, \tag{5.13}$$

where N_{opt} is given by either Eq. (5.10), Eq. (5.11) or Eq. (5.12), depending on the model used. Performing the same substitutions as Eq. (5.2), we can achieve the dimensionless form:

$$-\frac{I\Omega_c}{\gamma}\frac{d^2\phi}{d\tau^2} + \Omega_N - \frac{d\phi}{d\tau} = \sin(\phi) + \alpha\sin(\pi/2 - (\Omega_N\tau - \phi)) \tag{5.14}$$

where $\alpha = \dfrac{rF}{mB}$ is the ratio of the amplitudes of the optical torque to the magnetic torque and the normalized frequency we know as $\Omega_N = \Omega/\Omega_C$. Again, neglecting the inertial term, we obtain our modified nonuniform oscillator equation for a constant optical force pointed in the *z*-direction:

$$\frac{d\phi}{d\tau} = \Omega_N - \sin(\phi) - \alpha\sin(\pi/2 - (\Omega_N\tau - \phi))\,. \tag{5.15}$$

Note again, the final term in Eq. (5.15) must be appropriately adjusted for the model of optical torque being used.

The period T is no longer easily acquired by integration. A reliable numerical solution of ϕ can be acquired using a fourth order Runge-Kutta routine [92], from which we can also determine θ and its normalized derivative $d\theta/d\tau$. Eq. (5.14) itself can be reduced to two first order differential equations and also solved using Runge-Kutta. In this study, the low Reynolds number approximation holds; thus, we only numerically solve Eq. (5.15).

In summary, we've described the theoretical equations for three models of non-uniformly rotating magnetic particles influenced by an optical force which applies an additional torque. For all models, the external magnetic field drives the rotation in the counter-clockwise direction. In the first model, the optical torque that adds to the magnetic torque is applied when the particle is oriented with an absorptive or reflective portion on one side of the rotation center (+*x* side in this treatment). A torque that opposes the magnetic torque is applied when the particle is oriented with the scattering material on the opposite side. In the second model, an additive torque is again applied for orientations towards the +*x* side, but zero torque is applied for orientations on the other side. In the third model, the rotating object is optically symmetric and thus the optical force applies an additive torque for all orientations. The models go in increasing order of additive torque, thus in nonuniformly rotating regimes, we expect the first model to slip more often than the second which slips more often than the third one.

5.3 Numerical Analysis

Written in MATLAB, a 4th order Runge-Kutta algorithm was used to numerically solve Eq. (5.4) and the appropriate versions of Eq. (5.15) for each optical torque model. To test that the models were programmed properly, analysis using $\alpha = 0$ was conducted to ensure the results are what we expect for the uniform oscillator and the standard nonuniform oscillator equations with no optical beam present. In particular, we look at θ-angular trajectories, ϕ-phase space trajectories, the effect of bifurcations on the initial transient response, and the significance of saddle-node bifurcations. Throughout the analysis $\beta = \pi / 2$ and $\delta = 0$.

5.3.1 Uniform Oscillator

For comparison, we first illustrate typical results for a uniform oscillator using the parameters $\Omega_N = 0.5$, $\alpha = 0$ with the initial condition that at $\tau = 0$, $\phi = 0$ (thus also $\theta = 0$). For convenience, we define the initial angles $\phi(\tau = 0) \equiv \phi_0$ and $\theta(\tau = 0) \equiv \theta_0$. The plot in Figure 5.6 indicates the angular trajectory of the particle in polar coordinates as a function of τ. The polar angle of a point on the blue line corresponds to the angle of the moment ***m*** of the particle. To facilitate visibility of the trajectory after several rotations or if slipping occurs, the radius of any point on the line equals τ at that point. Thus, as we see for uniform oscillation, the curve starts at the origin at $\tau = 0$ and spirals outward uniformly in a counterclockwise motion.

The rotational dynamics for both θ and ϕ can be depicted individually. The graphs in Figure 5.7 all show one curve (solid or dashed line) and one line fit (dotted line) indicating that all three models give the same standard uniform oscillator result since $\alpha = 0$ in all cases. From the upper left graph (plot of θ vs. τ) we see that θ steadily

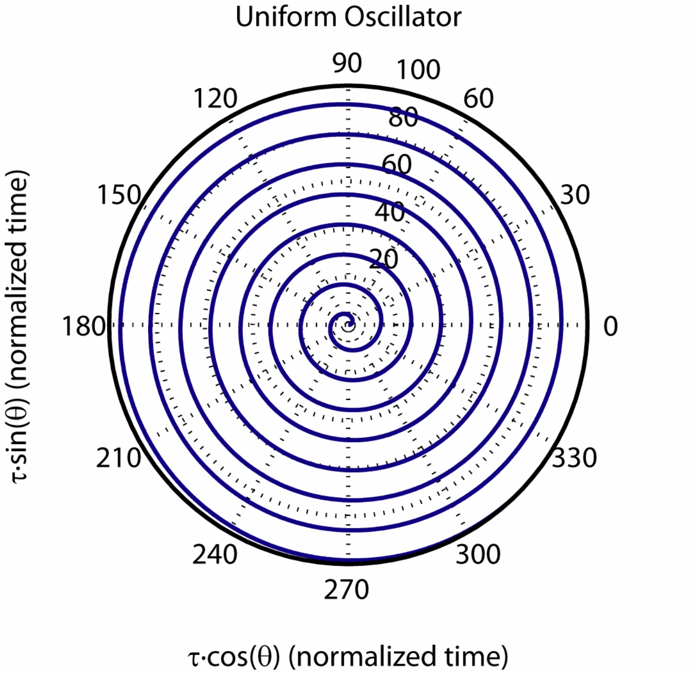

Figure 5.6 Polar trajectory of angle vs. dimensionless time τ (radial) for a uniformly rotating particle (α=0). $\Omega_N = 0.5$, $\phi_0 = 0$ and $\theta_0 = 0$.

increases with a linear slope. The slope is approximately $\Omega_N = 0.5$. The slope can also be seen in the lower left graph (plot of $d\theta / d\tau$ vs. τ) which indicates the instantaneous angular velocity as a function of τ. Initially, the magnetic moment ***m*** and the magnetic field ***B*** are aligned along the y-axis. As ***B*** begins to rotate, the magnetic torque increases, thus $d\theta / d\tau$ takes some time to reach its final value at $\Omega_N = 0.5$. Note the dotted line indicates the line fit of the data not including the early transients. Graphs on the right indicate the behavior of the angle ϕ and the angular velocity $d\phi / d\tau$ plotted in radians and radians/(normalized seconds). Recall that ϕ is the phase lag of the moment ***m*** behind ***B***. As we might expect, the phase ϕ starts at zero and ramps up but settles near 0.52 *rads* (or ~30° expected from $\phi = \sin^{-1}(\Omega_N)$ when $d\phi / d\tau = 0$). Correspondingly, the angular velocity $d\phi / d\tau$ starts near the normalized rate of magnetic rotation $\Omega_N = 0.5$ and decreases until the particle becomes phase-locked at which point $d\phi / d\tau$ is approximately zero.

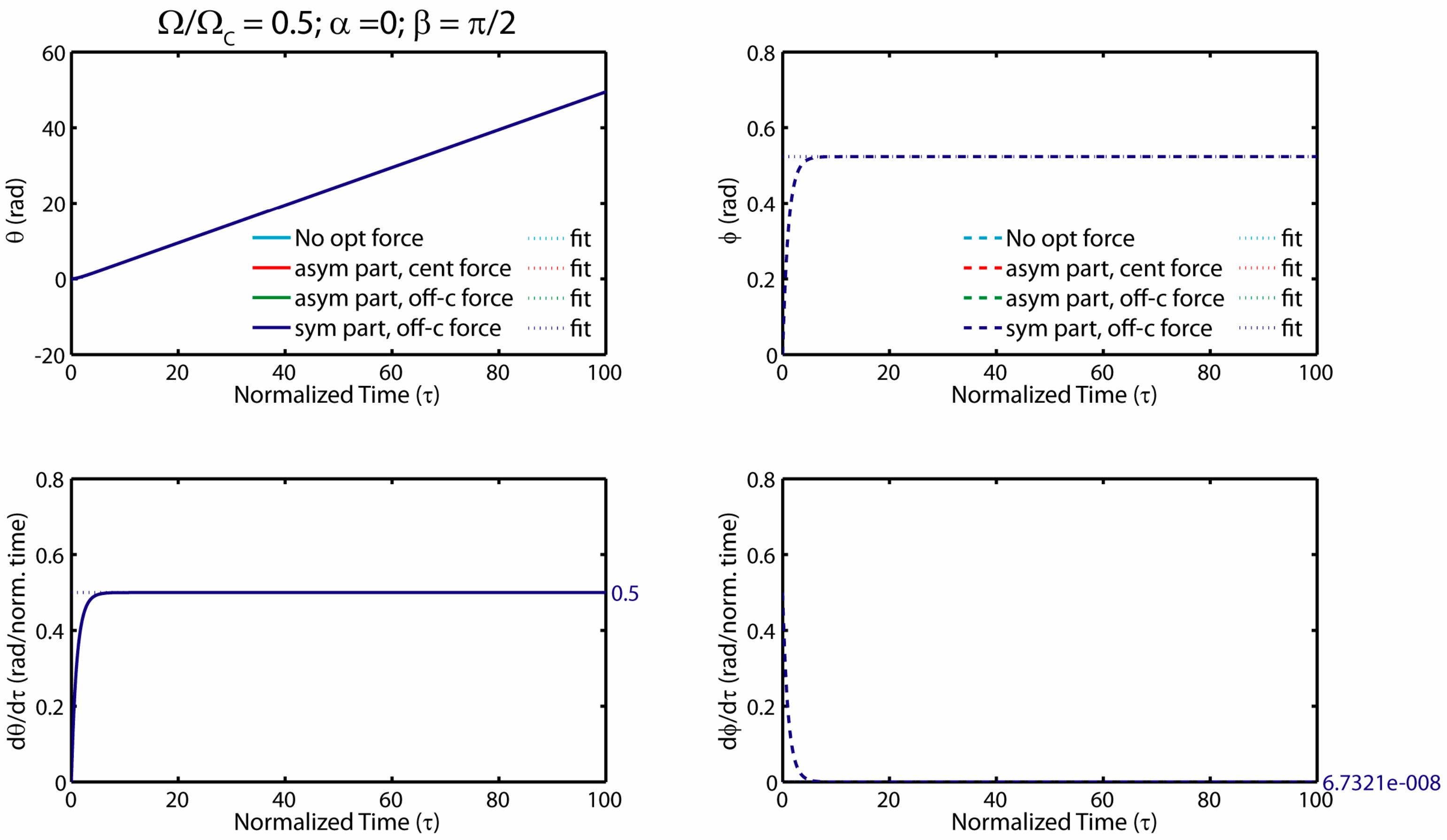

Figure 5.7 Angular displacement (top) and angular velocity (bottom) plots for a uniformly rotating particle. All four models overlap exactly since the optical force is set to zero $(\alpha=0)$. $\Omega_N = 0.5$, $\phi_0 = 0$ and $\theta_0 = 0$.

The term “uniform” comes from the notion that the particle is rotating at a uniform angular velocity at all angles. This should be clear by looking at the long time regimes of both θ and ϕ graphs in Figure 5.7.

Effect of Initial Conditions – Bifurcations

The graphs from Figure 5.7 do not show purely uniform oscillation. At early times, the transient behavior of both $d\theta / d\tau$ and $d\phi / d\tau$ are not constant. The initial condition $\phi_0 = 0$ determines the starting phase angle between the magnetic field ***B*** and moment vector ***m***. Changing this initial condition does not change the rotational dynamics at long times; in particular, by $\tau = 12$, the angular velocity remains approximately equal to the average magnetic rotational velocity $\Omega_N = 0.5$. This can also be seen in the plots of Figure 5.8 which are similar to those from Figure 5.7, but with varying initial conditions. We see from the upper right graph that when the initial phase angle $\phi_0 \leq 2.51$ *rad*, the phase approaches $\sin^{-1}(\Omega_N) = \pi / 6$ *rad* indicating that the particle never slips but rather phase locks immediately. When $\phi_0 \geq 3.77$ *rad* the particle is initially oriented with a phase so far from that of the ***B***-field that the particle slips once but then phase locks at $\phi = 2\pi + \sin^{-1}(\Omega_N) = 13\pi / 6$ *rad*. A finer range of ϕ_0 values (see Figure 5.9) gives us a slightly more precise value for the threshold between one slip and no slipping. The upper right graph of Figure 5.9 reveals the threshold lies somewhere in the range 2.600 *rad* $\leq \phi_{th} \leq$ 2.665 *rad*. We can analytically determine the threshold phase ϕ_{th} by assuming it is the phase at which $d\phi / d\tau = 0$. This gives values of $\pi/6$ and $5\pi/6$.

At this point, it is helpful to use the formalism of Strogatz [37]. The points at which $d\phi / d\tau = 0$ are fixed points in the flow around a circle. The phase space of this flow, shown in Figure 5.10, can aid in illustrating the significance of the initial conditions. The point at $\phi = \pi / 6$ (closed circle) is stable since for angles slightly smaller or larger, the flow ($d\phi / d\tau$) returns the phase to $\pi/6$. For $\phi = 5\pi / 6$ (open circle), flow is away from this angle, thus it is an unstable fixed point. This is also illustrated in the upper right graphs of Figure 5.8 and Figure 5.9. When ϕ_0 is close to $\pi/6$, the phase returns to that value. For ϕ_0 larger than $5\pi/6$, the phase moves away from ϕ_0 and stabilizes at $2\pi + \pi/6$.

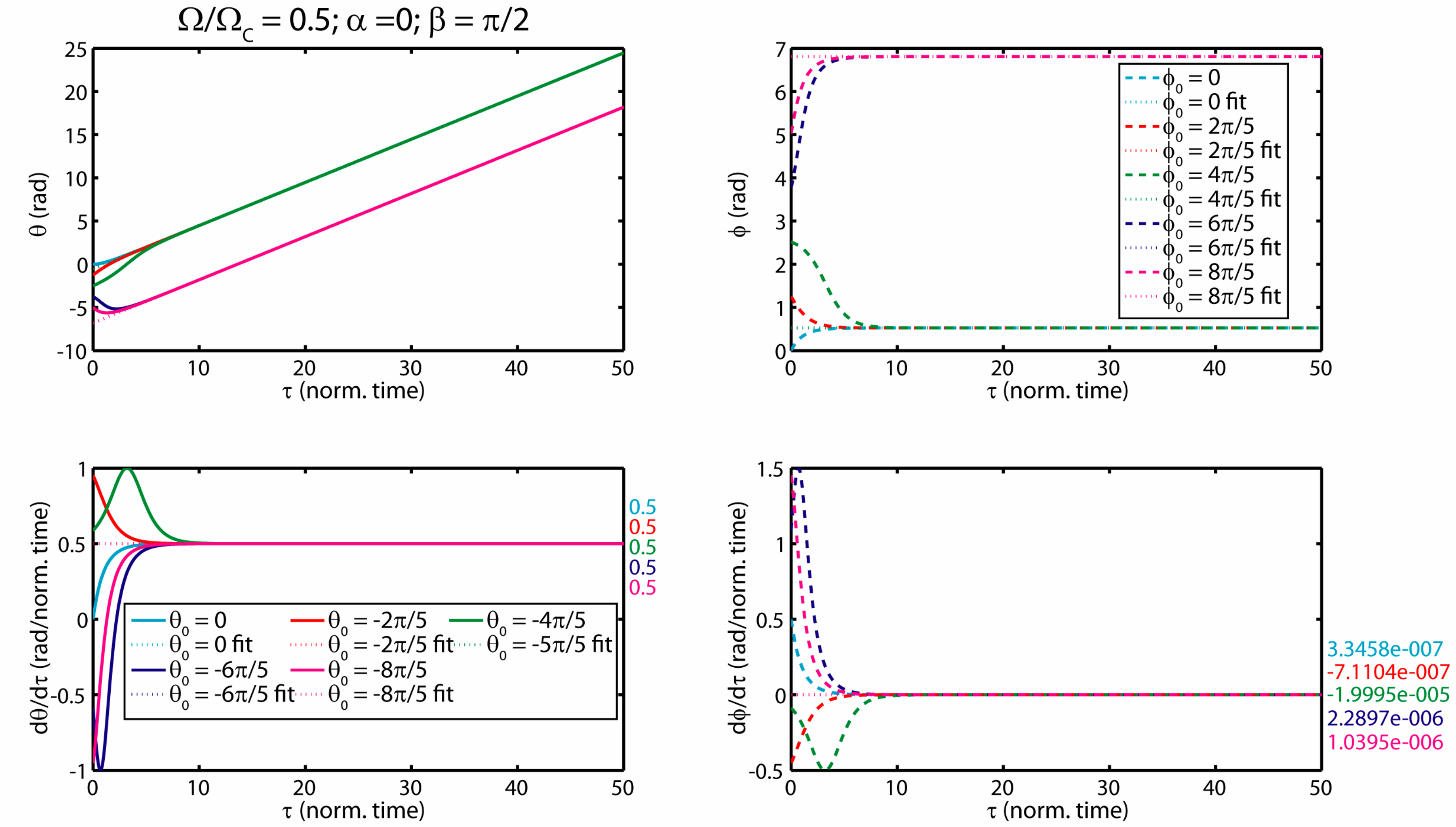

Figure 5.8 Angular displacement and angular velocity curves for different initial conditions ($\theta_0 = -\phi_0$). $\Omega_N = 0.5$.

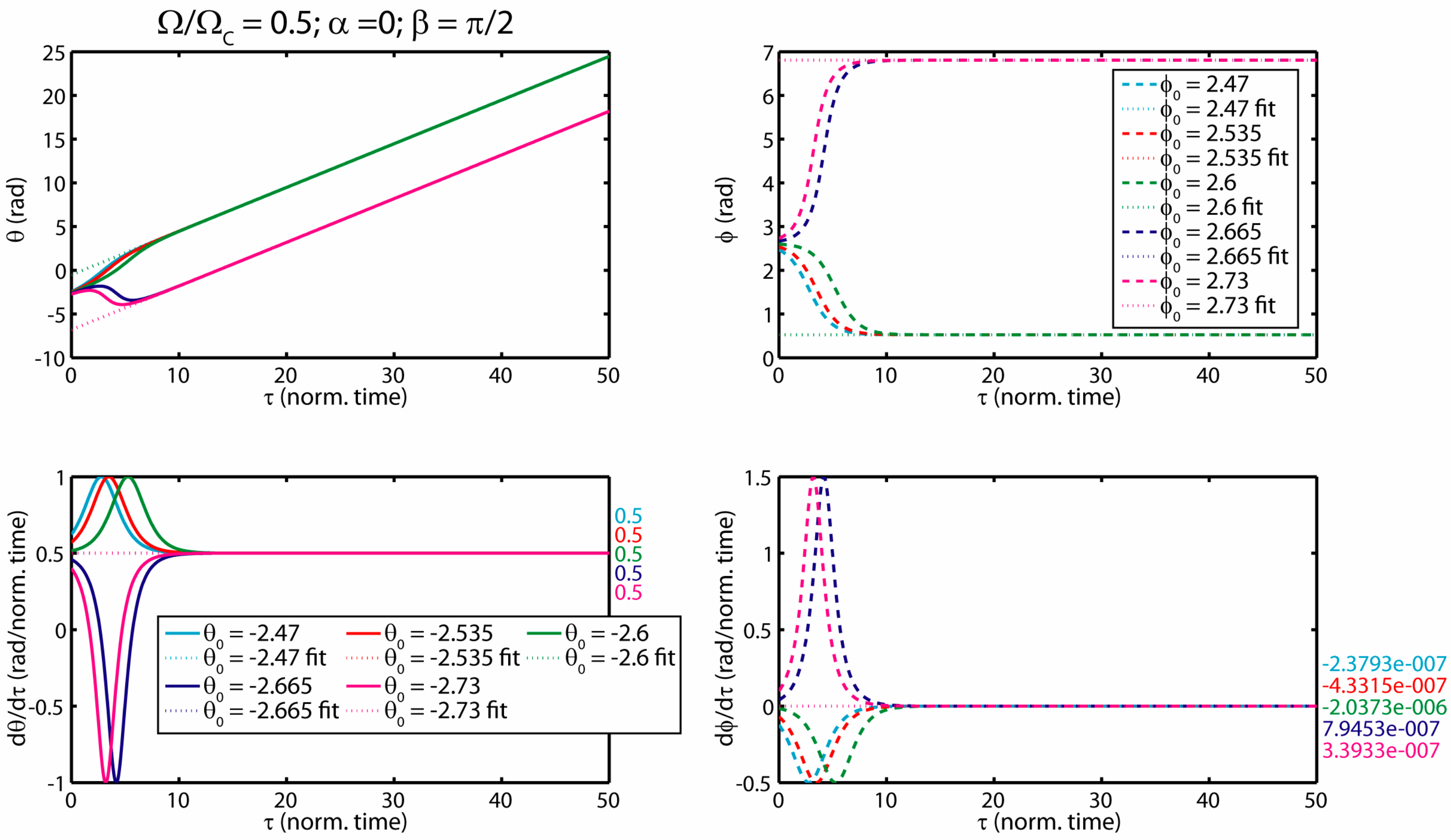

Figure 5.9 Angular displacement and angular velocity curves for different initial conditions. The range of ϕ_0 is finer than that of Figure 5.8.

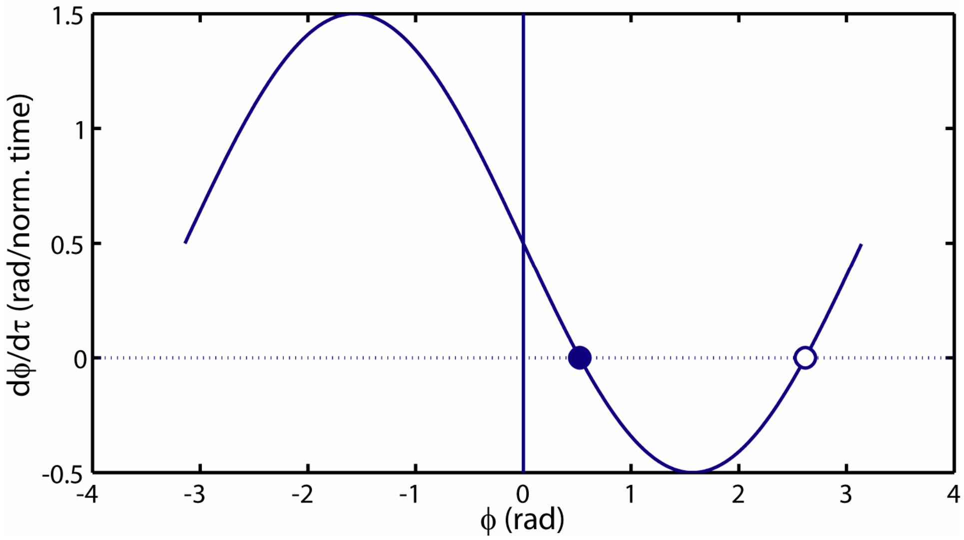

Figure 5.10 ϕ-Phase space for the motion of a uniform oscillator ($\Omega_N = 0.5$, $\alpha = 0$). Circles indicate fixed points in the motion of ϕ. The filled circle is stable while the unfilled circle is unstable.

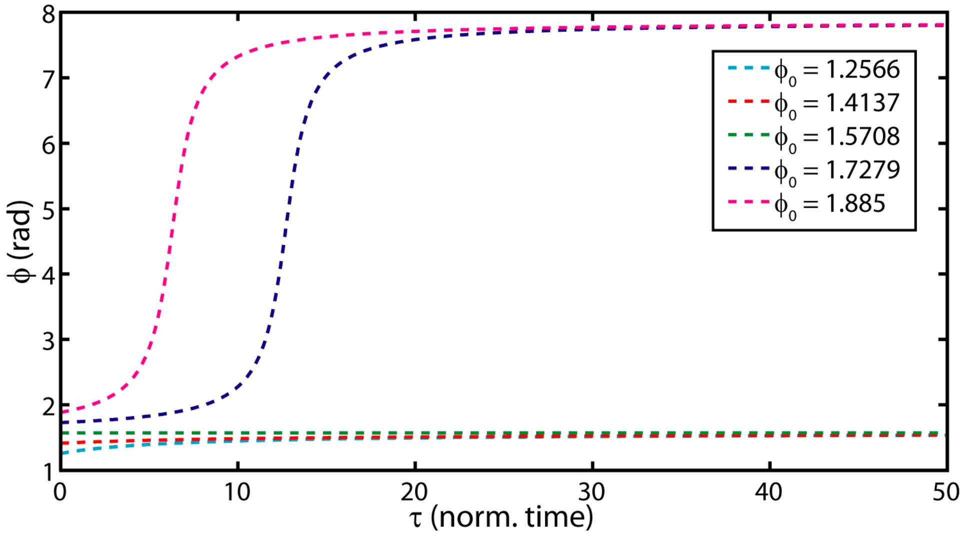

Figure 5.11 ϕ-trajectory at the critical frequency $(\Omega_N = 1.0)$ for different initial conditions ($\alpha = 0$).

Note that in Figure 5.10, all ϕ angles are plotted, but in any one trajectory, the ϕ angles actually visited will be some range that is a subset of $-\pi \to \pi$ depend on the initial conditions.

Saddle-Node Bifurcations

If we increase the magnetic rotation rate to $\Omega_N = 1.0$, the two fixed points of Figure 5.10 will collide to form a saddle-node bifurcation at $\phi = \pi/2$. Trajectories with initial phase angles slightly lower will be attracted back to $\phi = \pi/2$ while those with initial phase angles slightly higher move towards $\phi = 2\pi + \pi/2 = 5\pi/2$ (see Figure 5.11). In terms of particle rotation, this means that when rotating at the critical frequency, the moment vector ***m*** can lag the ***B***-field vector by, at most $\pi/2$. Practically speaking, this phase is extremely sensitive since any slight increase, even a fluctuation induced by Brownian motion, will cause the particle to slip to $\phi = 5\pi/2$, which is yet another saddle-node bifurcation.

5.3.2 Nonuniform Oscillator

To illustrate a typical case in the regime of nonuniform oscillation, we set the parameters $\Omega_N = 1.5$, $\alpha = 0$ and initial conditions $\phi_0 = 0$ and $\theta_0 = 0$. The angular displacement trajectory is shown in Figure 5.12. It is clear from the figure that the particle experiences phase-slipping represented by the zigzags in the trajectory. At these instances when the angular velocity is negative, the magnetic field vector ***B*** leads the particle moment ***m*** so far ahead that the particle experiences a torque from the opposite direction. Soon after, the *B*-field again surpasses the particle moment and the phase lag ϕ continues to accumulate.

We can plot the individual angles with respect to dimensionless time, as we did before, for comparison. These graphs appear in Figure 5.13. The upper left graph shows that θ increases with time in an oscillatory fashion. This oscillation is due to slipping incidents when θ decreases for brief moments. The y-axis is plotted in units of "cycles" and "cycles/normalized time" to illustrate that there are about three slipping incidents per cycle, which agrees with Figure 5.12. The average angular velocity can be calculated by

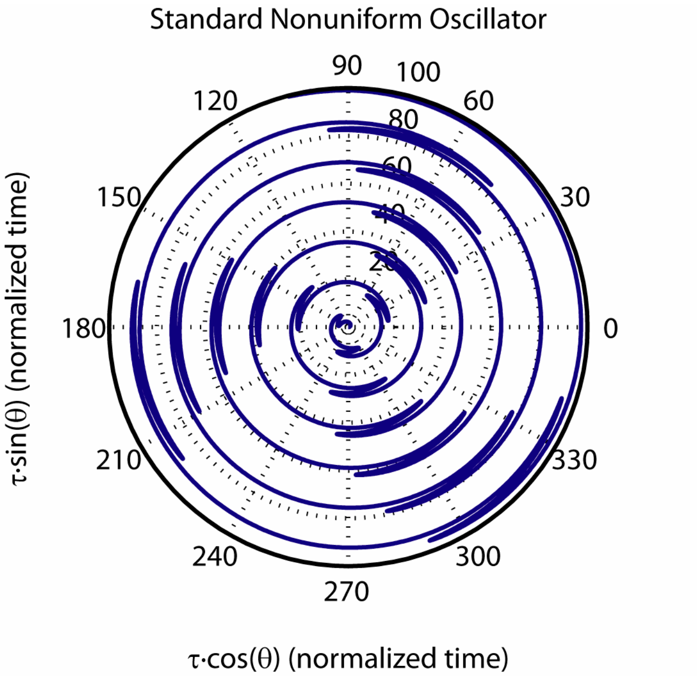

Figure 5.12 Polar trajectory of angle vs. dimensionless time τ for a nonuniformly rotating particle $(\alpha{=}0)$. $\Omega_N = 1.5$, $\phi_0 = 0$ and $\theta_0 = 0$.

fitting the data to a line (dotted line in graph). The slope of this line is indicated in the corresponding angular velocity plot in the lower left graph. In this plot, slipping events occur when $d\theta / d\tau < 0$. From Eqs. (5.2) and (5.7), we know the normalized angular velocity is

$$\langle d\theta / d\tau \rangle = \frac{\Omega - \sqrt{\Omega^2 - \Omega_c^2}}{\Omega_C} = \Omega_N - \sqrt{\Omega_N^2 - 1}\,. \tag{5.16}$$

Using Eq. (5.16), for $\Omega_N = 1.5$, we expect the normalized angular velocity to be 0.3820 *rad* = 0.06079 *cycles*. Our simulated result gives $\langle d\theta / d\tau \rangle = 0.0609$ *rad*. The discrepancy is due to integration over a finite number of cycles. Similar analysis can be done for ϕ. We can establish a relation between the normalized angular velocity and the angular phase velocity using Eqs. (5.2) and (5.16) to get

$$\langle d\phi / d\tau \rangle = \Omega_N - \langle d\theta / d\tau \rangle = \sqrt{\Omega_N^2 - 1}\,. \tag{5.17}$$

We expect $\langle d\phi / d\tau \rangle$ = 1.118 *rad* = 0.1779 *cycles* and our simulation gives 0.1778 cycles.

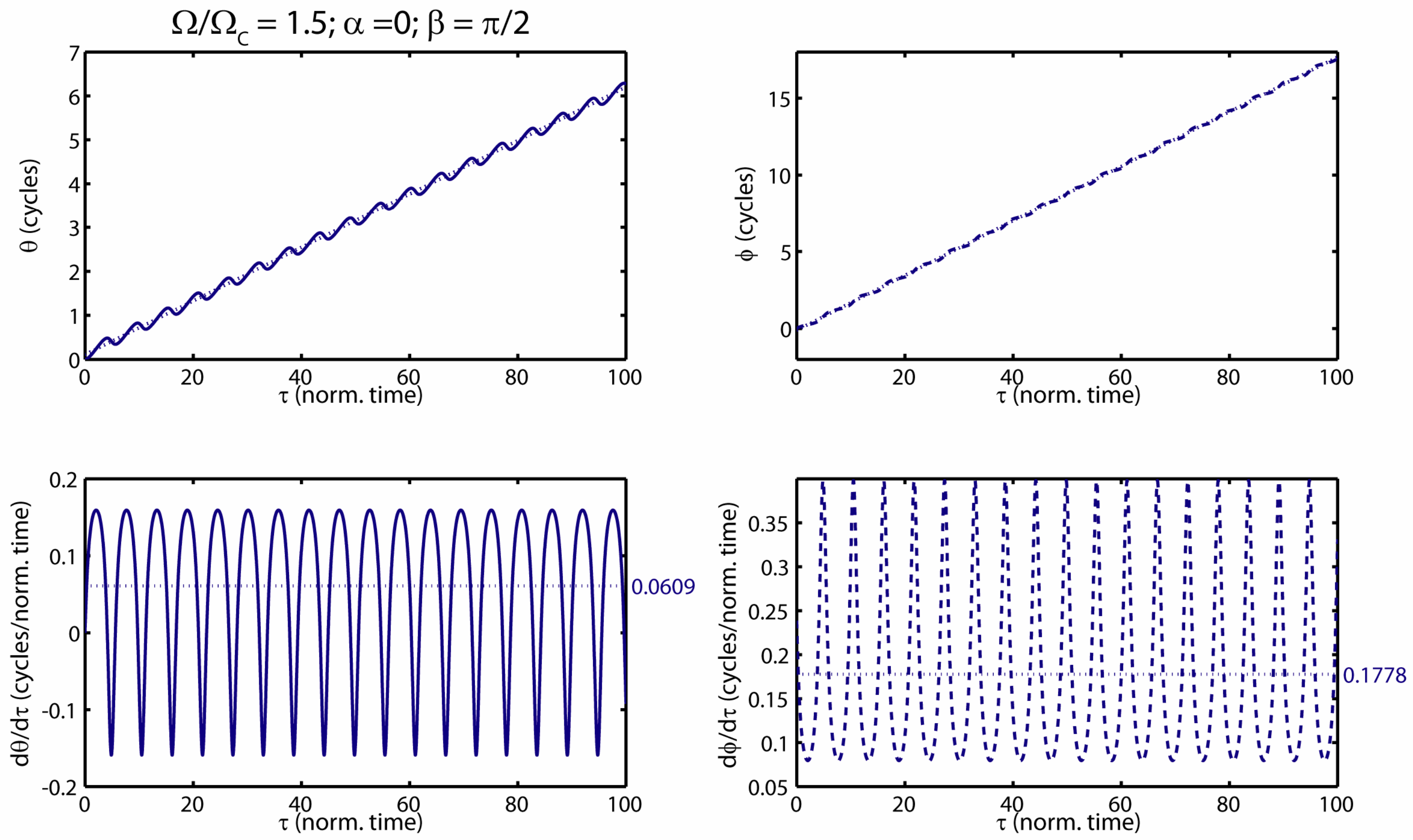

Figure 5.13 Angular displacement and angular velocity plots for a non-uniformly rotating particle. The legend is the same as in Figure 5.7. All four models overlap exactly since the optical force is set to zero $(\alpha = 0)$. $\Omega_N = 1.5$, $\phi_0 = 0$ and $\theta_0 = 0$.

If we look at the phase space of ϕ in Figure 5.14, we see that the oscillation is, in fact, nonuniform. Flow around the circle oscillates in strength but never changes direction ($d\phi / d\tau > 0$). We also notice there are now no fixed points (bifurcations). Instead there are minima at $\phi = \pi / 2 + 2n\pi$, where n is any integer. It should also be noted that since there are no bifurcations, all positive values of ϕ will eventually be visited.

If we change the parameters such that the minima are very close to $\phi = 0$, for example by setting $\Omega_N = 1.01$, the minima become what are known as bottlenecks [37]. In these cases, the minima have such low angular velocity that the particle spends most of its time at these phase points due to "saddle-node ghosts," and the particle experiences jumps in ϕ (slipping incidents) at brief isolated times. Angular and phase displacement and velocity graphs are shown in Figure 5.15. Notice the average angular velocity $\langle d\theta / d\tau \rangle$ is slightly slower than that for the case at the critical frequency. In addition, the average angular phase velocity $\langle d\phi / d\tau \rangle$ is non-zero, but very small due to the presence of bottlenecks.

5.4 An Interpretation of the Optical Perturbation

In the case of optical torque magnitudes much weaker than the magnetic torque $(\alpha << 1)$, we can treat the addition as an optical perturbation. The phase space formalism can provide a means of understanding the effect of the optical force on the angular phase lag of the magnetic moment behind the external rotating magnetic field.

Figure 5.10 and Figure 5.14 show the phase space for a uniform oscillator and nonuniform oscillator, respectively – both in the absence of optical torque. In both cases, the landscape of $d\phi / d\tau$ is sinusoidally periodic in ϕ with period 2π and constant in time. Thus, a fixed point at a specific phase will remain so throughout the flow, and the system is represented by a true vector field on the circle. The effect of the perturbative optical torque is to modify both the amplitude and the phase of this sine dependence by making them both time dependent.

We can delineate this time dependence for the optical force applied at the center of an anisotropic particle. Eq. (5.15) is the appropriate equation of motion for this model of

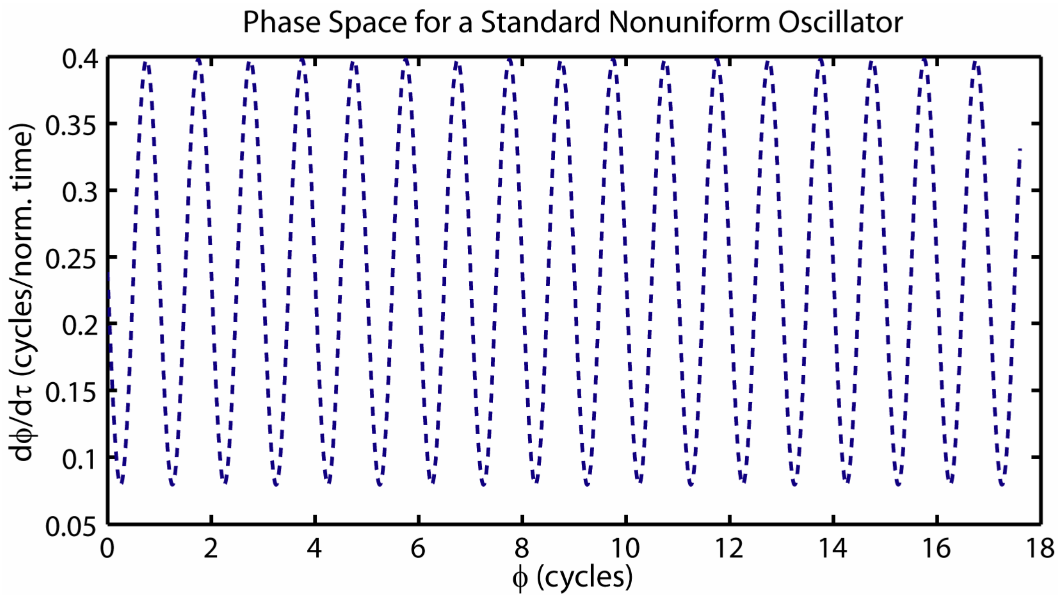

Figure 5.14 ϕ-Phase space for a nonuniform oscillator $(\alpha = 0)$. $\Omega_N = 1.5$, $\phi_0 = 0$ and $\theta_0 = 0$.

optical torque. Applying several trigonometric identities, the equation can be rearranged to give

$$\frac{\partial\phi}{\partial\tau} = \Omega_N - [1+\alpha\sin(\Omega_N\tau)]\sin\phi - \alpha\cos(\Omega_N\tau)\cos\phi. \tag{5.18}$$

Let us define the following time-dependent function:

$$\chi^2(\tau) = [1+\alpha\sin(\Omega_N\tau)]^2 + [\alpha\cos(\Omega_N\tau)]^2. \tag{5.19}$$

It follows that Eq. (5.18) can be written as

$$\frac{\partial\phi}{\partial\tau} = \Omega_N - \chi(\tau)[\cos\psi(\tau)\sin\phi + \sin\psi(\tau)\cos\phi] \tag{5.20}$$

where

$$\begin{aligned} \sin\psi(\tau) &= \frac{\alpha\cos(\Omega_N\tau)}{\chi(\tau)} \\ \cos\psi(\tau) &= \frac{1+\alpha\sin(\Omega_N\tau)}{\chi(\tau)} \end{aligned}. \tag{5.21}$$

Simplifying Eq. (5.20) to look like our original equation of motion, we get

$$\frac{\partial\phi}{\partial\tau} = \Omega_N - \chi(\tau)\sin(\phi+\psi(\tau)). \tag{5.22}$$

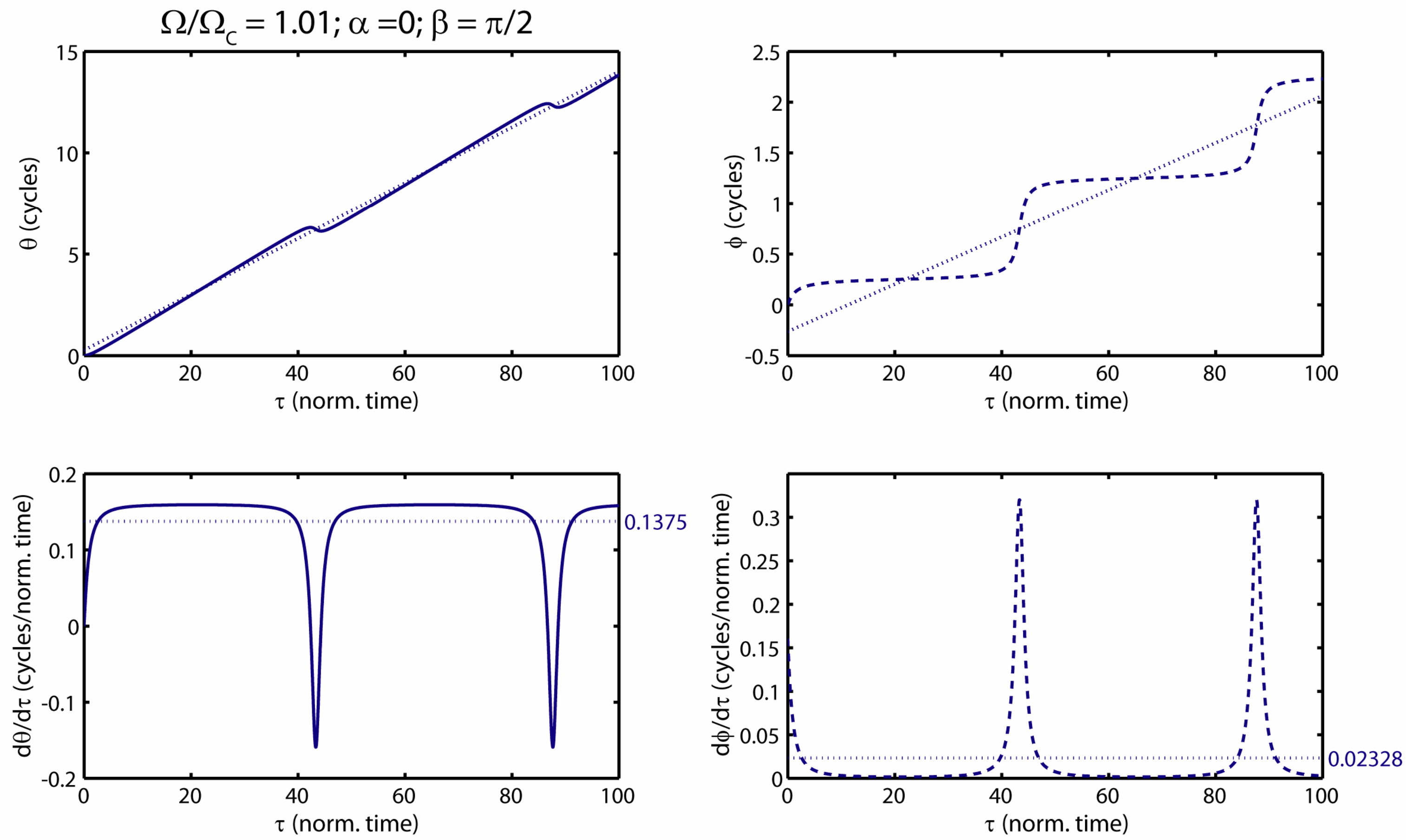

Figure 5.15 Angular displacement and angular velocity plots for non-uniformly rotating particle with bottlenecks. The legend is the same as in Figure 5.7. All four models overlap exactly since the optical force is set to zero $(\alpha = 0)$. $\Omega_N = 1.01$, $\phi_0 = 0$ and $\theta_0 = 0$.

As mentioned, the effect of the optical perturbation is to introduce a time-dependent amplitude and phase to the landscape of the ϕ-phase space trajectory. The system can no longer be considered a vector field on the circle. As the ϕ-phase space trajectory changes, so do the phase locations of fixed points. If the particle is at a stable phase at some instant τ, the fixed point will likely shift as time progresses. Although the analysis performed here was for the first model of optical torque, all three models introduce a time-dependence to the ϕ-phase space trajectory.

5.5 Comparison of Models

The previous section examined the standard uniform and nonuniform oscillators and introduced various graphical tools for illustrating the dynamic motion. This provides a basis to compare with results obtained when the optical torque was added using three different models. For simplicity, we've assumed a relatively weak-amplitude optical torque (α is small) which corresponds to actual experimental parameters used in practice.

5.5.1 Synchronous Rotation (Phase-Locking)

The simplest case of synchronous rotation is the otherwise uniform oscillator with an added optical torque weak enough that the particle never slips. This would occur if $\langle d\phi / d\tau \rangle < 0$ at some ϕ for all τ. This ensures there is always a stable fixed point somewhere, even if it were to change with τ. Parameters for one such case are $\Omega_N = 0.69$ and $\alpha = 0.3$ with the initial conditions $\phi_0 = 0$ and $\theta_0 = 0$. The theta trajectory and angle plots for this case are given in Figure 5.16 and Figure 5.17, respectively. This case is qualitatively similar to a case with the same parameters except $\Omega_N = 0.5$. Thus, results here can be compared to the uniform oscillator in Figure 5.6 and Figure 5.7.

The θ-trajectories in Figure 5.16 show that the particle never experiences slipping. Zooming on the origin, we also notice that when the moment $\boldsymbol{m}$ points towards the negative y-direction of the coordinate system, the three models can be best distinguished. In particular, curves closer to the origin represent models with more optical torque, thus

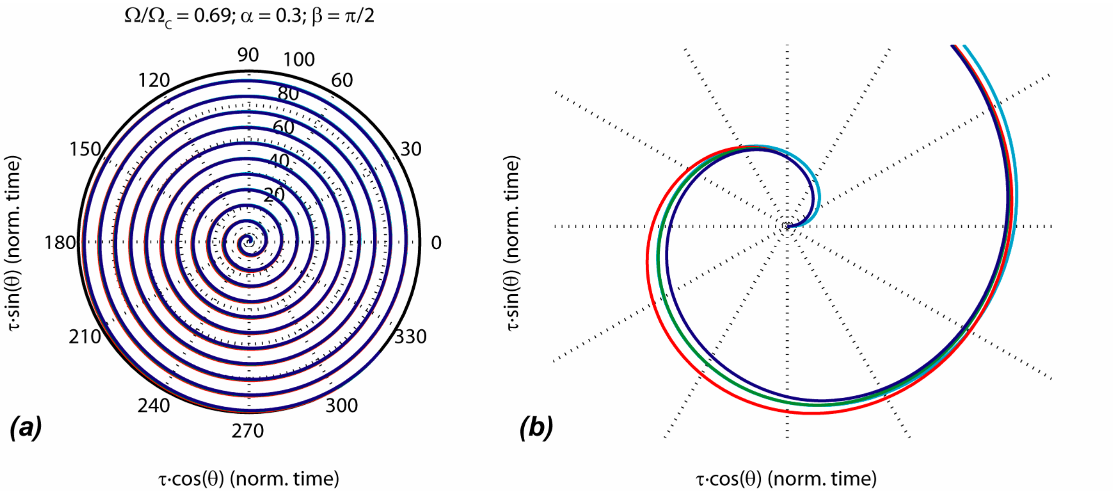

Figure 5.16 (a) Polar trajectory of angle vs. dimensionless time τ for a non-uniformly rotating particle with slow magnetic rotation in a non-slipping regime using 4 different models of optical torque. $\Omega_N = 0.69$, $\alpha = 0.3$, $\phi_0 = 0$ and $\theta_0 = 0$. (b) Zoom into origin.

causing θ-rotation to be quicker, at least over those regions. This agrees with the descriptions given for each optical torque model.

Although the particle never slips, the rotation is not strictly "phase-locked" since the phase ϕ actually oscillates very weakly about an average value. Despite the oscillation, the average angular velocity $\langle d\theta / d\tau \rangle \approx \Omega_N = 0.69 = 0.11$ *cycles/norm. time*. We can analyze the oscillatory motion easier by zooming into the bottom right graph of Figure 5.17. This is shown in Figure 5.18.

The light blue curve represents our standard uniform oscillator with no optical torque which starts at an initial phase far from the most stable. After some time the angular velocity decays to zero. The three models with optical torque show a slower initial phase increase due to the presence of the additional torque which slows the increase in the phase lag between ***B*** and ***m***. At around $\tau = 3$, the three models diverge.

The red curve represents results for the particle which experienced a different torque direction depending on which side the phase was at that moment. The curvature of the red curve at each negative $d\phi / d\tau$ minima is sharper than that for positive $d\phi / d\tau$ and the time extent is shorter. We expect this since negative $d\phi / d\tau$ corresponds to times when ***m*** approaches ***B*** due to the increase in optical torque as θ approaches $2n\pi-$ as the torque

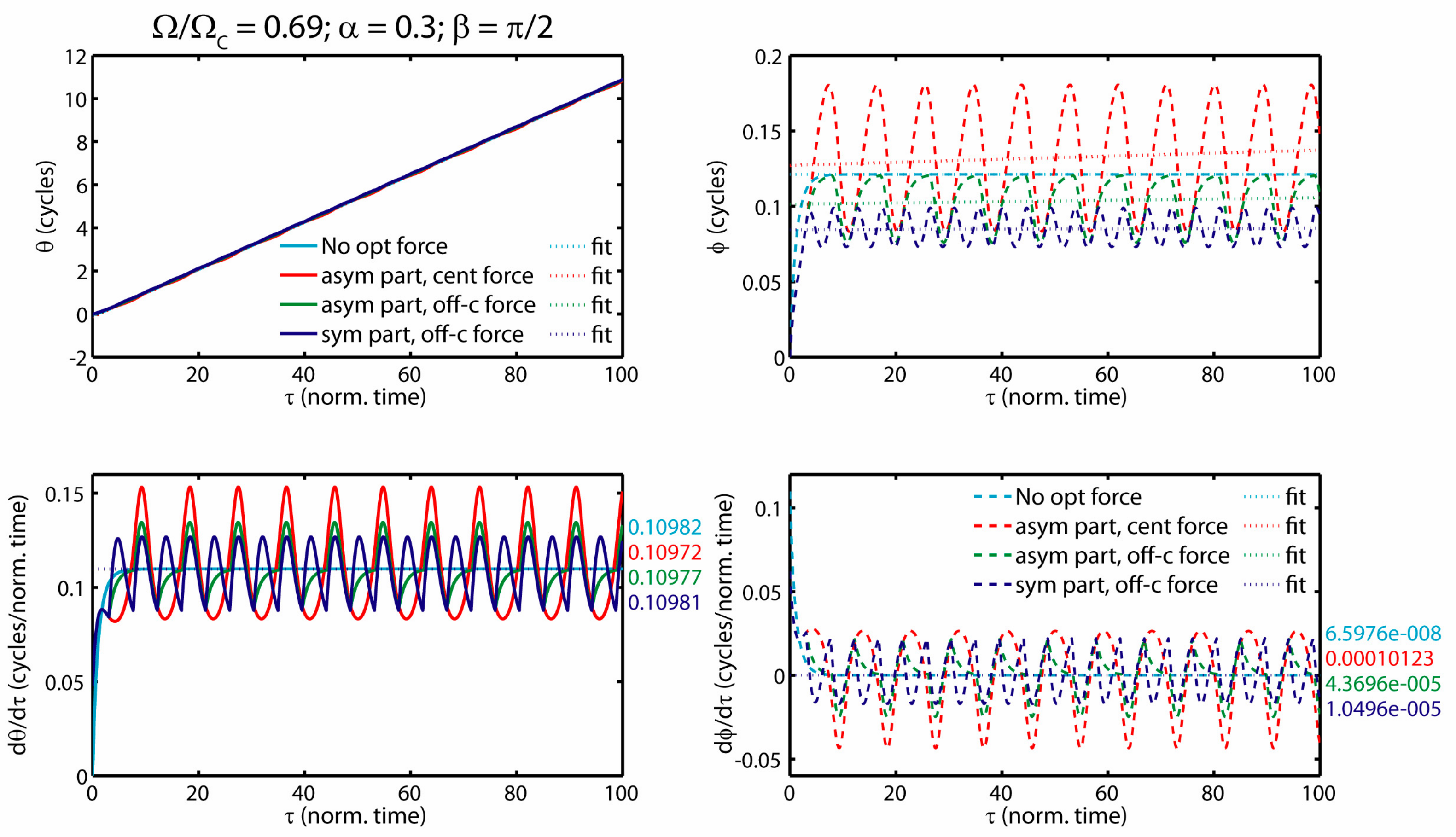

Figure 5.17 Angular displacement and angular velocity plots for nonuniformly rotating particle with slow magnetic rotation in a non-slipping regime using 4 different models of optical torque. The legend is the same as in Figure 5.7. $\Omega_N = 0.69$, $\alpha = 0.3$, $\phi_0 = 0$ and $\theta_0 = 0$.

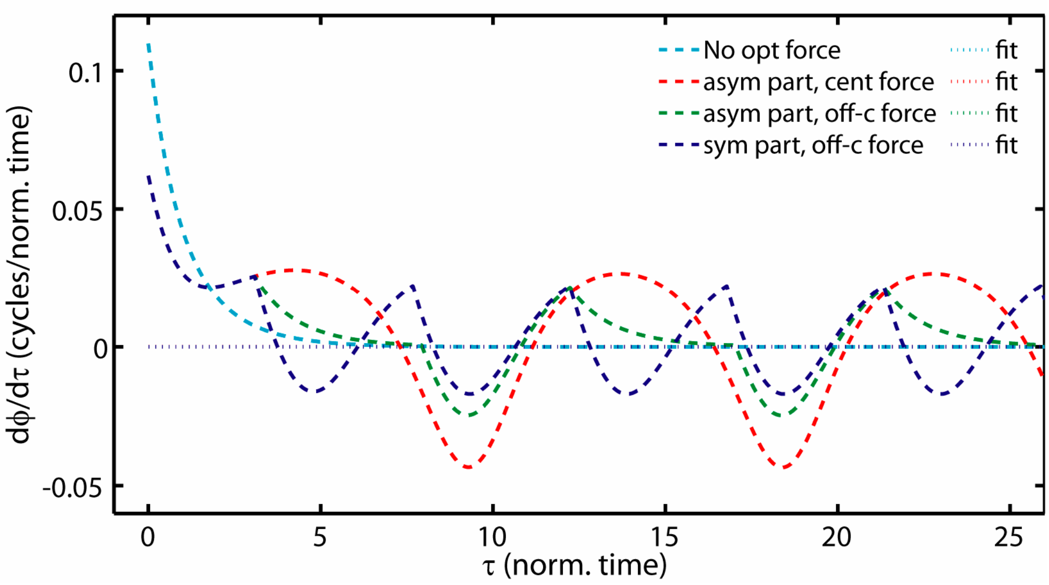

Figure 5.18 Expanded version of the bottom right graph of Figure 5.17.

increases, θ moves faster to a phase where the optical torque is more increased causing the phase ϕ to decrease more rapidly. Once $2n\pi$ is passed, the optical torque lessens, and the phase ϕ increases at a slower rate and for a longer time. The smoother maxima correspond to times when the moment points along the negative y-axis.

The dark blue and green curves both indicate a kink near $\tau = 3$ when the models diverge. This corresponds to the presence of an absolute value function in the model description for $d\phi / d\tau$. After that point, the green curve, which represents zero-optical torque for $\boldsymbol{m}$ pointing towards negative y-directions, shows the same behavior as our uniform oscillator with no optical torque at initial times. At about $\tau = 7.9$, the green curve experiences another kink, signifying the onset of the optical torque when $\theta = 3\pi / 2$. At this point, the angular phase velocity behaves similarly to that described for the red curve at negative $d\phi / d\tau$.

The dark blue curve represents the particle which experiences a torque in the same direction for all orientations of the $\boldsymbol{m}$ vector, thus we see double the frequency of periodicity in the function compared to that for the red and green curves. We can also look at the ϕ-phase space and try to understand the exhibited behavior (see Figure 5.19). The light blue curve represents a uniform oscillator that initially flows to a stable phase at

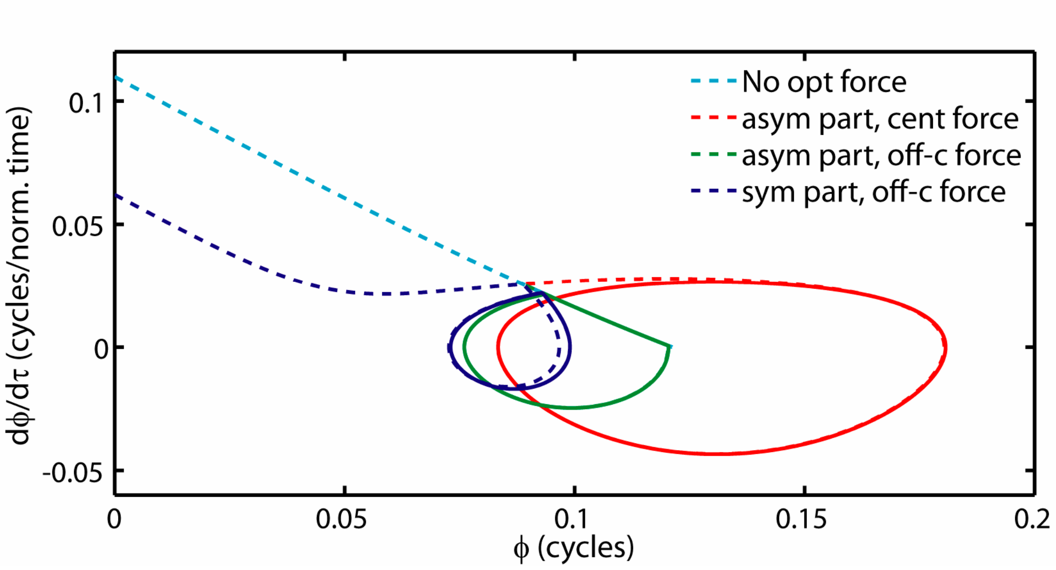

Figure 5.19 ϕ-Phase space for a nonuniformly rotating particle with slow magnetic rotation in a non-slipping regime using 4 different models of optical torque. $\Omega_N = 0.69$, $\alpha = 0.3$, $\phi_0 = 0$ and $\theta_0 = 0$.

$\sin^{-1}(\Omega_N) = 0.761\ rad = 0.121\ cycles$. All three optical torque models follow the dark blue curve until $\phi = \sim 0.56\ rad = 0.089\ cycles$ at which point the three models diverge. All three curves fall into closed loops indicating that the phase oscillates but is bounded. In the order red → green → dark blue, the accumulated counter-clockwise optical torque over one rotation increases. Thus, in the same order, the total phase-extent over which the particle's moment accumulates lag behind the ***B***-field decreases. For this reason, following the same order, the diameters of the phase space loops along the ϕ-axis decreases – the phase oscillation is smaller if the optical torque is always present for any particle orientation.

We can also see the non-continuously differentiable nature of the green and dark blue curves, which again comes about from the presence of absolute value functions to describe these models. The flat region of the green curve corresponds to moments when the particle is oriented such that no optical torque is applied, thus it follows the uniform oscillator trajectory.

5.5.2 Asynchronous Rotation (Phase-Slipping)

The other regime in which the particle is always slipping occurs when the magnetic rotation is fast enough to overcome both drag and the optical torque. Parameters for one such case are $\Omega_N = 1.5$, $\alpha = 0.49$ and $\phi_0 = 0$. Since the graphs become significantly different for each model, they will be plotted individually when necessary. The polar angle trajectories shown in Figure 5.20 quickly reveal the slipping dynamics for each model in which the phase ϕ accumulates lag in all cases (no bifurcations exist). The light blue curve is the familiar nonuniform oscillator we've already discussed previously. The red curve illustrates a particle that repeatedly slips at about the same θ for every cycle of the magnetic field rotation. The magnetic field ***B*** rotates fast enough that the particle can never complete a full rotation before the next slipping event, thus $\langle d\theta / d\tau \rangle = 0$ although θ oscillates about a stable angle. This angle appears in the 2nd quadrant of the coordinates system since this is the onset of optical torque that opposes the magnetic torque. This angle can also be controlled by changing the direction of the optical force vector.

The green trajectory represents the particle that experiences zero optical torque for ***m*** pointing towards negative *x*-directions. We see that slipping events appear to have similar patterns as the standard nonuniform oscillator, but primarily in quadrants 2 and 3, as we would expect. Again, we can change where slipping occurs on the circle by changing the direction of the optical force vector.

The dark blue trajectory shows overall fewer slipping events,. Most of the slipping appears to occur at angles close to the *z*-axis. This is explained by recalling the sine dependence of the optical torque. For angular positions of the magnetic moment near the *y*-axis, the optical torque is maximized, thus less slipping occurs. When the magnetic moment vector lies along the *z*-axis, the projection of the cross sectional area perpendicular to the optical torque direction is minimized, enabling more slipping events to occur.

This behavior is also supported by the angular displacement and angular velocity vs. τ graphs in Figure 5.21 through Figure 5.23. Potentially interesting is that the angular velocity plot for the 3rd optical torque model (dark blue) seem to show that the slipping events are not perfectly periodic. Such quasi-periodic behavior is known to occur in

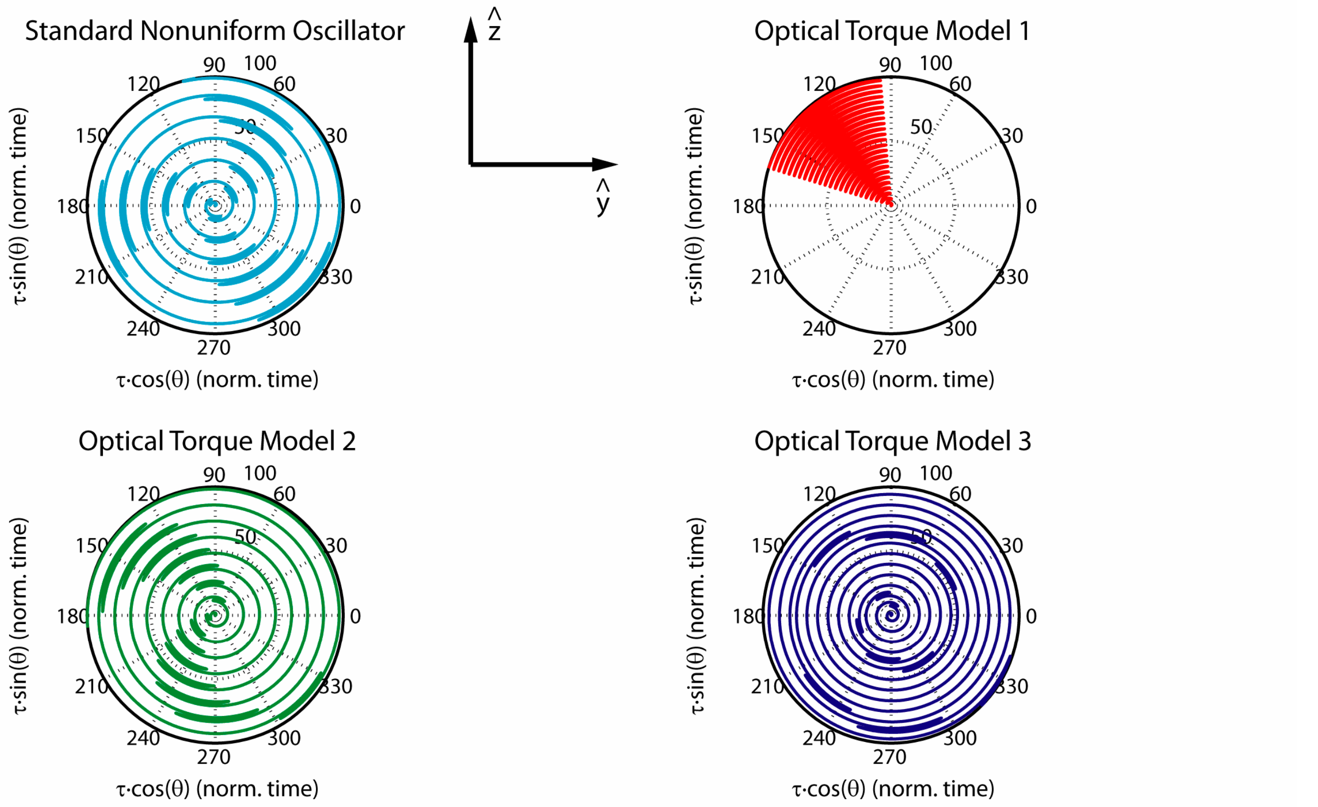

Figure 5.20 Polar trajectory of angle vs. normalized, dimensionless time τ for a nonuniformly rotating particle with fast magnetic rotation in a slipping regime using 4 different models of optical torque. $\Omega_N = 1.5$, $\alpha = 0.49$, $\phi_0 = 0$ and $\theta_0 = 0$. (top left, light blue) standard nonuniform oscillator with no additional optical torque (top right, red) nonuniform oscillator with cooperative optical torque applied when the magnetic moment ***m*** points towards +*y*-directions and opposing optical torque applied when ***m*** points towards –*y*-directions (bottom left, green) nonuniform oscillator with cooperative optical torque applied only when ***m*** points towards +*y*-directions (bottom, right, dark blue) nonuniform oscillator with cooperative optical torque applied when ***m*** points towards both + and –*y*-directions.

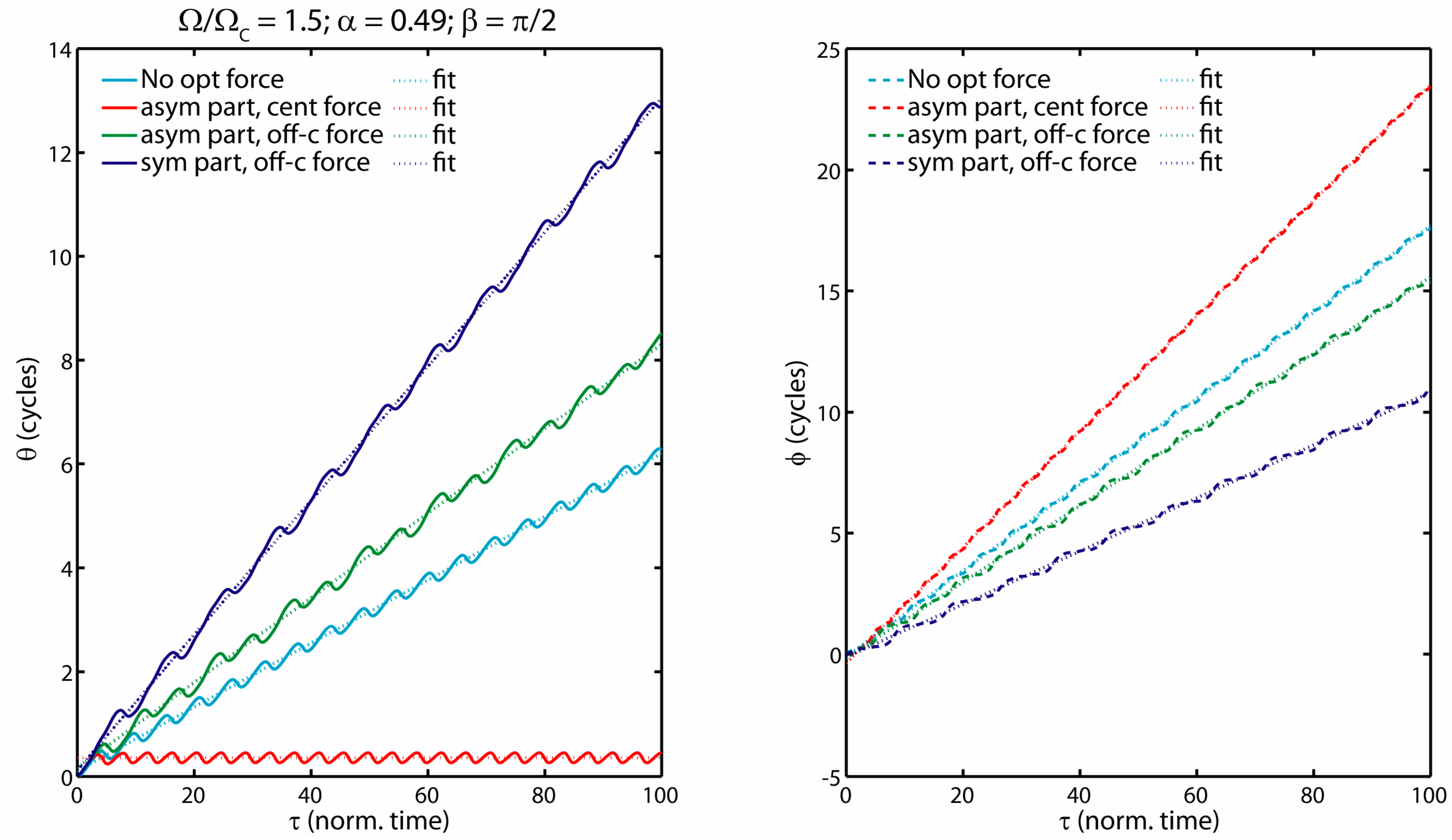

Figure 5.21 Angular displacement and phase for a nonuniformly rotating particle with fast magnetic rotation in a slipping regime using 4 different models of optical torque. The legend is the same as in Figure 5.7. $\Omega_N = 1.5$, $\alpha = 0.49$, $\phi_0 = 0$ and $\theta_0 = 0$.

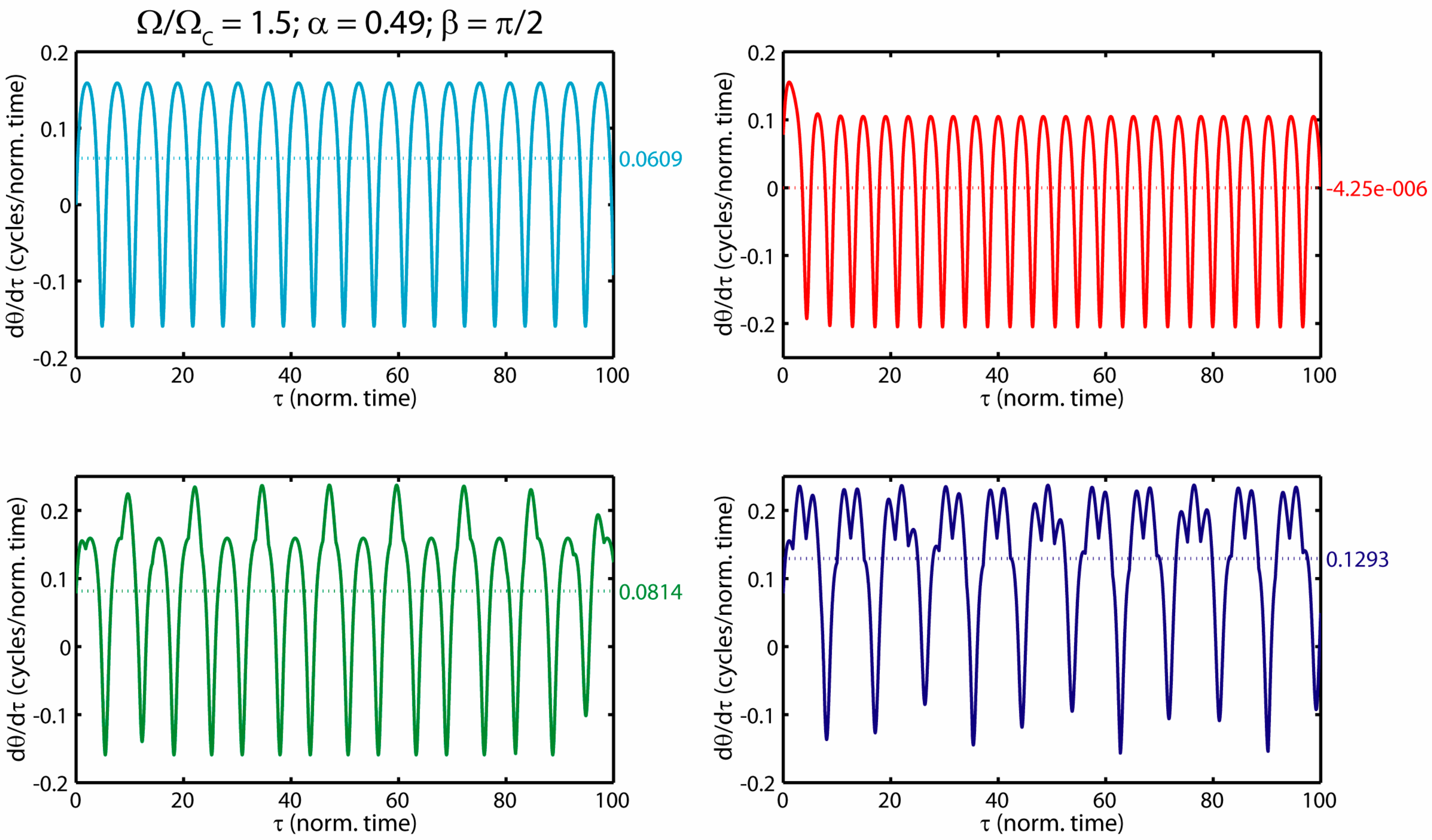

Figure 5.22 Angular velocity for a nonuniformly rotating particle with fast magnetic rotation in a slipping regime using 4 different models of optical torque. $\Omega_N = 1.5$, $\alpha = 0.49$, $\phi_0 = 0$ and $\theta_0 = 0$.

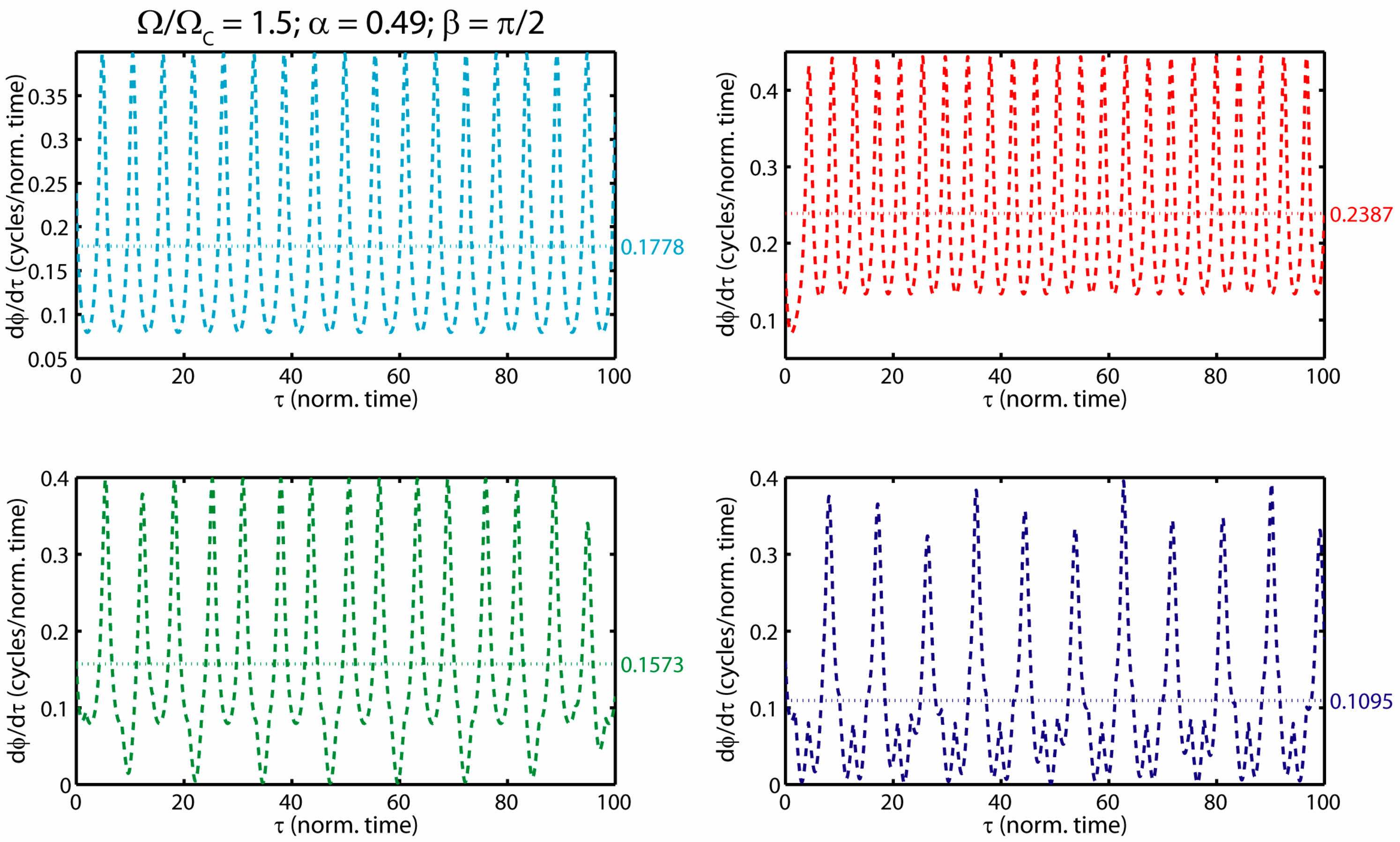

Figure 5.23 Angular phase velocity for a nonuniformly rotating particle with fast magnetic rotation in a slipping regime using 4 different models of optical torque. $\Omega_N = 1.5$, $\alpha = 0.49$, $\phi_0 = 0$ and $\theta_0 = 0$.

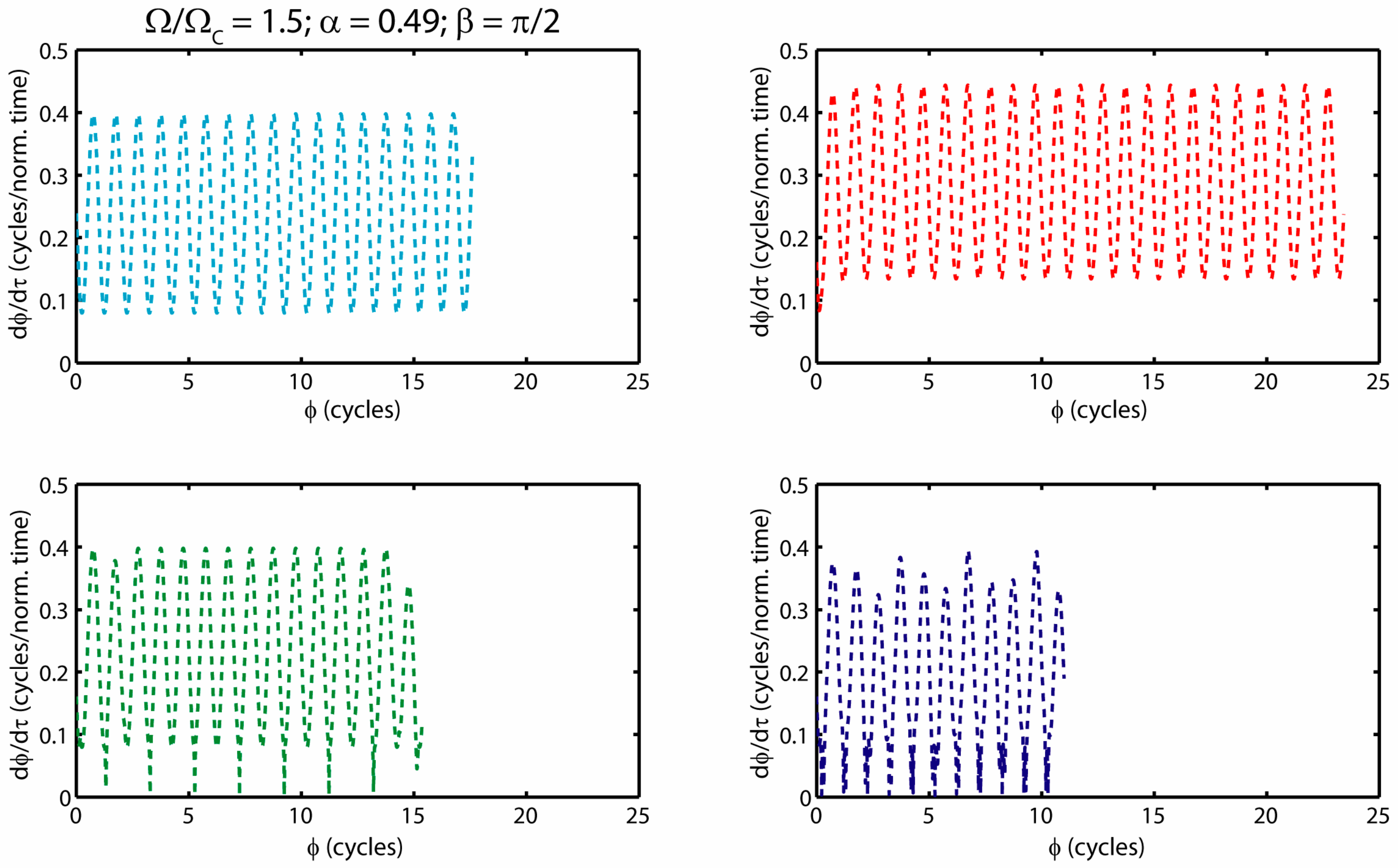

Figure 5.24 ϕ-Phase space for a nonuniformly rotating particle with fast magnetic rotation in a slipping regime using 4 different models of optical torque. $\Omega_N = 1.5$, $\alpha = 0.49$, $\phi_0 = 0$ and $\theta_0 = 0$.

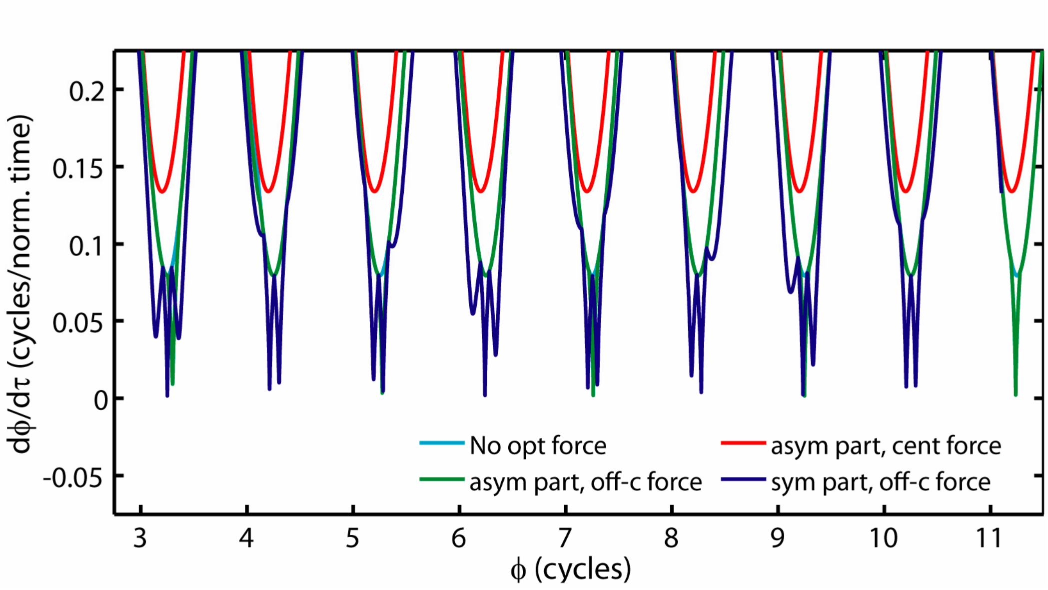

Figure 5.25 Zoom of low-magnitude angular phase velocities of Figure 5.24. Saddle-node ghosts grow increasingly more complex as the total accumulated optically torque increases for nonuniform oscillators with fast magnetic rotation..

systems where the applied forces have two incommensurate fundamental frequencies [167].

In the phase space plots of Figure 5.24, we see that the total extent of ϕ angles visited decreases with increasing accumulated optical torque over one rotation. We can zoom in on the low angular velocity saddle-node ghosts shown in Figure 5.25 to see that the trajectories become extremely jagged and complex. This seems to be the transition behavior just before the bounded phase space loops we saw with the non-slipping optically torqued system (Figure 5.19).

5.5.3 Optically Induced Phase-Locking

The final case considered is one in which the magnetic rotation is fast enough to induce nonuniform rotation in the absence of the optical torque. The optical torque, however, when present, may be strong enough to enable the particle to approach the phase of the magnetic field for most of the time. The qualitative details of the dynamics are similar for any initial phase condition ϕ_0, but the precise details such as the times or angles at which slipping events occur will likely be very sensitive to the initial conditions. The usual plots of polar angle trajectory, angular displacement, angular velocity, phase displacement, phase velocity and phase space are provided in Figure 5.26 through Figure 5.30.

The same general ideas already discussed can be used again for analysis. For models where the optical torque is present, the tendency for slipping is slightly stronger when the particle is pointing towards negative *y*-directions. In all four models, the particle slips, thus the phase accumulates beyond one cycle. The fourth model illustrates several bottlenecks since only a few slipping events occur over the times analyzed. Unlike the bottlenecks without the optical torque, the phase in between slipping events undergoes small amplitude, high frequency oscillations. The particle appears to briefly fall into a semi-stable phase space loop, but ϕ continues to accumulate slowly (see Figure 5.30) until eventually the particle slips with respect to the magnetic field and the oscillations begin again on the next cycle. A slight increase in the strength of the optical torque would probably be enough to enable the particle (at least in the third optical torque model) to follow the phase of the ***B***-field, without slipping for many cycles. The periods of motion where no slipping occurs, however, are still characterized as bottlenecks with small amplitude oscillations that may be gradually gaining phase until the next slipping event.

5.5.4 Dependence on Optical Strength

We've described the theoretical equations for three models of nonuniformly rotating magnetic particles influenced by a light beam which applies an additional optical torque. Our numerical analysis helped us illustrate the motion dynamics of each model for comparison. We now address the connection between this theoretical treatment and experiment. The 4 models are studied (1 without optical torque, 3 with), this time looking at the dependence of the average angular velocity $\langle d\theta / d\tau \rangle$ of the magnetic moment vector ***m*** over numerous cycles as a function of both the normalized magnetic rotation rate Ω_N and the ratio of optical torque strength to magnetic torque strength α.

In all cases there was some early-time nonuniform transient behavior that depended on the initial phase conditions ϕ_0 and θ_0. Since the average angular velocity was calculated by fitting θ vs. τ curves to a straight line and using the slope over a range of

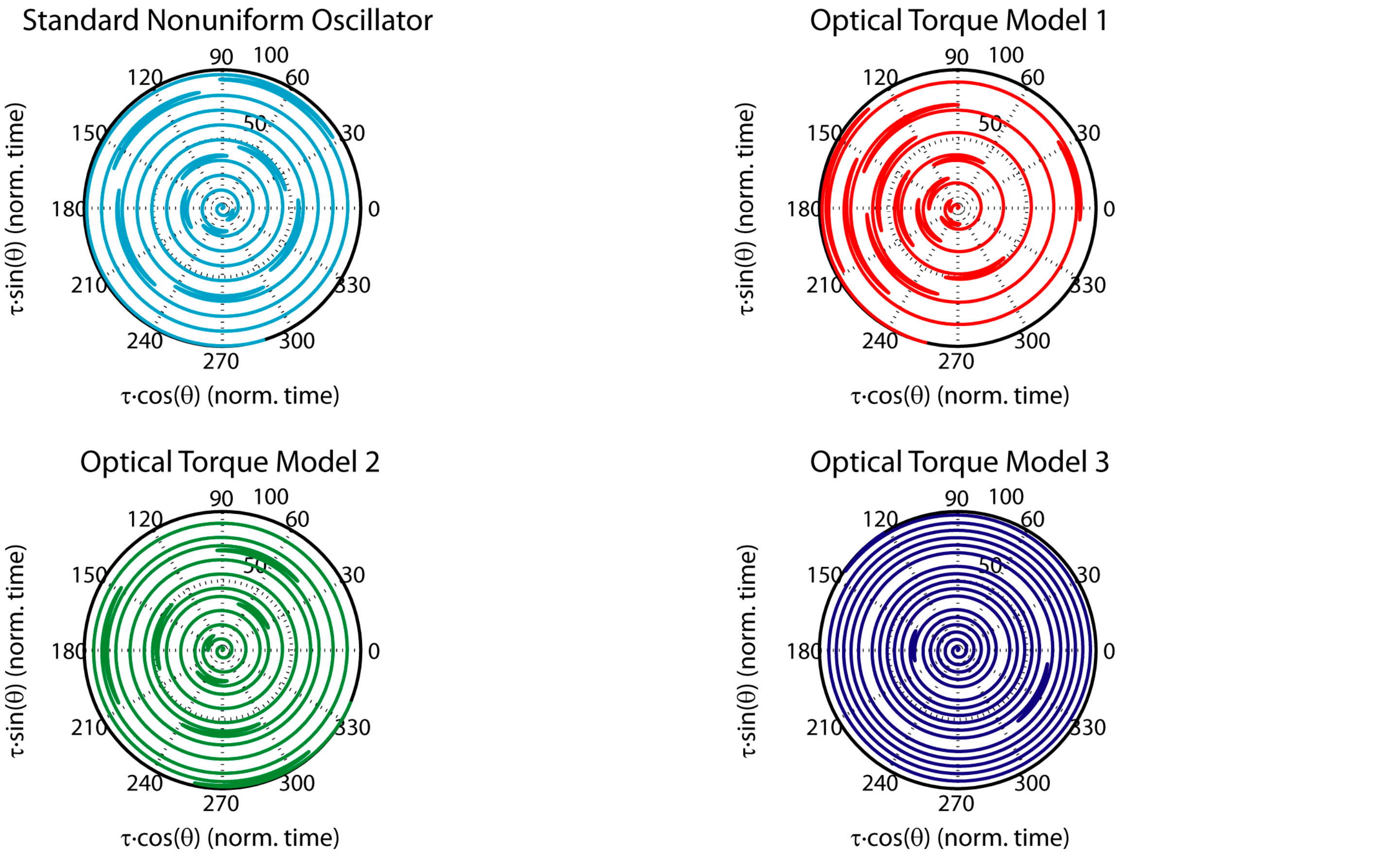

Figure 5.26 Polar trajectory of angle vs. dimensionless time τ for a nonuniformly rotating particle with fast magnetic rotation and medium optical torque. $\Omega_N = 1.2$, $\alpha = 0.3$, $\phi_0 = 0$ and $\theta_0 = 0$.

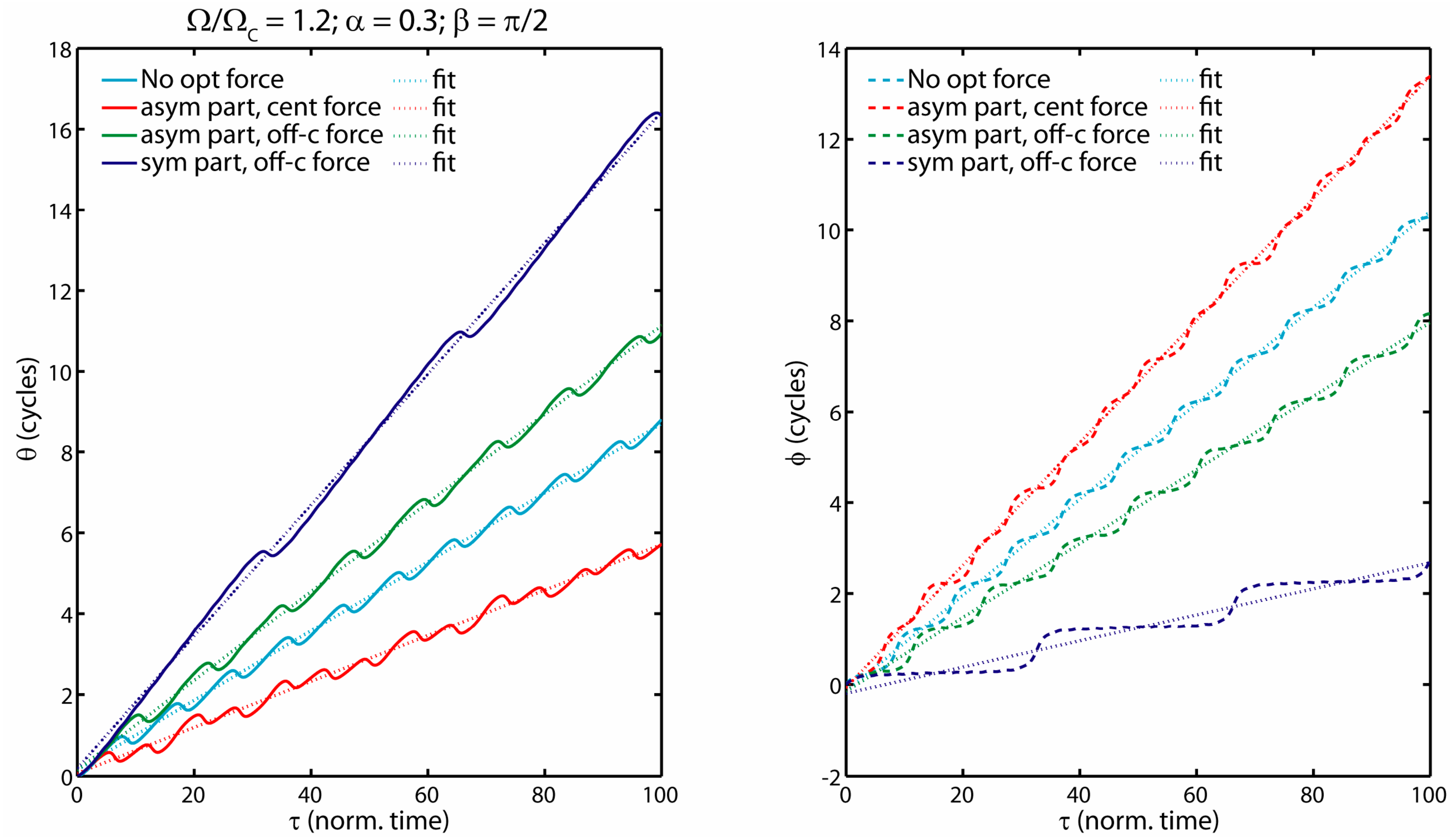

Figure 5.27 Angular displacement and phase for a nonuniformly rotating particle with fast magnetic rotation and medium optical torque. The legend is the same as in Figure 5.7. $\Omega_N = 1.2$, $\alpha = 0.3$, $\phi_0 = 0$ and $\theta_0 = 0$.

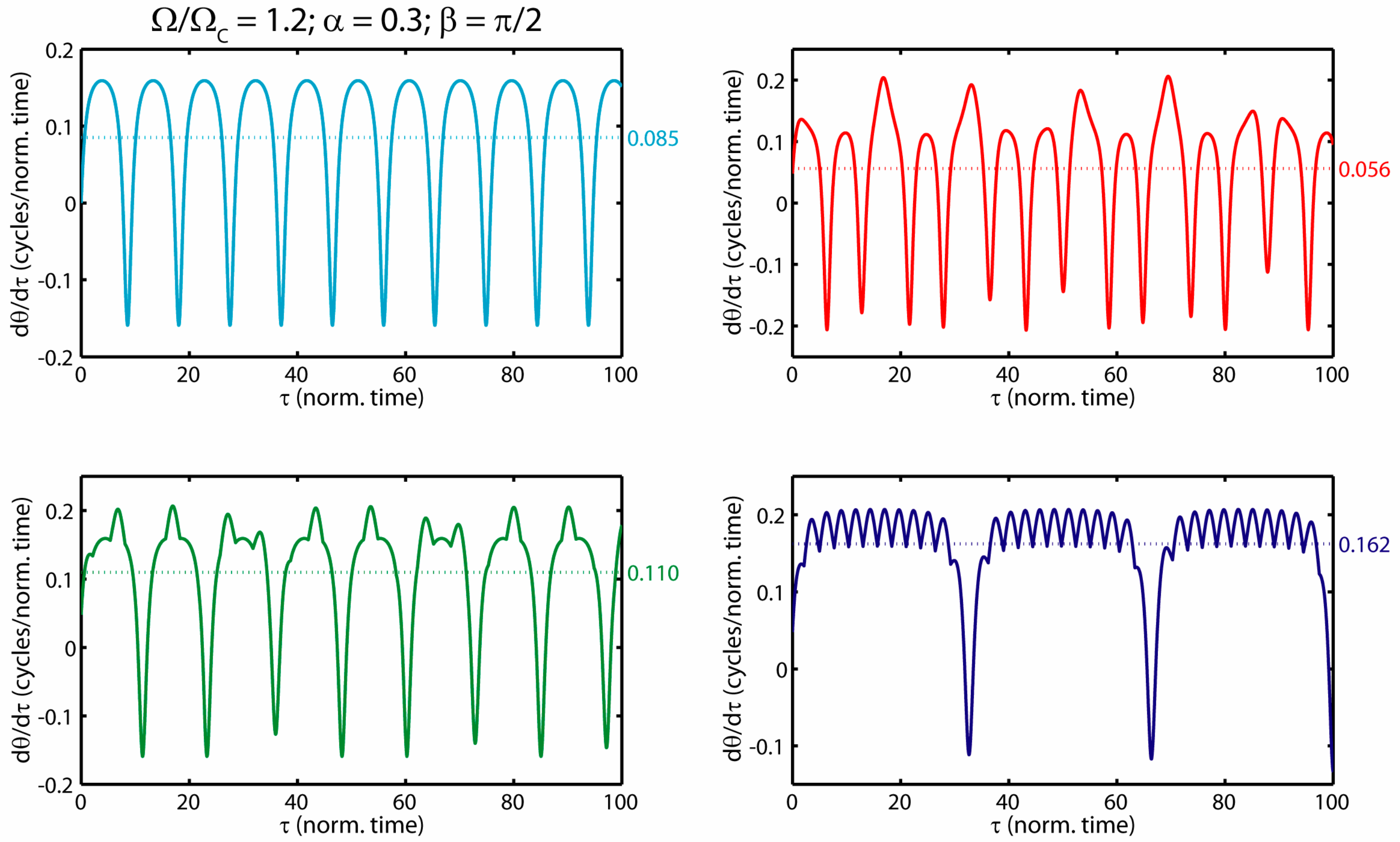

Figure 5.28 Angular velocity for a nonuniformly rotating particle with fast magnetic rotation and medium optical torque. $\Omega_N = 1.2$, $\alpha = 0.3$, $\phi_0 = 0$ and $\theta_0 = 0$.

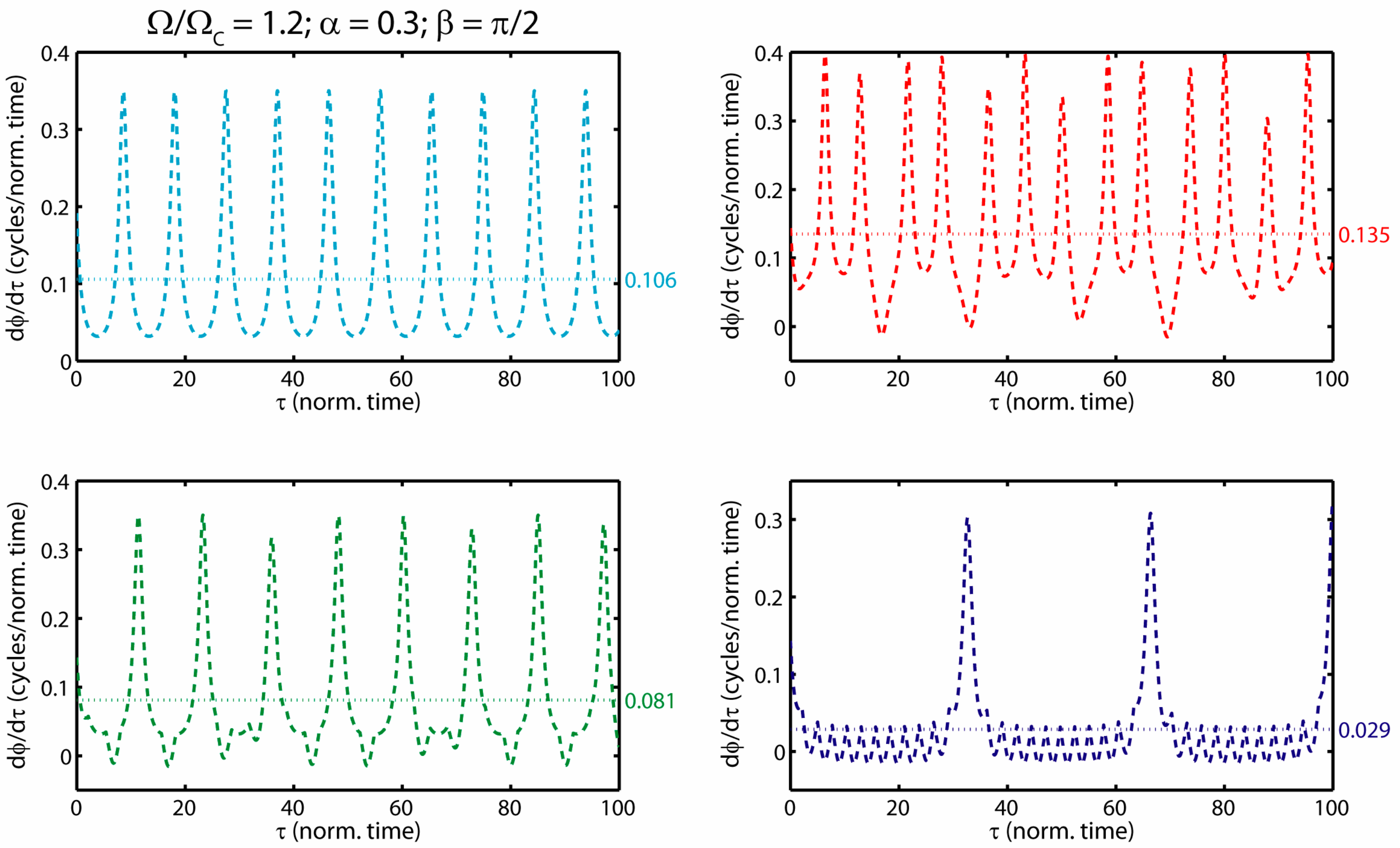

Figure 5.29 Angular phase velocity for a nonuniformly rotating particle with fast magnetic rotation and medium optical torque. $\Omega_N = 1.2$, $\alpha = 0.3$, $\phi_0 = 0$ and $\theta_0 = 0$.

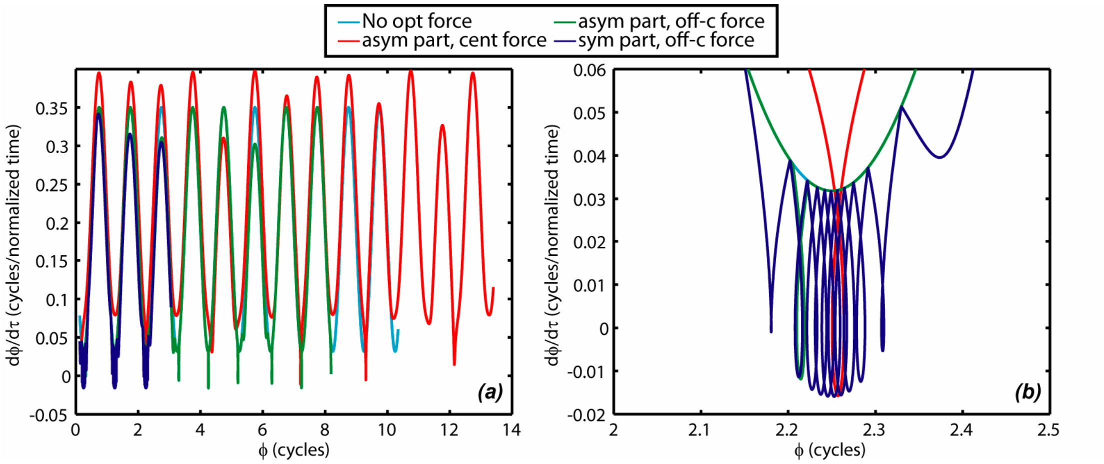

Figure 5.30 (a) ϕ-Phase space for a nonuniformly rotating particle with fast magnetic rotation and medium optical torque. $\Omega_N = 1.2$, $\alpha = 0.3$, $\phi_0 = 0$ and $\theta_0 = 0$. (b) Zoom of low-magnitude angular phase velocities of (a).

$\tau \sim 30\times$ the time required for the transient behavior to decay, the initial behavior can be neglected (typically, the transient behavior occurs within $\tau = 3$ while the linear fits were performed over $\tau = 0 \rightarrow 100$).

Standard Nonuniform Oscillator

We first consider the case of a standard nonuniform oscillator. Since there is no optical torque, $\alpha = 0$. We use the following parameter ranges: $0 < \Omega_N < 2$, $0 < \alpha < 2$, $\phi_0 = 0$ and $\theta_0 = 0$. A 3D-surface plot is shown in Figure 5.31 where the surface height and color correspond to the average angular velocity $\langle d\theta / d\tau \rangle$. The normalized magnetic rotation rate Ω_N is along the *x*-axis while the relative optical torque strength α is along the *y*-axis. The surface is represented by a 100 × 100 matrix of $\langle d\theta / d\tau \rangle$ values. Each value was calculated by using our 4th order Runge-Kutta algorithm to project the solution of the 1st order differential equation given in Eq. (5.15) from the initial conditions. 2000 points are used to calculate θ over the span of $0 < \tau < 100$ ($\Delta\tau = 0.05$). Every 5th point is recorded and a line is fit to these recorded points. The slope of this line gives us $\langle d\theta / d\tau \rangle$.

As we expect, the surface is constant along the *y*-axis since no optical torque is present. All solutions match the curve at $\alpha = 0$, which agrees with the standard nonuniform oscillator plot solution given by Eq. (5.8). The contour plot shown at

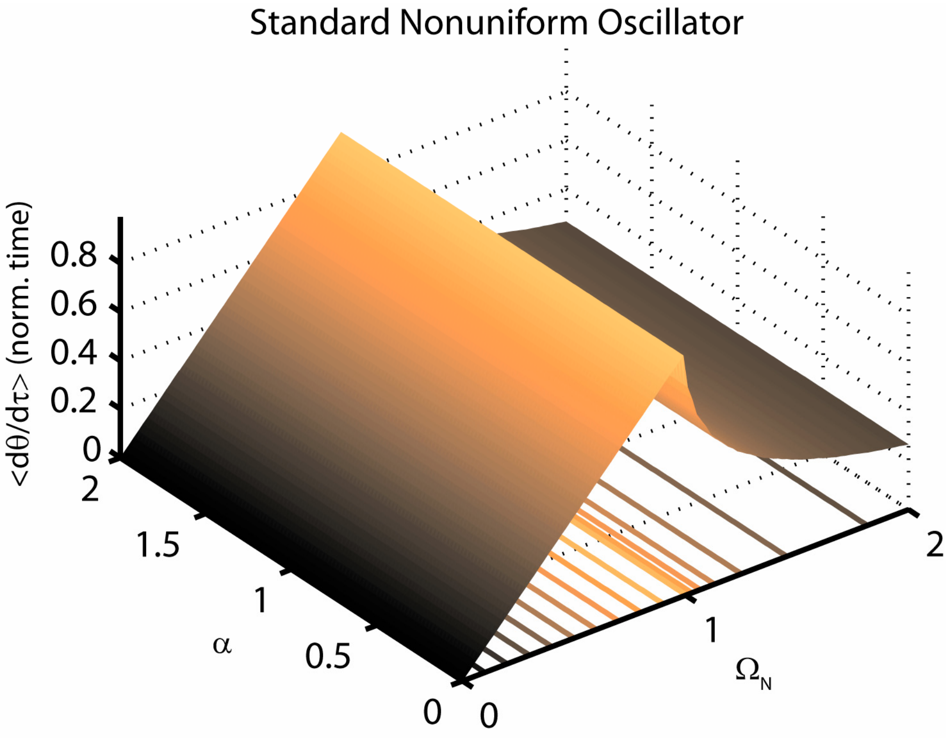

Figure 5.31 Average angular velocity surface for a standard nonuniform oscillator $(\alpha=0)$.

$z=0$ also indicates the constant surface as a function of α. For magnetic rotation rates less than unity, the average angular velocity matches the magnetic rotation rate. In such cases, the particle moment ***m*** is phase locked to the magnetic field vector ***B***. For larger magnetic rotation rates, the particle experiences slipping, thus the average angular rotation rate $\langle d\theta / d\tau \rangle$ drops below that of the magnetic field vector.

Optical Force Applied at Center of Anisotropic Particle

For this model, the optical torque adds to the magnetic torque when the particle moment ***m*** points toward positive y-directions. When the particle moment ***m*** points toward negative y-directions, the optical torque opposes the magnetic torque. The surface plot for the average angular velocity is shown in Figure 5.32.

We see that for $\alpha = 0$, we get the same familiar curve. If $\Omega_N < 1$, as α is increased, the average angular velocity seems to stay constant at the magnetic rotation rate. The contour plot reveals, however, that further increase in α causes a dramatic drop in the average angular velocity down to near zero values. The reason for this can easily be seen

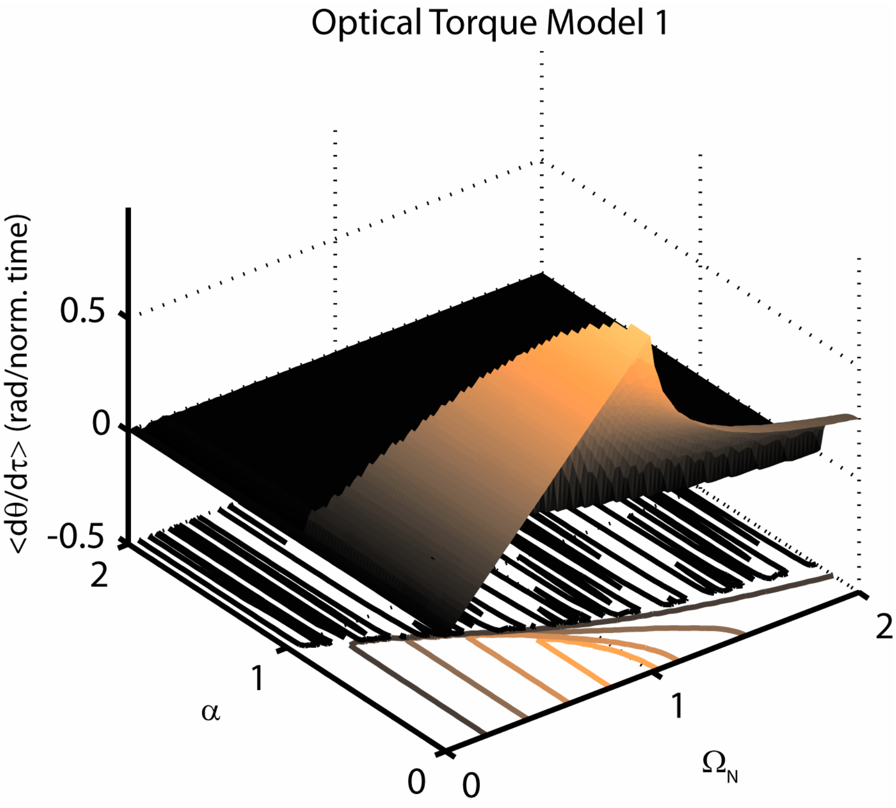

Figure 5.32 Average angular velocity surface for a nonuniform oscillator with optical force centered on an anisotropic particle.

by plotting the polar trajectory of angle vs. dimensionless time at one of these points of near-zero angular velocity. For the parameters $\Omega_N = 0.5$, $\alpha = 0.75$, $\phi_0 = 0$, shown in Figure 5.33(a) we see that when the optical torque opposes the magnetic rotation, the torque is strong enough to induce slipping The magnetic rotation is slow enough that moment ***m*** returns to about the same angle by the time the magnetic field vector returns to pass it again. This causes the particle to oscillate back and forth, never completing a full rotation cycle. As a result, the average angular velocity is zero. A similar result occurs when $\Omega_N > 1$. In this case, the magnetic rotation is faster so the onset of slipping occurs sooner once the optical torque is in opposition. The deviation from the *z*-axis is smaller so the optical torque that pushes the magnetic moment back is slightly weaker. As a result, the angular amplitude of oscillation is not as large. The polar trajectory of this case is shown in Figure 5.33(b).

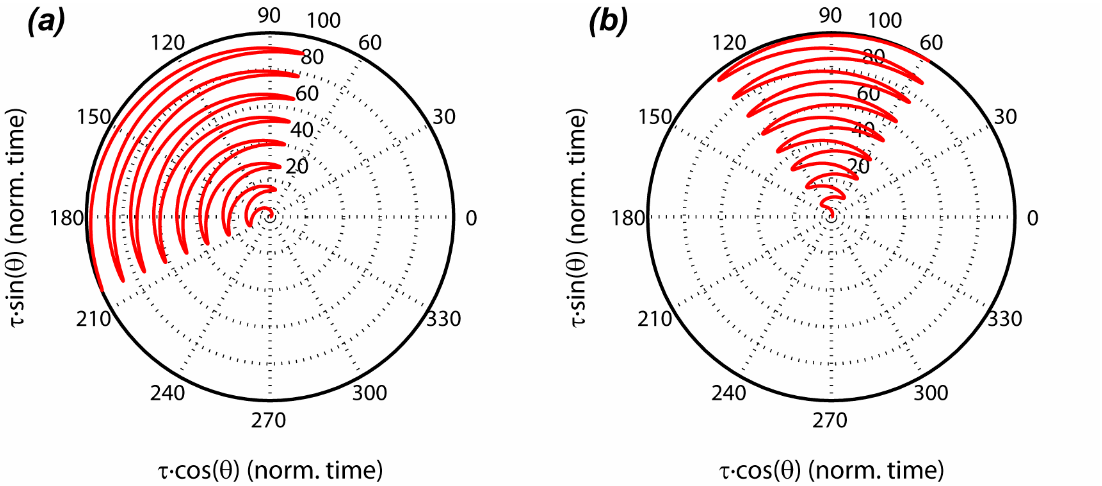

Figure 5.33 Polar trajectory of angle vs. dimensionless time for a nonuniform oscillator with optical force centered on an anisotropic particle. For both graphs, $\Omega_N = 0.5$, $\phi_0 = 0$ and $\theta_0 = 0$. (a) $\alpha = 0.75$ (b) $\alpha = 1.5$.

These results give us some notion of experimental difficulties. Practically speaking, if the particle moves directly into the laser focus such that both sides of the particle (or both particles of a dimer) are illuminated simultaneously, an increase in optical torque may not only prevent the particle from completing rotations, but also narrow the range of oscillations due to slipping as well as change the central angle. Similar effects may also occur if the gradient of the optical beam tends to align the particle.

Optical Force Applied Off-Center of Anisotropic Particle

In this case the optical torque is zero when the phase $\pi/2 - \Omega_N\tau - \phi$ between the optical force vector and the particle moment vector is in the range $n\pi < \pi/2 - \Omega_N\tau - \phi < (n+1)\pi$ where n is any odd number. When n is even, the optical torque varies sinusoidally with the phase. The average angular velocity surface plot is shown in Figure 5.34.

For magnetic rotation rates lower than the critical frequency without optical torque, the particle can always match the external magnetic rotation rate. For magnetic rotation rates higher than the critical frequency ($\Omega_N > 1$), an increase in the strength of the optical torque enables the particle to match a slightly higher maximum external magnetic rotation rate, thus shifting the actual "critical" threshold to slightly higher values. The

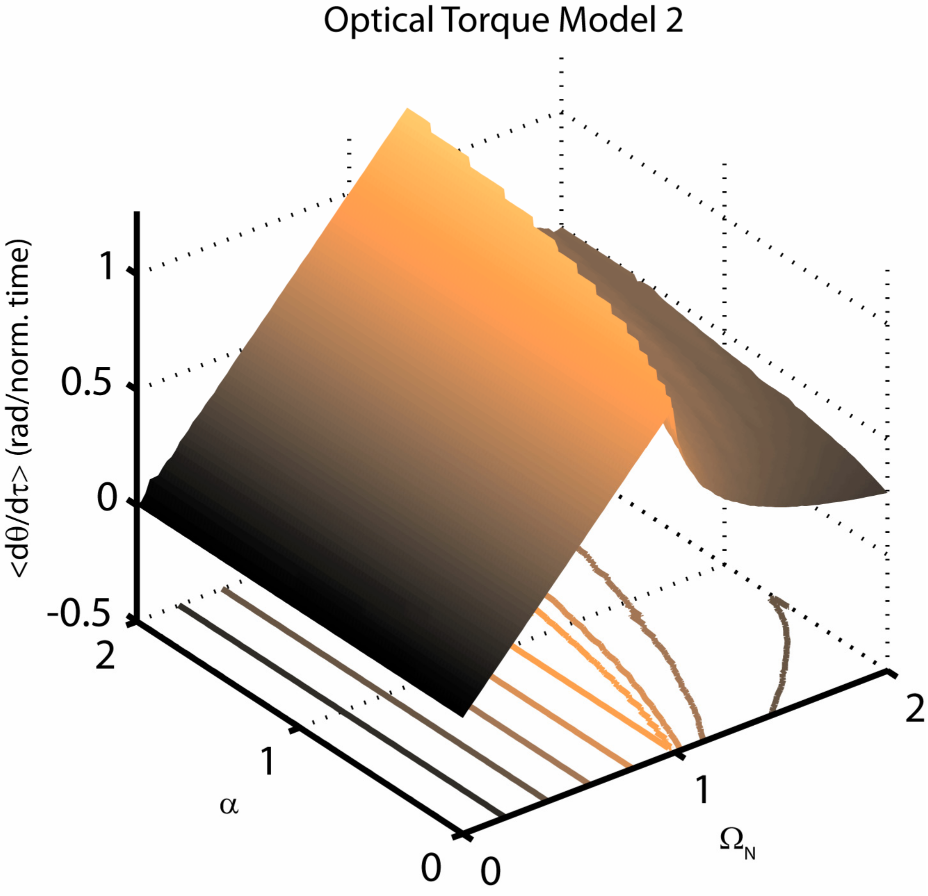

Figure 5.34 Average angular velocity surface for nonuniform oscillator with optical force applied off-center of an anisotropic magnetic particle.

new threshold can not be as high as the magnetic rotation rate because for half of the particle's rotation cycle, the particle does not experience the optical torque. During these periods, the phase lag of ***m*** behind ***B*** can accumulate and slipping events may occur.

The $\Omega_N > 1$ regime shows some other interesting features (see Figure 5.35 and Figure 5.36). We see a series of folds that appear once α gets as large as 0.5. The folds grow as α is increased. These folds appear to be real solutions, not artifacts of the programming code, since a decrease in the spacing between both individual Ω_N values and/or α values, as well as a decrease in the step size $\Delta\tau$, gave similar results. We can view the folds by a series of vertical slices plotted on the same graph as shown in Figure 5.36

First, there are a series of plateaus for $1 < \Omega_N < 1.22$. These plateaus indicate the extension of the critical frequency from the sub-unity normalized magnetic rotation rate

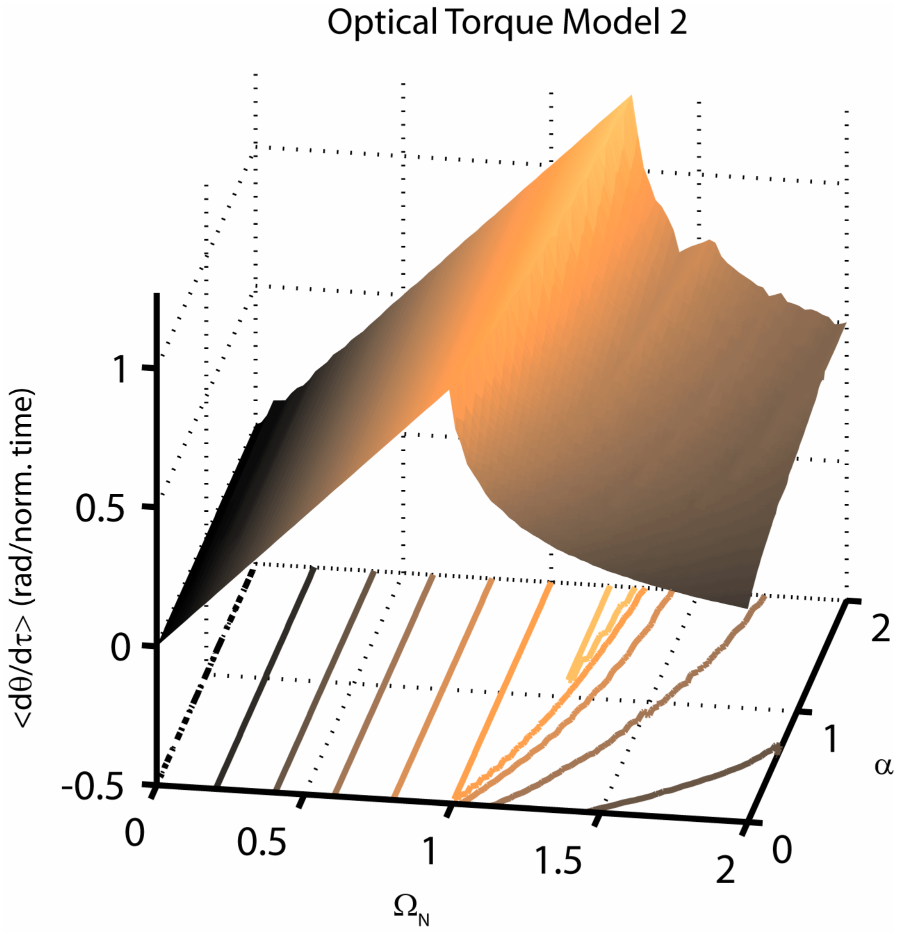

Figure 5.35 Average angular velocity surface for nonuniform oscillator with optical force applied off-center of an anisotropic magnetic particle (Same as Figure 5.34 but from a different viewpoint).

regime. For $\Omega_N > 1$ and weak optical torque strengths ($\alpha < 0.2$), it appears the rotation rate increases almost linearly with α. A number of intermediary plateaus also appear for slightly higher Ω_N. These correspond to the folds that appeared in the surface plot of Figure 5.35. It's not immediately clear what determines the length of these plateaus in α nor when to expect a plateau. Physically, it seems related to the fact that the optical torque is modulated by a sine function. Thus, no matter what the strength of the torque, it always approaches zero at two locations (for $\boldsymbol{m}$ having an angle $\theta = \pi/2$ and $\theta = 3\pi/2$). If a bifurcation exists near one of these phase points, an increase in the optical torque strength won't significantly change the dynamics since the optical torque at those phase points is still minimized. The lengths of the plateaus may not be easily predictable since

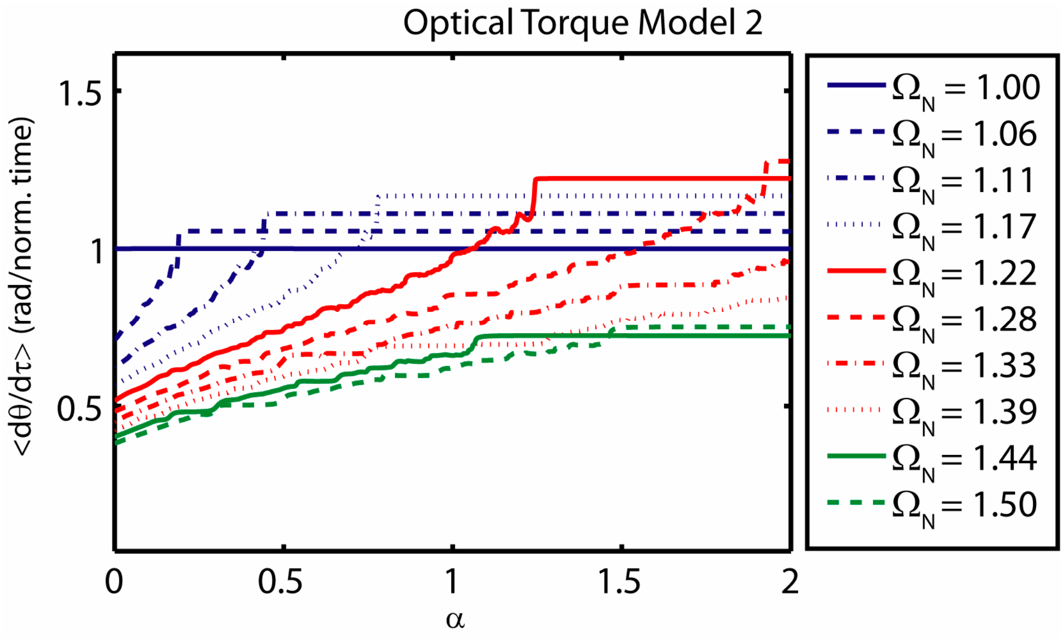

Figure 5.36 Vertical slices of the 3D surface plot of Figure 5.35.

the time between slipping events can be greatly affected by the presence of saddle-node ghosts and bifurcations.

Optical Force Applied Off-Center of a Symmetric Particle

In the final model, the optical torque is applied to a symmetric particle. The magnitude of the optical torque varies sinusoidally with the phase between the particle moment and the optical force vector. The average angular velocity surface plot is shown in Figure 5.37.

We see again the extension of the critical frequency well beyond that for the standard nonuniform oscillator. This time, since the optical torque is present and in the same direction, it always adds to the magnetic torque. At a specific Ω_N, the maximum average rotation rate is always Ω_N or less – the particle can never rotate faster than the magnetic field. Even if the optical torque is strong enough to cause the particle moment ***m*** to surpass the ***B*** field vector, the particle must always wait for the ***B*** field to catch up at $\theta = \pi/2$ and $\theta = 3\pi/2$.

Plotting vertical slices on a separate graph (see Figure 5.38), we can again see an approximately linear increase in $\langle d\theta/d\tau \rangle$ for small α (0 – 0.2). The rate of increase in

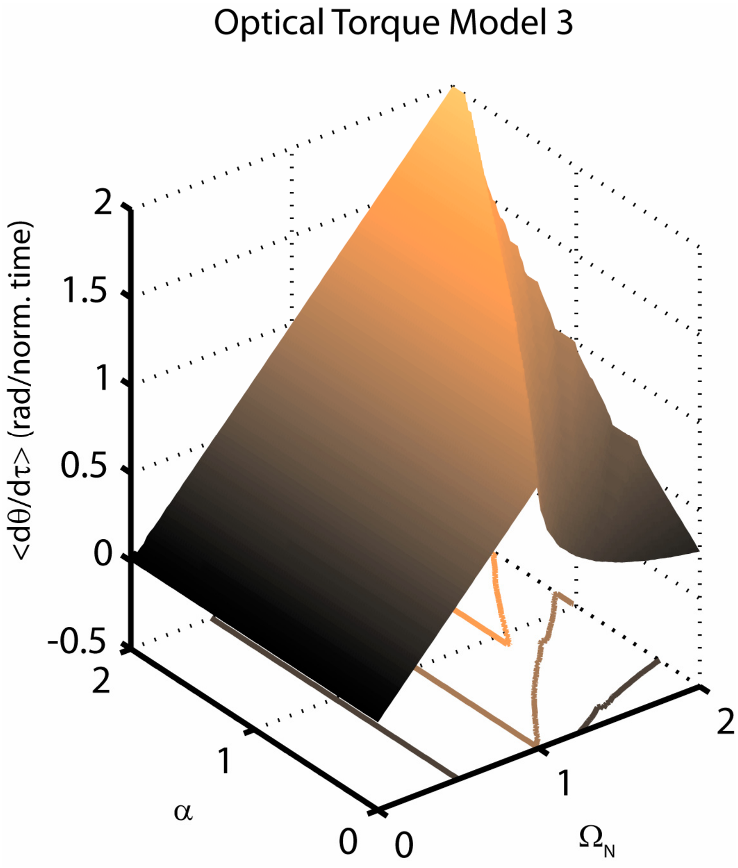

Figure 5.37 Average angular velocity surface for a nonuniform oscillator with optical force applied off-center of a symmetric magnetic particle.

$\langle d\theta / d\tau \rangle$ with α is greater than we saw for the previous model. Comparing this rate to experimentally acquired results may help determine the means of rotation in optically manipulated magnetic rotating systems. Again, we see folds in the surface at Ω_N larger than the new critical threshold.

5.6 Experimental Considerations

Our numerical analysis showed that the normalized nonuniform rotation rate $\langle d\theta / d\tau \rangle$ can be approximated as linearly increasing with the ratio of the applied optical torque to the magnetic torque, α, at least for very small ratios ($\alpha < 0.2$). Let us define the slope of this linear trend as:

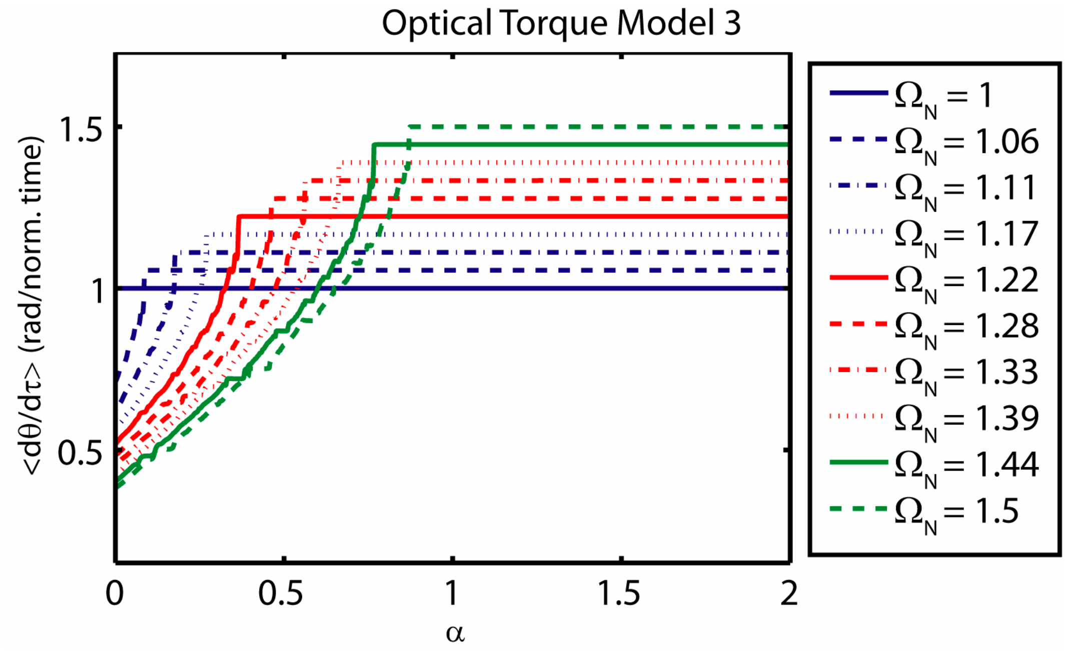

Figure 5.38 Vertical slices of the 3D surface plot of Figure 5.37.

$$m_S = \frac{\Delta\langle d\theta / d\tau\rangle}{\Delta\alpha} = \frac{\Delta\langle d\theta / dt\rangle\gamma}{\Delta(rF)} . \tag{5.23}$$

Each of the four models described, (1) no optical torque, (2) opposing torques on each side, (3) torque on one side, (4) same-direction torques on both sides - gives a different slope m_S. To determine if the slopes provided by our simulations are experimentally feasible, we must relate the parameters to measurable quantities. We can relate the optical torque strength to the applied laser power through [16, 20]:

$$rF = r\frac{n_m}{c}\sigma_{ext} I = r\frac{n_m}{c}\sigma_{ext}\frac{P}{A} \tag{5.24}$$

where n_m is the refractive index of the surrounding medium and I is the laser intensity at the sample plane equivalent to the power P per area A. Because our hybrid particles consist of highly scattering and absorptive material, we've assumed the dissipative component of the radiation force, or scattering force, is responsible for the induced rotation. This dissipative force depends on the extinction cross section of the sample, which can be estimated based on the relative size of the particle with respect to the laser wavelength. Nanoparticles, for example, are expected to have much less absorption, thus the extinction is dominated by the scattering cross-section. Rigorous Mie scattering theory must be used to calculate the cross-sections for particles approximately the same size as the laser wavelength. Much larger microspheres with full metal coatings could be treated in the geometrical optics regime using reflection and transmission coefficients. For hybrid particles consisting of both microscale dielectric spheres and nanoscale absorptive colloids, however, both absorption and scattering contribute and the best method of calculating the cross-section is unclear. There are several methods for estimating these cross sections. Svedberg and Käll [20] suggest that for large absorptive spherical particles, the extinction cross section can be approximated by a sum of absorption and scattering cross sections, defined as the following:

$$\sigma_{abs} = k_m \operatorname{Im}\{\alpha_0\}, \tag{5.25}$$

$$\sigma_{sca} = \frac{k_m^4}{6\pi}\left|\alpha_0\right|^2 . \tag{5.26}$$

where α_0 is the polarizability (not to be confused with our torque ratio α) and $k_m = 2\pi n_m / \lambda$ is the wavenumber of the light in the surrounding medium [16, 20]. The polarizability may also need to be adjusted for large particles [20]. In the Rayleigh regime, it is typically given as:

$$\alpha_0 = 4\pi r^3 (n^2 - 1)/(n^2 + 2) \tag{5.27}$$

where n is the complex, wavelength-dependent, relative refractive index $n = n_{sphere} / n_{medium}$. For hybrid particles comprised of aluminum-half-coated polystyrene, the refractive index of the sphere is standard. One might use an effective index of refraction that provides equivalent scattering properties. Literature on the subject typically deals with heterogeneous particles with sizes approximately equal to the illumination wavelength and inclusions that are more absorptive than the outer material of the particle [168].

Let us consider the optical properties of three cases: 215 nm aluminum nanopowders embedded in Teflon ($n_{\text{teflon}} = 1.3$, similar to $n_{\text{water}} = 1.33$) [169], bulk aluminum [170, 171], and a material with a complex index of refraction equal to the average of that for bulk aluminum and 1 μm polystyrene microspheres [172]. The absorption cross section of 215 nm aluminum nanopowders with thin outer aluminum oxide layers embedded in Teflon [169] was about 0.02 μm^2 at $\lambda = 1.053$ μm. Since much of the extinction

	Optical Property					
Sample	λ (nm)	n^2	α_0 ($\times 10^{-3} \mu m^3$)	α_{corr} ($\times 10^{-3} \mu m^3$)	Force (pN)	Torque ($\mu m \cdot pN$)
Al [170]	775	$-67.0+45.1i$	$0.858+0.0386i$	$0.107+0.0048i$	1.60	2.00
Al [171]	800	$-45.7+28.1i$	$0.111+0.00716i$	$0.118+0.0092i$	2.06	2.57
Polystyrene [172]	775	$2.49+0.00158i$	$0.00556+0.000022i$	$0.00557+0.000025i$	0.0058	0.0072
Ave. Al [170] & PS [172]	775	$-14.1+18.1i$	$0.115+0.0273i$	$0.122+0.032i$	6.98	8.73

Table 5.1 Optical properties of several hybrid particle constituents and the associated optical force and torque on a particle immersed in a 90% w/w glycerol-water mixture due to a 5 *mW* laser beam focused to a beamwaist of 0.5 μm. The polarizability α_0 is calculated for a 40 μm diameter colloidal sphere while the force and torque are calculated using the corrected polarizability α for a hexagonal close-packed layer of such colloids over the cross-sectional area of the beam. The colloids were either bulk aluminum, polystyrene, or a material with a complex index of refraction equal to the average of bulk aluminum and polystyrene.

dependence of these particles in the visible and near infrared is due to absorption [169], we can estimate the force applied to a layer of such particles in the beam focus using Eqs. (5.24) and (5.25) to get 12.1 *pN*. The corresponding torque was calculated assuming that all of the force of the beam is applied at a distance half the radius from the center of the particle. As a result, we get an expected torque range of up to 15 $\mu m \cdot pN$.

Other estimations of the force and torque can be carried out for particles with a non-negligible scattering cross section. A table summarizing some of the optical properties and associated optical force and torque at near infrared wavelengths, which are typically used in optical tweezers) is shown in Table 5.1. To perform the calculations for bulk aluminum, Eqs. (5.24) through (5.27) were used. We modeled a hybrid particle or a partially coated microsphere as a 5.0 μm diameter polystyrene sphere coated by a shell of colloids of 40 *nm* diameter in a 90% w/w glycerol-water mixture. The refractive index of this medium is taken as the weighted average of its constituents: $n_m = 0.9 n_{gly} + 0.1 n_{H_2O} = 0.9 \cdot 1.47 + 0.1 \cdot 1.33 = 1.46$. Eq. (5.27) is valid only when the skin depth of the scattering material is much larger than the particle size [16]. Svedberg and Käll [20] suggest a correction introduced by Meier and Wokaun [173] given as:

$$\alpha_{corr} = \frac{\alpha_0}{1 - \frac{2}{3} i k^3 \frac{\alpha_0}{4\pi} - \frac{1}{a} k^2 \frac{\alpha_0}{4\pi}}. \tag{5.28}$$

We assume the k in Eq. (5.28) is the same wavenumber in the medium k_m and a is the particle radius. The second term of the denominator accounts for dipole damping by radiative losses in large particles resulting in a decreased magnitude in enhancement that can occur with smaller particles. The third term comes from dynamic depolarization of the radiation across the finite particle surface which causes a red shift in the plasmon resonance for larger particles. This correction is valid up to particles sizes in which quadrupole resonance effects become important.

To estimate the force, we assumed a power of 5 mW at the sample plane focused to a beamwaist of 0.5 μm. Since the beamwaist was smaller than the diameter of the polystyrene matrix, only colloids on the surface within the cross sectional area of the beam contributed. We modeled the coating as a single hexagonal close-packed layer of colloids, thus about 90% of the surface area of the beam is occluded by a colloidal particle. The approximate magnitudes of the calculated forces shown in Table 5.1 are reasonable. They are about an order of magnitude smaller than our result for aluminum nanopowders, but still in the same ballpark.

From preliminary experimental results, it is known that the rotation rate of a 5.0 μm diameter sphere in a 90% w/w glycerol-water mixture driven by an external magnet of ~10 Oed at 1.57 *rad*/*s* is about 0.23 *rad*/*s* in the absence of an optical torque. For $\alpha = 0$, Eq. (5.7) can be rearranged to give:

$$\Omega_C = \sqrt{\dot{\theta}(2\Omega - \dot{\theta})}\,. \tag{5.29}$$

This gives a critical frequency of 0.82 *rad*/*s* thus, $d\theta / d\tau = 0.28\,rad$ and $\Omega_N = 1.9$. From the graphs shown in Figure 5.39, this value of Ω_N corresponds to a slope m_s of about 0.35 and 0.75 for the third and fourth models of optical torque, respectively.

The last piece of information needed is the rotational drag coefficient γ_rot. For a 90% *w*/*w* glycerol-water mixture at 20°C, the kinematic viscosity ν = 186 *cS* [174] and mixture density ρ = 1.24 gm/cm^3. For a sphere, the well-known Stokes drag,

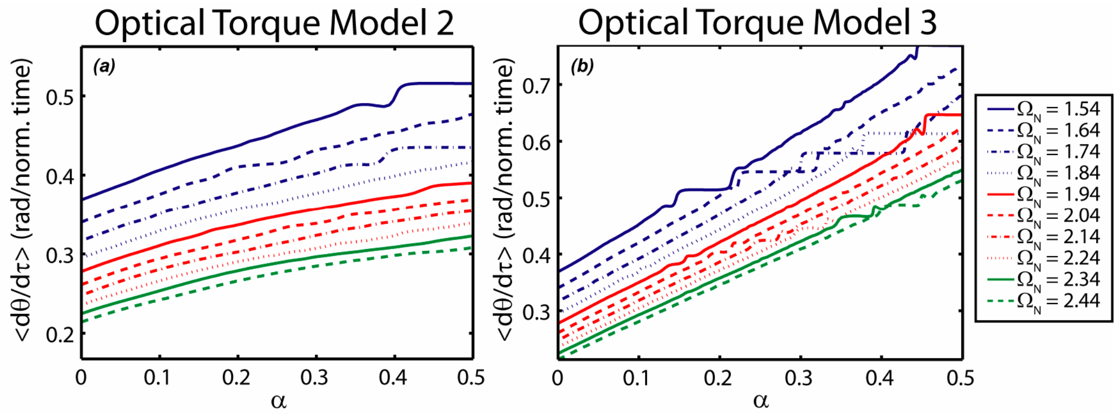

Figure 5.39 Vertical slices of the 3D surface plot for (a) model 3 and (b) model 4 for optical torque at values of Ω_N ranging from ~1.5 – 2.5.

$$\gamma_{rot} = 8\pi a^3 \nu\rho\,, \tag{5.30}$$

gives 90.3 *μm·pN·s*. Returning to Eq. (5.23) with our typical experimental values, we can expect application of the optical torque to result in a faster rotation rate of 0.29 rad/s and 0.36 rad/s for model 3 and model 4, respectively. These are increases of 26% and 57% over our original rotation rate of 0.23 *rad/s*, a feasible experimental measurement.

Numerous uncertainties could arise in estimating experimental parameters such as the true index of refraction of the particle, the actual relationship of scattering force to the extinction cross section, and the approximate viscosity of the glycerol mixture. All of these factors may contribute to error between our simulated results and actual experimental measurements.

Approximated Effect of Translational Drag and Rotational Drag

We estimate the effect of the force on our particle in inducing both translational and rotational motion in the absence of the magnetic torque. Since the beamwaist is smaller than a single particle diameter, we consider the force and torque on a single sphere. Calculations will provide a maximum estimate. For a sphere of radius $r = 2.5$ *μm* immersed in a 90% *w/w* glycerol-water mixture at 20°C with kinematic viscosity $\nu = 186$ *cS* and mixture density $\rho = 1.24$ gm/cm^3, the translational and rotational drag coefficients are given by the following:

$$\gamma_{trans} = 6\pi a \nu\rho\,, \tag{5.31}$$

$$\gamma_{rot} = 8\pi a^3 \nu \rho \,. \tag{5.32}$$

Neglecting inertia and in the absence of magnetic torque, the optical force and torque are in equilibrium with drag and we get:

$$\dot{x} = \frac{F}{\gamma_{trans}} \tag{5.33}$$

and

$$\dot{\theta} = \frac{rF}{\gamma_{rot}}, \tag{5.34}$$

where $\dot{x}$ and $\dot{\theta}$ are the translational velocity and angular velocity, respectively. The force F previously calculated was up to 12.1 *pN* (for aluminum nanopowders). For such a force, the translational and angular velocity of a sphere can be calculated as $\dot{x}$ = 1.12 *μm/s* and $\dot{\theta}$ = 0.168 *rad/s*. For $\Omega_N = 1.9$, the average time for one full rotation due to magnetic torque is 27 *s*. During this amount of time, in the absence of the magnetic torque, we would expect the particle to translate up to 30 *μm* and/or rotate up to 0.72 *rotations*. This translation and rotation are relatively large, suggesting the optical force, even at a magnitude ratio of $\alpha = 0.2$, can provide a noticeable perturbation. Such a large translation, however, sets a practical limit to the force we can apply while maintaining the particle close to the laser focus.

Approximated Effect of Translational and Rotational Brownian Motion

Again, we use the time for one full rotation ($t = 2\pi / \dot{\theta}$) to measure the effect of Brownian motion on the rotational and translational motion of our particles. Utilizing Einstein's diffusion, we estimate the root-mean-square displacement x_{rms} and angular displacement θ_{rms} by the following:

$$x_{rms} = \sqrt{2D_{trans}t} = \sqrt{\frac{2k_BT}{\gamma_{trans}\dot{\theta}}} = \sqrt{\frac{k_BT}{3\pi a\,\nu\rho\dot{\theta}}} \tag{5.35}$$

$$\theta_{rms} = \sqrt{2D_{rot}t} = \sqrt{\frac{2k_BT}{\gamma_{rot}\dot{\theta}}} = \sqrt{\frac{k_BT}{4\pi a^3\nu\rho\dot{\theta}}}\,. \tag{5.36}$$

Using the same parameters as given previously, we get $x_{rms} = 0.057$ *μm* and $\theta_{rms} = 0.20$ *rad* (3.1 × 10^{-3} *rotations*) in the time for one full rotation (27.0 *s*). Thus, the expected diffusion in position and orientation if no external optical or magnetic fields were present are much smaller than the effect due to the optical force/torque alone, as well as the combined optical and magnetic forces and torques.

5.7 Conclusions

The effect of simultaneous optical and magnetic manipulation of a rotating magnetic particle has been investigated for the case of a microsphere system larger in diameter than the laser focus. The optical torque provides a perturbation to the standard nonuniform oscillator that acts to introduce a time-dependent amplitude and phase into the phase space trajectory of the induced lag. Other effects include potential control of the frequency of slipping events in the nonlinear regime as well as the possibility of laser-induced "phase-following."

The combined manipulation scheme allows for the study of frictional properties inherent in the system. For example, the presence of a significant fluid viscosity enables observation of the transition from the linear regime to the nonlinear regime at easily manageable frequencies in practice. Systems in which the surrounding fluid is air do not show these transitions [175]. In addition, optical torques that oppose the applied magnetic torque may model systems with frictional components that vary in time, for example, the rotation of anisotropic microparticles near frictional surfaces. Even at optical torques near 20% the strength of magnetic torques, differences in the dynamic motion due to the combined manipulation scheme are expected to be measurable and distinguishable from effects due to Brownian motion or purely optical or purely magnetic torques alone.

CHAPTER 6

EXPERIMENTAL OBSERVATION OF OPTICALLY AND MAGNETICALLY MANIPULATED HYBRID MICROSPHERES

Simulations of the motion of nonuniform oscillators manipulated by optical and magnetic fields offer rich dynamics and valuable insight into the interplay between two distinctly different types of torques. In practice, however, such ideal systems rarely exist and there are often many aspects that can complicate observation of the desired effect. For example, the magnetic particles were modeled as perfect spheres; however, our hybrid particle systems typically have an outer shell of magnetic material that can alter the rotational drag by reducing sphericity as well as providing increased roughness. The particles were also modeled as perfectly absorbing cross-sectional areas that experience an optical torque that is sinusoidally dependent on the rotation angle. Actual particles tend to absorb and scatter at all angles and are likely subject to a more complex torque-angle dependence. Somewhat less crucial is the particle to particle uniformity. Even batches of commercially-made magnetic microspheres can have large variations in their magnetophoretic mobility [176]. These variations require the use of ensemble averaging to determine properties representative of the particle distribution. Otherwise, experiments performed on individual microspheres must involve adequate calibration methods to enable comparison of results from experiment to experiment.

More complications can arise from the finite size of the sample solution. Inter-particle interactions, even at far distances, can drastically affect the motional behavior of magnetic microspheres, thus requiring the use of very dilute concentrations to prevent particles from aggregating. This procedure can reduce the availability of samples that have an inherently low yield in the fabrication process or require two separate particles to be bound together, such as experiments on dimers or trimers of microspheres [177] or measurements involving particle binding [54, 66]. The use of high numerical aperture objectives with very short working distances can restrict the observation of samples to be in close proximity to the bottom glass interface where the viscosity (Eq. 4.3) and frictional or adhesive interactions may be increased. Although exchanging the surrounding media with more viscous fluids can slow down potentially detrimental effects like sedimentation, flotation or translation due to magnetic gradients, such measures also reduce the time scale of the motional dynamics of interest. Motional drift due to Brownian diffusion, although not crucial over relatively short time scales, can limit the maximum duration of an experiment and render instrumentation automation unfeasible, especially if the particle diffuses out of the field of view before adequate data has been recorded.

Even if one can establish adequate experimental conditions using only magnetic manipulation, the introduction of laser illumination hosts its own difficulties. The laser beam intensity does not typically have a uniform cross-section, as modeled in our simulations, but, rather, a Gaussian or similar profile. Other forms of optical torque such as that due to gradient force alignment may be present in non-negligible amounts. Furthermore, optical absorption of magnetic particles can reduce the magnetization of materials with low Curie temperatures or change the fluid viscosity if significant heating occurs.

In the previous chapter, numerical simulations suggested a linear increase in the average asynchronous rotation rate with low applied laser power due to an increase in the scattering force. Experimentally, a linear increase was also observed with laser power, but further studies revealed that the scattering force was not primarily responsible for the the observation. Heating of the solution to induce changes in the fluid viscosity and magnetic moments was another possible contribution. In this chapter, I describe my experimental methods to observe these effects of optical manipulation of magnetically rotated microsphere dimers. I address many of the issues mentioned above, paying particular attention to the consequences arising from the absorptive nature of our hybrid microsphere systems.

6.1 Experimental Procedures

The experimental procedures used here for combined optical and magnetic manipulation of hybrid microparticles were very similar to those already described in great detail in Chapter 4. Only key differences are explained here.

In this study, only nominally 4.8 and 9 μm diameter carboxylated magnetic polystyrene microspheres were used. The random distribution of magnetic colloids on the spherical surface often caused unpredictable intensity fluctuations, often at unexpected rotation frequencies different from both the external magnetic field rotation and the low frequency nonuniform oscillation. For this reason and to establish more material anisotropy, some batches of single particles were half-coated with aluminum, and only dimers of microspheres, half-coated (HC) or uncoated (UC), or single HC-microspheres with significant protrusions were analyzed. A similar half-coating procedure as described in Chapter 3 was performed using a custom-built vacuum deposition system. Approximately 50 nm coatings were applied These HC-microspheres were then magnetized in a 1.4 kG field.

1:100 aqueous dilutions of stock solutions or similar concentrations of HC-microspheres were further diluted in 1:10 aqueous sodium dodecyl sulfate (SDS) and glycerol. The final concentration of SDS was less than 1% of the total volume of the solution including the glycerol, thus its density was approximated to be the same as water in later calculations. The final concentration of glycerol was chosen so that the microspheres would be close to neutrally buoyant to minimize sedimentation or flotation. The solution must also be viscous enough that the critical frequency could be observed with the magnetic field strengths available. In addition, the glycerol provided a closer match to the index of refraction of polystyrene, thus reducing the gradient force and preventing optical tweezing effects.

To determine the glycerol/water mixture that would approximately match the density of our microspheres, we neglected the magnetic material, assuming its total volume is much smaller than that of the polystyrene. A simple approximation assuming no interaction between solvent molecules is to use the nominal density values of glycerol (ρ_G) and water (ρ_W) weighted by their percentage:

$$\rho_{PS} = x\rho_G + (1-x)\rho_W \tag{6.1}$$

where x is the volume fraction of glycerol/solution and ρ_{PS} is the density of the polystyrene. For $\rho_{\mathrm{PS}} = 1.05$ g/cm^3, $\rho_{\mathrm{G}} = 1.263$ g/cm^3, $\rho_{\mathrm{W}} = 0.9982$ g/cm^3 all at 20°C, we get $x = 19.6\%$ glycerol/solution v/v. Estimating the particle and SDS solutions to have the same density as water, this is equivalent to 23.2% mass fraction glycerol/solution. This percentage only provided an estimate of the best solution concentration since the presence of a magnetic gradient introduced an additional force. Furthermore, the distribution of colloidal loading per microsphere was wide enough that many microspheres would sink, others would float, while others remained near the center of the sample chamber, all in the same glycerol solution. For our system, we found that a 76% mass fraction glycerol/solution was adequate for the 4.8 *μm* microspheres and between 40-50% mass fraction glycerol/solution for the 9 *μm* microspheres. Only microspheres that did not stick to the glass surface or translate significantly due to rolling along the glass interface without laser illumination were measured.

To form dimers, both UC- and HC- microsphere glycerol solutions were placed in a magnetic separator for about 15 minutes to allow the microspheres to coalesce in a weak magnetic field. The solutions were then vortexed at 2000 *rpm* for 15 *sec*. As for our rolling microsphere samples, the solution was then inserted into a sample chamber consisted of two blank, untreated, cover slips. About 15%-25% of the particles observed under the microscope were initially dimers, the remaining majority were single microspheres and occasional aggregates of 3 or more.

Laser powers in the range of 0-15 mW were coupled to our 100X oil immersion objective, however, measurements using more than 5 mW typically resulted in significant translation of the microsphere, mostly upwards in the *z*-direction along the beam axis. In such cases, the microspheres were allowed to sediment to the original height above the bottom glass interface before the next measurement was performed. Magnetic field strengths at the sample plane ranged from 5-10 *Oe*.

Similar image analysis techniques were used as for our rolling experiments (Chapter 4). Instead of tracking the position of our microspheres, we used the Metamorph imaging software package to record intensity fluctuations as a function of time. Acquired movie files were intensity thresholded such that only reflection signals coming from the microspheres were used to calculate the average intensity of each frame, thus minimizing errors due to background signals. On some occasions, when the overall intensity changed significantly due to translation in the z-direction, the %-area of the thresholded region compared to the full frame area was used to represent the oscillating signal.

6.2 Data Analysis

For each magnetic particle explored, a series of intensity fluctuation or %-threshold time-traces were acquired. Examples of such raw data are shown in Figure 6.1. Curves (a), (c), (e), (g), and (i) were acquired with no laser illumination present. Curves (b), (d), (f), (h), and (j) were acquired with laser illumination present in with powers of 4.38 mW, 45.8 mW, 8.05 mW, 10.0 mW, and 12.0 mW, respectively. Upon first glance, the data

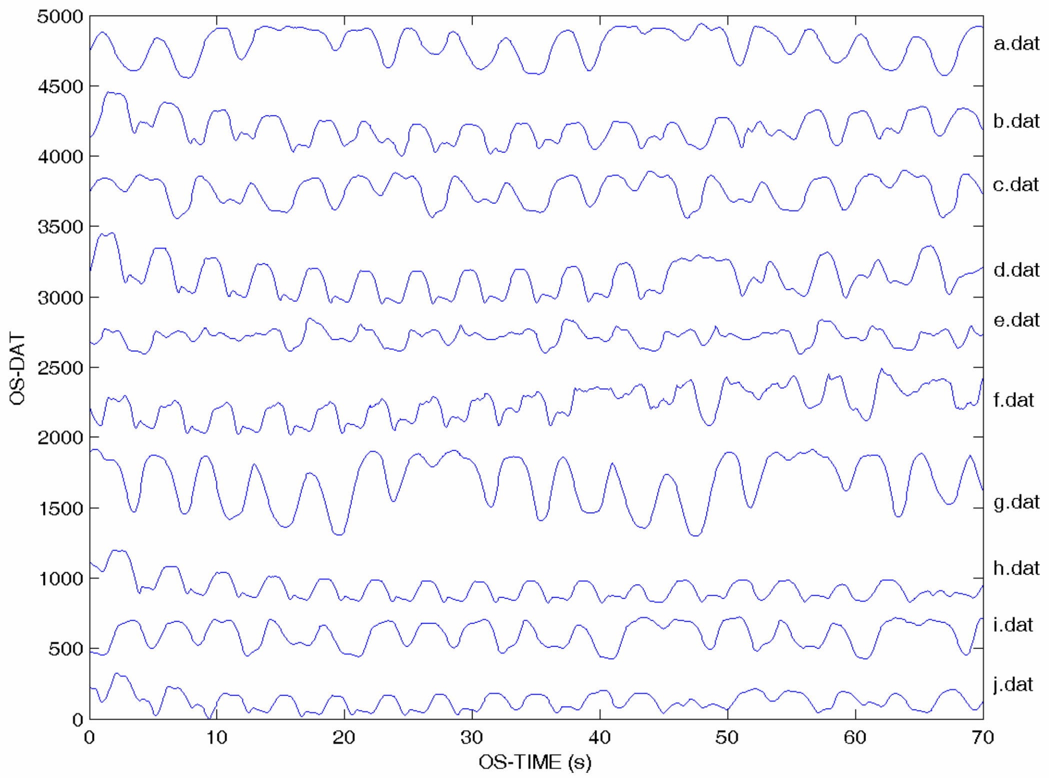

Figure 6.1 Examples of intensity fluctuation time-traces for a rotating magnetic microsphere. Curves (a), (c), (e), (g), and (i) were acquired with no laser illumination present. Curves (b), (d), (f), (h), and (j) were acquired with laser illumination present with powers of 4.38 mW, 5.8 mW, 8.05 mW, 10.0 mW, and 12.0 mW, respectively.

don’t seem to be significantly different curve to curve. But closer inspection reveals several key differences:

When no laser is applied, the curve tends to show a low frequency oscillation (~30 sec period) superimposed on a high frequency oscillation (~4 sec), e.g. see (a) and (g). These are the particle rotation period and external magnetic rotation period, respectively. Curves like (c), (e), and (i) show similar characteristics but are less recognizable.

When the laser is applied, the data curves typically show an initial gradual sloping mean, indicating the particle is drifting away from the imaging plane and moving out of focus., e.g. see (b), (d), (h). Because the particle center is not fixed, the laser beam also imparts a translational force causing the particle to gradually move away from the trap center.

Evidence indicating that the particle rotation is affected by the beam is shown by the fact that many of the data curves with the laser on show high frequency oscillations in phase with the external rotation rate for about the first 40 sec, after which the particle experiences slipping, e.g. (d) and (f).

Curves (a) and (g) are very similar despite (g) occurring after several applied laser treatments. This suggests that the laser powers used in this experiment did not alter the particles significantly. Data curves representing no laser illumination that are qualitatively different suggest that the intensity-time series crucially depends on reproducibility of the starting position of the dimer in the laser focus as well as similarity of the translational trajectory.

Each recorded intensity time trace was analyzed using Fourier transform filtration techniques implemented in MATLAB to obtain the average rotation rate. The raw data was first re-interpolated so that data points were evenly spaced in time. After this, a series of procedures are conducted on the dataset either in the time domain or the frequency domain. An example of time domain data for an asynchronously rotating particle and the corresponding frequency domain transform are shown for each step in Figure 6.2 and Figure 6.3, respectively. The data represents a particle rotated at an external frequency of 0.25 *Hz*. The interpolated data was then cropped to remove unnecessary signals. If a dataset contained gradual sloping overall intensity values due to

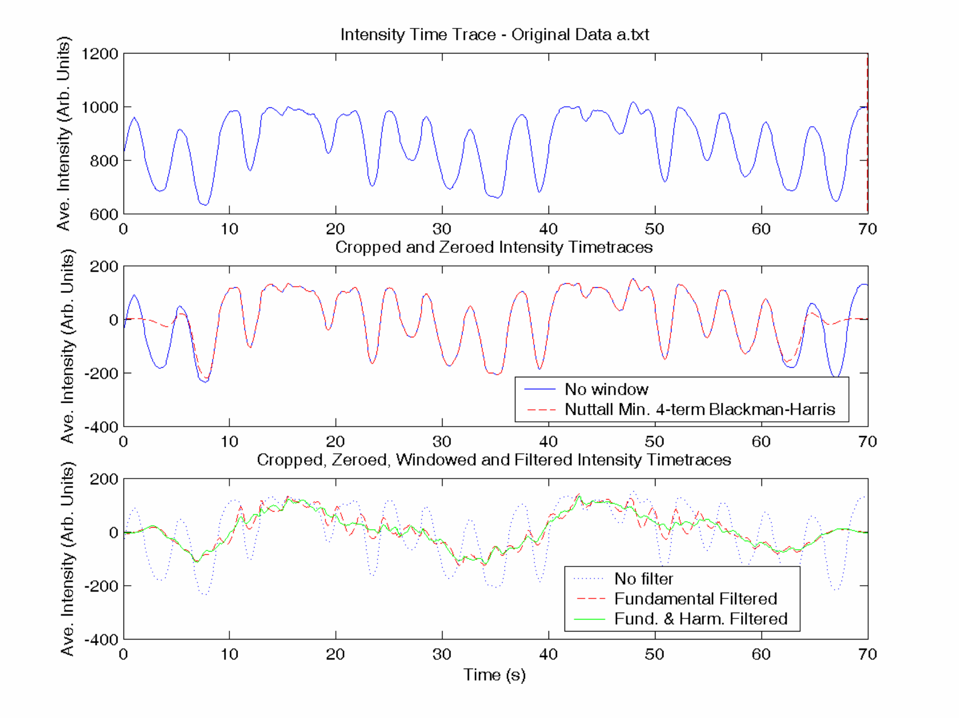

Figure 6.2 Example of original time-domain data and smoothed version.

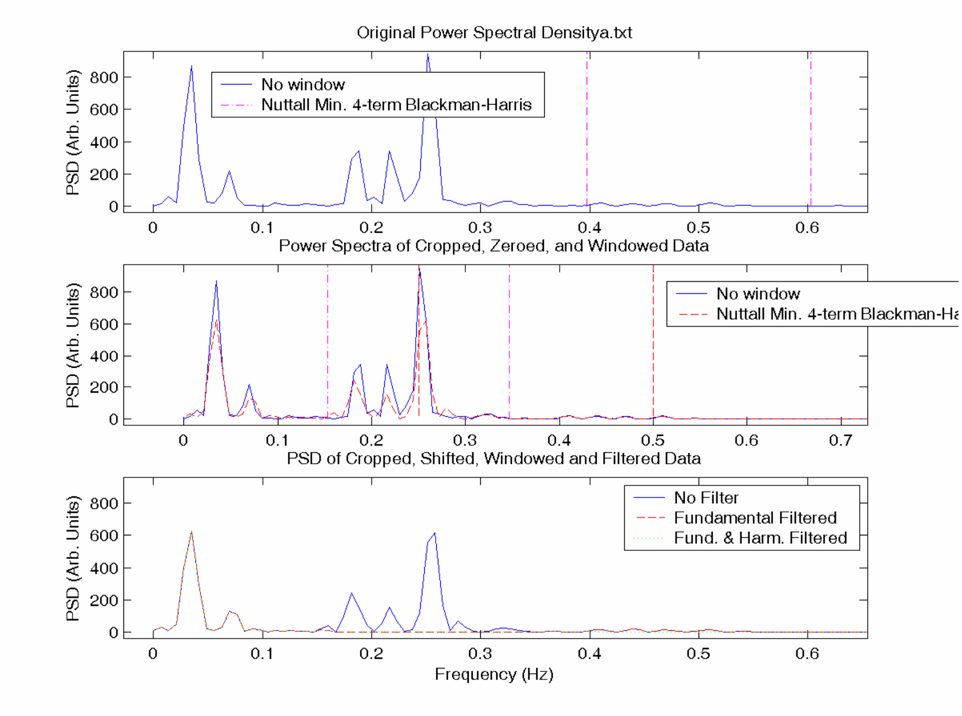

Figure 6.3 PSD's corresponding to data in Figure 6.2.

translation in the *z*-direction during the time of acquisition, the data was fit to a polynomial of up to 2nd order. The polynomial was then subtracted from the data to flatten it and shifted by the average intensity so that it hovered around y = 0. This minimized the DC value in the Fourier transform. A window function is then applied to the ends of the data to prevent aliasing that can occur due to Fourier transforming sharp edges. A 4-term Blackman-Harris window was used for most of the data in this work; however, many other standard windowing functions were adequate.

Each discrete time series was Fourier transformed and the one-sided power spectral density (PSD) calculated [92]. The corresponding PSDs are shown in Figure 6.3. The PSD was normalized using Parseval's Theorem [92] such that integration over all frequencies (0 and positive) of the PSD was equal to the mean square amplitude of the time series integrated over the entire measurement time for one dataset. Thus, the PSD at frequency f was an estimate of the probability that the original time series contained frequency components between f and $f + \Delta f$. Peaks at the average rotation rate of the particle, as well as one at the rotation rate of the external magnetic field, were expected. The PSD clearly reveals a peak at 0.25 *Hz*, indicating the external magnetic rotation rate. The large peak at 0.035 *Hz* indicates the average rotation rate, a frequency which corresponds to the time between the longer repetitive features in Figure 6.2. Smaller peaks also appear which can be attributed to mixing between the average rotation rate and the external rotation frequency. This external magnetic rotation rate was filtered by applying a modified rectangular function with Gaussian edges in the frequency domain, again to prevent aliasing. This essentially multiplied any frequency component occurring within the filter band by zero. The new filtered PSD is shown in the bottom graph of Figure 6.3. Dimers of microspheres were expected to have signals at the second harmonic of the external rotation rate, thus the PSD in which the second harmonic of the external rotation rate was also filtered is also plotted. This particular sample was a single microsphere with an aluminum coating, thus a second harmonic signal, if any, is very weak and the PSDs almost overlap exactly. Finally, a smoothed version of the original time series can be generated by inverse-transforming our filtered data back to the time domain. From this smoothed data, the average rotation frequency can be calculated consistently for each measurement. The corresponding smoothed time series are shown at the bottom of Figure 6.2

The filtered PSD can also be inverse transformed to calculate the autocorrelation of the smoothed data, as stated by the Wiener-Khinchin theorem [92]. The autocorrelation of each of the three time domain curves at the bottom of Figure 6.2 is shown in Figure 6.4. All three give a peak at ~27.5 *sec*, which corresponds to the average rotation rate of the particle. When this analysis procedure is conducted on a data for a particle that is synchronously rotating with the magnetic field, no secondary peaks occur in the smoothed autocorrelation since the fast magnetic rotation frequencies are filtered. Examples of such autocorrelations are shown in Figure 6.5.

The laser powers applied to the particle represented in Figure 6.1 appeared to be high enough to induce only synchronous rotation. Lower laser power can maintain the particle rotation in the nonlinear regime, but at a faster average rotation rate. Figure 6.6 shows the intensity fluctuation time traces at lower powers. The data were acquired after waiting approximately 1 second after shuttering the laser on to remove any initial slope due to translation that might have occurred. The filtered versions of the data are also shown in Figure 6.7. The first four curves (a-d) reveal the slower nonlinear rotation time of the particle gradually decreasing. The effect of the laser was to aid the particle in overcoming the drag that would normally cause it to slip in the absence of the laser beam. We can verify this with the filtered autocorrelation curves shown in Figure 6.8. The peak at the shortest delay time seems to decrease with increasing laser power. At higher powers (e-g) the particle translates away from the focus faster than enough particle rotation oscillations can be recorded.

It should be noted that with true experimental data, neither the time domain signals nor the frequency domain power spectra alone are sufficient to adequately determine the correct average rotation rate of the particle. Although these analysis procedures provide a means of consistently measuring rotation frequencies with few opportunities open to human bias, information from both domains should be compared with recorded image movies when possible. This ensures the measurements acquired agree with what is observed under the microscope. This method of analysis of nonuniformly rotating

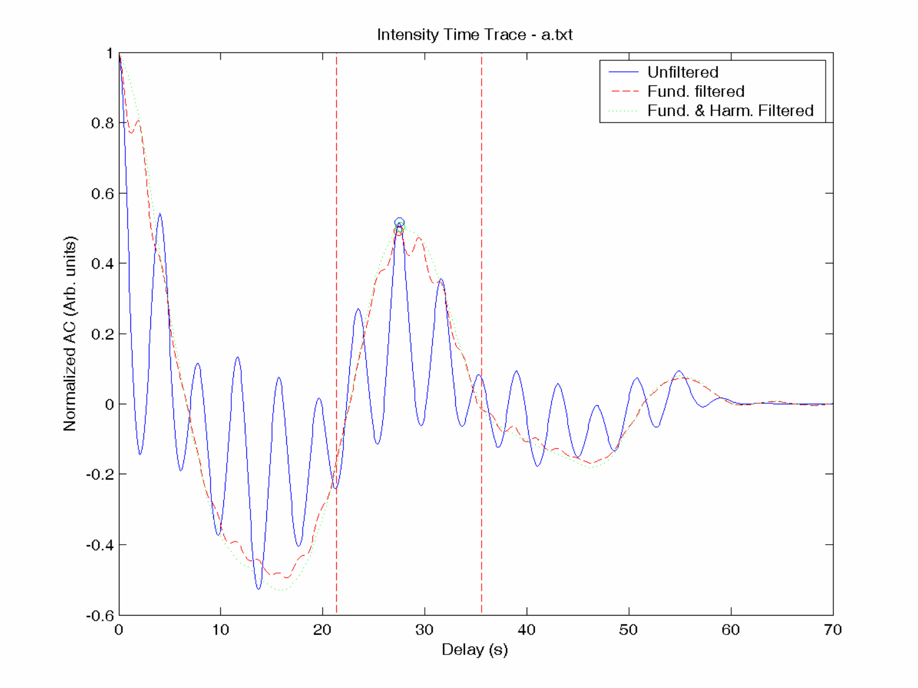

Figure 6.4 Autocorrelation of the unfiltered and filtered time-domain data appearing in Figure 6.2. The curves represent typical autocorrelations for an asynchronously rotating particle.

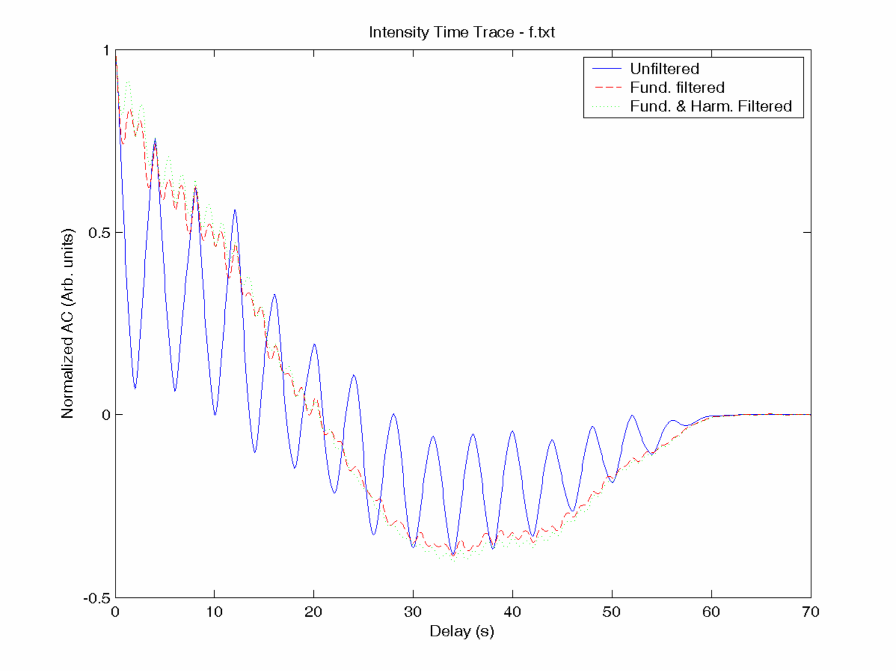

Figure 6.5 Autocorrelation of the unfiltered and filtered data for a synchronously rotating particle.

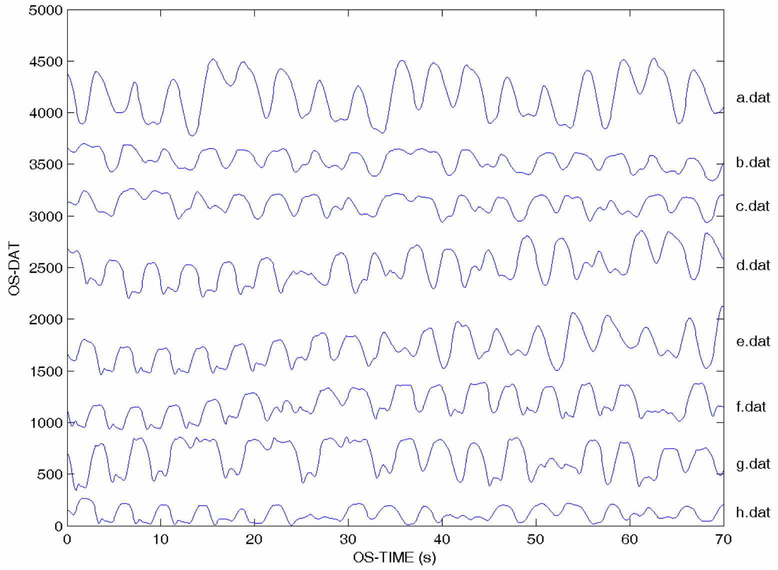

Figure 6.6 Intensity fluctuation time-traces for a rotating magnetic microsphere. Curves (a) – (h) were acquired with laser illumination with powers of 0 *mW*, 0.715 *mW*, 1.43 *mW*, 4.36 *mW*, 5.97 *mW*, 8.02 *mW*, 10.0 *mW*, and 12.0 *mW*,respectively.

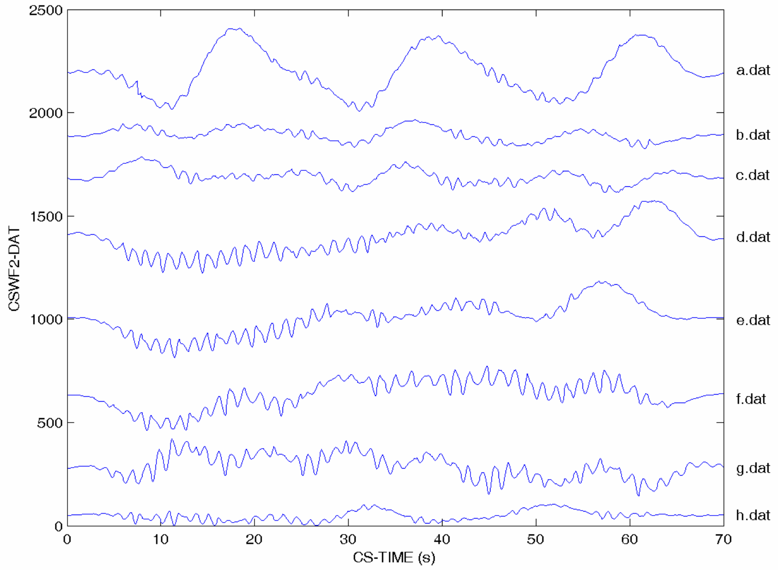

Figure 6.7 Smoothed versions of the data curves in Figure 6.6. Raw data was filtered to reduce frequency components at the external magnetic rotation rate and its second harmonic.

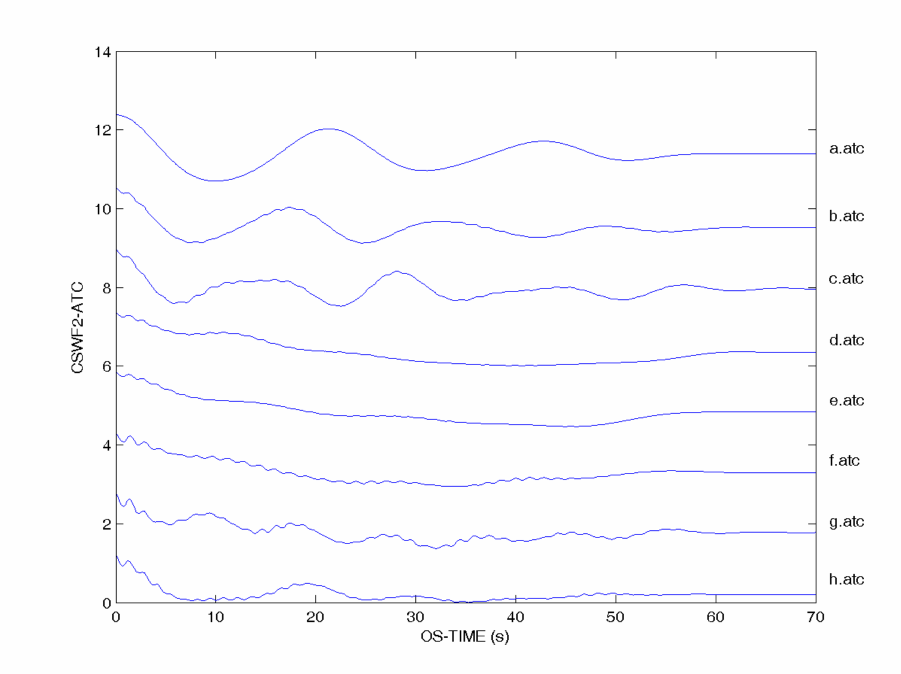

Figure 6.8 Autocorrelations of filtered data shown in Figure 6.7.

magnetic microspheres has already been applied to several applications including particle detection, bacteria detection and bacterial growth [54, 66].

6.3 Results

6.3.1 Magnetic Rotation

Before applying optical illumination to our particles, samples were first manipulated using only magnetic rotation. This enabled calculation of the critical frequency and allowed observation of sedimentation or flotation behavior. Slight deviations in the average rotation rate for a standard nonuniform oscillator described by (Eq. 5.8) were observed for microsphere dimers that were in close proximity to a glass interface. Analysis of these results is provided here. In addition, many dimers appeared to rotate with some precession at asynchronous rotation rates. This behavior is suggestive of 3-D rotational motion which is covered in more detail in Chapter 7.

Figure 6.9 and Figure 6.10 show the average rotation rate vs. external magnetic rotation rate for two different but nominally equivalent uncoated dimers, both in a 50% mass fraction glycerol/water solution with a magnetic field strength of 5 *Oe*. The data are

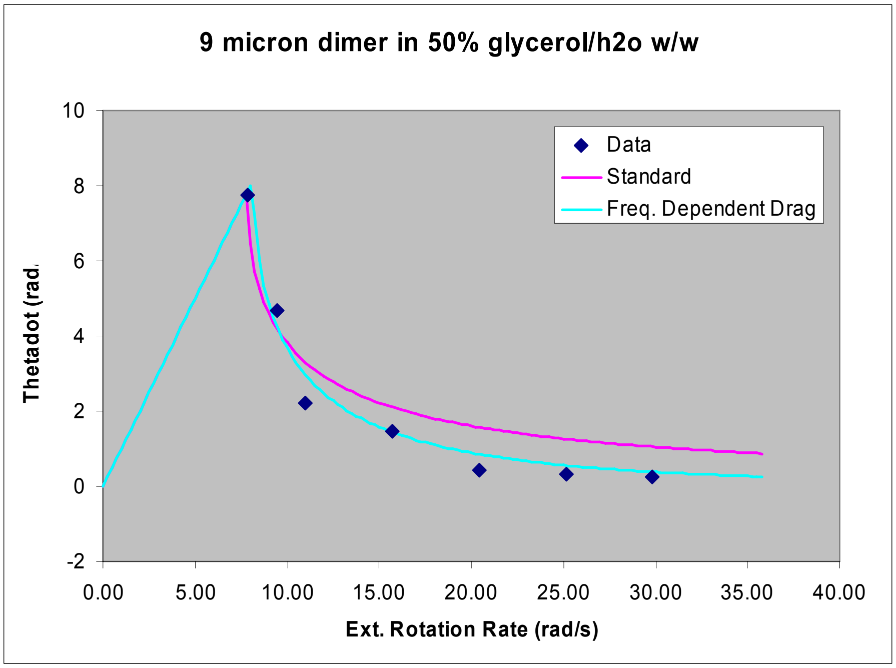

Figure 6.9 Average rotation rate for a 9 *μm* diameter microspheres nonuniformly rotating about 17 *μm* from a glass interface.

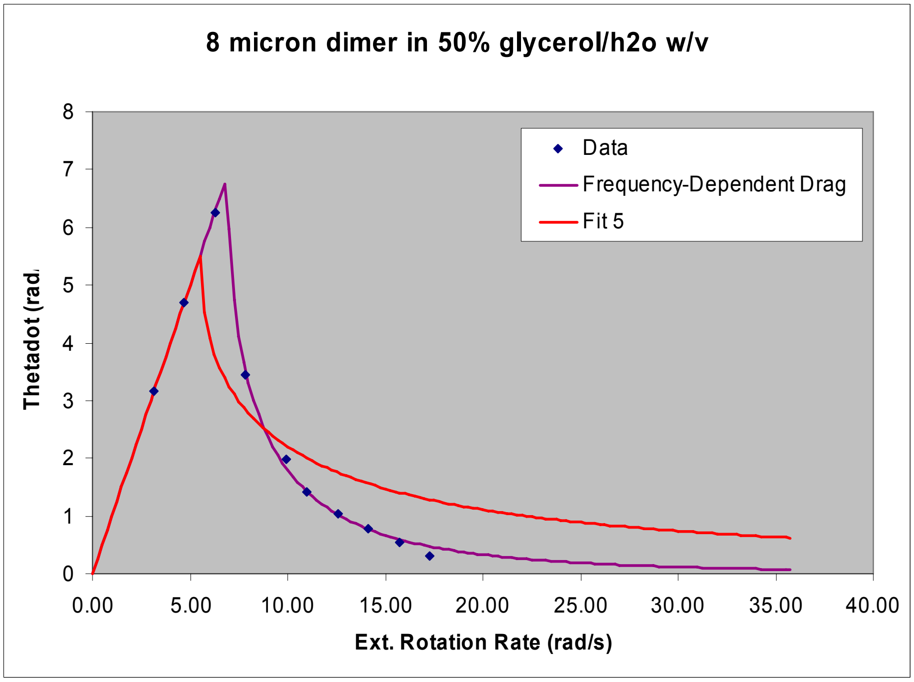

Figure 6.10 Average rotation rate for a 9 *μm* diameter microspheres nonuniformly rotating about 25 *μm* from a glass interface.

linear least-squares fit to our standard one-parameter nonuniform oscillator solution. In both cases, it appears this standard single-parameter (Ω_C) equation does not adequately describe our experimental results. In both cases, the presence of the glass interface increased the local viscosity of the fluid. This was verified by observing the height of the microsphere above the glass surface. By focusing on the dimer equator when the microsphere was oriented such that the dimer axis was parallel to the sample plane, a consistent measuring geometry was established. The equator of the dimer in Figure 6.9 was about 17 μm from the surface while the dimer in Figure 6.10 was about 25 μm from the surface. In the first case, when the dimer was vertically oriented, the smallest sphere-center-to-plane distance was 13.5 μm while the largest was 21.5 μm. Assuming the motion for a single microsphere was translational, based on Eq 4.3), the correction factors to the translational drag coeffiecient range from 1.1 – 1.2. The corrections are even smaller for the second case. Nevertheless, the data indicate there was some effect on the drag coefficient that slightly changes the motional behavior for asynchronous rotation. For simplicity, we assume that this effect on drag increases linearly with rotation rate. We can define a frequency-dependent adjustment to the rotational friction coefficient γ_{rot}:

$$\gamma_{adj}(\Omega) = [a\Omega + b]\gamma_{rot} \,. \tag{6.2}$$

Such a correction accounts for additional frequency-dependent drag due to the presence of the surface. If we further assume the correction is necessary only when the dimer is rotating asynchronously, we can find a relationship between the two parameters *a* and *b* since, at the critical rotation rate, the friction coefficient is the same:

$$\begin{aligned} \gamma_{adj}(\Omega_C) &= \gamma_{rot} \\ &= [a\Omega_C + b]\gamma_{rot} \end{aligned} \,. \tag{6.3}$$

The quantity in brackets must equal unity, thus we reduce the number of unknown parameters to get,

$$\gamma_{adj}(\Omega) = \left[1 + a(\Omega - \Omega_C)\right]\gamma_{rot} \,, \tag{6.4}$$

and the solution to our nonuniform equation for asynchronous rotation including a frequency dependent viscosity will look as follows:

$$\left\langle \dot{\theta} \right\rangle = \Omega - \sqrt{\Omega^2 - \frac{\Omega_{C,adj}^2}{\left[1 + a(\Omega - \Omega_{C,adj})\right]^2}} \,, \tag{6.5}$$

where $\Omega_{C,adj}$ now represents the adjusted critical frequency. If we experimentally measure a specific nonuniform average rotation rate $\langle\dot{\theta}\rangle$, Eq. (6.5) can be rearranged to solve for the adjusted critical frequency $\Omega_{C,adj}$ in terms of the unadjusted frequency $\Omega_C = \sqrt{\langle\dot{\theta}\rangle(2\Omega - \langle\dot{\theta}\rangle)}$:

$$\Omega_{C,adj} = \Omega_C \frac{a\Omega + 1}{a\Omega_C \pm 1}. \qquad (6.6)$$

The critical frequency must be positive, thus only the solution with the plus sign in Eq. (6.6) is physically valid. Using Eq. (6.5), we acquire a better fit to our data (see Figure 6.9 and Figure 6.10), but with an extra parameter. Using the frequency-dependent drag coefficient model, the fit parameters *a* (Figure 6.9: 0.033 *s*, Figure 6.10: 0.071 *s*) and $\Omega_{C,adj}$ (Figure 6.9: 8.20 *rad*/*s*, Figure 6.10: 6.95 *rad*/*s*) were acquired. We can attribute the uncertainty in the adjusted frequency to the difference in drag coefficients between the top sphere and bottom sphere of a vertically-oriented dimer due to the slight height difference. The drag correction factors calculated from Eq. (6.3) translate to errors in the adjusted critical frequency to give values of 8.20 ± 0.66 *rad*/*s* and 6.95 ± 0.20 *rad*/*s* for each dimer, respectively. This error is larger than the width of the appropriate peak in the frequency power spectrum. Thus, the difference in adjusted critical frequency between the two dimers is attributed to differences in magnetic moment since the microspheres were approximately the same size.

Dimers of HC-9 *μm* diameter magnetic microspheres gave similar results to the UC-microspheres. A lower glycerol/water mixture (40% mass fraction) and higher magnetic field strength (8 *Oe*) were needed to achieve similar critical frequencies, suggesting that these microspheres had lower initial magnetic moments. Parameters for the fit of a typical HC-dimer using the frequency dependent drag model were $\Omega_C = 7.95$ *rad*/*s* and $a = 0.032$ *s*. The equator of the particle appeared to be in focus at about 7-8 *μm* above the glass surface when the dimer axis was oriented horizontal to the sample plane. This distance is smaller than the diameter of a single microsphere which suggests the dimer rotation was not purely end over end, but rather consisted of some precession. This 3-dimensional rotation is covered in more detail in Chapter 7.

The smaller 4.8 μm microspheres remained in the bulk of the fluid, even during measurements with optical illumination. Standard two-regime nonuniform oscillator behavior was observed for these smaller microspheres.

6.3.2 Magnetic Rotation and Laser Illumination

Frequency-Dependent Drag

To investigate the effect of laser illumination on nonuniformly rotating dimers of magnetic microspheres, the average rotation rate was measured twice at numerous incrementing external rotation rates - once with no laser present and the second time with 1.3 mW entering the microscope objective. The experiment was conducted on both UC-dimers and HC-dimers. Typical results are shown in Figure 6.11 and Figure 6.12.
For the UC-dimer experiment, the fit parameters were as follows: Laser off: $a = 0.093\ s$, $\Omega_{C,adj} = 6.28$; Laser on: $a = 0.077\ s$, $\Omega_{C,adj} = 6.47$. In this experiment, the dimer was always at least about 20 μm from the glass surface. Nevertheless, the frequency-dependent drag assumption fits the data well. As shown in Figure 6.11 and consistently in other samples, the presence of the laser tended to increase $\Omega_{C,adj}$ a small but significant amount. The parameter a tends to decrease with increasing laser power, typically on the order of 0.1 s or less. It should be noted that for a given external rotation rate, the ratio of adjusted critical frequencies for two different laser powers will be:

$$\frac{\Omega_{C2,adj}}{\Omega_{C1,adj}} = \frac{\Omega_{C2}}{\Omega_{C1}} \cdot \frac{a_1\Omega_{C1}+1}{a_2\Omega_{C2}+1}. \tag{6.7}$$

The multiplication factor containing the a parameters tends to be largest for external rotation rates close to the critical frequency. Using Eq. (6.7), the ratio of adjusted critical frequencies was off of the ratio of unadjusted frequencies by a factor of less than 7% for all of our data. For this reason, when comparing critical frequencies for different laser powers, we utilize the ratio of unadjusted critical frequency rates and expect this error of 7% or less.

For the HC-dimers, an increase in the critical frequency is again seen, as shown in Figure 6.12. Fit parameters were as follows: Laser off: $a = 0.028\ s$, $\Omega_C = 7.81$; Laser on:

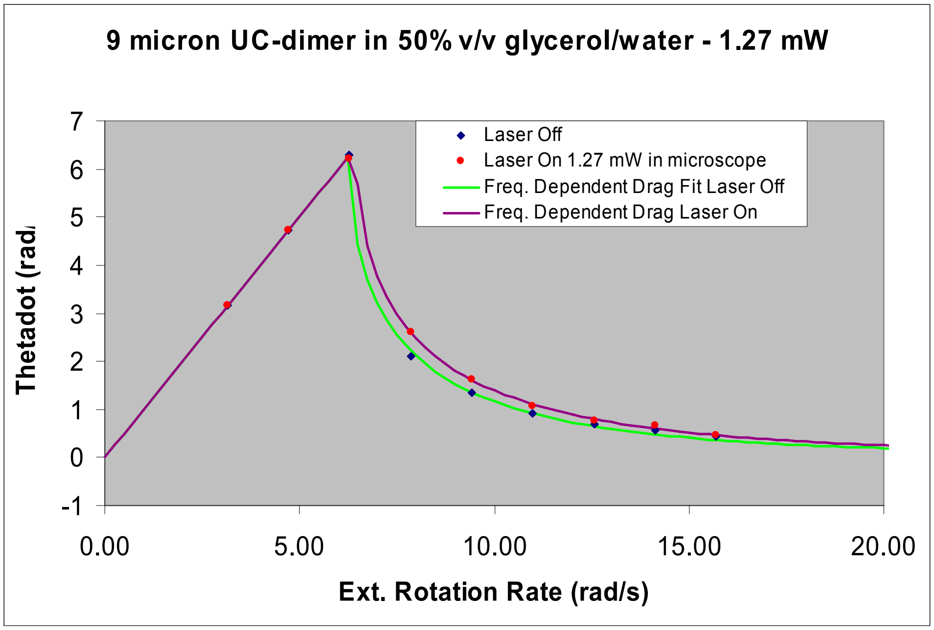

Figure 6.11 Average rotation rate for a dimer of uncoated 9 μm diameter microspheres nonuniformly rotating with and without laser illumination. The surrounding medium was 50% mass fraction glycerol/water and the laser power incident on the microscope objective was 1.3 mW. The dimer was always at least about 20 μm from the glass surface.

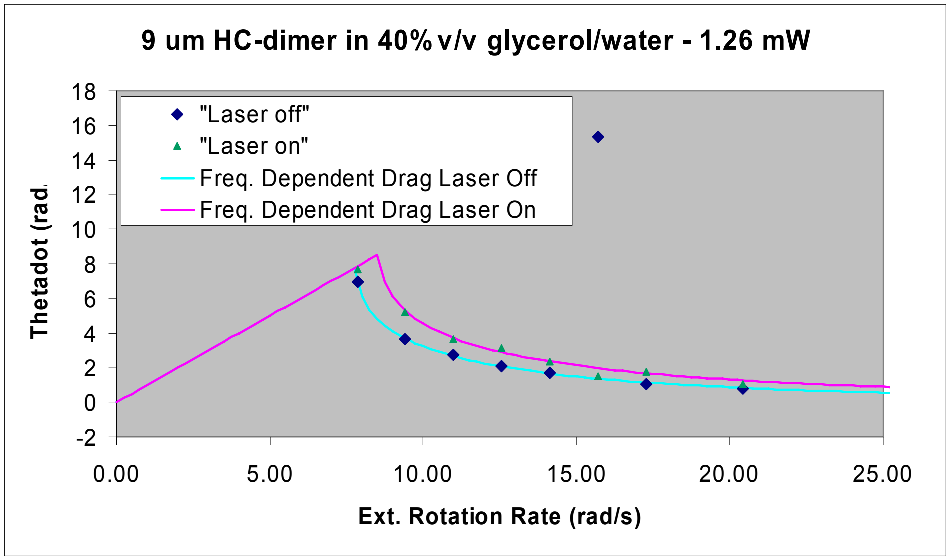

Figure 6.12 Average rotation rate for a dimer of aluminum half-coated 9 μm diameter microspheres nonuniformly rotating with and without laser illumination. The surrounding medium was 40% mass fraction glycerol/water and the laser power incident on the microscope objective was 1.3 mW. The dimer equator, defined in the text, was measured to be 7 μm from the glass surface.

$a = 0.018\ s$, $\Omega_C = 8.59$). The anomalous data point near 16 *rad/s* indicate measurements in which the dimer briefly bound to the glass surface. The measured average rotation rate at this point is equal to the external rotation rate indicating that intensity fluctuations were due to oscillations of the dimer tethered to the surface. These points were not included in calculating the fit parameters.

The presence of the laser beam increased the average rotation rate $\langle \dot{\theta} \rangle$ for all external rotation rates beyond the critical frequency, both for UC-dimers and HC-dimers. The maximum achievable rate without slipping $\Omega_{C,adj}$ was also slightly increased by the presence of the laser in both cases. It was shown in Chapter 5 that such an effect can occur due to an increase in the optically-induced scattering force. Another possible cause for the increased average rotation rates is a decrease in viscosity resulting from increased temperatures due to absorption of light.

Increase in Average Rotation Rate With Laser Power

The first four curves of Figure 6.8 show that the average rotation rate of the 4.8 μm HC-particle represented in Figure 6.6 increases with increasing applied laser power. We repeated this experiment and averaged the results to obtain the graph shown in Figure 6.13. The results reveal a linear dependence of the average rotation rate on laser power. Our simulations in Chapter 5 suggested that such an increase could be the result of an increased scattering force pushing on one side of the rotator to help it overcome drag, and thus slip less often. To test this, similar experiments were conducted on dimers of larger 9 μm magnetic microspheres. Using the reflection from a cover slip, the $1/e^2$ diameter of the beam at focus was measured to be about 1.2 μm., thus we expect that it was possible to illuminate only one microsphere at a time at its center. If the microspheres of the dimer were half-coated with a thick enough aluminum film, we expected that particle to reflect more than an uncoated particle. Thus, slightly increased rotation rates were expected due to the addition of the optical force compared to that for a dimer of uncoated spheres. In addition, if we change the rotation direction of the dimers while maintaining the location of application of the laser focus, we expected the average rotation rate to slow down since the optical torque associated with the scattering force would be

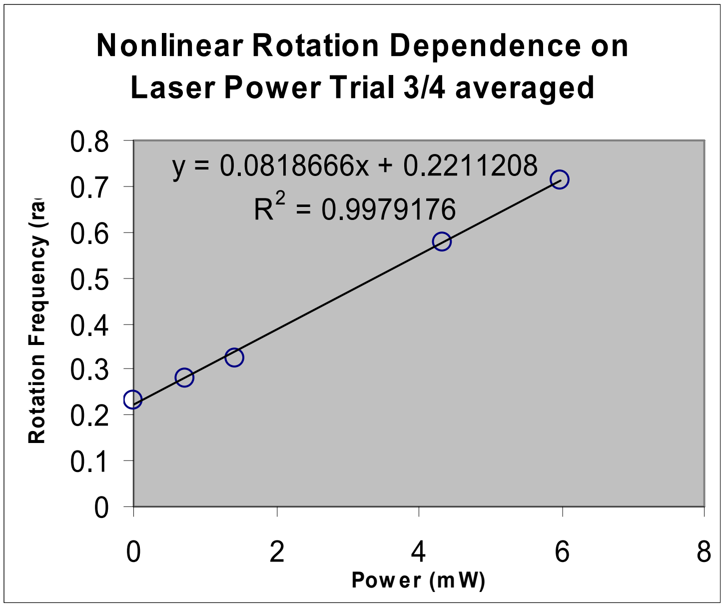

Figure 6.13 Average rotation rate vs. laser power for a magnetic 4.8 *μm* HC-particle rotated by a driving frequency of 0.25 *Hz* in a 76% mass fraction glycerol/water mixture.

opposing the magnetic torque. Results of these experiments are shown for UC-dimers in Figure 6.14 and for HC-dimers in Figure 6.15.

The results for larger dimers also suggest a general increasing trend, but the linear fit is not as good as in previous experiments with smaller particles. Numerous factors could cause the increased rotation rate with applied laser power. The optical scattering force provides a torque on the dimer, but the dependence is not linear. This was suggested by certain models in our simulations in Chapter 5 for larger laser powers such that the optical torque magnitude approached the magnetic torque magnitude. The increase in rotation rate could be due to a decrease in viscosity of the surrounding fluid caused by a temperature rise either from light absorption of the fluid itself or light absorption of the magnetic colloids which then transfer heat to the fluid. An increase in magnetic moment of the dimer would cause an increase in average rotation rate. This, however, is unlikely since the magnetic material is typically saturated and will only decrease with time or if perturbed. It is also possible that several of these effects were occurring simultaneously. We will look at each possibility and address the arguments for and against each one.

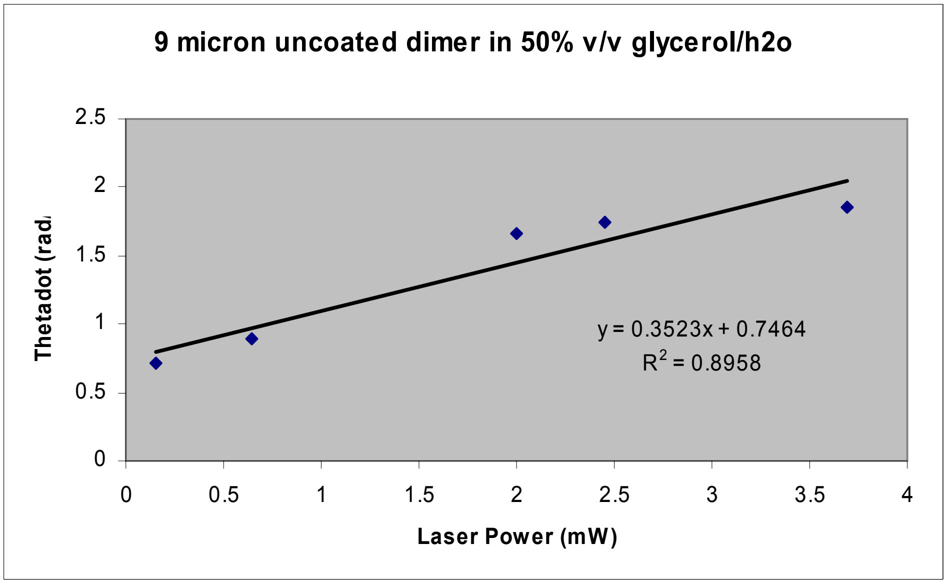

Figure 6.14 Average rotation rate vs. laser power for a dimer of 9 *μm* UC-magnetic microspheres rotated by a driving frequency of 1.25 *Hz* in a 50% mass fraction glycerol/water mixture.

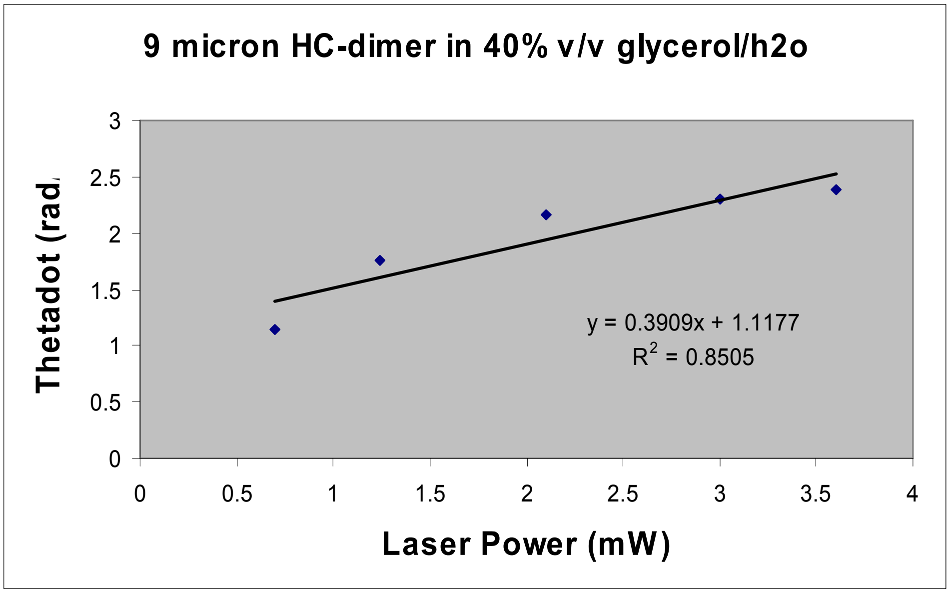

Figure 6.15 Average rotation rate vs. laser power for a dimer of 9 *μm* HC-magnetic microspheres rotated by a driving frequency of 2.75 *Hz* in a 40% mass fraction glycerol/water mixture.

Scattering Force

Without the presence of the external magnet, we observed that dimers of magnetic microspheres in solution could be rotated by the scattering force of the incident laser illumination. This rotation was slow and accompanied by significant translation. To determine the effectiveness of the scattering force in generating an optical torque on a rotating dimer of magnetic microspheres, we first considered the effect of the scattering force on translation of the rotating dimer in the *z*-direction. With the laser shuttered off, the external magnet was distanced enough that the rotating dimer tended to sediment very gradually at several microns per minute. When laser illumination was applied, the rotating dimer floated, indicating that a scattering force was present. We can neglect the possibility of a gradient force since it would maintain the dimer at a certain height rather than enable floatation. Such a force could induce orientational alignment of the optical polarization of the dimer and potentially impede its rotation if present; however, a reduction in rotation rate was rarely observed.

To quantify the flotation and relate the motion to optical parameters, we investigated the interaction between the particle and the laser focus in slightly more detail. The approximate distance of the dimer from the glass surface was measured as a function of the energy supplied to the particle. The energy supplied was calculated by multiplying the laser power applied by the total time the dimer spent in the beam. This total time was measured using image analysis techniques (see Figure 6.16) by integrating the percentage of overlap between the thresholded dimer image and a circular region representing the laser trap over the entire acquisition. The trap region was set to approximately twice the diameter of the measured laser focus to include proximity effects of the trap. For example, the image on the left of Figure 6.16 is 100% filled while on the right, about 30% filled.

Performing the integration of this percentage threshold for each measurement, we can calculate the approximate time the particle directly interacts with the beam, and thus the energy imparted to the dimer over the course of one measurement. Figure 6.17 indicates the integrated intensity and %-threshold versus time for one such measurement. We can see that while the dimer was in the beam the %-threshold was 100%. The integrated intensity appeared to decay as the dimer translated upwards in the *z*-direction. Once the

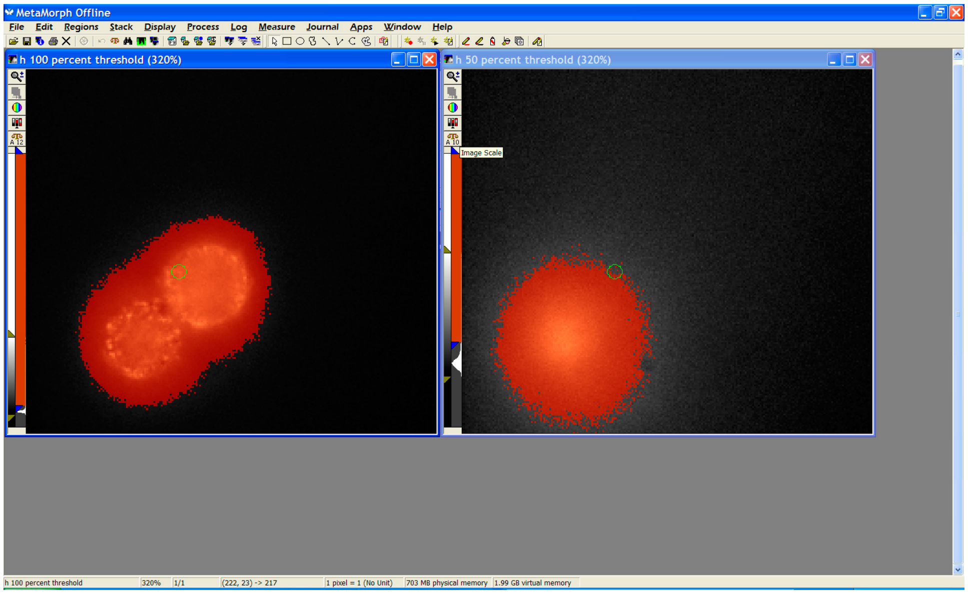

Figure 6.16 Snapshots from Metamorph Imaging Software of a dimer of magnetic microspheres rotated by a magnetic field. By integrating the percentage of overlap between the thresholded dimer image (orange) and a circular region (green) representing the laser focus over the entire acquisition, the interaction between laser and dimer can be tracked. The focus region was set to approximately twice the diameter of the actual measured laser focus to include proximity effects of the trap. The image on the left is 100% filled while on the right about 30% filled.

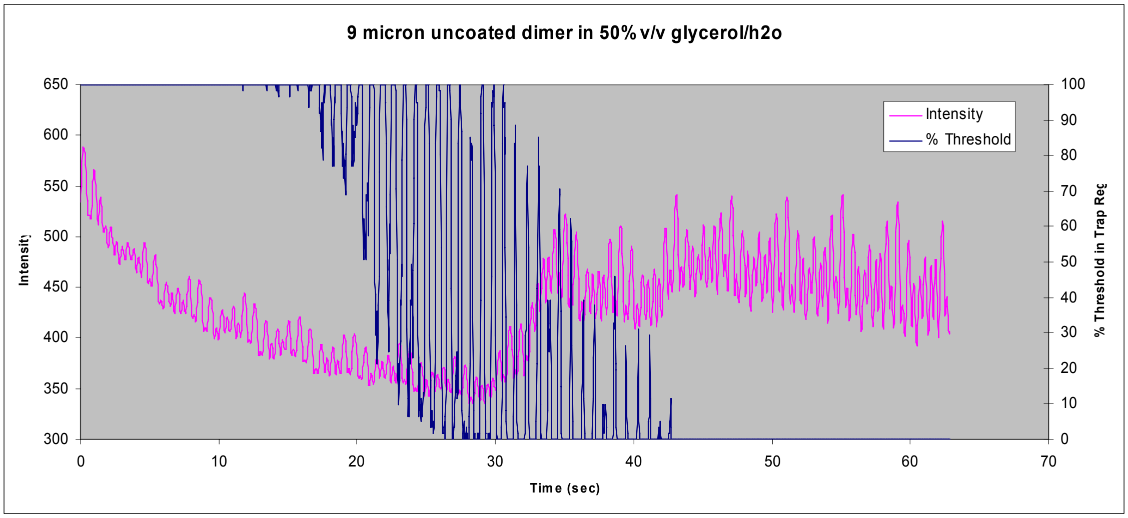

Figure 6.17 Integrated intensity and %-threshold vs. time for an UC-dimer of magnetic microspheres analyzed in Figure 6.16. The integrated intensity was the intensity of the dimer image summed over the entire frame. The %-threshold was the percentage of overlap between the thresholded dimer image and a circular region representing the location of the laser focus. While the particle was in the focus (100%-threshold) the intensity was dropping due to translation in the *z*-direction and the rotation rate was 1.75 *rad*/*s*. Once the dimer left the focus (~30 s), the intensity remained relatively flat while the rotation rate dropped to 1.66 *rad*/*s*.

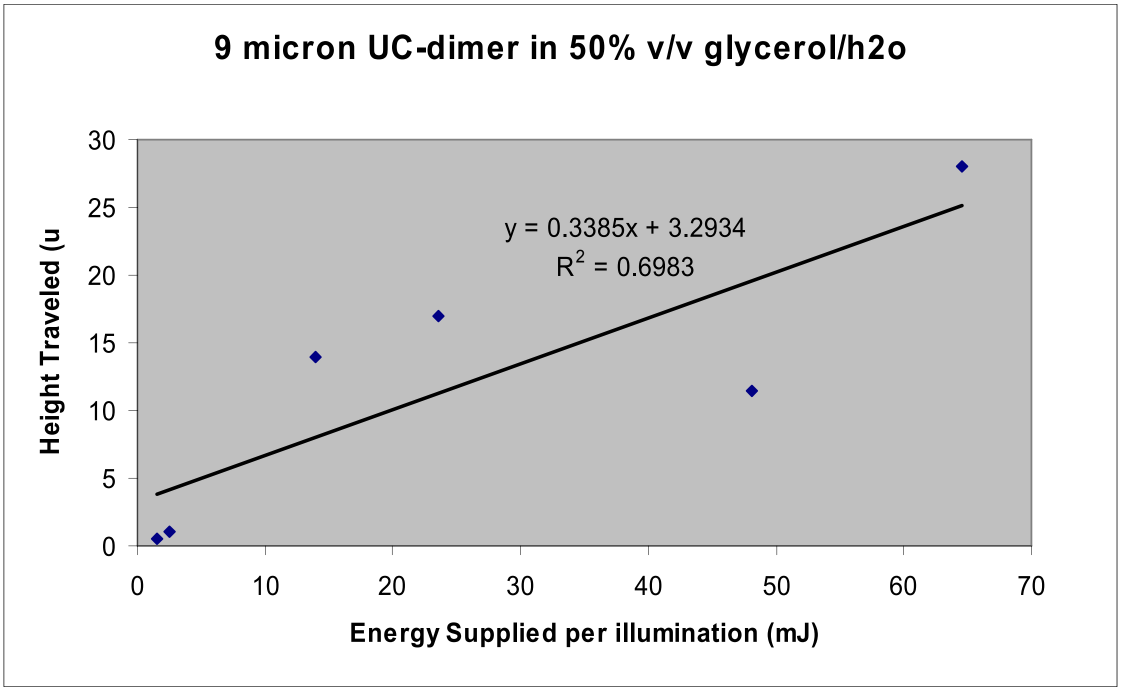

Figure 6.18 Height traveled by a rotating UC-dimer of magnetic microspheres due to a laser scattering force.

dimer was far enough from the vicinity of the focus the %-threshold dropped and the integrated intensity remained relatively flat. Thus a height increase was directly a result of the scattering force of the laser impinging on the dimer.

The results of UC-dimer height traveled vs. energy supplied are shown in Figure 6.18. There is a general increasing trend in height with energy supplied. Deviations from the trend are attributed to the fact that, on many occasions, the percentage of overlap between the thresholded image and the focus region could have been 100% even though the laser focus was impinging on one of the microspheres at a grazing angle. Any scattering force generated would push the microsphere at angles other than along the *z*-axis. Nevertheless, Figure 6.18 suggests a scattering force did exist; however, translational effects were more apparent than rotational effects.

For our system, the kinematic viscosity of a 50% glycerol/water w/v mixture at 20°*C* is 5.26 *cS* [174], the density is 1.13 g/cm^3, and the shape factor of a dimer is 11.22 [178]. Using Eq. (5.2) to calculate the rotational drag coefficient, the applied magnetic torque ranged from $\Omega_C \gamma_{rot} \approx$ 200-700 $pN \cdot \mu m$. Our previous calculations in Chapter 5 using similar laser powers gave an estimate of about 15 *pN·μm* of optical torque. Thus, although flotation is induced, the torque due to the light scattering force may not be enough to significantly affect the motion due to the rotating magnet.

The HC-dimers were in a slightly lower %-mass fraction glycerol/water mixture and tended to sink to the bottom glass surface (but did not roll significantly along the surface with magnetic rotation). Over laser powers ranging from 0.7-3 *mW*, these dimers did not experience a scattering force strong enough to overcome sedimentation, yet they still underwent an increase in average rotation rate at 1.3 *mW*, evidenced by Figure 6.12. This strongly suggests that the increase in rotation rate was due to something other than the scattering force of the applied laser.

This image analysis method using the %-threshold shows us that the dimer's rotational behavior directly depends on the light-dimer interaction as opposed to absorption by the surrounding solution. If we look again at the graph in Figure 6.17 more closely, we see that at early times (0-30 *sec*), the dimer is completely in the beam (100% threshold) and the rotation rate is 1.75 *rad/s*. After the dimer translates away from the laser spot (50% threshold) both translationally and axially (35-63 *sec*), the rotation rate slows to 1.66 *rad/s*. This behavior was also seen with the HC-dimers as shown in Figure 6.19 where in the focus, the average rotation rate was 2.34 *rad/s* but away from the focus, the average rotation rated dropped to 1.76 *rad/s*.

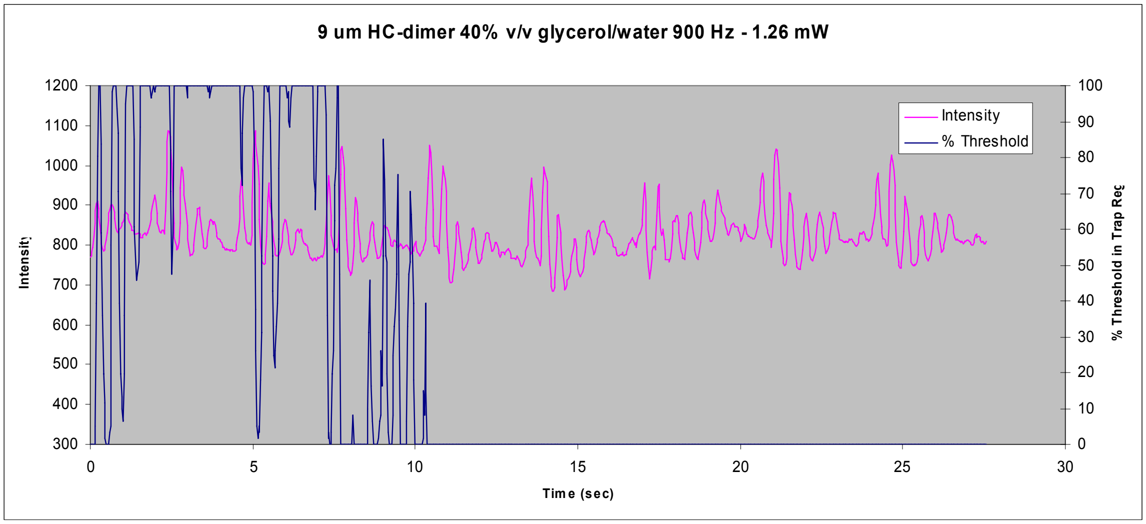

Figure 6.19 Integrated intensity and %-threshold vs. time for a HC-dimer of magnetic microspheres. While the dimer was in the focus (0-10 *s*) the average rotation rate was 2.34 *rad/s*. After the dimer translated laterally away from the vicinity of the focus (10-30 *s*), the average rotation rate dropped to 1.76 *rad/s*.

Because the rotation rate strongly depends on whether or not the dimer is in the beam, all rotation rates were measured only when directly in the beam or shortly after drifting away (usually <10 *s* after the % threshold drops to an average of 50%). This dependence also suggests that immediate effects due to the interaction between light and the dimer were observed more than effects due to the interaction between light and the surrounding fluid. If we ignore the possibility of a rotation rate increase due to a scattering force, the quick drop in rotation rate observed suggests there was an insignificant amount of heat accumulated in the fluid over the remainder of the illumination period in comparison to the heat generated while in the laser focus. This indicates either the glycerol-water mixture had a high thermal diffusivity or only a very small region of fluid immediately surrounding the dimer microspheres was heated.

We also notice that the effectiveness of the laser while the dimer is in the focus is more easily discernible for the half-coated particles. Upon leaving the focus, the rotation rate appeared to respond quickly, reducing within 5 seconds of the %-threshold dropping. This suggests a number of behavioral differences compared to the uncoated dimers including faster heat diffusion in the fluid and/or less heat transfer to the fluid. Both of these might be expected since the solution has a slightly lower concentration of glycerol and thus a higher heat capacity and higher thermal diffusivity. In addition, the half-coated dimers measured in these experiments experience little flotation or sedimentation during each illumination (<1 μm in almost every measurement) as evidenced by the relatively flat intensity fluctuation time traces as well as measurements of the *z*-distance from the bottom cover slip which remained at a constant 7 μm above the surface, as discussed previously. It appeared that the laser illumination induced lateral translation on the dimer until the dimer shifted far enough from the laser focus where it could sediment back to the glass surface.

Another indication that the scattering force was not applying a measurable torque is that the rotation rate never slowed, qualitatively nor quantitatively, when the position of the laser focus was changed. Applying the beam on either side of the dimer for a given rotation direction always caused an increase in rotation rate, even when the scattering torque direction should have opposed the motion due to magnetic torque. Keeping the focus location fixed and changing the direction of the magnetic rotation also produced the same increase in average rotation rate.

Viscosity Decrease Due to Temperature Rise

A decrease in viscosity can explain the increased rotation rate while the magnetic particle was illuminated. If this were the case, the decrease may be due to increased temperature caused by absorption of either the particle or the solution, or both. Previous results indicating the slowing rotational rate after the dimer translated away from the beam suggest that heat absorption by the solution itself is much less than heat transferred by the particles to the solution. If the magnetic colloids transfer heat only to a thin layer of fluid surrounding the dimer, the heat may be able to diffuse quickly to the remaining solution within the 2-3 minutes between measurement acquisitions, thus causing the rotation rate to return to a lower value. If, instead, heat diffusion is rather slow in the glycerol/water mixture and/or a thick layer around the particle is affected, we expect the dimer to maintain a higher rotation rate even after the laser is turned off.

Direct heating of the solution via the fluid absorption is negligible. Recall that the most noticeable changes in average rotation rate were seen when the dimer entered the beam. In addition, the increase in temperature at the focus of near infrared (1064 *nm*) laser light used to trap dielectric particles was measured to be about 40 *K*/*W* for a 100% glycerol solution [61]. For our system, the maximum energy supplied in one illumination was with a 2.45 *mW* beam for 26.4 *sec*. This roughly corresponds to a temperature increase of 2.6 *K*, not considering the reduction in intensity due to optical losses, reduced effects in water-glycerol mixtures, or differences in absorption at 780 *nm* vs. 1064 *nm.*

On the other hand, absorption of laser light by the magnetic colloids on the polystyrene core, followed by heat transfer to the immediately surrounding solution is probable. The increased rotation rate would reflect a change in temperature of the local fluid surrounding the particle. Let us assume that all of the light energy Q_{light} supplied to the dimer is absorbed and transferred to the surrounding solution as heat, raising its temperature ΔT by the following:

$$Q_{light} = mC\Delta T \,, \tag{6.8}$$

where m is the mass of the heated fluid and C is the specific heat capacity of the fluid. The temperature dependence of the kinematic viscosity of glycerol was shown by Shankar et al [174] to be:

$$\nu(T) = \exp(a_\nu + b_\nu T + c_\nu T^2)\,, \tag{6.9}$$

A fit of Shankar's experimental data for a 50% mass fraction glycerol/water mixture gives $A = 2.49, B = -0.0466, C = 0.000248$. For a 40% mass fraction glycerol/water mixture the values are $A = 1.97B = -0.0428, C = 0.000236$. An increase in the temperature $\Delta T = T_2 - T_1$ results in a decrease in viscosity as follows:

$$\begin{aligned} \nu(T_2) &= \exp(a_\nu + b_\nu(T_1 + \Delta T) + c_\nu(T_1 + \Delta T)^2) \\ &= \nu(T_1)\exp\left[(b_\nu + 2c_\nu T_1)\Delta T + c_\nu \Delta T^2\right] \end{aligned} \tag{6.10}$$

which can then be expressed using Eq. (6.8) in terms of the supplied energy as

$$\nu(T_2) = \nu(T_1)\exp\left[\frac{(b_\nu + 2c_\nu T_1)}{mC}Q + \frac{c_\nu}{(mC)^2}Q^2\right]. \tag{6.11}$$

Note that from Eq. (6.11), one can get the ratio of viscosities only if the temperature immediately before illumination is known.

The ratio of viscosities can also be expressed in terms of the corresponding critical frequencies:

$$\frac{\nu(T_2)}{\nu(T_1)} = \frac{\Omega_{C1}}{\Omega_{C2}} = \frac{\sqrt{\dot{\theta}_1(2\Omega - \dot{\theta}_1)}}{\sqrt{\dot{\theta}_2(2\Omega - \dot{\theta}_2)}}\,. \tag{6.12}$$

Eqs. (6.9) through (6.11) can also be used to determine the fluid temperature during each measurement.

We conducted experiments on our dimers in which we measured the average rotation rate for numerous laser illuminations. We alternated between no illumination and illumination with some recorded, non-zero laser power, waiting several minutes between each acquisition. We also performed the %-threshold analysis to determine the time each dimer spent in the laser focus, and ultimately the energy supplied to the dimer for each illumination. Assuming that all of this energy was transferred to the fluid as heat, we used (6.11) with the temperature during the first measurement, fitted parameters for Shankar's viscosity data, and calculated supplied energies. We obtained the ratio of critical frequencies which allowed us to calculate the expected rotation rate to within a

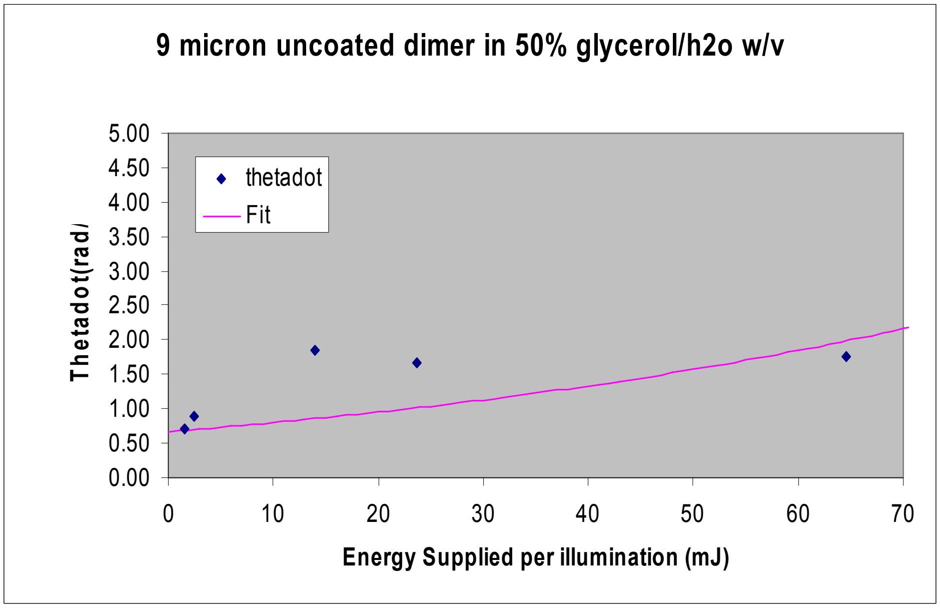

Figure 6.20 Average rotation rate vs. supplied energy for a dimer of 9 *μm* UC-magnetic microspheres rotated by a driving frequency of 1.25 *Hz* in a 50% mass fraction glycerol/water mixture. This is the same dimer represented by Figure 6.14.

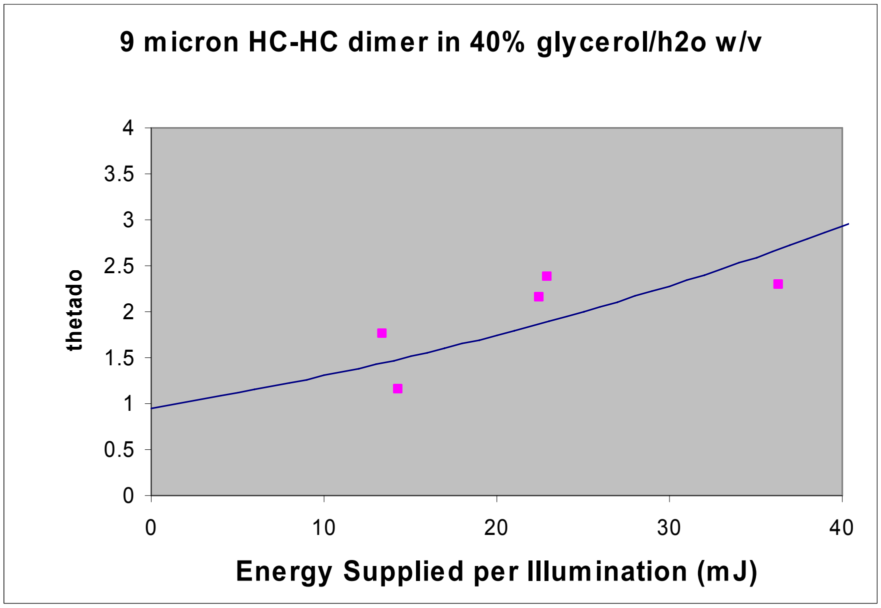

Figure 6.21 Average rotation rate vs. supplied energy for a dimer of 9 *μm* HC-magnetic microspheres rotated by a driving frequency of 2.75 *Hz* in a 40% mass fraction glycerol/water mixture. This is the same dimer represented by Figure 6.15.

single fit parameter. This was fit to our actual experimental data. Results are shown in Figure 6.20 for a UC-dimer and in Figure 6.21 for a HC dimer. We used an initial temperature of 20°*C* for the UC-dimer and 25°*C* for the HC-dimer, as was measured during the experiment. We also estimated the specific heat capacity of our glycerol/water mixture using a weighted binary distribution:

$$C_x = xC_{glyc} + (1-x)C_{water}, \tag{6.13}$$

where x is the mass fraction of glycerol, $C_{glyc} = 2.38\ J/g{\cdot}K$ and $C_{water} = 4.18\ J/g{\cdot}K$. We get $C_{50\%} = 3.28\ J/g{\cdot}K$ and $C_{40\%} = 3.46\ J/g{\cdot}K$.

Our model assuming the fluid absorbs all the heat indicates an increase with supplied energy that is slightly higher order than the linear dependence we expected for the scattering force. In both cases, the fit is not great, but the HC-dimer appears to be slightly better. This was expected based on our individual measurements for each dimer. In both cases, when laser illumination was present, the dimer rotation rate always increased relative to the immediately previous measured rate with the laser off. With the UC-dimers, there were often cases when the next measurement with the laser off resulted in an average rotation rate faster than the rate at the start of the experiment. This suggests the system had changed in some way during the interaction with the laser. If changes in dimer rotation rate were solely due to an optically induced scattering torque (neglecting distance from the glass surface) we would expect the system to return to its state prior to application of the laser since it is assumed little heat was generated. Instead, since the rotation rate did not return to its original frequency at the start of the experiment, we can conclude that heat was generated and the dimer did not have enough time to cool. Because of this, the temperature at the start of the next illumination was slightly higher than at the start of the experiment, thus resulting in rotation rates higher than our fitted trend in Figure 6.2. Our HC-dimers seemed to return to approximately the same rotation rate after each illumination ended; the normalized average rotation rate $\langle \dot{\theta} \rangle / \Omega_{C,adj}$ ranged from 0.125 to 0.134. This is in contrast to the range for UC-dimers which was 0.152 to 0.277.

The fit in Figure 6.21 can provide an estimation of the mass of fluid required for the temperature rise to cause the observed rotation rates, assuming all supplied energy were absorbed as heat. The calculated mass corresponds to a heated spherical volume of water surrounding a 9 μm sphere that extends to a radius 520 μm from the center of the sphere. Equivalently, this is about 100 μm × 2 mm × 2 mm (100 μm was the thickness of our fluidic sample cell). If we assume only 10% of the supplied energy we originally calculated actually gets absorbed by the sample/solution (the 90% goes to microscope optical loss and scattering, reflection or transmission, reduction in magnetic moment), the heated volume goes down to 100 μm × 0.75 mm × 0.75 mm or a spherical radius of 240 μm from the center of the sphere. Such a volume, although smaller than the solution volume typically used, seems large if one expects heat diffusion to be slow through the glycerol mixture. Using the dimensional considerations [61], we estimate the time scale for equilibrium across this distance d to be $d^2 C_V / k$ where k is the thermal conductivity. Assuming a binary distribution for the thermal conductivity k of our fluid ($k_{\text{water}} = 0.60\ W/m\cdot K$ and $k_{\text{glyc}} = 0.28\ W/m\cdot K$), we expect equilibration in less than 1 *sec* whereas the larger volume is about 2 *sec*. In addition, if one were able to observe other rotating particles far from the laser focus increasing in average rotation rate, this would verify the validity of such a large heated solution volume.

The constancy of the measured average rotation rate when the laser was off indicates that the HC-dimers had adequate time to cool to ambient temperature compared to the UC-dimers. In addition, since the rotation rate did not drop further, the magnetic moments of the particles were not being reduced. This differs from the UC-dimers in which rotation rates measured after illumination periods were often lower than at the start of the experiment. For the magnetic colloids coated by aluminum, since the coating is much thicker than the skin depth for 780 *nm* light, the magnetic colloids were partially protected from the illumination thus absorbing less light. Less absorption would suggest less heat was generated and transferred to the solution by the magnetic colloids. Our measured rotation rates were indicative of temperature increases of 1-16°C for UC-dimers and 4-18°C for HC-dimers. The discrepancy, however, is not absolute since many other factors could be involved including absorption of the fluid and changes in the magnetic moment for UC-dimers. As we calculated previously, temperature increases due to direct absorption by the solution are only several degrees. The small amount of light absorbed within the skin depth of the aluminum may be enough to raise the surface temperature significantly. If the aluminum transfers the generated heat to the solution, keeping the magnetic colloids safe, we don't expect a reduction in magnetic moment.

Heating of the surrounding fluid is the most viable cause of the increase in the average rotation rate of our dimers. A reduction in magnetic moment requires little energy as we'll see in the next section, and the laser powers used here were significantly lower than those used for optical tweezers, thus the direct absorption by the solution should have also been much weaker. Scattering forces and torques, although present due to non-zero absorption, do not cause significant rotation at such low laser powers. In addition, application of the optical illumination at opposite locations of the hybrid particle always induced an increase in rotation rate, despite the direction (clockwise or counter-clockwise) of magnetic rotation. Although heat generation via absorption by the metallic portions of our particles is likely, the heat must be diffusing to the remainder of the solution quickly since cooling back of the solution was observed. Thus, our particles were acting as truly localized viscosity sensors.

Changes in Magnetic Moments

It is unlikely that any increase in the average rotation rate $\dot{\theta}$ was due to an increase in magnetic moment since the microspheres reached their saturation magnetization by being placed in a strong magnet. Any observed reduction in rotation rate between 'laser off' states could not be attributed to a cooling effect if we assumed the initial 'laser off' state was in equilibrium with the ambient surrounding temperature and the system did not change otherwise. Instead, it must be attributed to a reduction in the magnetic moment of the particles. Such events occurred with our UC-dimers and here we estimate the percentage of supplied energy lost to this mechanism.

Using Eq. (6.7), we can calculate the reduction in magnetic moment given by the ratio of critical frequencies between 'laser off' states before and after illumination, assuming enough time was allowed to let the system equilibrate (several minutes). The ratio of the magnetic moment after illumination to before was 0.759. The saturation magnetization of CrO_2 follows Bloch's law at low temperatures ($\sim T^{3/2}$) and the 3-D Heisenberg model [179] ($\sim (T_C - T)^{\beta}$ near the critical temperature $T_C = 386.5\ K$ (for epitaxial films). At room temperature, we estimate the change in magnetization using digitized data on CrO_2 powders [180] which take into account native Cr_2O_3 layers on the CrO_2 grains. The corresponding change in temperature is from $T = 293°K$ to $T = 360°K$.

For this change in temperature, we can estimate the energy supplied to the particle to reduce the magnetization. We estimate the temperature rise as follows [181]:

$$\Delta T = \frac{(1 - R_{\%})Q}{C_V V}, \tag{6.14}$$

where $R_{\%}$ is the reflectivity of a CrO_2 film, C_V here is the volumetric heat capacity of CrO_2, and V is the heated volume. Use of Eq. (6.14) assumes electron diffusion is sufficient to transport much of the heat generated by light absorption to the lattice. The reflectivity of CrO_2 films [182-184] is about 25%. The film is estimated to be 500 *nm* thick from the SEM shown in Figure 6.22 around a previously measured 9 μm diameter polystyrene core. Since the illumination focal spot with a radius beamwaist of 0.579 μm is much smaller than the particle diameter, we model the surface of the magnetic colloids as a continuous film and assume the heat is distributed over the entire volume of the film. Otherwise, only a small region of colloids would be affected and we would not observe a decrease in rotation rate due to reduced magnetization.

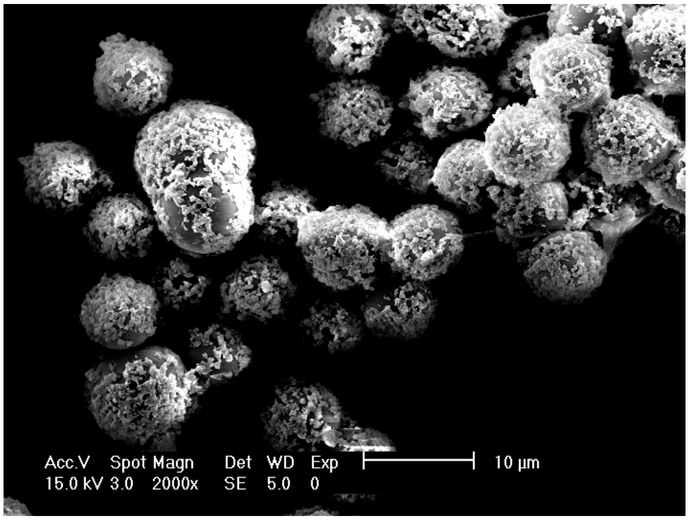

Figure 6.22 SEM of 9 μm magnetic microspheres used for both UC-dimers and HC-dimers. HC-dimers were further coated with approximately 50 *nm* of aluminum before dimers were formed.

The thermal properties of CrO_2 are difficult to obtain since ferromagnetic properties can become significant, and the best theoretical description for ferromagnetic behavior near the critical temperature is often controversial for each material. In addition, the properties for nanoparticles may differ from those for the bulk material and may be dependent on nanoparticle size [185, 186]. The specific heat of the CrO_2 colloids on our microspheres is comprised of a lattice contribution and a magnetic contribution. We estimate the lattice contribution by the Debye formulation for specific heat:

$$C_D = 9k_B N(\frac{T}{\theta_D})^3 \int_0^{\theta_D/T} \frac{e^x x^4}{(e^x - 1)^2} dx \, , \tag{6.15}$$

where k_B is Boltzmann's constant, $\theta_D = 593$ K is the Debye temperature [187] and N is the number of atoms per volume. This gives a volumetric heat capacity of $C = 3.59$ $J/cm^3 \cdot K$ at 20°C. Note, below the Curie temperature for CrO_2 (386.5 K for epitaxial films), the magnetic contribution to the specific heat can be significant, potentially doubling the heat capacity, but only for applied fields considerably larger than ours.

Using the above analysis, to within a factor of two, the energy contributed to reducing the magnetization was $Q = 0.159$ μJ. The energy supplied to the particle calculated by multiplying the laser power by the duration of interaction was 48.1 mJ. We see that a very small percentage of the supplied energy is sufficient to reduce the magnetization. Most of the energy goes to heating the solution, transmission of the sample, reflection/scattering of the sample. Approximately 75% of the energy entering the microscope was lost to optical loss in the mirrors and lenses. Heating of the solution was discussed previously. Optical loss due to scattering and transmission of a single dimer with magnetic colloids has not been characterized. For an uncoated particle (polystyrene only), the microsphere acts as a lens for the laser light, thus a higher intensity was observed to be transmitted than without the polystyrene sphere present. The fact that the magnetic dimers maintained some magnetization and continued to rotate despite the low energy required to reduce the magnetization is still unexplained. It is likely that the presence of the surrounding fluid helped to dissipate the heat away before irreversible damage was done.

6.4 Conclusions

We’ve shown that hybrid microsphere systems consisting of magnetic materials can be manipulated both magnetically and optically at the same time. With purely magnetic rotation, the microsphere behaves as a nonuniform oscillator. When the optical perturbation is combined with magnetic rotation, the dynamical motion indicated modifications of the behavior of the standard nonuniform oscillator. A consistent method of analyzing the motional behavior has been developed using Fourier domain filtering techniques. Our analysis reveals that application of laser illumination to the magnetically rotating microspheres resulted in increased rotation rates which were most likely due to heat generation induced by light-absorption of the hybrid particles. Effects due to increased scattering forces or a reduction in magnetic moment, although possible, were dominated by the consequences of the increase in temperature. Half-coatings of aluminum applied the to hybrid particle systems also appeared to protect the moment of the magnetic colloids present.

CHAPTER 7

NONLINEAR THREE-DIMENSIONAL MOTION OF A RIGID DIMER OF MAGNETIC MICROSPHERES IN A ROTATING MAGNETIC FIELD

In recent years, the dynamics of nonuniform oscillators have been observed in numerous microscale and nanoscale systems [33, 133, 139-142, 188-190]. The motion has even been exploited to detect microparticles [54] and bacteria [66] as well as observe bacterial growth [to be published]. In most of these systems the oscillator is assumed to be confined to rotate in a single plane. For example, Bonin et al. [133, 142] observed that optically torqued nanorods would tend to vertically align along the propagation axis of a narrowly focused laser beam unless confined by the surface. If the particle is not confined, however, 3-dimensional (3-D) nonuniform rotation can ensue.

Indications that objects driven by external rotating fields can rotate nonuniformly in 3-D have existed. Erglis [139] et al. simulated magnetotactic bacteria which were proposed to rotate and eventually escape out of the plane of the rotating field. The rolling-while-slipping hybrid particles in Chapter 4 showed motion along a surface in directions that deviated from the expected rolling perpendicular to the external magnetic rotation axis. In addition, the optically manipulated dimers consisting of hybrid magnetic microspheres showed signs of precession that made them difficult to illuminate consistently while in the focused laser beam.

Dimers were observed to tilt away from end-over-end rotation at high frequencies, thus causing the laser beam to never impinge on the particle evenly with every cycle. It is expected that at these high rotation rates, the dimer can no longer keep up, but instead of pure slipping, the dimer reorients itself to reduce the effective rotational torque about the axis of rotation. At even higher frequencies, the dimer appears to rotate in such a way that a bowtie-like image forms and precession occurs. The dimer rotates about an axis with a fast rotation that matches the external magnetic rotation rate. This axis, however, is not parallel to the external magnetic rotation axis (as it is for uniform end-over-end rotation). Instead, this axis appears to precess about the parallel, causing an overall envelope over intensity fluctuations similar to what we would expect from a single half-coated nonuniform oscillator asynchronously rotating in a plane.

Similar behavior was described theoretically for an isolated magnetic particle in liquid in the late 1960's by Caroli and Pincus [38]. To our knowledge, there has not yet been experimental verification of this phenomenon using a rigid dimer of magnetic microspheres. In this work, we describe our own experimental observations of a dimer of magnetic microspheres undergoing 3-D nonuniform motion due to an external magnetic field rotating about a single axis. We compare our results to the theory set forth by Caroli and Pincus. We also propose that differences between the steady state solutions provided in the theory paper and our experimental results are partially due to the orientation-dependent drag coefficient of our dimer microspheres. This is supported by numerical analysis of the simplified equations of motion given by the theory.

7.1 Theory

In this section, we review the results of the theoretical treatment given by Caroli and Pincus [38] for the response of a uniaxial, single-domain magnetic particle suspended in a liquid to an external magnetic field $\boldsymbol{B}$ in the case of zero static field. We try to maintain as much of the original notation as possible, except when relating to variables corresponding to those defined in previous chapters.

The treatment begins with the magnetic energy density given as:

$$U = -K(\boldsymbol{m} \cdot \boldsymbol{n})^2 - \boldsymbol{m} \cdot \boldsymbol{B} \tag{7.1}$$

where we define K as the anisotropy constant > 0 multiplied by the volume of the particle, $\boldsymbol{n}$ is the unit vector along the easy axis of the particle, and $\boldsymbol{m}$ is the magnetization or magnetic moment with nearly fixed magnitude m. The $\boldsymbol{B}$ field rotates in the yz-plane with rotation frequency Ω while $\boldsymbol{\Omega}$ points in the x-direction. For low frequencies considered here, the equation of motion for the magnetization derived from Eq. (7.1) reduces to:

$$\boldsymbol{m} = \lambda \boldsymbol{B}_{eff} = \lambda[\boldsymbol{B} + 2K(\boldsymbol{m} \cdot \boldsymbol{n})\boldsymbol{n}] \tag{7.2}$$

where λ is determined from the magnitude of the magnetization. The mechanical equation of motion describes a balance of torques:

$$I\ddot{\boldsymbol{\theta}} + \gamma\dot{\boldsymbol{\theta}} = -2K(\boldsymbol{m} \cdot \boldsymbol{n})\boldsymbol{m} \times \boldsymbol{n}. \tag{7.3}$$

where I is the moment of inertia, and γ is the 3-D drag tensor, and $\dot{\boldsymbol{\theta}}$ and $\ddot{\boldsymbol{\theta}}$ are the angular velocity and angular acceleration of our particle. The first term on the left is the inertial term, the second the viscous torque and the term on the right is the torque due to the magnetic field $\boldsymbol{B}$. Using the precession equation for the easy axis of the particle:

$$\dot{\boldsymbol{n}} = \dot{\boldsymbol{\theta}} \times \boldsymbol{n}, \tag{7.4}$$

we can obtain the equation of motion for the easy axis as

$$I(\ddot{\boldsymbol{n}} - \dot{\boldsymbol{\theta}} \times \dot{\boldsymbol{n}}) = -\gamma\dot{\boldsymbol{n}} - 2K(\boldsymbol{m} \cdot \boldsymbol{n})(\boldsymbol{m} \times \boldsymbol{n}) \times \boldsymbol{n}. \tag{7.5}$$

In the limit of low Reynold's number [150], the inertial term can be neglected. If we consider only steady state solutions that rotate with the magnetic field ($\dot{\boldsymbol{\theta}} = \boldsymbol{\Omega}$), Eq. (7.5) reduces to

$$\boldsymbol{n} \times [\gamma\boldsymbol{\Omega} + 2K(\boldsymbol{m} \cdot \boldsymbol{n})(\boldsymbol{m} \times \boldsymbol{n})] = 0. \tag{7.6}$$

The trivial solution to Eqs. (7.2) and (7.6) was discussed briefly by Caroli and Pincus [38]. This solution consists of a particle in which the easy axis points along $\boldsymbol{\Omega}$ while the magnetization, aligned along the hard axis, always points along the direction of the magnetic field. Such dimers have been prepared in practice by magnetizing them in a large field while they're still part of a monolayer on a glass substrate. The motions we observed of these types of dimers differ greatly from the dynamics described here, thus they will not be considered in any more detail.

Eq. (7.6) reveals that the term in brackets can be expressed as a scalar times $\boldsymbol{n}$. If we insert $\boldsymbol{m}$ from Eq. (7.2) into the last parentheses of Eq. (7.6) and cancel appropriate terms, we get:

$$\gamma\boldsymbol{\Omega} + 2\lambda K(\boldsymbol{m} \cdot \boldsymbol{n})\boldsymbol{B} \times \boldsymbol{n} = \mu\boldsymbol{n} \tag{7.7}$$

where μ is a constant. Taking the scalar product of Eq. (7.7) with $\boldsymbol{B}$, we obtain:

$$\mu \boldsymbol{n} \cdot \boldsymbol{B} = 0 . \tag{7.8}$$

The constant μ can be found to equal $\gamma \boldsymbol{\Omega} \cdot \boldsymbol{n}$. Thus if $\mu = 0$, then the easy axis of the particle remains perpendicular to the axis of rotation of the magnetic field tracing out the *yz*-plane as it rotates. If instead, $\boldsymbol{n} \cdot \boldsymbol{B} = 0$, the easy axis remains perpendicular to the magnetic field. If the easy axis points along the rotation axis of ***B*** (*x*-axis), then we recover the trivial solution previously discussed. Otherwise, ***n*** points somewhere between the *x*-axis and the *yz*-plane. In this case, as ***n*** rotates, it traces out the surface of a cone.

7.1.1 Planar Solution

For the planar solution $\boldsymbol{\Omega} \perp \boldsymbol{n}$. If we take the cross product of Eq. (7.2) with ***B*** and compare to (7.7), we get the following:

$$\boldsymbol{m} \times \boldsymbol{B} = \gamma \boldsymbol{\Omega} . \tag{7.9}$$

This is equivalent to the synchronously rotating standard nonuniform oscillator equation we previously derived in Chapter 5 for frequencies smaller than the critical frequency ($\Omega \leq \Omega_C = mB / \gamma$). Note, in this treatment we prescribed that the particle rotation rate was equal to the magnetic rotation rate. Thus, planar asynchronous rotation will not be acquired from these equations. Planar solutions were shown to exponentially relax to their steady states.

7.1.2 Conical Solution

For the non-trivial conical solution, $\boldsymbol{B} \perp \boldsymbol{n}$ and the scalar product of Eq. (7.2) with ***n*** results in the solution that $2\lambda K = 1$. In this case, ***n*** rotates about the *x*-axis in a plane perpendicular to ***B***. The sign of μ determines if ***n*** points towards the $+x$ or $-x$ direction. The cone half-angle ψ that ***n*** makes with the *x*-axis is given by:

$$\tan^2 \psi = \frac{1 - (B / B_A)^2}{(\Omega_N)^2 - 1 + (B / B_A)^2} \tag{7.10}$$

where $B_A = 2Km$ is defined as the anisotropy field and Ω_N is our normalized frequency ratio Ω/Ω_C. Neither the numerator nor the denominator can be negative, which defines several conditions for the steady state solutions. The external magnetic field cannot exceed this anisotropy field or the particle will change magnetization. We did not observe any changes in magnetization due to the weak magnetic field strengths used for rotation in our experiments (<10 *Oe*). From the denominator, we see that $\Omega_N > \sqrt{1-(B/B_A)^2}$. This suggests there are frequencies at which both planar and conical solutions exist. In practice, both conical and planar motions were observed at certain frequencies close to Ω_C depending on from what side the frequency value was approached.

Caroli and Pincus [38] also studied the stability of the conical solutions with respect to small disturbances. They showed that the solutions for ***n*** and ***m*** both oscillate about their initial positions with a characteristic frequency given by:

$$\Omega_p = \Omega\sqrt{1-\left(\frac{\Omega_C}{\Omega}\right)^2} . \tag{7.11}$$

Recall from Chapter 5 that for asynchronously rotating magnetic particles, the average rotation rate was observed to be $\langle\dot{\theta}\rangle = \Omega - \sqrt{\Omega^2 - \Omega_C^2}$. Thus, we see that oscillations in the conical solutions of motion could be observed as light fluctuations with frequency $\Omega_p = \Omega - \langle\dot{\theta}\rangle$.

Eq. (7.5) was re-written in terms of two first-order differential equations assuming $B \ll B_A$. Using our non-dimensional time $\tau = \Omega_C t$, these equations can written as

$$\frac{d\phi}{d\tau} = \Omega_N - \frac{\sin\phi}{n_t} \tag{7.12}$$

$$\frac{dn}{d\tau} = \Omega_N (1-n_t^2)\cos\phi . \tag{7.13}$$

Where $\boldsymbol{n}_t$ is the projection of ***n*** in the *yz*-plane and ϕ is the phase lag between ***B*** and $\boldsymbol{n}_t$. Note that if $n_t = 1$, we recover the planar solution for our original nonuniform oscillator.

7.2 Orientation-Dependent Friction Coefficient

The theory introduced by Caroli and Pincus [38] reviewed in the previous section was for an isotropic sphere with a symmetric rotational drag coefficient along all three axes given as $\gamma_{rot} = \kappa\eta V$ where κ is the shape factor = 6, η is the dynamic viscosity of the

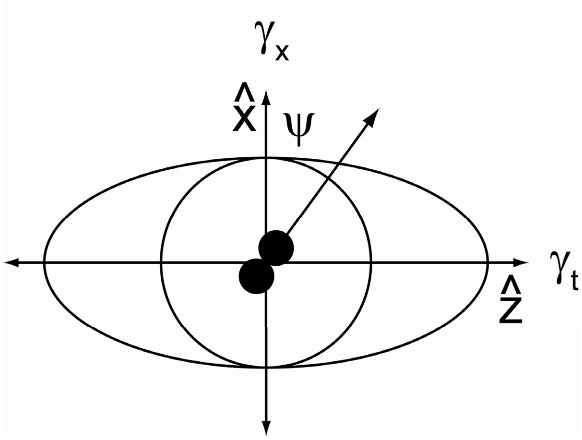

Figure 7.1 Rotational drag coefficient ellipsoid for a dimer. When the easy axis of the dimer (indicated by the arrow joining the two spheres) points along the *x*-direction, the drag coefficient is γ_x. When the easy axis lies in the *yz*-plane, the drag coefficient is γ_t. For a cone half-angle of ψ, the drag coefficient equals the length at which the arrow intersects the ellipsoid whose major and minor axes are $2\gamma_t$ and $2\gamma_x$, respectively.

surrounding fluid and *V* is the volume of the sphere. For a dimer of magnetic microspheres, the easy axis ***n*** is along the axis that connects the centers of each sphere. Dimers of spheres are only symmetric along two axis, thus the rotational drag coefficient about an axis perpendicular to the easy axis (let us call this γ_t) is different than the drag coefficient γ_x around the other two axes. For axes in between these two extremes, we define the drag coefficient ellipsoid shown in Figure 7.1.

We see that when the easy axis lies in the *yz*-plane, end-over-end rotation occurs and the drag coefficient is γ_t. For solutions where the easy axis points out of the *yz*-plane, the drag coefficient lies between γ_x and γ_t. The precise value can be acquired from the following equation for this ellipse:

$$\frac{1}{\gamma^2(\psi)} = \frac{\sin^2\psi}{\gamma_t^2} + \frac{\cos^2\psi}{\gamma_x^2}. \tag{7.14}$$

It is known that the shape factor for rotation about an axis perpendicular to the easy axis is 11.22 [178]. The shape factor for rotation about the easy axis can be determined by using the ratio of corresponding diffusion coefficients [191]:

$$G = \frac{\gamma_t}{\gamma_x} = \frac{D_x}{D_t} = \frac{3.3708}{1.5957}. \tag{7.15}$$

When the dimer is rotated at frequencies exceeding the critical frequency, the particle cannot keep up with the magnetic field due to the rotational drag. If the dimer escapes into the third dimension, ψ increases and the dimer's rotational drag coefficient reduces in order to keep up with the field. As a result, the tilted dimer will have a new critical frequency depending on its steady state ψ value. This new critical frequency can be derived from Eq. (7.14) to get:

$$\Omega_C(\psi) = \Omega_{C,t} \frac{\gamma_t}{\gamma(\psi)} = \Omega_{C,t}\sqrt{G^2 \cos^2 \psi + \sin^2 \psi} \tag{7.16}$$

where $\Omega_{C,t} = mB/\gamma_t$. Similarly, the cone half-angle formula must be adjusted:

$$\tan^2 \psi = \frac{G^2}{\left(\frac{\Omega}{\Omega_C, t}\right)^2 - 1}. \tag{7.17}$$

Last, Eqs. (7.12) and (7.13) must be adjusted to account for the anisotropic drag:

$$\frac{d\phi}{d\tau} = \frac{\Omega}{\Omega_C(\psi)} - \frac{\sin\phi}{n_t} \tag{7.18}$$

$$\frac{dn}{d\tau} = \frac{\Omega}{\Omega_C(\psi)}(1 - n_t^2)\cos\phi \tag{7.19}$$

where Eq. (7.16) is used for the cone half-angle dependent critical frequency.

7.3 Simulated Trajectories

Eqs. (7.18) and (7.19) were solved using a Runge-Kutta 4th order algorithm and trajectories were animated in 3-D space to aid in understanding the motional dynamics. If the initial conditions were chosen to coincide with steady state solutions of the equations, the motion of the dimer depicted periodic rotation about the x-axis with a constant half-angle ψ. Figure 7.2(a) shows a planar solution for $\Omega_N = 0.5$, $n_t = 1$ while (b) shows a conical solution for $\Omega_N = 1.5$, $n_t = 2/3$. In all cases, an isotropic drag coefficient is assumed unless otherwise mentioned. The trajectory of the tip of the ***n*** vector (blue) shows horizontal circles at different heights corresponding to $n_z = \sqrt{1 - n_t^2}$. The magnetic field vector is indicated as a green arrow. Also, the shading of the spheres

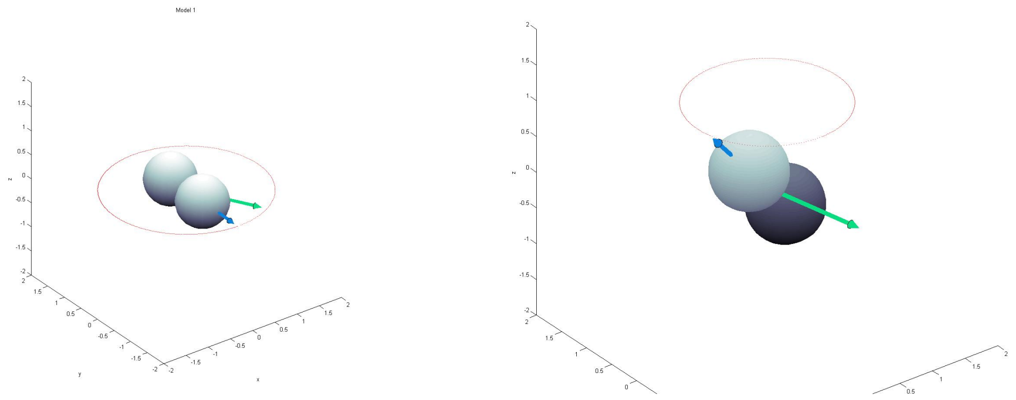

Figure 7.2 Simulated trajectories of a dimer undergoing 3-D rotation assuming an isotropic drag coefficient. (a) planar solution $\Omega_N = 0.5$, $n_t = 1$ (b) conical solution $\Omega_N = 1.5$, $n_t = 2/3$.

corresponds to the height along the *x*-axis (this coordinate system was chosen to coincide with experiments described in previous chapters.

The trajectories strongly depend on the initial conditions chosen. Figure 7.3(a) shows the case of $\Omega_N = 0.5$, $n_t = 0.8$ where $\boldsymbol{n}$ starts outside the *yz*-plane and slowly decays back to the planar solution because $\Omega_N < 1$. Figure 7.3(b) shows a similar conical solution as previously but with $\Omega_N = 1.5$, $n_t = 1/1.4$. The slight change in the initial condition resulted in persistent oscillations in the trajectory.

We can examine the trajectories using the same initial conditions, but using our anisotropic drag coefficient equations. These results appear in Figure 7.4 and Figure 7.5 In Figure 7.4(a), $\Omega_N = 0.5$, $n_t = 0.8$ and the same planar solution results since the drag

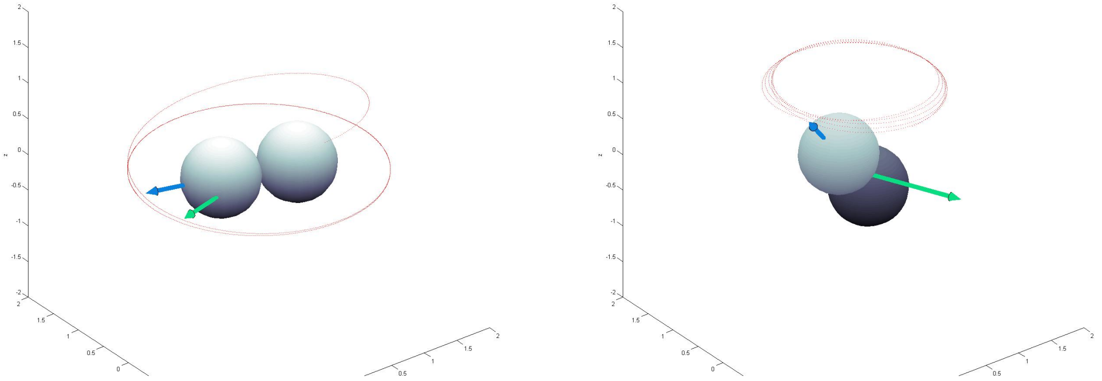

Figure 7.3 Simulated trajectories of a dimer undergoing 3-D rotation assuming an isotropic drag coefficient. (a) planar solution $\Omega_N = 0.5$ (b) conical solution $\Omega_N = 1.5$.

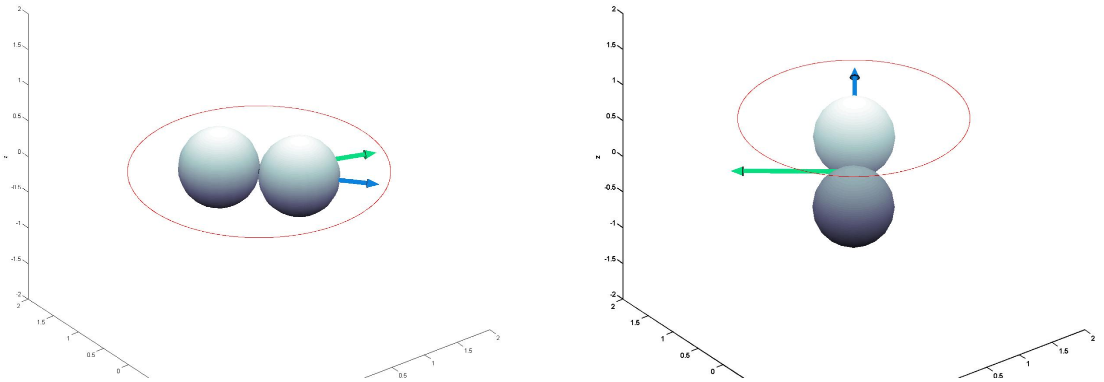

Figure 7.4 Simulated trajectories of a dimer undergoing 3-D rotation assuming an isotropic drag coefficient. (a) planar solution $\Omega_N = 0.5$, $n_t = 1$ (b) conical solution $\Omega_N = 1.5$, $n_t = 0.8838$.

coefficient doesn't change. Figure 7.4(b) shows the conical solution including anisotropic drag. The diameter of the trajectory is wider since the dimer can flatten out a little more with its reduced drag compared to the isotropic drag solution. In Figure 7.5(a), the reduced drag out of the plane can support slightly higher rotation rates, thus dimer can relax into the plane slightly (almost imperceptibly) more quickly. In Figure 7.5(b) the slight change in initial conditions from the steady state solution causes considerable precession and nutation of the dimer. One should note, however, that Eqs. (7.8) and (7.9) including anisotropic drag are not rigorous for solutions other than steady state ones in which n_t does not change. Small perturbations from steady state may show gradual oscillations in the trajectories whereas larger perturbations could change

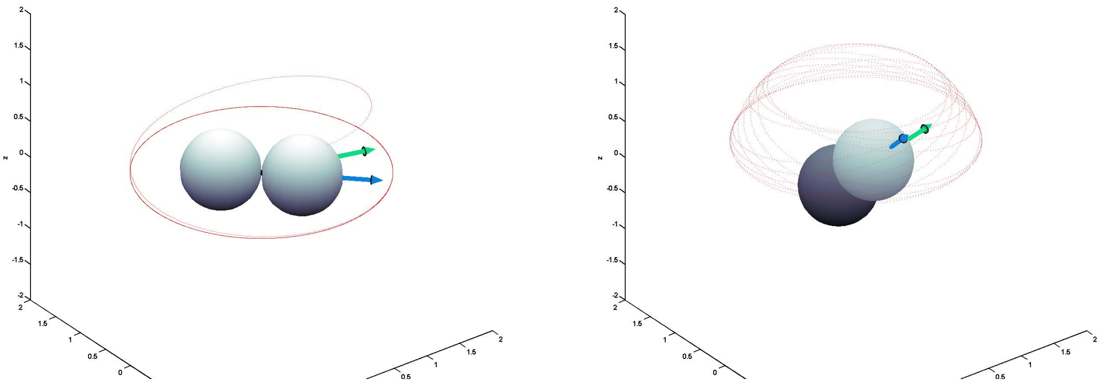

Figure 7.5 Simulated trajectories of a dimer undergoing 3-D rotation assuming an anisotropic drag coefficient. (a) planar solution $\Omega_N = 0.5$, $n_t = 0.8$ (b) conical solution $\Omega_N = 1.5$, $n_t = 2/3$.

the trajectories drastically and no longer be physically relevant.

7.4 Comparison to Experiment

In our experiments on nonuniformly rotating dimers of magnetic microspheres, we observed particles exhibiting planar end-over-end rotation at frequencies below Ω_C. In such cases, the dimer axis remained in the *yz*-plane perpendicular to the axis of rotation of the magnetic field. When the frequency was increased just beyond Ω_C, the dimer was seen to rotate with a slight angle outside of the plane. After increasing the magnetic rotation rate further, the dimers exhibited precession-like motion rotating about an axis which itself was very slowly rotating about the magnetic rotation axis. Even with some single half-coated particles, the nature of the rotation often appears to exhibit precession-like motion rather than purely planar rotation.

Performing the usual data analysis on these systems entails the use of Fourier transform techniques to observe the periodic fluctuations in the frequency domain. Standard procedure for analyzing nonuniform rotation data is to locate the external driving frequency and disregard any peaks at higher values. Any fluctuations that are faster than the magnetic rotation rate are likely due to inconsistencies in the half-coating or scattering/reflection from magnetic colloids distributed from each other at distances less than half the circumference of the particle (for example, if 4 colloids are distributed around the equator of the particle, we expect to see harmonics indicating fluctuations at 4x the rotation rate frequency). If no discernible peaks can be found at frequencies lower than the driving frequency, the system is likely rotating synchronously. When low frequency peaks appear, they can either be true asynchronous rotation fluctuations, or low frequency drift due to the particle translating out of the focus.

We typically get results that agree with those predicted by our standard nonuniform equation. For example, Figure 7.6 shows the power spectrum for a half coated particle rotating at $\Omega = 0.25\ Hz$. The average rotation rate was measured to be $\left\langle \dot{\theta} \right\rangle = 0.035\, Hz$. According to Eq. (7.11), we should expect to see light fluctuations due to oscillations at the characteristic frequency $\Omega - \left\langle \dot{\theta} \right\rangle = 0.215\ Hz$. If we look to the left of the external magnetic rotation rate, we see two smaller peaks which correspond to this characteristic

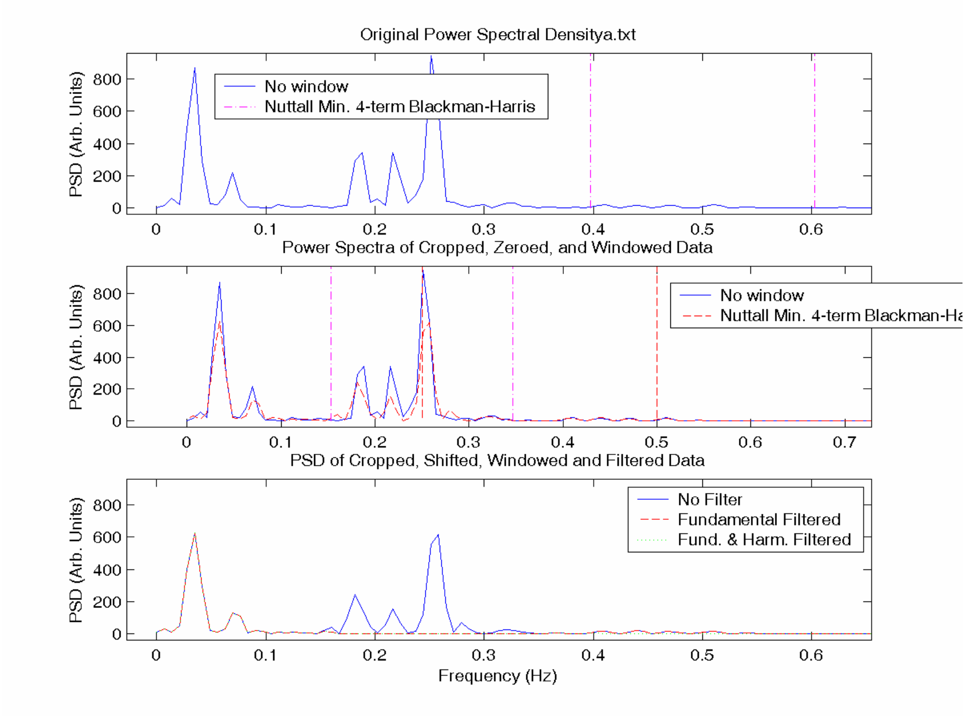

Figure 7.6 PSD's of a nonuniformly rotating dimer of magnetic microspheres driven by a magnetic field at $\Omega = 0.25$ *Hz*. Mixing between the average rotation rate and its second harmonic appear as peaks just the left of the peak of the external driving frequency. These peaks are due to the characteristic frequency of oscillations in the steady state solutions of the 3-dimensional rotation.

frequency. The second of the two is due to the subtraction of the second harmonic of the average rotation rate which also has a sizable peak in the graph of Figure 7.6.

7.5 Conclusions

The motional dynamics of a 3-D nonuniformly rotating dimer of magnetic microspheres has been analyzed theoretically, experimentally and numerically. All methods seem to agree in the qualitative description of the steady state motion. Two distinct regimes exist. One is a planar rotation at in which the dimer appears to be confined to rotate in a plane perpendicular to the axis of rotation. These planar solutions include both synchronous and asynchronous rotation with the magnetic field. The other regime occurs at higher rotation frequencies in which the magnetic dimer can no longer keep up with the magnetic field due to rotational drag. In this case, if the dimer experiences the slightest perturbation to adjust its angle out of the plane, it will escape the plane and undergo 3-D rotation. The concept of slipping in 3-D rotation is intuitively similar to that for restricted planar motion – when the dimer cannot keep up with the magnetic field, it assumes the quickest route to re-align with the field, which would be out of the plane of rotation.

The knowledge and understanding of nonlinear dynamics systems like these 3-D rotators can also be of practical use. For example, for particles with strong frictional anisotropy, the dynamics may be distinctly different. If one can detect motional differences due to anisotropic drag on microscale rotating objects, the recognition of such motion could enhance already existing techniques of pathogen detection using nonuniform oscillators. For example, in addition to detecting the presence of bacteria, one could use motional information to help identify the strain based on shape or orientation.

CHAPTER 8

CONCLUSIONS AND FUTURE DIRECTIONS

8.1 Conclusions

Hybrid particle systems can serve as valuable sensors controlled by magnetic and optical manipulation schemes as long as one can establish a balance between the most beneficial properties of each constituent material. For example, near-resonance trapping of our hybrid particles showed weak enhancements, if any, and considerable heat generation. Instead of augmenting optical tweezing forces, the high particle-number-density shells of our core-shell and half-shell systems served to destabilize the trap [128] by increasing forces due to scattering and reflection. Wavelength-tunable trapping and assembly of much smaller particle sizes [19, 95, 96] and molecules [127], however, have shown evidence that resonance-based manipulation can, in fact, occur.

Optical and magnetic manipulation is a natural choice for controlling the behavior of dielectric and magnetic hybrid microspheres. But, as we saw with the optical illumination of dimers of magnetic microspheres, an increased magnetic content makes it easier to probe high-viscosity media by shifting the nonlinear region to more accessible frequencies. At the same time, increased magnetic content renders the system more likely to absorb optical illumination and cause potentially destructive heating. Once again, a balance must be achieved between the material distribution of hybrid particles and the manipulation schemes being used.

The interplay between magnetic and optical manipulation can reveal opportunities for cooperative control. Numerical simulations suggest an optical scattering force can increase the average rotation rate of nonlinearly rotating hybrid microspheres, as long as absorption and heat generation do not obscure the effect. As was calculated in Chapter 5, magnetic field strengths achievable in practice offer a superior means of rotating appropriate micro-objects compared to optical torques typically found with optical tweezers. But optical tweezers can provide a non-invasive method of translating or translationally confining individual microparticles, as was done to study the frictional properties of particles rolling while slipping along surfaces. By reducing the laser intensity, we can control absorption and mitigate its effects of heat generation and scattering force to gain a potentially powerful sensor. It is this synergistic balance between the particle materials and the manipulation schemes that provides opportunities for innovative research.

8.2 Future Directions

The work described in this thesis is far from an exhaustive account of even the most popular non-invasive manipulation methods and particle sensor architectures used in present day science. Advances in optical and magnetic tweezers design continue to evolve as do developments in sensor probe design for nanobiotechnology. Incorporation of these improvements into the research described here is just one possible future direction. The microscopic size scale is ideal for the creation of cellular biomimetic devices and probes for extra-cellular studies while nano- and mesoscopic-sized probes can explore systems of smaller dimensions such as intra-cellular mechanisms, protein mechanics or virus morphology. The scaling of our systems to the nanometer size regime is yet another prospective direction worth investigating.

Numerous alternatives exist for the optical and magnetic manipulation of micro- and nanoscale particles. Optical tweezing geometries other than the single beam gradient TEM_{00} mode trap could be used to three-dimensionally hold metallic and hybrid particles. Two counter-propagating beams can trap absorptive particles by squeezing the particle axially using the scattering force from each side while radially trapping the particle using the gradient force of both beams. Another option is to use spatial beam shaping to trap absorptive particles, such as TEM_{01} donut mode beams. Such shaped helical mode beams can also transfer angular orbital momentum to particles [192] causing them to rotate due to applied optical torque. Instead of having a single trap, holographic arrays of optical tweezers can be constructed using spatial light modulators to create computer-generated light distributions [193, 194]. By trapping magnetic particles in such arrays, the dynamic motion of nonlinearly rotating particles interacting with each other can be studied. Such systems may exhibit chaotic behavior or serve as models that mimic coupled-oscillating neurons. Also, the use of electromagnets or electrically controlled magnetic pole structures could enable significantly increased magnetic field strengths that can be shut off or pulsed without affecting instrumentation alignment. Increased magnetic torque as well as the introduction of optical torque may allow microrheology measurements in highly viscous or complex fluids. Merging these manipulation alternatives [163-165] further enhances the flexibility of mechanically controlling hybrid particles.

Our hybrid particles are mechanical sensors that measure properties such as viscosity, friction, and temperature in viscous fluids. The devices, developed in the Kopelman Group, can naturally be extended to incorporate other sensing capabilities. Hybrid particles containing gold or silver colloids can show evidence of surface enhanced Raman scattering. Other hybrid particle architectures may provide easier plasmon tunability such as metal-dielectric core-shell particles [48, 107, 195]. Combining plasmonic hybrid particles [46-49] with optical tweezing [128, 196, 197] may provide developments toward new single-molecule spectral analysis techniques. With the aid of optical tweezers, ultrafast characterization [198] and control [199] of nanoparticles could also yield new directions in research. Ultrafast spectroscopy of single trapped nanoparticles or nanoparticle systems may offer a means of studying single-particle and single-molecule femtochemistry. Ultrafast optical tweezing of magnetic colloids and hybrid particles could also be used to measure demagnetization caused by laser-induced optical breakdown [200].

There are also many biological directions to which our hybrid particle systems and manipulation schemes can be applied. The three-dimensional nonlinear rotation of hybrid particles likely depends on the shape anisotropy of the rotating particle. Sensing changes in the nonlinear dynamical motion may allow shape or orientation differentiation of detected pathogens [66]. The rolling behavior of neutrophils along blood vessel walls [132, 137, 138] can be mimicked with our magnetic particle surface rolling experiments. Further studies on adhesion and binding properties of the rolling objects could be relevant in the fabrication of cell sorting and cell separation microfluidic [138, 201] and optofluidic [202] devices.

Finally, unexpected behaviors often emerge at the nanoscale. It is unclear whether the motional behavior of our rotating hybrid particles is preserved at nanometer dimensions. Small nanoparticles will absorb less light and thus generate less total heat when optically perturbed. By scaling down our hybrid particles in size, not only can the spectral properties change, but the maximum achievable magnetic and optical torque magnitudes are also reduced. Thermal fluctuations due to Brownian rotation can become significant thus affecting the nonlinear dynamical motion of the particles [203]. Such small nanosensors can serve as models of sub-cellular structures, be used to probe intra-cellular environments themselves, as well as provide a platform for detecting even smaller biological entities such as proteins and viruses.

APPENDIX

APPENDIX A

NANOPARTICLES FOR TWO-PHOTON PHOTODYNAMIC THERAPY IN LIVING CELLS

VOLUME 6, NUMBER 11, NOVEMBER 2006

NANO
LETTERS

Letters

Nanoparticles for Two-Photon Photodynamic Therapy in Living Cells

De Gao,[†] Rodney R. Agayan,[†,‡] Hao Xu,[§] Martin A. Philbert,[§] and Raoul Kopelman*[,†,‡]

Department of Chemistry, University of Michigan, Ann Arbor, Michigan 48109-1055, Department of Applied Physics, University of Michigan, Ann Arbor, Michigan 48109-1120, Department of Environmental Health Sciences, University of Michigan, Ann Arbor, Michigan 48109-2029

Received July 24, 2006; Revised Manuscript Received October 9, 2006

ABSTRACT

We describe here a nontoxic two-photon photodynamic nanoparticle platform and its cellular application. We demonstrate that the dye's potential toxicity can be circumvented by its permanent encapsulation into a biocompatible nanoparticle polymer matrix; this was examined by dye leaching experiments and confirmed by cell uptake experiments. Infrared two-photon nanoplatform phototoxicity was demonstrated for rat C6 glioma cells, while the controls showed no dark toxicity for these living cells.

Brain cancers are the most aggressive human cancers. No single treatment has yet been found to arrest the fast growth of malignant gliomas. Photodynamic therapy (PDT), a light-activated chemotherapeutic treatment, may be an effective approach, possibly in combination with others, such as neurosurgical operative techniques and radiotherapy. In PDT, irradiated photosensitizers that surround or enter cells transfer their energy to molecular oxygen, thus forming highly reactive singlet oxygen ($^1O_2$) and other reactive oxygen

---

* Corresponding author. E-mail: kopelman@umich.edu. Telephone: 734-764-7541. Fax: 734-936-2778.

[†] Department of Chemistry.

[‡] Department of Applied Physics.

[§] Department of Environmental Health Sciences.

10.1021/nl0617179 CCC: $33.50

species which, in turn, kill the nearby cells. This method has been developed for the treatment of a variety of cancerous tumors.[1] Serious challenges arise, however, with the traditional single-photon PDT for glioma tissues.[2] For example, currently approved single-photon PDT drugs have the drawback of requiring excitation by visible light, which has limited penetration depth due to the restrictive tissue transparency window for target cells that are located deep inside living tissues; photons in this spectral region do not penetrate deep enough, thus making single-photon PDT less effective for glioma tissue treatment. As an alternative method, two-photon PDT (TP-PDT) has more advantages than that of one-photon PDT. In TP-PDT, dye molecules can simultaneously absorb two less-energetic photons into the excited electronic state. The excited molecules then react with oxygen to produce singlet oxygen. The excitation of two-photon dyes in the near-infrared region (tissue infrared spectral window is between 700 and 1100 nm) avoids tissue absorbing or scattering and makes it possible to treat deeper diseased tissues in vivo. However, the direct application of drugs to the brain is limited by the drug's distribution and toxicity. These drug molecules usually also harm normal cells even before they reach their target cells. For example, 5,10,15,20-tetrakis(1-methyl 4-pyridinio) porphyrin tetra(*p*-toluenesulfonate) (TMPyP) is a positively charged molecule that can bind to DNA. In cultures, it binds to negatively charged cell surfaces and then it is internalized into the cells; the consequent binding between TMPyP and DNA affects cell viability.[3] Although several recent reports directly applied water-soluble dyes to living HeLa cells and YPEN-1 rat prostate endothelial cells,[4] the dyes' own toxicity to cells remains an open question.

Entrapping TP photosensitizers in biologically inert nanoparticles can eliminate or limit the photosensitizer's toxicity to normal cells, provide deeper light penetration, and cause less photodamage to normal cells and tissues than single-photon PDT. Therefore, TP dye-encapsulating photodynamic nanoplatforms offer an avenue for circumventing the above problems. Various molecules with relatively large TP absorption cross sections have been designed as TP singlet oxygen sensitizers in order to achieve high TP quantum yield.[5] This made it possible for us to evaluate TP-PDT nanoplatforms for their toxicity and phototoxicity in living cells. The objective of the present study was the evaluation of TMPyP encapsulating nanoparticles as to both their dark toxicity and their TP-PDT efficiency for rat C6 glioma cells. This is the first investigation on such nanoplatform safety as well as their TP-PDT for glioma cell cultures, to the best of our knowledge. We demonstrate here that the long-term encapsulation of a commercially available TP dye (TMPyP) by nanoparticles can prevent the dye from direct contact with cells, but at the same time, the dye can still kill cells efficiently by singlet-oxygen production when exposed to near-infrared light.

Polyacrylamide-based nanoparticles offer numerous advantages compared to other nanoplatforms. They are hydrophilic polymers that are physically similar to tissues due to their relatively high water content and soft, flexible consistency. These nanoparticles show minimal aggregation or adsorption of proteins from body fluids, owing to their low interfacial tension and neutral surface charge. Also, the size of polyacrylamide-based nanoparticles is easily controlled by varying the synthesis conditions. Furthermore, polyacrylamide can be easily copolymerized with other monomers so as to introduce functional groups as targeting tags or to control their rate of biodegradation.

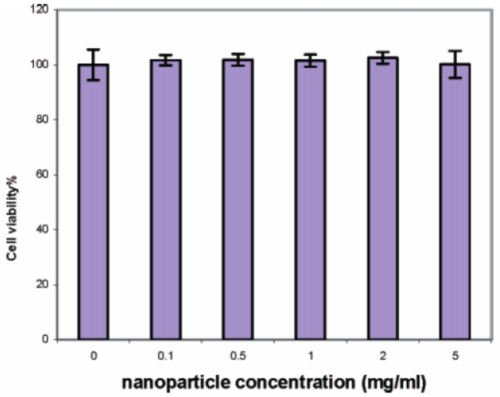

Figure 1. Cell viability evaluated by MTT assay. Each calculation was an average of eight measurements.

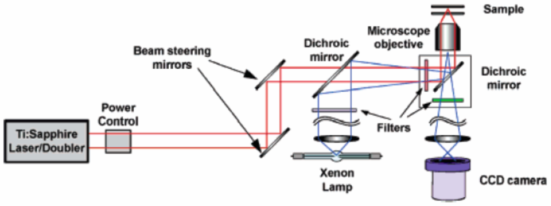

Figure 2. Two-photon microscopy setup

To apply nanoparticles to cells or tissues, the nanoplatform's toxicity must be taken into account. Inverse microemulsion was used to fabricate blank or dye-encapsulating polyacrylamide nanoparticles in a water/hexane system.[6] The blank nanoparticle's toxicity to cells was then tested. 3-(4,5-Dimethylthiazol-2-yl)-2, 5-diphenyl tetrazolium bromide (MTT) was used to examine cell viability after 24 h incubation with various concentrations of blank polyacrylamide-based nanoparticles. Cell toxicity assays showed almost 100% cell viability, even after incubation with 5 mg/mL of polyacrylamide nanoparticles (Figure 1). This nontoxicity of polyacrylamide-based nanoparticles agrees with extensive studies on such carriers for drug delivery.[7,8]

To demonstrate that the nanoparticle matrix can prevent the dye from direct contact with the surroundings, fluorescent dye-encapsulating nanoparticles were used for leaching tests. Calcein-AM (0.5 mL, 1 mg/mL, Molecular Probes) was dissolved in DMSO and further diluted into 1 mL water. This aqueous solution was used to encapsulate calcein into polyacrylamide-based nanoparticles by the previously mentioned synthetic method.[6] The nanoparticles were extensively washed with ethanol and water. Calcein AM is a fluorogenic esterase substrate that can be hydrolyzed to produce green

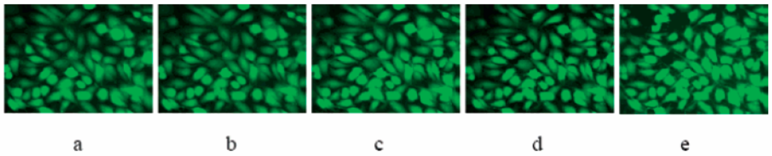

Figure 3. Cell viability after exposing to filtered xenon lamp: (a) before xenon lamp irradiation; (b) after xenon lamp irradiation, 0 min; (c) after xenon lamp irradiation, 10 min; (d) after xenon lamp irradiation, 30 min; (e) after xenon lamp irradiation, 90 min. Cells remain viable up to 90 min after exposure.

fluorescence. The calcein fluorescence of the nanoparticles increased after hydrolysis but was not observed in the filtrate, indicating that the calcein dye remained within the matrix and did not leach out into the surrounding solution (Supporting Information Figure 1S and Figure 2S). The protection of the cell from the dye molecules was further confirmed by incubating the dye-containing nanoparticles with rat C6 glioma cells. Calcein-encapsulating particles (1 mg/mL) were incubated with rat C6 glioma cells for 1 h. After that, the cells were washed with fresh medium and monitored by confocal fluorescence microscopy. No calcein fluorescence was observed within the cells, indicating again that the calcein was still encapsulated inside the polyacrylamide matrix without leaching. This was consistent with our previous leaching experiments and demonstrated that the nanoparticles can keep the dye molecules within the matrix and thus prevent direct dye contact with the surroundings. Therefore, it is quite plausible that the nanoplatforms did not cause cellular toxicity. One should also note that the polymer's neutral surface, high hydrophilicity, low tendency for protein absorption, as well as its high water content, generally could enable these nanoparticles to evade cellular endocytosis. Furthermore, our polyacrylamide-based nanoparticles have high water solubility and therefore reduced cell uptake.

To develop a TP-PDT nanoplatform, TMPyP was encapsulated into nanoparticles by a method similar to the previous one.[6] The nanoparticle's diameter was observed by SEM to be 20−30 nm (Figure 3S). Singlet oxygen generation by these particles was studied using a fluorescence-based method.[6a] In a typical experiment, a 1 mg/mL nanoparticle suspension was repeatedly irradiated with a 780 nm laser source in the presence of 1 μM of anthracene-dipropionic acid (ADPA). ADPA fluorescence spectra excited at 378 nm were then recorded after every irradiation. Results showed that the TP dye-encapsulating nanoparticles did produce significant amounts of singlet oxygen under 780 nm laser irradiation.

Although many new TP-PDT dyes were synthesized and were tested for their PDT effect,[5] there is no previous report of TP-PDT in living cells yet. This absence may be the result of the toxicity of these drugs to cells and/or their limited solubility in aqueous environment. To evaluate the nanoparticles' TP-PDT efficiency on the cellular level, a TP microscopy system was set up as shown in Figure 2. A pulsed laser source at 780 nm (Tsunami, Spectra Physics) was coupled to a 40× objective on an inverted microscope, exposing the dye to TP excitation. Reported irradiance values were calculated at the sample plane by multiplying the irradiance measured before the objective by the estimated scaling factor of the microscope system. A xenon lamp was used to excite fluorescent cell stains to indicate live cells (calcein, green) or dead cells (propidium iodide, red). Optical filters were inserted to restrict the excitation wavelength regions of both light sources.

We initially found that the cells were dying after exposure to xenon lamp light alone during cell viability imaging. Thus, conditions for xenon lamp control experiments were first established to maintain cell viability during microscopy monitoring. Rat C6 glioma cells on glass cover slips were placed in a temperature-controlled sample chamber at 37 °C in culture medium and exposed to xenon lamp light for different durations. After insertion of the appropriate optical filter to block wavelengths below 450 nm (Figure 4S), the cells remained alive in all control experiments (Figure 3).

The laser fluence was a critical parameter for cell survival. Rat C6 glioma cells were exposed to 3 W/cm^2 of 780 nm laser light for 30 s (100 J/cm^2). Cells appeared to be damaged 10 min later. All exposed cells appeared to be dead after 30 min (Figure 5S). When the laser exposure was optimized to 100 mW/cm^2 for 1 s (100 mJ/cm^2), all exposed cells were still alive 30 min later. We used this lower approximate fluence for the next experiments (Figure 6S).

Under the above-optimized experimental conditions, cells were incubated with 1 mg/mL of nanoparticles, and the cells were monitored using fluorescence microscopy at different time points. Without nanoparticles, all cells were viable even after 120 min (Figure 4a−d). Cells incubated with TMPyP-encapsulating nanoparticles started to show cell death 90 min after exposure to 100 mW/cm^2 pulsed light for 1 s (100 mJ/cm^2) (Figure 7S). When the exposure time was extended to about a minute (10 J/cm^2), cells started to die 30 min later and most exposed cells were dead after 120 min (Figure 4e−h). The exposure time can be further optimized if necessary. These results show that TP-PDT was an effective tool for killing cells. We note that the nanoparticle's phototoxicity was only triggered by exposure to light, specifically to low-power pulsed near-infrared laser illumination over a short time period.

The above test tube and in vitro results indicate that polyacrylamide-based nanoparticles are feasible platforms for TP-PDT. The relatively small size of these nanoparticles facilitates the diffusion of singlet oxygen from particle to cell, although even much larger polyacrylamide particles also exhibited efficient phototoxicity in single-photon PDT experiments.[9] Because the biocompatible nanoplatform is not taken up by C6 glioma cells or other cell lines, it is expected that nonspecific cell binding would be reduced.

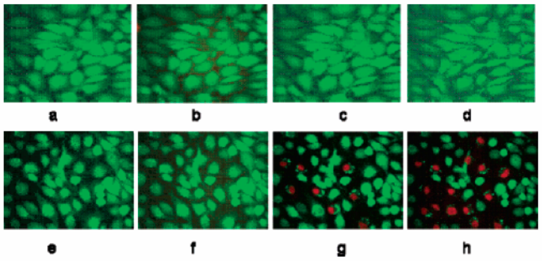

Figure 4. (a–d) Rat C6 glioma cells exposed to 100 mW/cm^2, 780 nm laser for 1 min. Images were taken at different time points: (a) before irradiation; (b) right after irradiation; (c) 40 min after irradiation; (d) 120 min after irradiation. (e–h) Rat C6 glioma cells incubated with 1 mg/mL TMPyP-encapsulated nanoparticles and exposed to 100 mW/cm^2 780 nm laser for 1 min. Images were taken at different time points: (e) before irradiation; (f) right after irradiation; (g) 30 min after irradiation; (h) 130 min after irradiation.

In conclusion, we have demonstrated that toxic drugs can be encapsulated into a neutral, hydrophilic matrix by microemulsion so as to avoid drug toxicity to cell cultures. This nontoxic matrix is biologically inert and is not usually ingested by endocytosis or other internalization mechanisms. Further modification of the nanoplatform with cancer surface biomarkers such as folic acid or other anticancer antibodies could guide the particle to specifically targeted cancer cells with less nonspecific damage.[10] As near-infrared TP excitation can give deeper tissue imaging there is no doubt that NP-TP-PDT will enable deeper tissue photodynamic therapy.[11] Our results demonstrate that, while safe, this TP-PDT nanoplatform does kill glioma cancer cells in vitro and may thus have potential for application to deep tissue therapy.

Acknowledgment. This work was supported by National Cancer Institute UIP contract N01-CO-37123.

Supporting Information Available: Calcein-AM encapsulated in nanoparticle; dye-encapsulating nanoparticle's SEM; light filter transmittance for blocking xenon lamp; laser power optimization for cell culture. This material is available free of charge via the Internet at http://pubs.acs.org.

References

(1) (a) Dougherty, T. J.; Gomer, C. J.; Henderson, B. W.; Jori, G.; Kessel, D.; Korbelik, M.; Moan, J.; Peng, Q. *J. Natl. Cancer Inst.* **1998**, *90*, 889–905. (b) Sharman, W. M.; Allen, C. M.; van Lier, J. E. *Drug Discovery Today* **1999**, *4*, 507–517. (c) Gross, S.; Gilead, A.; Scherz, A.; Meeman, M.; Salomon, Y. *Nat. Med.* **2003**, *9*, 1327–1331. (d) Dennis, E. J.; Dolmans, G. J.; Fukumura, D.; Jain, R. K. *Nat. Rev.* **2003**, *3*, 380–387.

(2) Noske, D. P.; Wolbers, J. G.; Sterenborg, H. J. C. M. *Clin. Neurol. Neurosurg.* **1991**, *93–94*, 293–307.

(3) (a) Zebger, I.; Snyder, J. W.; Andersen, L. K.; Poulsen, L.; Gao, Z.; Lambert, J. D. C.; Kristiansen, U.; Ogilby, P. R. *Photochem. Photobiol.* **2004**, *79*, 319–322. (b) Romanova, N. A.; Brovko, L. Y.; Moore, L.; Pometun, E.; Savitsky, A. P.; Ugarova, N. N.; Griffiths, M. W. *Appl. Environ. Microbiol.* **2003**, *69*, 6393–6398.

(4) (a) Ogawa, K.; Hasegawa, H.; Inaba, Y.; Kobuke, Y.; Inouye, H.; Kanemitsu, Y.; Kohno, E.; Hirano, T.; Ogura, S.; Okura, I. *J. Med. Chem.* **2006**, *49*, 2276–2283. (b) Karotki, A.; Khurana, M.; Lepock, J. R.; Wilson, B. C. *Photochem. Photobiol.* **2006**, *82*, 443–452

(5) (a) Nielsen, C. B.; Johnsen, M.; Arnbjerg, J.; Pittelkow, M.; McIlroy, S. P.; Ogilby, P. R.; Jrgensen, M. *J. Org. Chem.* **2005**, *70*, 7065–7079. (b) Oar, M. A.; Serin, J. M.; Dichtel, W. R.; Fréchet, J. M.; Ohulchanskyy, T. Y.; Prasad, P. N. *Chem. Mater.* **2005**, *17*, 2267–2275. (c) Frederiksen, P. K.; McIlroy, S. P.; Nielsen, C. B.; Nikolajsen, L.; Skovsen, E.; Jrgensen, M.; Mikkelsen, K. V.; Ogilby, P. R. *J. Am. Chem. Soc.* **2005**, *127*, 255–269. (d) Drobizhev, M.; Stepanenko, Y.; Dzenis, Y.; Karotki, A.; Rebane, A.; Taylor, P. N.; Anderson, H. L. *J. Am. Chem. Soc.* **2004**, *126*, 15352–15353.

(6) (a) Moreno, M. J.; Monson, E.; Reddy, R. G.; Rehemtulla, A.; Ross, B. D.; Philbert, M.; Schneider, R. J.; Kopelman, R. *Sens. Actuators, B* **2003**, *90*, 82–89. (b) Clark, H. A.; Hoyer, M.; Philbert, M. A.; Kopelman, R. *Anal. Chem.* **1999**, *71*, 4831–4836.

(7) Ross, B.; Rehemtulla, A.; Koo, Y. E. L.; Reddy, R.; Kim, G.; Behrend, C.; Buck, S.; Schneider, R. J.; Philbert, M. A.; Weissleder, R.; Kopelman, R. *Proc. SPIE-Int. Soc. Opt. Eng.* **2004**, *5331*, 76–83.

(8) Schneider, R. J., Ph.D. Thesis, University of Michigan, Ann Arbor, MI, 2005

(9) Tang, W.; Kopelman, R.; Xu, H.; Philbert, M. *Photochem. Photobiol.* **2005**, *81*, 242–249.

(10) (a) Harrell, J. A.; Kopelman, R. *Biophotonics Int.* **2000**, *7*, 22–24. (b) Kopelman, R.; Philbert M.; Koo, Y.-E. L.; Moffat, B. A.; Reddy, G. R.; McConville, P.; Hall, D. E.; Chenevert, T. L.; Bhojani, M. S.; Buck, S. M.; Rehemtulla, A.; Ross, B. D. *J. Magn. Magn. Mater.* **2005**, *293*, 404–410.

(11) Cahalan, M. D.; Parker, I.; Wei, S. H.; Miller, M. J. *Nat. Rev. Immunol.* **2002**, *2*, 872–880.

NL0617179

Nanoparticles for Two-photon Photodynamic Therapy in Living Cells

De Gao[1], Rodney R. Agayan[1,2], Hao Xu[3], Martin A. Philbert[3], Raoul Kopelman[1,2*]

[1.] *Department of Chemistry, University of Michigan, Ann Arbor, MI 48109-1055*

[2.] *Department of Applied Physics, University of Michigan, Ann Arbor, MI 48109-1120*

[3.]*Department of Environmental Health Sciences, University of Michigan, Ann Arbor, MI 48109-2029*

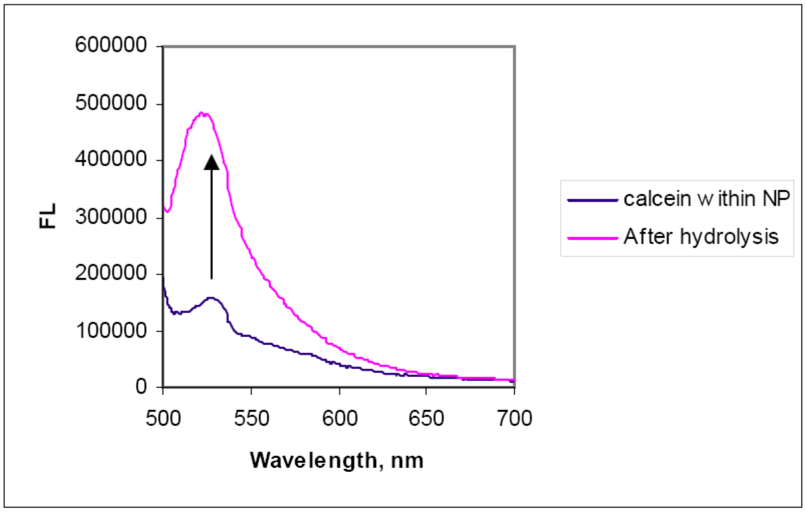

Figure 1S. Calcein-AM was encapsulated in nanoparticle. The Calcein fluorescence increased after it was hydrolyzed with NaOH. This indicated the dyes were encapsulated within nanoparticles

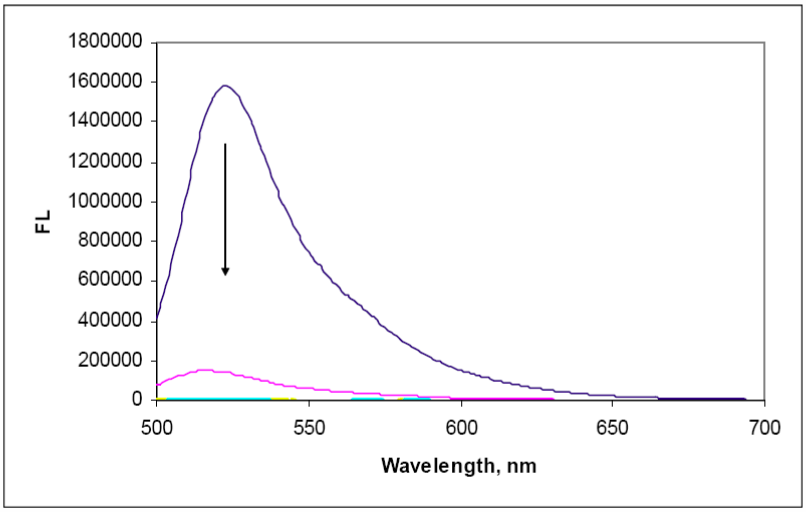

Figure 2S. This experiment indicated that the nanoparticles matrix can protect dye from interacting with surrounding. There is not any calcein in filtrate after several washings with ethanol and water. This experiment indicated no dye leaching from the nanoparticles

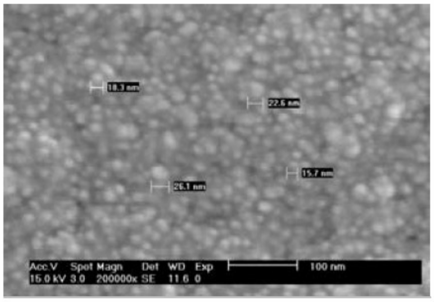

Figure 3S. Dye-encapsulating nanoparticle's SEM. The typical nanoparticle's size is around 30nm in diameter

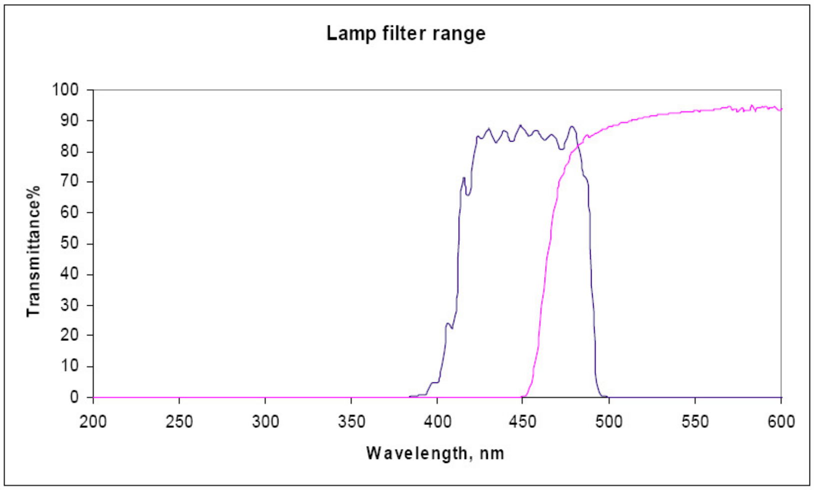

Figure 4S. Light Filter transmittance for blocking xenon lamp. We found that the xenon lamp can also cause cell killing. A filter was used to block xenon lamp emission light above 450 nm and below 500 nm. This will let calcein and PI emission spectra passing through the filter and block xenon lamp emission when we take imaging

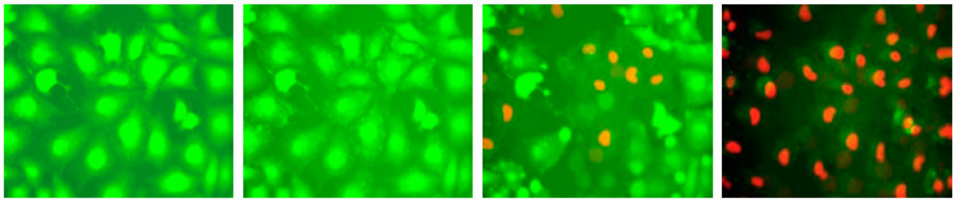
a b c d

Figure 5S. Laser power optimization for cell culture. Rat C6 glioma cells were exposed to 2 mW of 780 nm laser for 30 seconds. Then the cells were monitored with fluorescence microscopy at different time points. a: before laser irradiation; b: after laser irradiation, 0 minute; c: after laser irradiation, 10 minutes; d: after laser irradiation, 30 minutes. The experiment showed that the cells started to death after them exposed to 2mW laser power for 30 seconds.

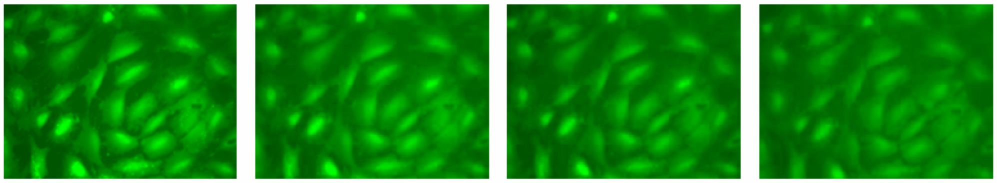

a b c d

Figure 6S. Cells were exposed to 78 uW of 780 nm laser for 1 minute. The cell viability was assayed by fluorescence microscopy a: before laser irradiation; b: after laser irradiation, 0minute; c: after laser irradiation, 10minutes; d: after laser irradiation, 30minutes. These results showed that the laser power was cells were alive for 30minutes after irritated with 780 nm laser.

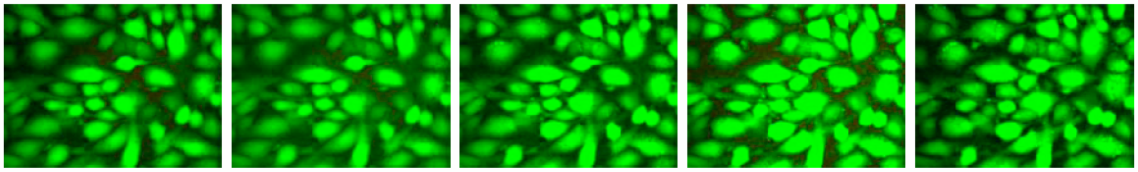

Without irritation After irritation 0min After irritation 10min After irritation 30min After irritation 60min

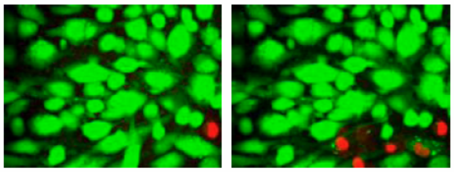

After irritation 90min After irritation 120min

Figure 7S. Laser exposing time optimization. Cell viability exposed to 78 uW of 780nm laser for 1 second, with nanoparticles incubation. these results showed that the 1 second exposure time was short. Cell killing only started after 90 min.

BIBLIOGRAPHY

[1] S.M. Buck, H. Xu, M. Brasuel, M.A. Philbert, and R. Kopelman, "Nanoscale probes encapsulated by biologically localized embedding (PEBBLEs) for ion sensing and imaging in live cells*," Talanta* **63**(1), 41-59 (2004).

[2] H. Xu, S.M. Buck, R. Kopelman, M.A. Philbert, M. Brasuel, B.D. Ross, and A. Rehemtulla, "Photoexcitation-based nano-explorers: Chemical analysis inside live cells and photodynamic therapy*," Israel J. Chem.* **44**(1-3), 317-337 (2004).

[3] S.L.R. Barker, R. Kopelman, T.E. Meyer, and M.A. Cusanovich, "Fiber-optic nitric oxide-selective biosensors and nanosensors*," Anal. Chem.* **70**(5), 971-976 (1998).

[4] S.L.R. Barker and R. Kopelman, "Development and cellular applications of fiber optic nitric oxide sensors based on a gold-adsorbed fluorophore*," Anal. Chem.* **70**(23), 4902-4906 (1998).

[5] S.L.R. Barker, H.A. Clark, S.F. Swallen, R. Kopelman, A.W. Tsang, and J.A. Swanson, "Ratiometric and fluorescence lifetime-based biosensors incorporating cytochrome c' and the detection of extra- and intracellular macrophage nitric oxide*," Anal. Chem.* **71**(9), 1767-1772 (1999).

[6] A. Ashkin, "Forces of a single-beam gradient laser trap on a dielectric sphere in the ray optics regime*," Biophys. J.* **61**(2), 569-582 (1992).

[7] A. Ashkin, "Optical trapping and manipulation of neutral particles using lasers*," P. Natl. Acad. Sci. U.S.A.* **94**(10), 4853-4860 (1997).

[8] A. Ashkin, J.M. Dziedzic, J.E. Bjorkholm, and S. Chu, "Observation of a single-beam gradient force optical trap for dielectric particles*," Opt. Lett.* **11**(5), 288-290 (1986).

[9] A. Ashkin and J.P. Gordon, "Stability of radiation-pressure particle traps - an optical Earnshaw theorem*," Opt. Lett.* **8**(10), 511-513 (1983).

[10] A. Ashkin, J.M. Dziedzic, and T. Yamane, "Optical trapping and manipulation of single cells using infrared laser beams*," Nature* **330**, 769-771 (1987).

[11] A. Ashkin and J.M. Dziedzic, "Internal cell manipulation using infrared laser traps*," P. Natl. Acad. Sci. U.S.A.* **86**, 7914-7918 (1989).

[12] K.O. Greulich, G. Pilarczyk, A. Hoffmann, G. Meyer Zu Hörste, B. Schäfer, V. Uhl, and S. Monajembashi, "Micromanipulation by laser microbeam and optical tweezers: From plant cells to single molecules*," J. Microsc.* **198**(Pt 3), 182-187 (2000).

[13] A. Ashkin, K. Schütze, J.M. Dziedzic, U. Euteneuer, and M. Schliwa, "Force generation of organelle transport measured in vivo by an infrared laser trap," *Nature* **348**(6299), 346-348 (1990).

[14] H. Liang, W.H. Wright, S. Cheng, W. He, and M.W. Berns, "Micromanipulation of chromosomes in PTK2 cells using laser microsurgery (optical scalpel) in combination with laser-induced optical force (optical tweezers)," *Exp. Cell Res.* **204**(1), 110-120 (1993).

[15] K. Sasaki, Z.Y. Shi, R. Kopelman, and H. Masuhara, "Three-dimensional pH microprobing with an optically-manipulated fluorescent particle," *Chem. Lett.*(2), 141-142 (1996).

[16] K. Svoboda and S.M. Block, "Optical trapping of metallic Rayleigh particles," *Opt. Lett.* **19**(13), 930-932 (1994).

[17] R.R. Agayan, C. Schmidt, F. Gittes, and R. Kopelman. "Laser tweezing near resonance absorption," in *Photon Migration, Optical Coherence Tomography, and Microscopy*. 2001: SPIE.

[18] R.R. Agayan, F. Gittes, R. Kopelman, and C.F. Schmidt, "Optical trapping near resonance absorption," *Appl. Optics* **41**(12), 2318-2327 (2002).

[19] J.R. Arias-González and M. Nieto-Vesperinas, "Optical forces on small particles: attractive and repulsive nature and plasmon-resonance conditions," *J. Opt. Soc. Am. A* **20**(7), 1201-1209 (2003).

[20] F. Svedberg and M. Käll, "On the importance of optical forces in surface-enhanced Raman scattering (SERS)," *Faraday Discuss.* **132**, 35-44 (2006).

[21] F.H.C. Crick and A.F.W. Hughes, "The physical properties of cytoplasm : A study by means of the magnetic particle method Part I. Experimental," *Exp. Cell. Res.* **1**(1), 37-80 (1950).

[22] F. Ziemann, J. Radler, and E. Sackmann, "Local measurements of viscoelastic moduli of entangled actin networks using an oscillating magnetic bead micro-rheometer," *Biophys. J.* **66**(6), 2210-2216 (1994).

[23] F. Amblard, B. Yurke, A. Pargellis, and S. Leibler, "A magnetic manipulator for studying local rheology and micromechanical properties of biological systems," *Rev. Sci. Instrum.* **67**(3), 818-827 (1996).

[24] T.R. Strick, J.F. Allemand, D. Bensimon, A. Bensimon, and V. Croquette, "The elasticity of a single supercoiled DNA molecule," *Science* **271**, 1835-1837 (1996).

[25] A. Bausch, W. Moller, and E. Sackmann, "Measurement of local viscoelasticity and forces in living cells by magnetic tweezers," *Biophys. J.* **76**(1), 573-579 (1999).

[26] A. de Vries, B. Krenn, R. van Driel, and J. Kanger, "Micro magnetic tweezers for nanomanipulation inside live cells," *Biophys. J.* **88**(3), 2137-2144 (2005).

[27] M. Tanase, N. Biais, and M. Sheetz, "Magnetic tweezers in cell biology," *Methods Cell. Biol.* **83**, 473-493 (2007).

[28] C.J. Behrend, J.N. Anker, and R. Kopelman, "Brownian modulated optical nanoprobes," *Appl. Phys. Lett.* **84**(1), 154-156 (2004).

[29] J. Anker, C. Behrend, and R. Kopelman, "Aspherical magnetically modulated optical nanoprobes (MagMOONs)," *J. Appl. Phys.* **93**(10), 6698-6700 (2003).

[30] J. Anker and R. Kopelman, "Magnetically modulated optical nanoprobes," *Appl. Phys. Lett.* **82**(7), 1102-1104 (2003).

[31] C.J. Behrend, J.N. Anker, B.H. McNaughton, M. Brasuel, M.A. Philbert, and R. Kopelman, "Metal-capped Brownian and magnetically modulated optical nanoprobes (MOONs): Micromechanics in chemical and biological microenvironments," *J. Phys. Chem. B* **108**(29), 10408-10414 (2004).

[32] C.J. Behrend, J.N. Anker, B.H. McNaughton, and R. Kopelman, "Microrheology with modulated optical nanoprobes (MOONs)," *J. Magn. Magn. Mater.* **293**(1), 663-670 (2005).

[33] B.H. McNaughton, K.A. Kehbein, J.N. Anker, and R. Kopelman, "Sudden breakdown in linear response of a rotationally driven magnetic microparticle and application to physical and chemical microsensing," *J. Phys. Chem. B* **110**(38), 18958-18964 (2006).

[34] J.N. Anker, *Modulated Optical Nanoprobes (MOONs) in the Nanokitchen*, in *Applied Physics*. 2005, University of Michigan: Ann Arbor.

[35] B.H. McNaughton, *Magnetic micro and nano nonlinear oscillators with applications to the dynamic detection of a single bacterium and to physical and chemical sensing*, in *Applied Physics*. 2007, University of Michigan: Ann Arbor.

[36] F. Gittes and C.F. Schmidt, "Thermal noise limitations on micromechanical experiments," *Eur. Biophys. J. Biophy.* **27**(1), 75-81 (1998).

[37] S.H. Strogatz, *Nonlinear Dynamics and Chaos*. 1994: Addison-Wesley Reading, MA.

[38] C. Caroli and P. Pincus, "Response of an isolated magnetic grain suspended in a liquid to a rotating field," *Z. Phys. B Con. Mat.* **9**(4), 311-319 (1969).

[39] F. Caruso, "Nanoengineering of particle surfaces," *Adv. Mater.* **13**(1), 11-22 (2001).

[40] E. Katz and I. Willner, "Integrated nanoparticle-biomolecule hybrid systems: Synthesis, properties, and applications," *Angew. Chem. Int. Edit.* **43**(45), 6042-6108 (2004).

[41] A. Burns, H. Ow, and U. Wiesner, "Fluorescent core-shell silica nanoparticles: towards 'Lab on a Particle' architectures for nanobiotechnology," *Chem. Soc. Rev.* **35**(11), 1028-1042 (2006).

[42] D.M. Willard, T. Mutschler, M. Yu, J. Jung, and A. Van Orden, "Directing energy flow through quantum dots: Towards nanoscale sensing," *Anal. Bioanal. Chem.* **384**(3), 564-571 (2006).

[43] P. Jain, X. Huang, I. El-Sayed, and M. El-Sayed, "Review of some interesting surface plasmon resonance-enhanced properties of noble metal nanoparticles and their applications to biosystems," *Plasmonics* **2**(3), 107-118 (2007).

[44] S. Link and M.A. El-Sayed, "Spectral properties and relaxation dynamics of surface plasmon electronic oscillations in gold and silver nanodots and nanorods," *J. Phys. Chem. B* **103**(40), 8410-8426 (1999).

[45] W.A. Murray and W.L. Barnes, "Plasmonic materials," *Adv. Mater.* **19**(22), 3771-3782 (2007).

[46] S.D. Hudson and G. Chumanov, "Synthesis and characterization of plasmonic asymmetric hybrid nanoparticles," *Chem. Mater.* **19**(17), 4222-4227 (2007).

[47] W. Shi, Y. Sahoo, M.T. Swihart, and P.N. Prasad, "Gold nanoshells on polystyrene cores for control of surface plasmon resonance," *Langmuir* **21**(4), 1610-1617 (2005).

[48] H. Wang, D.W. Brandl, F. Le, P. Nordlander, and N.J. Halas, "Nanorice: A hybrid plasmonic nanostructure," *Nano Lett.* **6**(4), 827-832 (2006).

[49] E. Prodan, C. Radloff, N.J. Halas, and P. Nordlander, "A hybridization model for the plasmon response of complex nanostructures," *Science* **302**(5644), 419-422 (2003).

[50] K.E. Peceros, X. Xu, S.R. Bulcock, and M.B. Cortie, "Dipole-dipole plasmon interactions in gold-on-polystyrene composites," *J. Phys. Chem. B* **109**(46), 21516-21520 (2005).

[51] J. Crowley, N. Sheridon, and L. Romano, "Dipole moments of gyricon balls*,"* *J. Electrostat.* **55**(3-4), 247-259 (2002).

[52] J. Choi, Y. Zhao, D. Zhang, S. Chien, and Y.H. Lo, "Patterned fluorescent particles as nanoprobes for the investigation of molecular interactions*,"* *Nano Lett.* **3**(8), 995-1000 (2003).

[53] F.S. Merkt, A. Erbe, and P. Leiderer, "Capped colloids as light-mills in optical traps*,"* *New J. Phys.* **8**(9), 216 (2006).

[54] B.H. McNaughton, R.R. Agayan, J.X. Wang, and R. Kopelman, "Physiochemical microparticle sensors based on nonlinear magnetic oscillations*,"* *Sens. Actuators B* **121**(1), 330-340 (2007).

[55] D. Pissuwan, S. Valenzuela, and M. Cortie, "Therapeutic possibilities of plasmonically heated gold nanoparticles*,"* *Trends Biotechnol.* **24**(2), 62-67 (2006).

[56] L.P. Ghislain, N.A. Switz, and W.W. Webb, "Measurement of small forces using an optical trap*,"* *Rev. Sci. Instrum.* **65**(9), 2762-2768 (1994).

[57] Y. Liu, D.K. Cheng, G.J. Sonek, M.W. Berns, C.F. Chapman, and B.J. Tromberg, "Evidence for localized cell heating induced by infrared optical tweezers*,"* *Biophys. J.* **68**(5), 2137-2144 (1995).

[58] A. Schönle and S.W. Hell, "Heating by absorption in the focus of an objective lens*,"* *Opt. Lett.* **23**, 325-327 (1998).

[59] S.P. Gross, "Application of optical traps *in vivo,"* *Method. Enzymol.* **361**, 162-174 (2003).

[60] H. Mao, J.R. Arias-González, S.B. Smith, I. Tinoco Jr., and C. Bustamante, "Temperature control methods in a laser tweezers system*,"* *Biophys. J.* **89**(2), 1308-1316 (2005).

[61] E. Peterman, F. Gittes, and C. Schmidt, "Laser-induced heating in optical traps*,"* *Biophys. J.* **84**(2), 1308-1316 (2003).

[62] R. Zondervan, F. Kulzer, H. van der Meer, J. Disselhorst, and M. Orrit, "Laser-driven microsecond temperature cycles analyzed by fluorescence polarization microscopy*,"* *Biophys. J.* **90**(8), 2958-2969 (2006).

[63] A. Govorov and H. Richardson, "Generating heat with metal nanoparticles*,"* *Nano Today* **2**(1), 30-38 (2007).

[64] Y. Seol, A. Carpenter, and T. Perkins, "Gold nanoparticles: Enhanced optical trapping and sensitivity coupled with significant heating," *Opt. Lett.* **31**(16), 2429-2431 (2006).

[65] R.R. Agayan, T. Horvath, B.H. McNaughton, J. Anker, and R. Kopelman. "Optical manipulation of metal-silica hybrid nanoparticles," in *Optical Trapping and Optical Micromanipulation*. 2004: SPIE.

[66] B.H. McNaughton, R.R. Agayan, R. Clarke, R. Smith, and R. Kopelman, "Single bacterial cell detection with nonlinear rotational frequency shifts of driven magnetic microspheres," *Appl. Phys. Lett.* **91**(22) (2007).

[67] A. Ashkin, "Acceleration and trapping of particles by radiation pressure," *Phys. Rev. Lett.* **24**(4), 156-159 (1970).

[68] A. Ashkin, "Trapping of atoms by resonance radiation pressure," *Phys. Rev. Lett.* **40**(12), 729-732 (1978).

[69] M.P. Sheetz, *Laser Tweezers in Cell Biology*. Methods in Cell Biology. Vol. 55. 1998, New York: Academic Press.

[70] K. Svoboda and S.M. Block, "Biological applications of optical forces," *Annu. Rev. Bioph. Biom.* **23**, 247-285 (1994).

[71] A. Ashkin, "Atomic-beam deflection by resonance-radiation pressure," *Phys. Rev. Lett.* **25**(19), 1321-1324 (1970).

[72] J.P. Gordon, "Radiation forces and momenta in dielectric media," *Phys. Rev. A* **8**(1), 14-21 (1973).

[73] J.P. Gordon and A. Ashkin, "Motion of atoms in a radiation trap," *Phys. Rev. A* **21**(5), 1606-1617 (1980).

[74] J.D. Jackson, *Classical Electrodynamics*. 1999, John Wiley & Sons, Inc.: New York. p. 309, 456-459.

[75] Y. Harada and T. Asakura, "Radiation forces on a dielectric sphere in the Rayleigh scattering regime," *Opt. Commun.* **124**(5-6), 529-541 (1996).

[76] A. Ashkin, J.M. Dziedzic, and P.W. Smith, "Continuous-wave self-focusing and self-trapping of light in artificial Kerr media," *Opt. Lett.* **7**(6), 276-278 (1982).

[77] J.E. Bjorkholm, R.R. Freeman, A. Ashkin, and D.B. Pearson, "Observation of focusing of neutral atoms by dipole forces of resonance-radiation pressure," *Phys. Rev. Lett.* **41**(20), 1361-1364 (1978).

[78] S. Chu, J.E. Bjorkholm, A. Ashkin, and A. Cable, "Experimental-observation of optically trapped atoms*,"* *Phys. Rev. Lett.* **57**(3), 314-317 (1986).

[79] P. Meystre and M. Sargent III., *Elements of Quantum Optics*. 1999, New York: Springer.

[80] P.C. Chaumet and M. Nieto-Vesperinas, "Time-averaged total force on a dipolar sphere in an electromagnetic field*,"* *Opt. Lett.* **25**(15), 1065-1067 (2000).

[81] B.T. Draine, "The discrete-dipole approximation and its application to interstellar graphite grains*,"* *Astrophys. J.* **333**(2), 848-872 (1988).

[82] H.C. van de Hulst, *Light Scattering by Small Particles*. 1957, New York: John Wiley & Sons, Inc.

[83] A. Yariv, *Quantum Electronics*. 1989, New York: John Wiley & Sons, Inc.

[84] J.P. Barton and D.R. Alexander, "5th-order corrected electromagnetic-field components for a fundamental Gaussian-beam*,"* *J. Appl. Phys.* **66**(7), 2800-2802 (1989).

[85] P.W. Milonni and J.H. Eberly, *Lasers*. 1988, New York: John Wiley & Sons, Inc.

[86] A.E. Siegman, *Lasers*. 1986, Sausalito: University Science Books.

[87] L.D. Landau and E.M. Lifshitz, *Course of Theoretical Physics*, in *Electrodynamics of Continuous Media*. 1960, Pergamon Press: New York. p. 280-281.

[88] N.W. Ashcroft and N.D. Mermin, *Solid State Physics*. 1976, New York: Saunders College Publishing.

[89] R. Loudon, *The Quantum Theory of Light*. 1973, New York: Oxford University Press.

[90] D.C. Cronemeyer, "Optical absorption characteristics of pink ruby*,"* *J. Opt. Soc. Am.* **56**(12), 1703-1706 (1966).

[91] C.D. Keefe, "Curvefitting imaginary components of optical properties: Restrictions on the lineshape due to causality*,"* *J. Mol. Spectrosc.* **205**(2), 261-268 (2001).

[92] W.H. Press, S.A. Teulosky, W.T. Vetterling, and B.P. Flannery, *Numerical Recipes in C*. 2nd ed. 1992, Cambridge: Cambridge University Press.

[93] Goodfellow. *Ruby*. 2001 [cited 2001 September 3]; Available from: http://www.goodfellow.com/static/E/AJ60.HTML.

[94] G.M. Hale and M.R. Querry, "Optical constants of water in the 200 nm to 200 μm wavelength region," *Appl. Optics* **12**, 555-563 (1973).

[95] K.C. Toussaint, M. Liu, M. Pelton, J. Pesic, M.J. Guffey, P. Guyot-Sionnest, and N.F. Scherer, "Plasmon resonance-based optical trapping of single and multiple Au nanoparticles," *Opt. Express* **15**(19), 12017-12029 (2007).

[96] A.S. Zelenina, R. Quidant, G. Badenes, and M. Nieto-Vesperinas, "Tunable optical sorting and manipulation of nanoparticles via plasmon excitation," *Opt. Lett.* **31**(13), 2054-2056 (2006).

[97] U. Bockelmann, "Single-molecule manipulation of nucleic acids," *Curr. Opin. Struc. Biol.* **14**(3), 368-373 (2004).

[98] D.G. Grier, "A revolution in optical manipulation," *Nature* **424**(6950), 810-816 (2003).

[99] J.E. Molloy, K. Dholakia, and M.J. Padgett, "Preface: Optical tweezers in a new light," *J. Mod. Optic* **50**(10), 1501-1507 (2003).

[100] J.E. Molloy and M.J. Padgett, "Lights, action: Optical tweezers," *Contemp. Phys.* **43**(4), 241-258 (2002).

[101] K. Sasaki, M. Koshioka, H. Misawa, N. Kitamura, and H. Masuhara, "Pattern-formation and flow-control of fine particles by laser-scanning micromanipulation," *Opt. Lett.* **16**(19), 1463-1465 (1991).

[102] H.M. Warrick, R.M. Simmons, J.T. Finer, T.Q.P. Uyeda, S. Chu, and J.A. Spudich, "*In vitro* methods for measuring force and velocity of the actin-myosin interaction using purified proteins," *Methods Cell. Biol.* **39**, 1-21 (1993).

[103] E.R. Dufresne and D.G. Grier, "Optical tweezer arrays and optical substrates created with diffractive optics," *Rev. Sci. Instrum.* **69**(5), 1974-1977 (1998).

[104] J. Liesener, M. Reicherter, T. Haist, and H.J. Tiziani, "Multi-functional optical tweezers using computer-generated holograms," *Opt. Commun.* **185**(1-3), 77-82 (2000).

[105] A. Ashkin and J.M. Dziedzic, "Observation of light-scattering from nonspherical particles using optical levitation," *Appl. Optics* **19**(5), 660-668 (1980).

[106] P. Galajda and P. Ormos, "Complex micromachines produced and driven by light," *Appl. Phys. Lett.* **78**(2), 249-251 (2001).

[107] P. Viravathana and D.W.M. Marr, "Optical trapping of titania/silica core-shell colloidal particles," *J. Colloid Interf. Sci.* **221**(2), 301-307 (2000).

[108] W.E. Doering and S.M. Nie, "Spectroscopic tags using dye-embedded nanoparticies and surface-enhanced Raman scattering," *Anal. Chem.* **75**(22), 6171-6176 (2003).

[109] X.H. Gao and S.M. Nie, "Quantum dot-encoded mesoporous beads with high brightness and uniformity: Rapid readout using flow cytometry," *Anal. Chem.* **76**(8), 2406-2410 (2004).

[110] H. Furukawa and I. Yamaguchi, "Optical trapping of metallic particles by a fixed Gaussian beam," *Opt. Lett.* **23**(3), 216-218 (1998).

[111] J. Prikulis, F. Svedberg, M. Kall, J. Enger, K. Ramser, M. Goksor, and D. Hanstorp, "Optical spectroscopy of single trapped metal nanoparticles in solution," *Nano Lett.* **4**(1), 115-118 (2004).

[112] F. Yan, H. Xu, J. Anker, R. Kopelman, B. Ross, A. Rehemtulla, and R. Reddy, "Synthesis and characterization of silica-embedded iron oxide nanoparticles for magnetic resonance imaging," *J. Nanosci. Nanotechnol.* **4**(1-2), 72-76 (2004).

[113] R.M. Simmons, J.T. Finer, S. Chu, and J.A. Spudich, "Quantitative measurements of force and displacement using an optical trap," *Biophys. J.* **70**(4), 1813-1822 (1996).

[114] W. Singer, S. Bernet, N. Hecker, and M. Ritsch-Marte, "Three-dimensional force calibration of optical tweezers," *J. Mod. Optic* **47**(14-15), 2921-2931 (2000).

[115] H. Felgner, O. Muller, and M. Schliwa, "Calibration of light forces in optical tweezers," *Appl. Optics* **34**(6), 977-982 (1995).

[116] N. Malagnino, G. Pesce, A. Sasso, and E. Arimondo, "Measurements of trapping efficiency and stiffness in optical tweezers," *Opt. Commun.* **214**(1-6), 15-24 (2002).

[117] K. Berg-Sørensen and H. Flyvbjerg, "Power spectrum analysis for optical tweezers," *Rev. Sci. Instrum.* **75**(3), 594-612 (2004).

[118] A. Buosciolo, G. Pesce, and A. Sasso, "New calibration method for position detector for simultaneous measurements of force constants and local viscosity in optical tweezers," *Opt. Commun.* **230**(4-6), 357-368 (2004).

[119] K. Berg-Sørensen, L. Oddershede, E.L. Florin, and H. Flyvbjerg, "Unintended filtering in a typical photodiode detection system for optical tweezers," *J. Appl. Phys.* **93**(6), 3167-3176 (2003).

[120] I.M. Tolic-Nørrelykke, K. Berg-Sørensen, and H. Flyvbjerg, "MatLab program for precision calibration of optical tweezers," *Comput. Phys. Commun.* **159**(3), 225-240 (2004).

[121] F. Osterloh, H. Hiramatsu, R. Porter, and T. Guo, "Alkanethiol-induced structural rearrangements in silica-gold core-shell-type nanoparticle clusters: An opportunity for chemical sensor engineering," *Langmuir* **20**(13), 5553-5558 (2004).

[122] Y.A. Sun and Y.N. Xia, "Triangular nanoplates of silver: Synthesis, characterization, and use as sacrificial templates for generating triangular nanorings of gold," *Adv. Mater.* **15**(9), 695-699 (2003).

[123] M. Born and E. Wolf, *Principles of Optics*. 6th ed. 1980, New York, NY: Cambridge University Press.

[124] F. Gittes and C.F. Schmidt, "Interference model for back-focal-plane displacement detection in optical tweezers," *Opt. Lett.* **23**(1), 7-9 (1998).

[125] F. Gittes and C.F. Schmidt, "Signals and noise in micromechanical measurements," *Methods Cell. Biol.* **55**, 129-156 (1998).

[126] A.T. O'Neil and M.J. Padgett, "Three-dimensional optical confinement of micron-sized metal particles and the decoupling of the spin and orbital angular momentum within an optical spanner," *Opt. Commun.* **185**(1-3), 139-143 (2000).

[127] H. Li, D. Zhou, H. Browne, and D. Klenerman, "Evidence for resonance optical trapping of individual fluorophore-labeled antibodies using single molecule fluorescence spectroscopy," *J. Am. Chem. Soc.* **128**(17), 5711-5717 (2006).

[128] P. Jordan, J. Cooper, G. McNay, F.T. Docherty, W.E. Smith, G. Sinclair, and M.J. Padgett, "Three-dimensional optical trapping of partially silvered silica microparticles," *Opt. Lett.* **29**, 2488-2490 (2004).

[129] Y. Xia, B. Gates, Y. Yin, and Y. Lu, "Monodispersed colloidal spheres: Old materials with new applications," *Adv. Mater.* **12**(10), 693-713 (2000).

[130] B. Bhushan, J. Israelachvili, and U. Landman, "Nanotribology: Friction, wear and lubrication at the atomic scale," *Nature* **374**(6523), 607-616 (1995).

[131] S. Kim, D. Asay, and M. Dugger, "Nanotribology and MEMS," *Nano Today* **2**(5), 22-29 (2007).

[132] I. Gebeshuber, "Biotribology inspires new technologies," *Nano Today* **2**(5), 30-37 (2007).

[133] K.D. Bonin, B. Kourmanov, and T.G. Walker, "Light torque nanocontrol, nanomotors and nanorockers," *Opt. Express* **10**(19), 984-989 (2002).

[134] Z. Cheng, T. Mason, and P.M. Chaikin, "Periodic oscillation of a colloidal disk near a wall in an optical trap," *Phys. Rev. E* **68**(5), 051404 (2003).

[135] Z. Burton and B. Bhushan, "Hydrophobicity, adhesion, and friction properties of nanopatterned polymers and scale dependence for micro- and nanoelectromechanical systems," *Nano Lett.* **5**(8), 1607-1613 (2005).

[136] R. Duffadar and J. Davis, "Interaction of micrometer-scale particles with nanotextured surfaces in shear flow," *J. Colloid Interf. Sci.* **308**(1), 20-29 (2007).

[137] D.A. Hammer and S.M. Apte, "Simulation of cell rolling and adhesion on surfaces in shear flow: General results and analysis of selectin-mediated neutrophil adhesion," *Biophys. J.* **63**(1), 35-57 (1992).

[138] S. Hong, D. Lee, H. Zhang, J.Q. Zhang, J.N. Resvick, A. Khademhosseini, M.R. King, R. Langer, and J.M. Karp, "Covalent immobilization of P-selectin enhances cell rolling," *Langmuir* **23**(24), 12261-12268 (2007).

[139] K. Erglis, Q. Wen, V. Ose, A. Zeltins, A. Sharipo, P.A. Janmey, and A. Cēbers, "Dynamics of magnetotactic bacteria in a rotating magnetic field," *Biophys. J.* **93**(4), 1402-1412 (2007).

[140] A. Cēbers and M. Ozols, "Dynamics of an active magnetic particle in a rotating magnetic field," *Phys. Rev. E* **73**(2) (2006).

[141] G. Helgesen, P. Pieranski, and A.T. Skjeltorp, "Nonlinear phenomena in systems of magnetic holes," *Phys. Rev. Lett* **64**, 1425-1428 (1990).

[142] W.A. Shelton, K.D. Bonin, and T.G. Walker, "Nonlinear motion of optically torqued nanorods," *Phys. Rev. E* **71**(3), 036204 (2005).

[143] B. Lin, J. Yu, and S. Rice, "Direct measurements of constrained Brownian motion of an isolated sphere between two walls," *Phys. Rev. E* **62**(3), 3909 (2000).

[144] R. Schlapak, P. Pammer, D. Armitage, R. Zhu, P. Hinterdorfer, M. Vaupel, T. Fruhwirth, and S. Howorka, "Glass surfaces grafted with high-density poly(ethylene glycol) as substrates for DNA oligonucleotide microarrays," *Langmuir* **22**(1), 277-285 (2006).

[145] B.C. Carter, G.T. Shubeita, and S.P. Gross, "Tracking single particles: A user-friendly quantitative evaluation," *Physical Biology* **2**(1), 60-72 (2005).

[146] A.J. Goldman, R.G. Cox, and H. Brenner, "Slow viscous motion of a sphere parallel to a plane wall--I Motion through a quiescent fluid," *Chem. Eng. Sci.* **22**(4), 637-651 (1967).

[147] A. Davis, M. Kezirian, and H. Brenner, "On the Stokes-Einstein model of surface diffusion along solid surfaces: Slip boundary conditions," *J. Colloid Interf. Sci.* **165**(1), 129-140 (1994).

[148] K.P. Galvin, Y. Zhao, and R.H. Davis, "Time-averaged hydrodynamic roughness of a noncolloidal sphere in low Reynolds number motion down an inclined plane," *Phys. Fluids* **13**(11), 3108-3119 (2001).

[149] J.R. Smart, S. Beimfohr, and D.T. Leighton Jr., "Measurement of the translational and rotational velocities of a noncolloidal sphere rolling down a smooth inclined plane at low Reynolds number," *Phys. Fluids A* **5**(1), 13-24 (1993).

[150] E.M. Purcell, "Life at low Reynolds number," *Am. J. Phys.* **45**(1), 3-11 (1977).

[151] M.R. Falvo, J. Steele, R.M. Taylor, and R. Superfine, "Gearlike rolling motion mediated by commensurate contact: Carbon nanotubes on HOPG," *Phys. Rev. B* **62**(16), R10665 (2000).

[152] J. Walz and L. Suresh, "Study of the sedimentation of a single particle toward a flat plate," *J. Chem. Phys.* **103**(24), 10714-10725 (1995).

[153] J. Smart and D. Leighton, "Measurement of the hydrodynamic surface roughness of noncolloidal spheres," *Phys. Fluids A* **1**(1), 52-60 (1989).

[154] A.B. Djurisic and B.V. Stanic, "Modeling the temperature dependence of the index of refraction of liquid water in the visible and the near-ultraviolet ranges by a genetic algorithm," *Appl. Optics* **38**, 11-17 (1999).

[155] M.A. Brown and E.J. Staples, "Measurement of absolute particle-surface separation using total internal reflection microscopy and radiation pressure forces," *Langmuir* **6**(7), 1260-1265 (1990).

[156] M.E.J. Friese, T.A. Nieminen, N.R. Heckenberg, and H. Rubinsztein-Dunlop, "Optical alignment and spinning of laser-trapped microscopic particles," *Nature* **394**(6691), 348-350 (1998).

[157] A. Bishop, T. Nieminen, N. Heckenberg, and H. Rubinsztein-Dunlop, "Optical application and measurement of torque on microparticles of isotropic nonabsorbing material," *Phys. Rev. A* **68**(3), 033802 (2003).

[158] A.T. O'Neil and M.J. Padgett, "Rotational control within optical tweezers by use of a rotating aperture," *Opt. Lett.* **27**, 743-745 (2002).

[159] L. Paterson, M.P. Macdonald, J. Arlt, W. Sibbett, P.E. Bryant, and K. Dholakia, "Controlled rotation of optically trapped microscopic particles," *Science* **292**(5518), 912-914 (2001).

[160] Z. Luo, Y. Sun, and K. An, "An optical spin micromotor," *Appl. Phys. Lett.* **76**(13), 1779-1781 (2000).

[161] Y. Song, S. Chang, and J. Jo, "Optically induced rotation of combined Mie particles within an evanescent field of a Gaussian beam," *Jpn. J. Appl. Phys.* **38**, L380-L383 (1999).

[162] M. Capitanio, D. Normanno, and F.S. Pavone, "High-precision measurements of light-induced torque on absorbing microspheres," *Opt. Lett.* **29**(19), 2231-2233 (2004).

[163] L. Sacconi, G. Romano, R. Ballerini, M. Capitanio, M. De Pas, M. Giuntini, D. Dunlap, L. Finzi, and F.S. Pavone, "Three-dimensional magneto-optic trap for micro-object manipulation," *Opt. Lett.* **26**(17), 1359-1361 (2001).

[164] G. Romano, L. Sacconi, M. Capitanio, and F.S. Pavone, "Force and torque measurements using magnetic micro beads for single molecule biophysics," *Opt. Commun.* **215**(4-6), 323-331 (2003).

[165] D. Normanno, M. Capitanio, and F. Pavone, "Spin absorption, windmill, and magneto-optic effects in optical angular momentum transfer," *Phys. Rev. A* **70**(5) (2004).

[166] J.R. Robbins, D.A. Tierney, and H. Schmitzer, "Optically driven bacterial screw of Archimedes," *Appl. Phys. Lett.* **88**(2) (2006).

[167] M. Gitterman, "Order and chaos: Are they contradictory or complementary ?," *Eur. J. Phys.* **23**, 119-122 (2002).

[168] G. Videen and P. Chylek, "Scattering by a composite sphere with an absorbing inclusion and effective medium approximations," *Opt. Commun.* **158**(1-6), 1-6 (1998).

[169] Y. Yang, S. Wang, Z. Sun, and D.D. Dlott, "Near-infrared and visible absorption spectroscopy of nano-energetic materials containing aluminum and boron," *Propell. Explos. Pyrot.* **30**(3), 171-177 (2005).

[170] *CRC Handbook of Chemistry and Physics*, ed. D.R. Lide. 1997, New York: CRC Press.

[171] M.A. Ordal, L.L. Long, R.J. Bell, S.E. Bell, R.R. Bell, R.W. Alexander Jr., and C.A. Ward, "Optical properties of the metals Al, Co, Cu, Au, Fe, Pb, Ni, Pd, Pt, Ag, Ti, and W in the infrared and far infrared*," Appl. Optics* **22**(7), 1099-1119 (1983).

[172] X. Ma, J.Q. Lu, R.S. Brock, K.M. Jacobs, P. Yang, and X.H. Hu, "Determination of complex refractive index of polystyrene microspheres from 370 to 1610 nm*," Phys. Med. Biol.* **48**, 4165-4172 (2003).

[173] M. Meier and A. Wokaun, "Enhanced fields on large metal particles: Dynamic depolarization*," Opt. Lett.* **8**, 581-583 (1983).

[174] P.N. Shankar and M. Kumar, "Experimental determination of the kinematic viscosity of glycerol-water mixtures*," Proc. R. Soc. London, Ser. A* **444**, 573-581 (1994).

[175] R. Omori, K. Shima, and A. Suzuki, "Rotation of optically trapped particles in air*," Jpn. J. Appl. Phys.* **38**(7 A) (1999).

[176] U.O. Hafeli, R. Ciocan, and J.P. Dailey, "Characterization of magnetic particles and microspheres and their magnetophoretic mobility using a digital microscopy method*," Eur. Cells Mater.* **3**(Suppl. 2), 24-27 (2002).

[177] L. Hong, S.M. Anthony, and S. Granick, "Rotation in suspension of a rod-shaped colloid*," Langmuir* **22**(17), 7128-7131 (2006).

[178] T.G.M. van de Ven, *Colloidal Hydrodynamics*. 1989, New York: Academic Press Limited.

[179] F.Y. Yang, C.L. Chien, X.W. Li, G. Xiao, and A. Gupta, "Critical behavior of epitaxial half-metallic ferromagnetic CrO_2 films*," Phys. Rev. B* **63**(9), 092403 (2001).

[180] H. Liu, R.K. Zheng, Y. Wang, H.L. Bai, and X.X. Zhang, "Transport and magnetotransport properties of cold-pressed CrO_2 powder*," Phys. Status Solidi A* **202**, 144-150 (2005).

[181] G. Tas and H. Maris, "Electron diffusion in metals studied by picosecond ultrasonics*," Phys. Rev. B* **49**(21), 15046 (1994).

[182] L.L. Chase, "Optical properties of CrO_2 and MoO_2 from 0.1 to 6 eV*," Phys. Rev. B* **10**(6), 2226 (1974).

[183] H. Brändle, D. Weller, S.S.P. Parkin, J.C. Scott, P. Fumagalli, W. Reim, R.J. Gambino, R. Ruf, and G. Gäntherodt, "Magneto-optical properties of CrO_2," *Phys. Rev. B* **46**(21), 13889 (1992).

[184] E.J. Singley, C.P. Weber, D.N. Basov, A. Barry, and J.M.D. Coey, "Charge dynamics in the half-metallic ferromagnet CrO_2," *Phys. Rev. B* **60**(6), 4126 (1999).

[185] C.R. Wang, D.S. Yang, Y.Y. Chen, and J.C. Ho. "Magnetic and spin-glass-like behavior of CrO_2 nanoparticles," in *AIP Conference Proceedings*. 2006: AIP.

[186] Zhang, Xiaoyu, Chen, Yajie, Lu, Liya, Li, and Zhenya, "A potential oxide for magnetic refrigeration application: CrO_2 particles," *J. Phys. Condens. Matter* **18**(44), L559-L566 (2006).

[187] J.M.D. Coey and M. Venkatesan. "Half-metallic ferromagnetism: Example of CrO_2 (invited)," in *Journal of Applied Physics*. 2002: AIP.

[188] K. Keshoju, H. Xing, and L. Sun, "Magnetic field driven nanowire rotation in suspension," *Appl. Phys. Lett.* **91**(12) (2007).

[189] S. Biswal and A. Gast, "Rotational dynamics of semiflexible paramagnetic particle chains," *Phys. Rev. E* **69**(4), 041406 (2004).

[190] G. Korneva, H. Ye, Y. Gogotsi, D. Halverson, G. Friedman, J.C. Bradley, and K.G. Kornev, "Carbon nanotubes loaded with magnetic particles," *Nano Lett.* **5**(5), 879-884 (2005).

[191] B. Carrasco and J.G. de la Torre, "Improved hydrodynamic interaction in macromolecular bead models," *J. Chem. Phys.* **111**(10), 4817-4826 (1999).

[192] H. He, M.E.J. Friese, N.R. Heckenberg, and H. Rubinsztein-Dunlop, "Direct observation of transfer of angular momentum to absorptive particles from a laser beam with a phase singularity," *Phys. Rev. Lett.* **75**(5), 826-829 (1995).

[193] D. Grier and Y. Roichman, "Holographic optical trapping," *Appl. Optics* **45**(5), 880-887 (2006).

[194] S. Chapin, V. Germain, and E. Dufresne, "Automated trapping, assembly, and sorting with holographic optical tweezers," *Opt. Express* **14**(26), 13095-13100 (2006).

[195] H. Hah, J. Um, S. Han, and S. Koo, "New synthetic route for preparing rattle-type silica particles with metal cores," *Chem. Commun.*, 1012-1013 (2004).

[196] C. Xie and Li, "Raman spectra and optical trapping of highly refractive and nontransparent particles*,"* *Appl. Phys. Lett.* **81**, 951-953 (2002).

[197] F. Svedberg, Z. Li, H. Xu, and M. Käll, "Creating hot nanoparticle pairs for surface-enhanced Raman spectroscopy through optical manipulation*,"* *Nano Lett.* **6**(12), 2639-2641 (2006).

[198] J.W. Chan, H. Winhold, S.M. Lane, and T. Huser, "Optical trapping and coherent anti-Stokes Raman scattering (CARS) spectroscopy of submicron-size particles*,"* *IEEE J. Sel. Top. Quantum Electron.* **11**(4), 858-863 (2005).

[199] Y. Jiang, Y. Matsumoto, Y. Hosokawa, H. Masuhara, and I. Oh, "Trapping and manipulation of a single micro-object in solution with femtosecond laser-induced mechanical force*,"* *Appl. Phys. Lett.* **90**(6) (2007).

[200] J. Ye, L. Balogh, and T. Norris, "Enhancement of laser-induced optical breakdown using metal/dendrimer nanocomposites*,"* *Appl. Phys. Lett.* **80**(10), 1713-1715 (2002).

[201] H. Andersson and A. van den Berg, "Microfluidic devices for cellomics: A review*,"* *Sens. Actuators B* **92**(3), 315-325 (2003).

[202] A.H.J. Yang and D. Erickson, "Stability analysis of optofluidic transport on solid-core waveguiding structures*,"* *Nanotechnology* **19**(4), 45704-45714 (2008).

[203] E. Bouzarth, A. Brooks, R. Camassa, H. Jing, T. Leiterman, R. McLaughlin, R. Superfine, J. Toledo, and L. Vicci, "Epicyclic orbits in a viscous fluid about a precessing rod: Theory and experiments at the micro- and macro-scales*,"* *Phys. Rev. E* **76**(1) (2007).